GROWTH, CHARACTERIZATION AND APPLICATIONS OF METAL OXIDES ON GRAPHITIC SYSTEMS

A thesis submitted in partial fulfillment for the degree of
DOCTOR IN ADVANCED MATERIALS AND NANOTECHNOLOGY

Universidad Autónoma de Madrid

FACULTAD DE CIENCIAS

Author:

CARLOS MORALES SÁNCHEZ

Advisor:

LEONARDO SORIANO DE ARPE

Submission at the General Regestry of the Universidad Autónoma de Madrid on.

PhD Advisor: Prof. Dr. Leonardo Soriano de Arpe.

External Expert members of the Evaluation Tribunal:

- President: Rodolfo Miranda Soriano (Universidad Autónoma de Madrid)
- Secretary: María del Pilar Prieto Recio (Universidad Autónoma de Madrid)
- Chair 1: Virginia Altoe (Molecular Foundry, Berkeley Lab)
- Chair 2: José Ángel Martín Gago (Instituto de Ciencias de Materiales de Madrid–CSIC)
- Chair 3: Lucía Aballe Aramburu (ALBA synchrotron
- Substitute 1: Javier Méndez Pérez-Camarero (Instituto de Ciencias de Materiales de Madrid–CSIC)
- Substitute 2: Juan Rubio Zuarzo (ICMM-CSIC, Dpto BM25-SpLine en el ESRF)

Date of doctoral thesis defense: October 3rd 2019

carlos.morales@uam.es

Coatings, Interfaces, Nanostructures and Surfaces Group
Applied Physics Department, Faculty of Science
Institute of Materials Sciences Nicolás Cabrera
Universidad Autónoma de Madrid (UAM)

Grupo de Recubrimientos, Intercaras, Nanostructuras y Superficies
Departamento de Física Aplicada, Facultad de Ciencias
Instituto Universitario de Ciencias de Materiales Nicolás Cabrera
Universidad Autónoma de Madrid (UAM)

A mis padres y mis amigos. Mis pilares.

A los nadie sobre cuyos hombros reposan los cimientos de la Torre de Marfil de la ciencia.

"Los nadie: los hijos de nadie, los dueños de nada.
Los nadie, que cuestan menos que la bala que los mata"

Los Nadie, Eduardo Galeano

Contents

List of Acronyms

AFM …….…. Atomic Force Microscopy

ALD …….. Atomic Layer Deposition

CRM ……..... Confocal micro-Raman Spectroscopy

CVD ……. Chemical Vapor Deposition

EDX ……. Energy Dispersive X-ray spectroscopy

EELS …… Electron Energy Loss Spectroscopy

EXAFS ……. Extended X-ray Absorption Fine Structure

HAPEXS …….. High X-Ray Photoelectron Spectroscopy

HOPG ……... Highly Oriented Pyrolytic Graphite

IMFP ……. Inelastic Mean Free Path

KPFM ……..... Kelvin Probe Force Microscopy

MOVPE ……. Metalorganic Vapour Phase Epitaxy

NAP-XPS ……... Near Ambient Pressure X-Ray Photoelectron Spectroscopy

PEEM ……. Photoemission Electron Microscopy

PMMA …… Poly (methyl methacrylate)

PVD …… Physical Vapor Deposition

QNM……... Quantitative Nanomechanical Mapping

QUASES …… Quantitative Analysis of Surfaces by Electron Spectroscopy

SEM …… Scanning Electron Microscopy

STXM…….. Scanning Transmission X-ray Microscopy

TEM …… Transmission Electron Microscopy

TMA …… Trimethylaluminum

UHV ……. Ultra High Vacuum

UPS …….. Ultraviolet Photoelectron Spectroscopy

XANES ……..... X-Ray Absorption Near-Edge Spectroscopy

XAS …….……. X-Ray Absorption Spectroscopy

XPEEM …… X-Ray Photoemission Electron Microscopy

XPS ……... X-Ray Photoelectron Spectroscopy

List of Figures

Chapter 2. Experimental details

Chapter 3. CoO on HOPG: carbon gasification reaction

Chapter 4. Interaction of ZnO with HOPG and CVD graphene

Chapter 5. Free standing ultra-thin Al_2O_3 membranes

List of Tables

Chapter 2. Experimental details

Chapter 4. Interaction of ZnO with HOPG and CVD graphene

Chapter 5. Free standing ultra-thin Al_2O_3 membranes

Acknowledgements

Me permito el lujo de escribir el grueso de los agradecimientos en castellano dado que la inmensa mayoría de este viaje lo he llevado a cabo en mi país natal, España, y más precisamente en Madrid, donde reside la mayor parte de mi familia y mis amigos, de los cuales no todos tienen el inglés como primera lengua extranjera. Tampoco comparto la fórmula recurrida en ciertos trabajos de traducción de ciertas secciones, como por ejemplo los agradecimientos o la introducción, mientras que el conjunto de los resultados están escritos en una única lengua (aunque por motivos burocráticos de forma tanto la introducción como las conclusiones han sido traducidas al castellano). Creo que en un trabajo en el que se entremezcla una autoría puramente personal y una exposición de resultados, lo más concisa y rigurosa posible, es pertinente escribir cada sección en la lengua que más útil puede resultar. En este sentido, la exposición de resultados está escrita en inglés, con el objetivo de aumentar la proyección de la presente memoria y que un mayor público, internacional, pueda recurrir al presente trabajo a la hora de completar la discusión científica que se encuentra publicada en revistas internacionales. Por el contrario, las dos secciones de carácter más personal, los agradecimientos y el epílogo reflexivo en torno al estado actual del trabajo científico, las he preferido escribir en español. La razón de ello es simple: me encuentro más a gusto en mi lengua nativa cuando se trata de hablar desde dentro, desde el sentimiento.

***

La historia de cómo llegué a hacer la tesis doctoral bajo la dirección del profesor Leonardo Soriano es una maravillosa anécdota. Fue en una playa del Caribe, de una pequeña y perdida isla perteneciente a Nicaragua, Corn Island, donde le conocí. Es increíble lo pequeño que resulta a veces un mundo tan grande. A partir de ahí vino la beca Colaboración y posteriormente el doctorado a través de una ayuda de Formación de Profesorado Universitario (FPU). A Lalo no puedo sino agradecerle inmensamente que me haya introducido en el mundo del sincrotrón, de esas catedrales modernas de la ciencia experimental que me enamoraron desde el primer momento en que puede visitar una de ellas, aun durante el último año del grado. Podría haber empezado el agradecimiento hacia

Lalo por otros derroteros, como por ejemplo que haya establecido una red de contactos y colaboraciones tan amplia y que han enriquecido de forma tan decisiva el trabajo que tienes entre manos. O por sus consejos y dirección durante los cuatro años de trabajo. Todo ello es cierto, pero sin restar ni un ápice de importancia a ello, creo que sin duda la huella más duradera es la de transmitir la pasión por la física aplicada, el trabajo fino y bien hecho que requiere la física de superficies, y la necesidad imperiosa de entremezclar en la figura del científico una dosis de conocimiento de la teoría básica y otra dosis, a partes iguales, de pragmatismo experimental. Y esa receta creo que la encarna a la perfección el mundo de la radiación sincrotrón. Quiero agradecerte además que antes que jefe hayas sido una buena persona, no obsesionado con el trabajo y con los resultados, sino por el contrario, por el bienestar vital de los que trabajamos bajo tu dirección. Los resultados han acabado llegando, a pesar del desesperante primer año, y sin duda han sido por tu dirección laboral pero también humana. No han sido pocas las veces que me he tenido que ir antes del trabajo, sobre todo en los dos últimos años, por cuestiones personales, la mayoría por motivos ilusionantes y otras pocas por motivos tristes, las dos caras de una vida que se vive profundamente. Con la idea de que eran cuatro años y que lo importante era sacar adelante el proyecto, he podido trabajar con calma, recuperando ese tiempo en otro momento, muchas veces en jornadas maratonianas donde entraba y salía de noche de la universidad, aun en los meses estivales. Te quiero dar las gracias por tu paciencia, cariño y comprensión ante estas situaciones. Al final esta tesis demuestra que no es necesario anteponer trabajo al resto de cuestiones para obtener un correcto resultado.

A nivel científico y laboral, no me quiero olvidar de todas aquellas personas que me han enseñado técnicas y teoría para una mejor realización y entendimiento de mis experimentos. De esta forma, quiero acordarme de Carlos Palacio (UAM), Paco Yubero (ICMSE-CSIC), Javier Méndez (ICMM-CSIC), Adolfo del Campo (ICV-CSIC), Dietmar Leinen (UMA) y Daniel Granados (IMDEA-Nanociencia). Mención aparte requiere quizás Fernando Jiménez (IMDEA-Nanociencia), doctorando durante el mismo periodo que yo y que me ha crecido el grafeno que tanto se ha utilizado durante mi tesis. Los experimentos realizados en instalaciones de sincrotrón no hubiesen sido posibles sin la ayuda de los científicos de línea, Juan Rubio y Germán Castro en el ESRF y Lucía Aballe, Michael Foester, Carlos Escudero y Virginia Pérez-Dieste en ALBA. Muchísimas gracias a todos vosotros. Pilar Prieto (UAM) ha sido también una de esas personas que además

de ayudar a nivel científico y compartir jornadas sincrotroneras ha estado en esa imprescindible tarea de dar ánimos en los momentos más complicados en el laboratorio. Así mismo, agradecer a los profesionales del Servicio Interdepartamental de Investigación (SIdI-UAM) su trabajo para con las muestras que he medido en sus instalaciones haciendo uso de diferentes técnicas. Sin el servicio técnico de José Antonio Rodríguez en nuestro laboratorio hubieran sido necesarios muchos más meses de trabajo para llegar a los mismos resultados. Y finalmente, quisiera agradecer el servicio prestado por SEGAINVEX UAM, que gracias a su buen hacer y experiencia han facilitado el trabajo experimental.

Durante estos años, además de llevar a cabo la tarea investigadora, he tenido la oportunidad de formarme como profesor a través de la colaboración en tareas docentes. Quisiera acordarme de los profesores Carlos Palacio, Raúl de Palma, Máximo León, David Martín-Malero, Rafael Pérez y Nair López, que han compartido conmigo esta primera experiencia y me han ayudado a ser un mejor comunicador. Desde la otra cara de la moneda, en estos cuatro años he podido asistir a diferentes cursos. Me gustaría destacar el curso europeo HERCULES sobre grandes instalaciones, realizado en Grenoble en el 2017, y dar las gracias a todos los profesionales del ESRF, CNRS, CEA y SLS y demás organismos internacionales que lo hicieron posible y de los que tanto pude aprender.

I switch to English just for a second to remember the fantastic six months I spent at Berkeley, California, in 2018. First of all, I would like to stand out professor Miquel Salmerón, from whom I could enjoy his hospitality and learn a new way of doing science. The entire group, from of course Miquel to Yi-Hsien Lu, Heath Kersell and Judit Oliver-Meseguer, besides their scientific help, treat me so well that in every moment I felt as I was one more of the group. I thank all of them the opportunity to enjoy their beamtime at the ALS and SSRL facilities, what certainly has improved my experience. I really appreciate Yi-Hsien and Heath for their help on my work regarding the two proposals in which I worked at the Molecular Foundry: the study of CoO/HOPG re-oxidation final products and the Al_2O_3 ultra-thin membranes. Finally, I cannot forget the expertise and support of the Molecular Foundry staff, especially from Adam Schwartzberg, Virginia Altoe and Paul Ashby during the course of my stay.

No quiero olvidarme de todas las personas que forman parte del grupo MIRE en la UAM, y donde de alguna forma me empecé a formar realmente como científico en la realización del trabajo de fin de máster, un proyecto puramente experimental que solo

puede definirse como precioso. Muchísimas gracias a Paco Fernández, Fabrice Leardini, Eduardo Flores, José Ramón Ares, Carlos Sánchez e Isabel Jiménez, tanto por el fantástico ambiente de trabajo, como por las estimulantes discusiones científicas en las que pude participar. Quizás lo más bonito de esto es que a lo largo de estos años de tesis la amistad y la colaboración científica han continuado, compartiendo experimentos, artículos y congresos.

Finalmente quiero agradecer a los que siempre estuvieron ahí: mis amigos y sobre todo, mi familia. De ellos he recibido el apoyo y el ánimo que tanto hace falta en una carrera de fondo de cuatro años. En estos momentos en los que se terminan de escribir las páginas que condensan un trabajo tan largo en el tiempo, creo que es necesario recordar lo que hubo antes del primer día de tesis. Esto es, una estresante carrera académica durante el grado de físicas que me desquició completamente en el tercer año. Fueron mis padres, fundamentalmente, los que soportaron esta carga, los que me consolaron mis lágrimas nacidas de la frustración y la ansiedad. Gracias por animarme y por insistirme en que me lo tomase con calma, porque no había año perdido si extendía el grado y con ello mejoraba calidad de vida. No os hice caso, es cierto. Pero la presión que me quitasteis de encima fue determinante. Sería imposible nombrar a todos los que han sido mis pilares a lo largo de la vida y que han hecho que llegase hasta aquí: cuidadoras en prescolar, maestras, profesores en el instituto, amigos, familia… son tantos y tantas, que ante el riesgo de dejarme a alguien prefiero no dar ningún nombre. Muchísimas gracias a todos vosotros y vosotras, a las que estuvisteis a mi lado en alguna parte del camino hasta que la vida divergió caminos. Esta tesis se ha podido redactar gracias al trabajo invisible de todos vosotros.

Chapter 1
Introduction

"Physics is like sex: sure, it may give some practical results, but that's not why we do it."

Richard P. Fayman

1.1 The wide world of metal oxides

Firmly, it is very difficult to imagine a world without compounds as familiar to us as metal oxides. It is not only that oxygen and metallic elements are essential bricks in the composition and structure of the Universe, but also they occupy essential roles in a great variety of physical, chemical and biological processes. Actual technology and deep understanding of new fundamental physics is supported by the accumulative work done in this field by thousands of scientists from the last hundred years until our days.

However, if all metal oxides are considered under the same umbrella, we will be over simplifying the entire picture. These materials exhibit properties which are characteristic of conductors, semiconductors and insulators, so alone, or in combination with other materials, can be applied in a wide set of devices. This wide range of possibilities is supported by basically two factors: the different crystal structures, polymorphs and geometric arrangements that can be found, and the electronic structure of each metal together with its electronic interaction with the oxygen [1]. In this way, metallic elements almost cover the whole Periodic Table, excluding those with high electronegativity at the right side of the table. This means that electronic configurations as *ns* (alkali and alkaline earth metals), *nd* (transition metals) and *np* (post-transition metals) are going to interact in different ways with the oxygen electronic configuration $[He]2s^2 2p^4$, leading to different types of bonding (ionic, covalent or, more commonly, mixture of both models) and diverse electronic configurations of the new compuound. Therefore, different chemical and physical properties are expected as a function of the band structure of the solid.

The aim of this introduction chapter is not to discuss in detail the physics behind the metal/oxygen interaction and further consequences, but to give an overview of the

exciting world of metal oxides and the reason why this work has dealt with three different metal oxides (CoO_x, ZnO and Al_2O_3) in combination with graphite and graphene substrates. Thus, I encourage the reader to be patient and wait for the next chapters for a deeper discussion of all these items.

Continuing with the last question, both cobalt and zinc are transition metals, while aluminum is a post-transition metal, in some cases considered as metalloid. Regarding the transition metals, the multiple *nd* configurations lead to different properties depending on the number of electrons occupying the *d* orbitals, the *d-d* hybridization and correlation, metal-anion (*p-d*) hybridization, spin configuration and the crystal field of the oxide, among other aspects. Precisely, almost all the new phenomena discovered and studied on the field of condensed matter physics during the XX century (Pauli paramagnetism, Mott transition, high-T_c superconductivity, ferromagnetism, antiferromagnetism, low-spin/high-spin transitions, ferroelectricity, antiferroelectricity, colossal magnetoresistance, charge ordering, bipolaron formation...) are related with transition metals [2,3,4]. In the case of cobalt, its electronic configuration is [Ar] $4s^2$ $3d^7$, where the 3d electrons strongly hybridize and participate on the valence band. Two different cobalt oxides are stable: CoO (Co^{2+}, rocksalt structure) and Co_3O_4 (Co^{2+} and Co^{3+} in a spinel structure). Both oxides have been deeply studied in the last decades due to their high reactivity [5,6], becoming very interesting materials for gas sensors [7,8], magnetic devices [9], energy storage [10,11] and catalysis applications [12,13]. Precisely, the catalytic behavior of cobalt oxide is predominant in the prior art, without doubt due to its role at the *well-known* (at least at the macroscopic level) Fischer−Tropsch process [14]. However, the details at the atomic scale of the interactions between cobalt with different substrates and reactants continue under discussion.

On the other hand, the case of zinc oxide (ZnO, Zn^{2+}, mostly hexagonal wurtzita structure under standard conditions) is different precisely due to the zinc electronic configuration: [Ar] $4s^2$ $3d^{10}$ [15]. For this element the 3d orbital is complete, slightly participating in the valence band of the oxide [16,17]. This circumstance reduces its reactivity in comparison with cobalt oxides, although it is used in several chemical applications such as vulcanization of rubber photocatalysis [18] or antibacterial surfaces [19]. Nevertheless, its high bandgap (3.3 eV), large exciton binding energy (60 meV) and easiness to become n-dope with high electrical conductivity while preserving

transparency [20] allows ZnO to become an excellent material for many optoelectronic applications, such as solar cells [21], supercapacitors [22], sensors [23], etc.

Finally, the aluminum oxide (Al_2O_3, Al^{3+}, stable α-phase with a hexagonal close packed structure, corundum) is completely different from the other two oxides [24]. It is an electrical insulator, on the group of the ceramic materials, characterized by its hardness and strength [25]. It has been extensively used as substrate for multiple applications due to its poor reactivity with the enviroment [26,27,28]. In fact, as it will be presented in the next chapters, these properties can also be used in the nano-scale.

1.2 Graphitic systems as substrates: from monolayer to bulk

The 2010 Physics Nobel prize granted to Andre Geim and Konstantin Novoselov for their experiments with 2D graphene opened a new era for the materials science [29]. The movement from 3D to 2D materials has meant a revolution on the properties and applications expected for many compounds. Furthermore, their combination in multilayer structures with other 2D or 3D materials offers infinity of novel designs and applications [30].

Maybe graphene remains as the most amazing 2D material, among other reasons due to the time it has been studied by science and the amount of funds and human efforts dedicated to its investigation since its recent discovery. This carbon allotrope is a two-dimensional sheet of hexagonally arranged sp^2-hybridized atoms. It has incredible electrical [31] (high electrical conductivity as it is a zero-gap semi-conductor), mechanical [32] (it is said to be the strongest material ever tested, with a Young's Modulus of 1TPa) and optical [33] (absorption of approximately 2.3% of the white light) properties. In addition, the understanding of its electronic properties from fundamental quantum mechanics has extended the knowledge and domain of quasiparticles, as the graphene electrons propagate through the lattice losing their effective mass, resulting in quasiparticles which are described by a Dirac-like equation rather than the usual Schrödinger equation [34].

The number of stacked graphene layers determine the properties of the whole system. As it has been shown in the literature, changes on the Raman spectra are reported from one to seven layers, from which graphite bulk is measured [35]. This indicates a transition on the properties of 2D graphene through 3D graphite [36]. In particular, highly oriented pyrolytic graphite (HOPG) is the most realistic picture of graphene *bulk*. It

consist on stacked graphene sheets bonded by weak Van der Waals interactions. As before, due to the delocalized electron of each carbon atom, high electrical conductivities are measured (especially *in-plane*), while it is easily exfoliated due to the weak interactions between layers [37]. In fact the first isolated graphene was achieved by HOPG mechanical exfoliation.

The changes on the properties of sp^2 hybridized carbon with the thickness suggest other variations depending on the type of materials grown or deposited on the graphene sheets. In fact, graphene doping and functionalization by substrates, ultra-thin films or molecules has been the main purpose of many researches [38,39,40,41]. But this is a problem of two sides: the substrates, ultra-thin films or molecules in contact with graphene may also be influenced by it [42,43,44].

1.3 A complex interaction: graphitic-metal oxide interfaces

The previous last paragraph is the key for the present work. The cross interaction between substrates and ultra-thin films or nano-clusters can modify the properties of both. In fact, interfaces (solid/solid, solid/liquid and solid/gas) and surfaces (solid/vacuum) are gaining increased attention, as many properties can be modified in a controlled manner at this zones and many reactions happen precisely on them.

In this way, two different approaches can be pursued in the fields of applied physics and surfaces and interfaces science. First, the research on the fundamental interaction between substrates and deposited materials (interfaces). A deep understanding of how different materials interact and share charge and elements through the same frontier will determine a precise control of the mode of growth and also of the modification of chemical and physical properties [45]. It should be pointed that this precise control is indispensable for future applications on realistic devices. Besides, if the deposit is very thin, then the interface will be near enough to the surface, making possible that the ambient (gas or liquid) also interacts with both materials at the interface. The complexity is presented now in three angles (substrate-deposit-ambient) [46].

The second approach concerns the study of solid/gas and solid/liquid interfaces, much less investigated than the previous solid/solid interfaces due to the substantial interference from the bulk materials and the technical limitations regarding gas/liquid ambient. In this case, the actual challenge is the development of new devices and techniques which enable the measurement of these interfaces [47]. This kind of research

is especially important for catalytic processes. Catalysts performance is directly related to its atomic structure and composition, and therefore the ability to image catalysts *in situ* at the atomic scale is essential to develop a deep scientific understanding on how the catalyst composition and structure control the activity and selectivity in each chemical reaction. Thus, in the last years graphene membranes have been developed for XPS measurements performed at high pressures of solid/liquid and solid/gas interfaces [48,49], although chemical and mechanical stability of graphene limits further applications.

In summary, the interest to combine metal oxides and graphitic substrates seems clear. The great variety of types and properties of metal oxides combined with the impresive properties of graphene can stimulate our imagination and lead to new heterostructures with novel properties and uses. For instance, CoO_x nanoparticles could promote the nano-patterning of graphite and graphene surfaces at lower temperatures than other metallic nanoparticles [50]. The combination of graphene and ZnO may lead to the fabrication of devices useful for important technological applications such as energy production and storage [51,52]. And finally, the excellent mechanical properties and inert surface of Al_2O_3 can help to develop new research devices overtaking the shortfalls which presents graphene on separating vacuum from liquid and gas phases.

1.4 Aim and structure of this Ph.D. scientific work

The main aims of this work are the explanation of the interaction between different metal oxides and graphitic substrates, such as monolayer graphene and HOPG, and search for potential applications. For "interaction", we will understand the growth characteristics and the physical and chemical interactions between substrate and metal oxides. In particular, three different metal oxides will be studied. First it will be described and explained the CoO_x interaction with HOPG, specially the interface between both and the kinetic of the gasification reaction that occurs when the CoO/HOPG system is re-oxidized at low temperatures (~400 °C). Next point will be the ZnO interaction with both HOPG and graphene grown on polycrystalline Cu by chemical vapor deposition (CVD). We will focus on the influence of the initial state of graphene on the ZnO growth and the changes on the electronic coupling between graphene and Cu substrate due the presence of ZnO. Finally, we will deal with the development of ultra-thin Al_2O_3 membranes as electron transparent windows for atmospheric pressure photoelectron spectroscopy and atomic-

scale imaging. For this purpose suspended graphene sheets will be used as supports for the metal oxide.

In this way, the body of the work will be divided into four chapters. Chapter 2 will describe the experimental details: characterization of materials (oxides and substrates) and presentation of the fundamental principles of the experimental techniques used during the research. Each of the following chapters will be dedicated to one of the metal oxides mentioned. Chapter 3 corresponds to CoO_x. It is a continuation of the previous work started in the laboratory of the GRIN group, and complements with new results the Ph.D thesis presented by Dr. Daniel Díaz Fernández and supervised by Professor Leonardo Soriano de Arpe in 2015 [53]. As it was previously pointed out, in first place it will be presented a brief discussion about the CoO-HOPG interface, with new data from X-ray photoelectron spectroscopy (XPS), hard X-ray photoelectron spectroscopy (HAXPES) and near ambient pressure XPS (NAP-XPS) techniques. After this, the *in situ* study through NAP-XPS and X-Ray absorption spectroscopy (XAS) of the gasification reaction under oxygen atmosphere at 400 °C will be presented. *Ex situ* atomic force microscopy (AFM) and Kelvin probe force microscope (KPFM) has been used to characterize the interesting nano-structures (nanostrips and nanorings) appeared after the re-oxidation process.

Chapter 4 represents the main topic of the present work. Results regarding the ZnO growth on HOPG and graphene/Cu substrates will be presented. In this way, first it will be described the mode of growth of ZnO on HOPG and the interactions between oxide and graphite. The *in situ* study has been done by XPS, meanwhile AFM, scanning electron microscopy (SEM) and Raman spectroscopy measurements have complemented the discussion. In addition and for comparison purposes, the ZnO/HOPG system was subjected to the same re-oxidation process than for CoO/HOPG. Next point will be the characterization of the growth of ZnO on graphene/Cu, with especial emphasis on the early stages of growth of ZnO and the influence on them of the local initial state of graphene/Cu substrate. For this study, *in situ* XPS has been performed, complemented with *ex situ* AFM, SEM, Raman spectroscopy and photoemission electron microscopy (PEEM) measurements. Changes on electronic coupling between graphene and Cu after the ZnO growth will be discussed, relating them with the electronic uncoupling induced by water on the graphene/Cu system. With this purpose, mainly XPS, AFM, transmission electron microscopy (TEM) and Raman spectroscopy techniques have been used.

Finally, Chapter 5 is devoted to the development of Al_2O_3 membranes of 1-3 nm thickness for separating high vacuum from liquids and gases, and so be able to perform XPS measurements of solid/liquid and solid/gas interfaces. This chapter corresponds to the work done at the Lawrence Berkeley National Laboratory, under the supervision of Professor Miquel Salmerón. The oxide was first grown on a free standing support (graphene or Formvar on SiN membranes coated by Au/Cr) by atomic layer deposition (ALD). These membranes were characterized by means of *ex situ* XPS, AFM, SEM, TEM, Raman spectroscopy techniques, and were tested under realistic conditions performing *in situ* NAP-XPS measurements.

Each of the previous chapters will contain a discussion of the results and a last sections regarding the main conclusions. As a closing chapter, a critic evaluation of the progresses presented in this work in each of these scientific and technological fields will be discussed in order to emphasize the scientific context of the present work.

The last section, the only part written in Spanish, does not have any scientific content. Nevertheless, it is a personal discussion about Spanish national scientific policy, highlighting its weakness and strengths. In particular, the notions of *competitiveness* and *excellence,* which since the last decades define the *production* of science and the promotion rules based on*(ly)* the publication criteria, will be discussed. I really believe in the need of a review of how we do science in order to improve and try to fix the negative elements and reinforce the positive ones. This last section is not necessary for a consistent understanding of the work.

Bibliography

[1] V. E. Henrich, P. A. Cox; 1996; *The Surface Science of Metal Oxides*; New York, USA; Cambridge University Press

[2] J. Manhart, D. G. Schlom; "Oxide Interfaces-An Opportunity for Electronics"; *Science* 327, (2010); pp: 1607-1611; DOI: 10.1126/science.1181862.

[3] H. Y. Hwang, Y. Iwasa, M. Kawasaki, B. Keimer, N. Nagaosa, Y. Tokura; "Emergent phenomena at oxide interfaces"; *Nature materials* 11, (2012); pp: 103-113; DOI: 10.1038/nmat3223

[4] P. Yu, Y. H. Chu, R. Ramesh; "Oxide interfaces: pathways to novel phenomena"; *Materials Today* 15, (2012); pp: 320-327; DOI: 10.1016/S1369-7021(12)70137-2

[5] T. Takami; 2011, *Functional Cobalt Oxides: Fundamentals, Properties and Applications*; Singapore, Republic of Singapure; Pan Stanford Publishing

[6] B. Raveau, M. Seikh; 2012, *Cobalt Oxides: From Crystal Chemistry to Physics*; Weinheim, Germany; Wiley

[7] J. Park, X. Shen, G. Wang; "Solvothermal synthesis and gas-sensing performance of Co3O4 hollow nanospheres"; *Sensor. Actuator. B Chem*. 136, (2009); pp: 494-498; DOI: 10.1016/j.snb.2008.11.041

[8] J. Yang, W.-D. Zhang, S. Gunasekaran; "A low-potential, H2O2-assisted electrodeposition of cobalt oxide/hydroxide nanostructures onto vertically-aligned multi-walled carbon nanotube arrays for glucose sensing"; *Electrochim. Acta* 56, (2011); pp: 5538-5544; DOI: doi.org/10.1016/j.electacta.2011.03.087

[9] H. Xing, W. Kong, C. Kim, S. Peng, S. Sun, Z. Xu, H. Zeng; "Giant positive magnetoresistance in Co@CoO nanoparticle arrays"; *J. Appl. Phys*. 105, (2009); pp: 063920; DOI: 10.1063/1.3099594

[10] X.-C. Dong, H. Xu, X.-W. Wang, Y.-X. Huang, M.B. Chan-Park, H. Zhang, L.-H. Wang, P. Cheng; "3D Graphene-Cobalt Oxide Electrode for High-Performance Supercapacitor and Enzymeless Glucose Detection"; *ACS Nano* 6, (2012); pp: 3206-3213.; DOI: 10.1021/nn300097q

[11] T.-Y. Wei, C.-H. Chen, K.-H. Chang, S.-Y. Lu, C.-C. Hu; "Cobalt Oxide Aerogels of Ideal Supercapacitive Properties Prepared with an Epoxide Synthetic Route"; *Chem. Mater.* 21, (2009); pp: 3228-3233; DOI: 10.1021/cm9007365

[12] F. Jiao, H. Frei,; "Nanostructured Cobalt Oxide Clusters in Mesoporous Silica as Efficient Oxygen-Evolving Catalysts"; *Angew Chem. Int. Ed*. 48, (2009); pp: 1841-1844; DOI: 10.1002/anie.200805534

[13] Y. Liang, Y. Li, H. Wang, J. Zhou, J. Wang, T. Regier, H. Dai; "Co3O4 nanocrystals on graphene as a synergistic catalyst for oxygen reduction reaction"; *Nat. Mater*. 10, (2011); pp: 780-786; DOI: 10.1038/NMAT3087

[14] G. Melaet, W. T. Ralston, C-S. Li, S. Alayoglu, K. An, N. Musselwhite, B. Kalkan, and G. A. Somorjai; "Evidence of Highly Active Cobalt Oxide Catalyst for the Fischer-Tropsch Synthesis and CO2 Hydrogenation"; *J. Am. Chem. Soc*.,136, (2014); pp: 2260-2263; DOI: 10.1021/ja412447q

[15] C. F. Klingshirn, B. K. Meyer ,A. Waag, A. Hoffmann, J. Geurts; 2010; *Zinc Oxide: From Fundamental Properties Towards Novel Applications*; Berlin, Germany; Springer

[16] P. Mikheeva, G. M. Zhidomirov, S. F. Ruzankin, S. A. Leontiev, V. G. Devyatov, S. V. Koshcheev, A. E. Cherkashin; "Modeling the photoelectron spectra of the valence O-2p band of Zinc Oxide by the Xα-scattered wave method"; *J. Struct. Chem*, 38, (1997); pp: 732-741; DOI: 10.1007/BF02763885

[17] S. A. Leontiev, S. V. Koshcheev, V. G. Devyatov, A. E. Cherkashin, and P. Mikheeva; "Detailed XPS and UPS studies of the band structure of Zinc Oxide"; *J. Struct. Chem*, 38, (1997); pp: 725-731; DOI: 10.1007/BF02763884

[18] M. C. Yeber, J. Rodríguez, J. Freer, N. Durán, H. D. Mansilla; "Photocatalytic degradation of cellulose bleaching effluent by supported TiO2 and ZnO"; *Chemosphere* 41, (2000); pp: 1193-1197; DOI: 10.1016/S0045-6535(99)00551-2

[19] A. Sirelkhatim, S. Mahmud, A. Seeni, N. H. M. Kaus, L. C. Ann, S. Khadijah M. Bakhori, H. Hasan, D. Mohamad; "Review on Zinc Oxide Nanoparticles: Antibacterial Activity and Toxicity Mechanism"; *Nano-Micro Lett*.7, (2015); pp: 219-242; DOI: 10.1007/s40820-015-0040-x

[20] Ü. Özgür, Ya. I. Alivov, C. Liu, A. Teke, M. A. Reshchikov, S. Doğan, V. Avrutin, S.-J. Cho, H. Morkoç; "A comprehensive review of ZnO materials and devices"; *J. Appl. Phys*. 98, (2005); pp: 041301; DOI: 10.1063/1.1992666

[21] I. Gonzalez-Valls, M. Lira-Cantu; "Vertically-aligned nanostructures of ZnO for excitonic solar cells: a review"; *Energy Environ. Sci*., 2, (2009); pp: 19-34; DOI: 10.1063/1.1992666

[22] Y. Zhang, H. Li, L. Pan, T. Lu, Z. Sun; "Capacitive behavior of graphene-ZnO composite film for supercapacitors"; *J. Electroanal. Chem*. 634, (2009); pp: 68-71; DOI: 10.1016/j.jelechem.2009.07.010

[23] L. Zhu, W. Zeng; "Room-temperature gas sensing of ZnO-based gas sensor: A review"; Sens. Actuators, A, 267. (2017); pp: 242-261; DOI: 10.1016/j.sna.2017.10.021

[24] S. Ciraci , Inder P. Batra "Electronic structure of a-alumina and its defect states"; *Phys. Rev. B* 28, (1984); pp: 982-992; DOI: 10.1103/PhysRevB.28.982

[25] E. Dörre, H. Hübner, 1984, *Alumina: Processing, Properties, and Applications, Berlin*, Germany; Springer

[26] P. C. Bormant, K. R. Westerterp;" An Experimental Study of the Kinetics of the Selective Oxidation of Ethene over a Silver on a-Alumina Catalyst"; *Ind. Eng. Chem. Res.* 34, (1995); pp: 49-58; DOI: 10.1021/ie00040a002

[27] M. Trueba, S. P. Trasatti ; "γ-Alumina as a Support for Catalysts: A Review of Fundamental Aspects"; *Eur. J. Inorg. Chem.* 2005, (2005); pp: 3393-3403; DOI: 10.1002/ejic.200500348

[28] J. Y. Parka, J. M. Leeb, J. H. Jeb, S. S. Kim; "Early stage growth behavior of ZnO nanoneedle arrays on Al2O3 (0001) by metalorganic chemical vapor deposition"; *J. Cryst. Growth*, 281, (2005); pp: 446-451; DOI: 10.1016/j.jcrysgro.2005.04.035

[29] K. S. Novoselov, A. K. Geim, S. V. Morozov, D. Jiang, Y. Zhang, S. V. Dubonos, I. V. Grigorieva, A. A. Firsov; "Electric Field Effect in Atomically Thin Carbon Films"; *Science* 306, (2004); pp: 666-669; DOI: 10.1126/science.1102896

[30] A.Gupta, T. Sakthivel, S. Seal; "Recent development in 2D materials beyond graphene"; *Prog. Mater Sci.* 73, (2015); pp: 44-126 DOI: 10.1016/j.pmatsci.2015.02.002

[31] D. R. Cooper, B. D'Anjou, N. Ghattamaneni, B. Harack, M. Hilke, A. Horth, N. Majlis, M. Massicotte, L. Vandsburger, E. Whiteway, V. Yu; "Experimental Review of Graphene"; *ISRN Condensed Matter Physics*, 2012, (2011); pp: 1-56; DOI: 10.5402/2012/501686

[32] C. Lee, X. Wei, J.W. Kysar, J. Hone; "Measurement of the Elastic Properties and Intrinsic Strength of Monolayer Graphene". *Science* 321, (2008); pp: 385-388; DOI: 10.1126/science.1157996

[33] R. R. Nair, P. Blake, A. N. Grigorenko, K. S. Novoselov, T. J. Booth, T. Stauber, N. M. R. Peres, A. K. Geim; "Fine Structure Constant Defines Visual

Transparency of Graphene"; *Science* 320, (2008); pp: 1308-1308; DOI: 10.1126/science.1156965

[34] A. Bostwick, T. Ohta, T. Seyller, K. Horn, E. Rotenberg; "Quasiparticle dynamics in graphene"; *Nature Physics*, 3, (2007); pp: 36-40; DOI: 10.1038/nphys477

[35] A. C. Ferrari, J. C. Meyer, V. Scardaci, C. Casiraghi, M. Lazzeri, F. Mauri, S. Piscanec, D. Jiang, K. S. Novoselov, S. Roth, A. K. Geim; "Raman Spectrum of Graphene and Graphene Layers"; *PRL* 97, (2006); pp: 187401 DOI: 10.1103/PhysRevLett.97.187401

[36] B. Partoens, F. M. Peeters; "From graphene to graphite: Electronic structure around the K point"; *Phys. Rev. B* 74, (2006); pp: 075404; DOI: 10.1103/PhysRevB.74.075404

[37] See: http://nanoprobes.aist-nt.com/apps/HOPG%20info.htm

[38] G. Giovannetti, P. A. Khomyakov, G. Brocks, V. M. Karpan, J. van den Brink, P. J. Kelly "Doping Graphene with Metal Contacts"; *Phys. Rev. Lett.* 101; (2008); pp: 026803; DOI: 10.1103/PhysRevLett.101.026803

[39] Y. Shao, J. Wang, H. Wu, J. Liu, I. A. Aksay, Y. Lin; "Graphene Based Electrochemical Sensors and Biosensors: A Review"; *Electroanal*, 22, (2010); pp: 1027-1036; DOI: 10.1002/elan.200900571

[40] H. Liu, Y. Liu, D. Zhu; "Chemical doping of graphene"; *J. Mater. Chem.*, 21, (2011); pp: 3335-3345; DOI: 10.1039/C0JM02922J

[41] M. Pykal , P.Jurečka , F. Karlický, M. Otyepka; "Modelling of graphene functionalization"; *Phys. Chem. Chem. Phys.*, 18, (2016); pp: 6351-6372; DOI: 10.1039/C5CP03599F

[42] A. Mishchenko, J. S. Tu, Y. Cao, R. V. Gorbachev, J. R. Wallbank, M. T. Greenaway, V. E. Morozov, S. V. Morozov, M. J. Zhu, S. L. Wong, F. Withers, C. R. Woods, Y-J. Kim, K. Watanabe, T. Taniguchi, E. E. Vdovin, O. Makarovsky, T. M. Fromhold, V. I. Fal'ko, A. K. Geim, L. Eaves, K. S. Novoselov; "Twist-controlled resonant tunnelling in graphene/boron nitride/graphene heterostructures" *Nature Nanotechnology* 9, (2014); pp: 808-813; DOI: 10.1038/NNANO.2014.187

[43] R. S. Weatherup, L. D'Arsié, A. Cabrero-Vilatela, S. Caneva, R. Blume, J. Robertson, R. Schloegl, S. Hofmann; "Long-Term passivation of strongly interacting metals with single-layer graphene"; *J. Am. Chem. Soc.* 137, (2015); pp: 14358-14366; DOI: 10.1021/jacs.5b08729

[44] M. Schriver, W. Regan, W. J. Gannett, A. M. Zaniewski, M. F. Crommie, A. Zettl; "Graphene as a long-term metal oxidation barrier: worse than nothing" *ACS Nano*; 7, (2013); pp: 5763-5768; DOI: 10.1021/nn4014356

[45] X. Liu, C. Z. Wang , M. Hupalo , W. C. Lu , M. C. Tringides , Y. X. Yao, K. M. Ho; "Metals on graphene: correlation between adatom adsorption behavior and growth morphology"; *Phys. Chem. Chem. Phys.*, 14, (2012); pp: 9157-9166; DOI: 10.1039/C2CP40527J

[46] R. Wu, L. Gan, X. Ou, Q. Zhang, Z. Luo; "Detaching graphene from copper substrate by oxidation-assisted water intercalation"; *Carbon*, 98, (2016); pp: 138-143; DOI: 10.1016/j.carbon.2015.11.002

[47] C. Hao Wu, R. S. Weatherup, M. B. Salmeron; "Probing electrode/electrolyte interfaces in situ by X-ray spectroscopies: old methods, new tricks"; *Phys.Chem.Chem.Phys*.17, (2015); pp: 30229-30239; DOI: 10.1039/c5cp04058b

[48] R. S. Weatherup, B. Eren, Y. Hao, H. Bluhm, M. B. Salmeron; "Graphene Membranes for Atmospheric Pressure Photoelectron Spectroscopy"; *J. Phys. Chem. Lett.*, 7, (2016); pp: 1622−1627; DOI: 10.1021/acs.jpclett.6b00640

[49] J. J. Velasco-Velez, V. Pfeifer, M. Hävecker, R. S. Weatherup, R. Arrigo, C.-H. Chuang, E. Stotz, G. Weinberg, M. Salmeron, R. Schlçgl, A. Knop-Gericke "Photoelectron Spectroscopy at the Graphene-Liquid Interface Reveals the Electronic Structure of an Electrodeposited Cobalt/Graphene Electrocatalyst"; *Angew. Chem. Int. Ed*., 54, (2015); pp: 1-6; DOI: 10.1002/anie.201506044

[50] D. Díaz-Fernández, J. Méndez , A. del Campo, R.J.O. Mossanek, M. Abbate, M.A. Rodrıíguez, G. Domínguez-Cañizares, O. Bomatí-Miguel, A. Gutiérrez, L. Soriano; "Nanopatterning on highly oriented pyrolytic graphite surfaces promoted by cobalt oxides"; *Carbon*, 85, (2015); pp: 85-89; DOI: 10.1016/j.carbon.2014.12.049

[51] T.G.U. Ghobadi, M. Kunduraci, E. Yilmaz; "Improved lithium-ion battery anode performance via multiple element approach"; *J. Alloys Compd*, 730, (2018); pp: 96-102; DOI: 10.1016/j.jallcom.2017.09.297

[52] G. Zamiri, S. Bagheri; "Fabrication of green dye-sensitized solar cell based on ZnO nanoparticles as a photoanode and graphene quantum dots as a photo-sensitizer"; *J. Colloid Interface Sci.* 511, (2018); pp: 318-324; DOI: 10.1016/j.jcis.2017.10.026

[53] D. Diaz-Fernández; 2015; Ph.D Thesis "*Study of the growth and interaction of cobalt oxides on graphite and oxides surfaces*"

Chapter 2
Experimental details

"Play is experimenting with the accident"

Novalis

In this chapter, the most important features related with the materials, techniques and procedures used within this research will be described. It is not the aim to discuss deeply and in detail each section. There exists an extensive literature refered to metals oxides and graphitic substrates, as well as for the experimental techniques used in this work. Therefore, the purpose is to give a concise information to guarantee the understanding and reproducibility of the experiments described in the next chapters. Likewise, regarding the experimental techniques, a brief description of the fundamental principles will serve as a basis for the future discussion of the results.

2.1 Materials: metal oxides

2.1.1 Cobalt oxides

2.1.1.1 Cobalt oxides properties

Cobalt presents three oxidation states: Co^{2+}, Co^{3+} and Co^{4+}, but only two stable oxides: CoO and Co_3O_4 [1,2]. The last oxide is the most thermodynamically stable form under room conditions [3], consisting on a spinel structure with Co^{2+} cations tetrahedrally **c**oordinated and Co^{3+} cations octahedrally coordinated with a ratio of 1:2. It presents antiferromagnetic behavior at low temperatures (T_N=40 K), and at 950 °C it dissociates into CoO. On the other hand, CoO normally crystallizes with rock salt structure, where Co^{2+} ions are octahedrally coordinated. However, wurtzite [4] and zinc-blende [5] CoO structures have also been synthesized. It is antiferromagnetic (T_N = 290 K), and when heated in air over 610 °C, it oxidizes to Co_3O_4. Figure 2.1 plots the typical crystallographic structures of both oxides, while Table 2.1 summarizes the most important physical and structural properties.

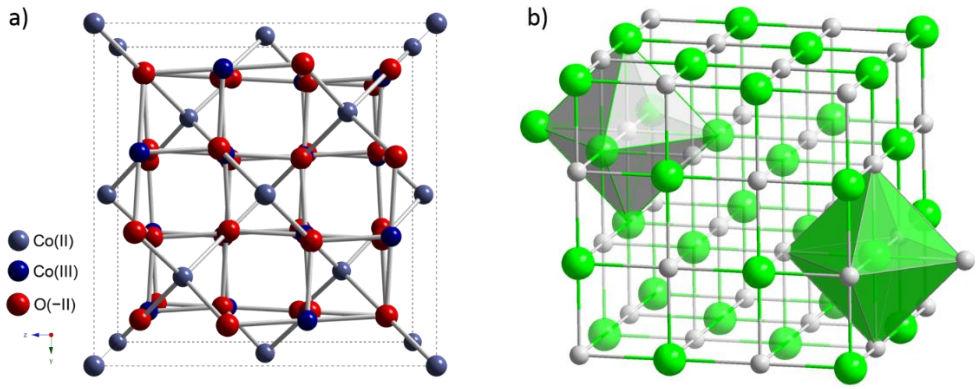

Figure 2.1 a) Co_3O_4 spinel crystallographic structure; b) CoO rocksalt crystallographic structure. Pictures taken from [6].

Parameter	Co_3O_4	CoO
Molar mass (g/mol)	240.80	74.93
Density (g/cm^3)	6.11	6.44
Crystal structures (point group)	Cubic, spinel structure (Fd3m)	Rock salt (Fm3m)
Lattice (Å)	a = 8.084	a = 4.260
Melting Point (°C)	895	1993

Table 2.1 Structural and physical parameters of cobalt oxides.

Cobalt oxides belong to the transition metal oxides group. Their stability and bonding can be explained by the Crystal Field Theory. In this picture the metallic atom is surrounded by the ligand atoms, which are represented by point negative charges. These repel each other and interact with the d-orbitals from the metal. In the case of an isolated metallic atom, the spherical symmetry implies that all d-orbitals have the same energy, i.e. are degenerate. But in the case of a solid, the ligands will break this symmetry as they are geometrically distributed around the metal. The degree of interaction between the ligands and d-orbitals is going to depend on the geometrical orientation of the molecule. In other words, the electrostatic field surrounding the metallic atom creates a splitting of the d-orbitals, and its value is known as crystal field splitting energy.

The previous introduction to the Crystal Field Theory [7] is necessary to successfully understand XPS and XAS measurements done on the early stages of growth of CoO_x on HOPG. As mentioned above, octahedral and tetrahedral geometries are presented in these oxides. Due to the spatial projection of the d-orbitals, under an

octahedral symmetry the $d_{x^2-y^2}$ and d_{z^2} orbitals increase their energy, while the d_{xy}, d_{yz} and d_{xz} orbitals decrease it. In the opposite way, tetrahedral symmetry provokes d_{xy}, d_{yz} and d_{xz} orbitals to increase the energy and $d_{x^2-y^2}$ and d_{z^2} orbitals to decrease it. Furthermore, if the crystal structure is distorted then the degeneracy will change. This description is summarized in Figure 2.2.

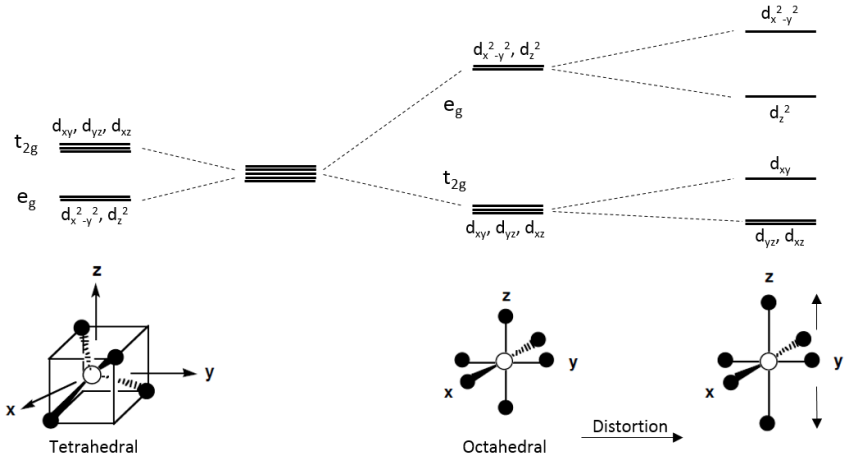

Figure 2.2 Separation of the d-orbitals in octahedral and tetrahedral symmetries. Picture taken from [8], minor modifications performed.

Another important aspect is the high-spin and low-spin character. In the case of Co the 3d-orbitals are only partially occupy, and the electron distribution depends on a compromise between the crystal field energy and the energy that take place on paring electrons and lose exchange (pairing/exchange energy). In the high-spin configuration the crystal field energy is lower than pairing/exchange energy, so it takes more energy to pair electrons than occupying orbitals with higher energies. By contrast, in low-spin configuration, the crystal field energy is higher and will favor the electron pairing at lower energetic orbitals. In chapter 3, the CoO is considered a high-spin octahedral complex, while Co_3O_4 is a combination of Co^{2+} ions in high-spin tetrahedral configuration and Co^{3+} ions in low-spin octahedral configuration, adopting a normal spinel structure.

2.1.1.2 Metallic Cobalt

Cobalt (Co) is a metallic element with atomic number 27, belonging to the transition metal category, group 9 and period 4 on the Periodic Table. Its electronic configuration is [Ar] $4s^2$ $3d^7$ and presents ferromagnetism, with a magnetic moment of 1.6-1.7 Bohr magnetons per atom. It is only found in the Earth's crust chemically bounded

to other elements, and in fact it is usually produced as a by-product of copper and nickel mining. In its metallic forms, Co is mainly used in the manufacture of magnetic, wear-resistant and high-strength alloys.

Cobalt wire of Ø 0.25 mm (supplied by Goodfellow [9], 99.99+ % purity) and cobalt rods (supplied by HMW Hauner [10], 99.99+ % purity), have been used as the precursor material for the growth of cobalt oxides.

Parameter	Cobalt
Molar mass (g/mol)	58.93
Density (normal conditions, g/cm^3)	8.90
Atomic configuration	[Ar] 4s2 3d7
Structure (space group)	hcp (P63/mmc) & fcc (Fm3m)
Phase transition temperature (°C)	450 °C
Lattice (Å)	hcp: a = b = 2.507, c = 4.069. fcc: 3.54
Melting Point (°C)	1495
Boiling Point (°C)	2927

Table 2.2 Structural and physical parameters of cobalt

2.1.2 Zinc oxide

2.1.2.1 Zinc oxide properties

Zinc has only one oxidation state, Zn^{2+}, affording ZnO [11,12]. The crystal structures shared by ZnO are wurtzite, zinc-blende and rocksalt, shown in Figure 2.3. The thermodynamically stable phase at normal conditions is hexagonal wurtzite, characterized by a tetrahedral coordination and a sp^3 covalent bonding with also ionic character. On the other hand, zinc-blende structure is only stabilized when growing on cubic substrates [13,14], while rocksalt is obtained at high pressures (10 GPa) from wurtzite [15]. The most important properties of ZnO are related with its optoelectronic applications due to its wide bandgap (E_g ~ 3.3 eV at room temperature) and a large exciton binding energy (~ 60 meV). Besides, the easiness on controlling the n-type doping level allows to change the electrical properties from semiconductor to metal while preserving optical transparency. Table 2.3 summarizes the most important physical and structural properties.

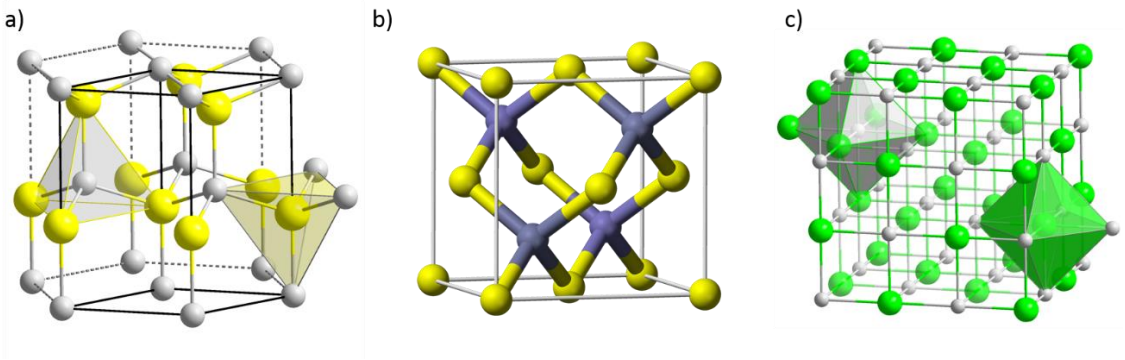

Figure 2.3 a) ZnO wurtzite crystallographic structure; b) ZnO zinc-blende structure; c) ZnO rocksalt structure. Pictures taken from [16].

Parameter	**ZnO**
Molar mass (g/mol)	81.41
Density (g/cm^3)	5,61
Crystal structure (point group)	Wutzite (B4)
Lattice (Å)	a = 3.249, c = 5.207
Melting Point (°C)	1975 °C

Table 2.3 Structural and physical parameters of ZnO.

The electronic configuration [Ar] $4s^2$ $3d^{10}$ of zinc determines a completely different electronic behavior of ZnO in comparison with cobalt oxides. In the ZnO, the 3d-orbitals are full and participate in a limited form in the Zn-O bonding. Theoretical and experimental works [17,18] show that the fraction of Zn 3d states participating in the Zn-O bond, and thus contributing to the photoemission from the O 2p-band, is only around 9%. Therefore, 3d states cannot be completely handle as core levels and will be slightly influenced by the chemical environment. On the other hand, the complete occupation of the 3d-orbitals restricts the number of final states available during the desexcitation of the hole after the photoemission of a Zn 2p electron, suppressing the appearance of shake-up contributions on the Zn 2p XPS spectra (see section 2.4.1). In addition, although the metallic and oxide initial and final states for Zn 2p states are different, their final binding energies in the XPS spectra are identical for both compounds [19]. This implies that in contrast with other transition metals (as Co), the 2p states cannot be used to identify the oxidation state of Zn. In fact, the $L_3M_{45}M_{45}$ Auger transition (see section 2.4.1) is sensitive to the chemical environment as the 3d-orbitals participate on this desexcitation

channel. Consequently, the oxidation state of Zn will be discussed by means of Zn-$L_3M_{45}M_{45}$ and Zn 3d XPS spectra rather than typical Zn 2p. These three regions are shown for ZnO and metallic Zn in Figure 2.4.

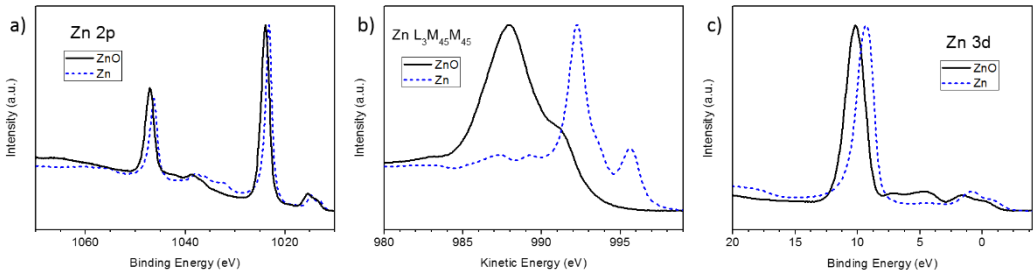

Figure 2.4 a) Zn 2p, b) Zn LMM, c) Zn 3d XPS spectra for both ZnO and metallic Zn.

2.1.2.2 Metallic Zinc

Zinc (Zn) is a post transition metal element with atomic number 30, group 12 and period 4 on the Periodic Table. Its electronic configuration is [Ar] $4s^2$ $3d^{10}$ and presents diamagnetism. Zn is the 24^{th} most abundant element on Earth, and it is usually in association with other metals such as copper or lead. Besides, it is typically bonded to sulfur and other heavy chalcogens rather than oxygen forming minerals. In its metallic form it is used as an anti-corrosion agent for coatings, brass alloys and as anodes for batteries.

Parameter	Zinc
Standard atomic weight	65.38
Density (normal conditions, g/cm^3)	7.14
Atomic configuration	[Ar] $4s^2$ $3d^{10}$
Structure (space group)	hcp (P63/mmc)
Phase transition temperature	450 °C
Lattice (Å)	hcp: a = b = 2.665, c = 4.069. fcc: 3.947
Melting Point (°C)	419.5
Boiling Point (°C)	907

Table 2.4 Structural and physical parameters of zinc

Zinc breads (supplied by Goodfellow [9], 99.99 % purity), have been used as the precursor material for the growth of ZnO.

2.1.3 Aluminum oxide

2.1.3.1 Aluminum oxide properties

Aluminum (Al) is a metallic element with atomic number 13, group 13 and period 3 on the Periodic Table. It presents three oxidation states: Al^{+}, Al^{2+} and the most common, Al^{3+} and an electronic configuration [Ne] $3s^2$ $3p^1$. Aluminum is the third most abundant element on Earth's crust and due to its high reactivity it is mostly found forming compounds, such as bauxite.

Regarding the oxides, Al_2O_3 is the solid stable form [20], although unstable solid Al_2O [21] and Al_2O and AlO gases are reported in the literature [22]. Al_2O_3 usually presents crystalline polymorphic phase α-Al_2O_3, known as corundum, where the oxygen ions form a nearly hexagonal close-packed structure with the aluminum ions filling two-thirds of the octahedral interstices. Other Al_2O_3 phases as cubic γ-Al_2O_3 has important technical applications [23]. This oxide is an electrical insulator, although has a relatively high thermal conductivity (~30 W/mK). It should be noted that Al_2O_3 has very high hardness and strength, so it finds applications as an abrasive and as component of cutting tools. It presents a low chemical activity with the environment, becoming a very popular substrate.

Parameter	**Al_2O_3**
Molar mass (g/mol)	101.96
Density (g/cm^3)	3.99
Crystal structure (point group)	Trigonal, hR30
Lattice (Å)	a = 4.785, c = 1.299
Melting Point (°C)	2072

Table 2.5 Structural and physical parameters of Al_2O_3.

2.1.3.2 Trimethylaluminum

Trimethylaluminum is an organoaluminum compound with chemical formula $Al_2(CH_3)_6$, abbreviated as TMA. At normal conditions is a dimer, with the two aluminum atoms surrounded by three methyl groups, sharing two of them by a methyl bridge. Thus, the carbon of the bridging methyl groups are surrounded each by 5 atom: two aluminum atoms and three hydrogen atoms [24]. TMA is used as a metalorganic source of Al in

different deposition techniques, such as metalorganic vapour phase epitaxy (MOVPE) for semiconductors compounds or atomic layer deposition (ALD) for Al_2O_3 [25].

In fact, TMA has been used as the metalorganic precursor for Al_2O_3 growth by ALD at the nano-fabrication facility of the Molecular Foundry.

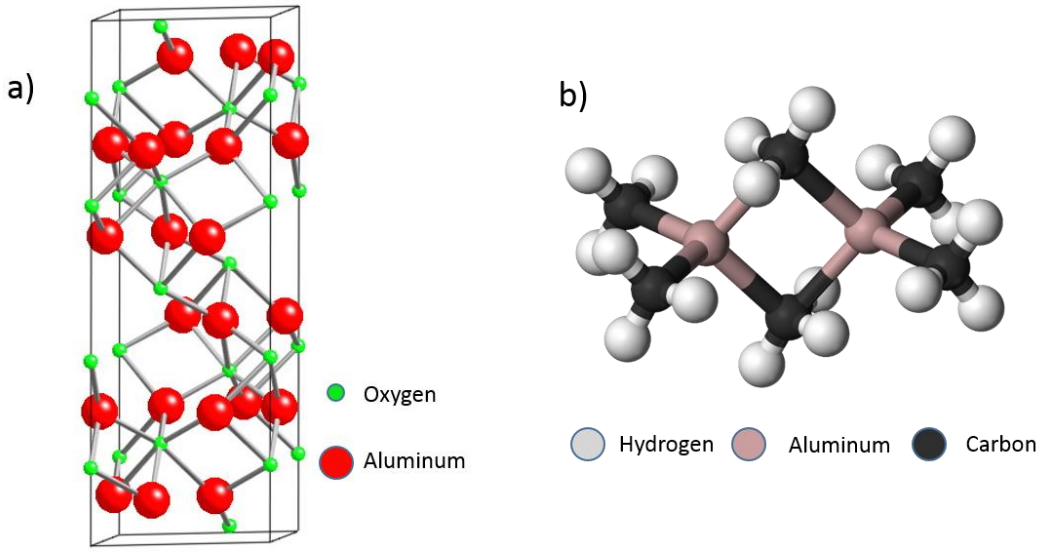

Figure 2.5 a) α-Al_2O_3 crystallographic structure; b) Trimethylaluminum dimer [26].

2.2 Substrates: HOPG and graphene

2.2.1 HOPG

Highly oriented pyrolytic graphite (HOPG) is a highly pure and ordered type of synthetic graphite characterized by a low mosaic spread angle. This implies that all the graphite crystallites are well aligned with each other, reaching mosaic spreads of less than 1 degree. HOPG structure is characterized by a stacked collection of single layers of carbon atoms with sp^2 hybridization, which are known as graphene. As it is shown in Figure 2.6, the lattice of these single layers consists of two equivalent interpenetrating triangular carbon sublattices A and B. Each carbon atom has three neighbors from the opposite sublattice, situated in the same plane and distance, spaced from each other by 120 degrees, meaning that atoms form a grid of hexagons with distances between atoms equal to 1.42 Å. Graphene layers follow a Bernal ABAB stacking, where the carbon atoms from sublattice A are situated directly above A-site carbon atoms of the previous layer, while B-sites are situated above the center of the hexagon. The distance between layers is equal to 3.35 Å. The interaction between carbon atoms from the same layer is very strong because of the covalent bonding of the sp^2 hybridization, while weaker Wan der

Waals forces are established between stacked layers. Due to this structure HOPG belongs to the group of lamellar materials, whose surface can be easily exfoliated.

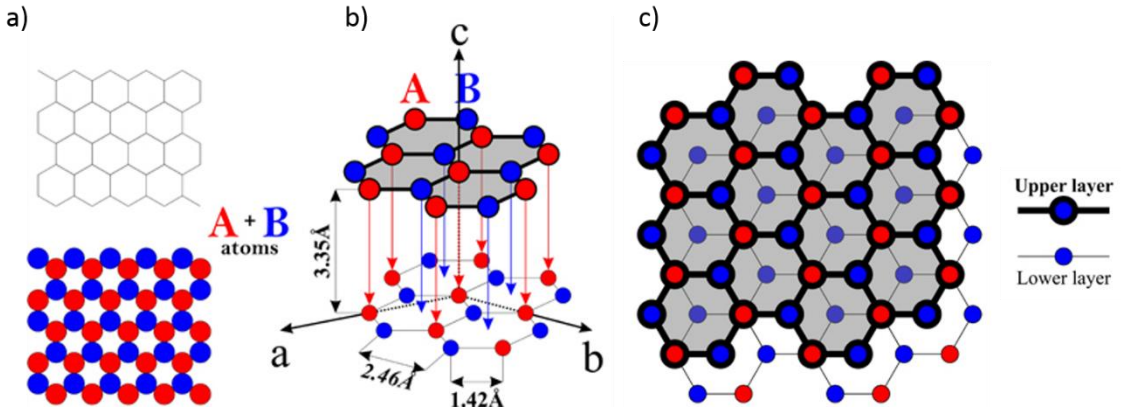

Figure 2.6 a) Graphene single layer hexagonal lattice with the A and B arrays of carbon atoms; b) 3D HOPG structure; c) top view of ABAB stacking [27].

The intrinsic anisotropy of HOPG derived from its structure implies different physical properties for the different crystallographic directions. In this way, thermal and electrical conductivities present higher values on the basal-plane direction (1800 ± 200 W/mK and $4 \pm 1 \cdot 10^{-5}$ Ωcm) than along the c axis direction (8±2 W/mK and 0.2 ± 0.05 Ωcm), respectively. From the chemical point of view HOPG remains stable at temperatures up to 500 °C in air and up to 2000-3000 °C under vacuum or inert environment. It also exhibits a general high chemical inertness.

The HOPG used in this work were from Bruker [28], with ZYB grade and 12x12x2 mm dimensions. In order to clean the HOPG substrates before the experiments, immediately before their introduction into vacuum conditions the surface was cleaved with scotch tape.

2.2.2 Graphene

Graphene is a 2D material recently re-discovered in 2004, with a honeycomb lattice of carbon atoms as described previously in section 2.2.1 and shown in Figure 2.6 a). The most remarkable properties of graphene are its high electrical conductivity as a zero-gap semi-conductor, its mechanical strength with a Young's Modulus of 1TPa, and finally the optical absorption of approximately 2.3% of the white light by only one layer of atoms.

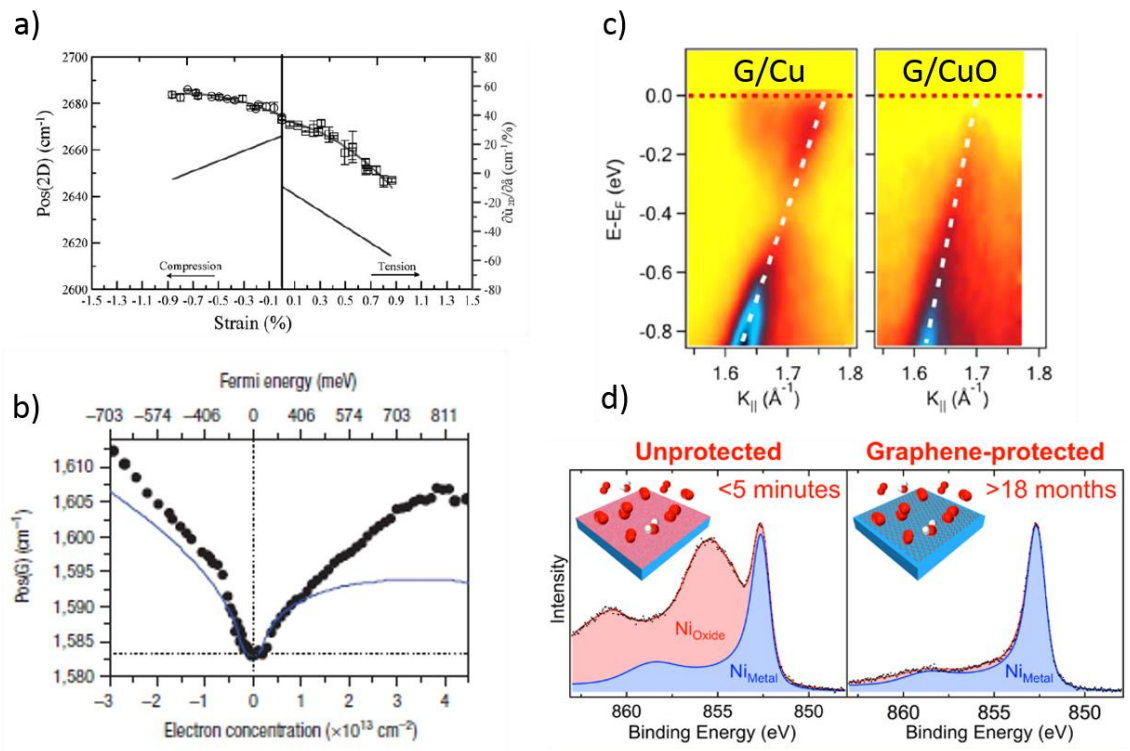

Figure 2.7 a) 2D band position of single layer graphene as a function of strain [29]; b) G band position of single layer graphene as a function of doping [31]; c) Detail of the Dirac cone at the K-point of the graphene Brillouin zone for graphene grown on Cu (111) (doped) and on oxidized Cu (111) (non-doped, uncoupled) [34]; d) graphene passivation of Ni surface [32].

The present work will focus mainly on two characteristics of graphene: the electronic interaction with the substrate and its impermeability to gases. Although both properties will be further described and discussed in the corresponding chapters, these lines can set some general ideas. Firstly, the electronic interaction between graphene and substrates and/or deposited materials will determine the grade and type of doping of the graphene due to charge transfer. This interaction can be measured by Raman spectroscopy and photoelectron spectroscopies. In the first case, the 2D band shift is basically sensitive to the strain of the net, while the G band shift is related with the grade of doping, as has been extensively studied [29,30,31]. On the other hand, C 1s spectra can be shifted depending on the electronic interaction with the substrate. As summarized for metals by Robert S. Weatherup et. al. [32], depending on the position of the d valence band states respect to the Fermi level [33], two different interactions are reported. In the case of Ni, Co, Fe, or Pd, the strong hybridization between π graphene states and metal d states leads

to the destruction of the linear dispersion of graphene at the K point, while for weak interaction, such as for Cu, Au, Ag or Pt, this linearity is preserved but charge transfer between metal and graphene normally shifts the Fermi level position, i.e. doping the graphene. Moreover, photoelectron spectroscopies measurements of the valence band show how the electronic coupling between graphene and the metallic substrate can be modified by the oxidation of the metal [34] or by the intercalation of other atoms, such as alkali species [35]. Figure 2.7 summarizes some of the above mentioned results.

In second place, graphene is almost impermeable to most gases [36] and therefore can be used as a passivation coating. However, this property strongly depends on the metallic substrate. In this way, for Ni and Co is a good passivation cover, but a wide range of reports show how for Cu substrates, the exposure to air conditions can lead to oxygen and water intercalation [37,38], and subsequent oxidation of the Cu. The impermeability of free standing graphene to gases has been also extensively studied and used for different applications [39].

2.2.2.1 Graphene/Cu (G/Cu)

The single layer graphene used in this work has been produced by chemical vapor deposition (CVD) on polycrystalline Cu foils. This low cost method is extensively used as it allows the growth of large-area of graphene with a low density of defects [40]. In fact, available commercial sheets of graphene are produced by this way. We distinguish two types of graphene/Cu substrates used in this work:

- **Non-commercial graphene/Cu from IMDEA Nanociencia** institute, Madrid, Spain [41]. This graphene sheets were grown on 25 mm thick polycrystalline copper foils. The CVD recipe consist firstly on heating the Cu foils to 1000 °C while flowing 100 standard cubic centimeters (sccm) of hydrogen. After temperature stabilization for 10 minutes, hydrogen flow was increased to 500 sccm and added 1 sccm of methane for 25 min in order to induce graphene growth. The furnace was then rapidly cooled down to room temperature while flowing 100 sccm hydrogen. The entire process was carried out at 10 mbar.

These G/Cu foils have been used as substrate in chapter 4 for the ZnO growth. The samples dimensions were 1x1 cm^2 and no heating for surface cleaning was applied in

order to avoid metal zinc contamination (see 2.3.1 section) and the modification of the pristine graphene, including its *natural* contamination by oxygen and water intercalation. In less than 24 hours after their growth, G/Cu substrates were kept in low vacuum conditions to avoid further Cu oxidation.

- **Commercial graphene/Cu** grown by CVD from Graphenea (18 μm foils, [42]), Graphene Supermarket (20 μm foils, [43]), ACS (45 μm foils, [44]) and Sigma Aldrich (18 μm foils, [45]). From these, Sigma Aldrich graphene was the best choice due to the lower development of defects and ruptures after the transfer process.

As it will be described in chapter 5, and also in the methodology section 2.5.3., this graphene has been used to prepare the free standing graphene that will serve as support for the later Al_2O_3 deposition. These G/Cu foils were used as received without any cleaning.

2.2.2.2 Free standing graphene

To create the free standing support, the graphene was transferred from commercial G/Cu foils by a free polymer process and also by the traditional way using PMMA (poly(methyl methacrylate)), supplied from Micro Chem [46]). For more details of the transfer method see section 2.5.2.

The SiN TEM perforated membranes (supplied from Norcada [47]) consisted of a 100 nm thick SiN window with either a 25 × 25 array of Ø 1 μm and 0.5 μm circular holes at a 2 and 1 μm pitch, respectively, or a 150 × 150 array of Ø 1 μm circular holes at a 2 μm pitch. The smaller array was used for characterization purposes, whereas bigger arrays were used on testing experiments at the ALS facility. These SiN membranes were coated with Au (30 nm)/ Cr (3nm) conductive layer by thermal evaporation.

In addition to graphene, Formvar (polyvinyl formal solution 0.25% on Ethylene Dichloride, supplied from Electron Microscopy Science (EMS) [48]) polymer has been also used as free standing material. The possibility to dissolve it in chloroform in addition to its electron transparency and easy operation, have extended its use as nanoparticles support for TEM measurements.

2.3 Experimental facilities

In the next lines the main scientific facilities where this work has been carried out will be presented. Only those where I have done, as a Ph.D. student, a direct and personal work will be presented. In any case, it is necessary to express my gratitude to those scientific experts, groups and facilities where part of the measurements have been done but not directly by me, although I have been present and I have tried to understand and learn the theoretical and practical knowledge. This is the case of AFM measurements (Instituto de Ciencias de Materiales de Madrid, ICMM-CSIC), confocal Raman microscopy (Instituto de Cerámica y Vidrio, ICV-CSIC), TEM, SEM-EDX mapping and XPS microscopy (Servicios Centrales de Apoyo a la Investigación, SCAI, Universidad de Málaga) and SEM (SiDI, Universidad Autónoma de Madrid). I encourage the reader to re-visit the acknowledgements.

2.3.1 GRIN: CLAM 4-Camarón and Chambao systems

2.3.1.1 CLAM 4-Camarón System

The main heart of the work related with cobalt and zinc oxides has been carried out at the CLAM 4-Caramon system, which belongs to the GRIN group, at the Applied Physics Department of the Universidad Autónoma de Madrid (UAM), Spain. The system offers the possibility to combine different growth, cleaning and annealing processes under controlled atmosphere and *in situ* XPS measurements. For these purposes the system is divided into three independent chambers, which have been designed by our group and fabricated in SEGAINVEX workshops:

- Introduction chamber: small chamber equipped with a Pfeiffer turbo-molecular pump (Pfeiffer TMU 071P, pump speed: 70 l/s) that allows quick introduction of samples from atmospheric pressure to high vacuum (10^{-7}-10^{-8} mbars). The pressure is controlled by a full range gauge (Pfeiffer, IKR 251).

- Preparation chamber: this camber has cylindrical symmetry to allow the installation of different growth and treatment techniques. The flanges are distributed in vertical planes to allow the simultaneous combination of different physical processes. The position and orientation of the sample holder on the

cylinder axis can be changed by a linear bar attached to a magnetic manipulator controlled from outside. This movement system is also used for transferring the samples between the three chambers. The preparation chamber has a Zn evaporator (see section 2.3.1) attached to a variable leak valve of pure oxygen. The pressure is controlled by a cold cathode gauge (Pfeiffer, IKR 270). It also has a Penning ion gun (SPECS IQP 10/63) used for the cleaning of the samples with Ar^+ ions, and a heating system made up by an halogen bi-pin lamp bulb (24 V, 275 W) that enables to reach temperatures up to 400 °C. A sapphire window in the same plane as the heating system allows to monitor the temperature by an infrared pyrometer (Lumasense IMPAC IP140-LO, 100-700 °C). In addition, a quadrupole mass spectrometer (Pfeiffer PrismaPlus QMG 220 M, resolution: 0.5 a.m.u.) makes possible to study the composition of the chamber atmosphere during different sample treatments. Finally, the chamber is pumped by a turbo pump (Varian TV301, pump speed: 300 l/s) and the base pressure is in the range 10^{-9}-10^{-8} mbars. Both turbo pumps, from the introduction and preparation chambers, share the same backing pump (nXDS scroll pump, Edwards).

Figure 2.8 General view of the CLAM4-Camarón system.

- Analysis chamber: the XPS measurements are done in this chamber. It has an ionic pump (Varian VacIon Plus 500, model 919-0106, pump speed: 410 l/s) and a titanium sublimation pump (Varian 916-0017, maximum sublimation rate: $9 \cdot 10^{-2}$ gr/h). Its working pressure is usually in the range of 10^{-9} mbar, i.e. ultra-high vacuum condition (UHV). The XPS system consists on a X-ray twin anode source (model number: XR3E2), with Mg and Al anodes, and a 9 channeltron hemispherical analyzer (CLAM-4, ThermoVG Scientific). Besides, the chamber is also provided with an electron gun (SPECS PU-EQ22) and a UV source (SPECS UVS300) for UPS, although these instruments have not been used in this work.

2.3.1.2 Chambao System

The Chambao system is a sputtering magnetron growth chamber with cylindrical symmetry where most of the flanges point to the focus of the chamber. The sample holder is situated at this precise point and can rotate around its axis while is heated up to 300 °C by three halogen lamp bulbs. However, during this work its design has been slightly modified in order to allow the re-oxidation of CoO/HOPG at 400 °C.

In this way, an e-beam evaporator (dual e-beam evaporator e-flux 2, from Tectra) has been installed to evaporate metallic Co under oxygen atmosphere. Oxygen was delivered through a stainless still pipe connected to a leak valve and with the outlet very close to the HOPG surface. The rotation and heating systems were replaced by a fixed sample holder formed by a mineral insulated heater wire (Thermocoax [49], 50 cm long and 1.0 mm Ø) embedded between two copper discs, reaching temperatures up to 500 °C. The temperature was controlled by a thermocouple situated under the sample and by an infrared pyrometer (Lumasense IMPAC IP140-LO, 100-700 °C) installed on a sapphire wiewport. The chamber is equipped with a turbo pump from Varian (Turbo.V 300 HT, pump speed: 280 l/min) supported by a backing pump (nXDS scroll pump, Edwards). The base pressure is around 10^{-8} mbar and is controlled by a full range gauge (Leybold Ionivac, ITR 90).

2.3.2 LBNL: MSD and Molecular Foundry

Chapters 3 and mostly 5 include the results obtained during the Ph.D. stay at the group of Professor Miquel Salmerón in the Material Science Division (MSD) of the

Lawrence Berkeley National Laboratory (LBNL). This multiprogram scientific campus belongs to the U.S. national laboratory system and is supported by the U.S. Department of Energy through its Office of Science [50]. The main research lines of Professor Miquel Salmerón's group are devoted to the study of the chemical, electronic, and mechanical properties of surfaces and interfaces at the nano-scale [51].

The Molecular Foundry is a Department of Energy-funded nanoscience research facility situated at the LBNL campus and it is open to scientist from around the world through a competitive peer-reviewed proposal process [52]. It has up to seven different facilities, covering a wide range of fields related to theoretical and experimental approaches to applied biology, chemistry, condensed matter physics and material science. These seven facilities are not isolated from each other, but interrelated in multidisciplinary projects in order to take advantage of the expertise gathered in these facility from the scientific and technician staff. In particular, in this work will be presented growths and measurements done in the Imaging and Manipulation of Nanostructures Facility, which give access to state-of-the-art characterization techniques, and the Nanofabrication Facility, dedicated to advanced deposition and fabrication techniques. The scientific equipment used from these facilities was:

- Imaging and Manipulation of Nanostructures Facility: it has a chemical room for sample manipulation equipped with a Denton Vacuum DV-502A thermal evaporation chamber used for Au/Cr coatings on SiN TEM grids and a plasma cleaner PDC 32G. In addition, deionized water (Milli Q Advantage A10) was used. This facility also harbors AFM (AFM Veeco: Ikon 8, from Bruker), SEM (Gemini Ultra-55 Analytical Field Emission Scanning Electron Microscope, from Zeiss), TEM (2100-F 200 kV Field-Emission Analytical Transmission Electron Microscope, from JEOL), XPS (K-Alpha Plus XPS/UPS from Thermo Fischer Scientific) instruments.

- Nanofabrication Facility: it has a 450 m^2 cleanroom, mainly Class 1000, including Class 100 and Class 10 areas for nanofabrication/lithography, clean measurements and electron beam lithography. The Oxford FlexAl -Plasma Enhanced ALD resides within the cleanroom.

In addition, a limited number of Raman spectroscopy measurements (Horiba Jobin Yvon LabRAM ARAMIS automated scanning confocal Raman microscope) were performed at the Inorganic Nanostructures Facility.

In the next chapters several measurements done at the Molecular Foundry and MSD facilites will be discussed. Chapter 3 presents the Molecular Foundry KPFM measurements done on CoO/HOPG samples that were grown and re-oxidized at the Professor Miquel Salmerón laboratories at the MSD. On the other hand, chapter 5 mostly condense the work done on the Molecular Foundry facilities related with the Al_2O_3 ultra-thin membranes. For more technical information see sections 2.3 and 2.4.

2.3.3 Synchrotron facilities

Synchrotron radiation has become an indispensable tool for biology, medicine, chemistry, condensed matter physics and environmental and material sciences. The ability to use it among so different fields is due to the emitted continuum spectra, from infrared to hard X-rays, and its high brilliance, defined by the compromise of highly parallel and narrow beams of X-rays with very high flux of photons. The combination of these two characteristics, among the control of other features such as light polarization or pulsed emission, allows understanding the flexibility of these kind of facilities and the consequent development of an entire new set of spectroscopic and imaging techniques not available in the usual laboratories.

The synchrotron radiation is emitted by bunches of relativistic electrons which are accelerated by deflecting their trajectory. The kinetic energy of these electrons determine the spectrum energy of the emitted photons, while their relativistic velocities induce the concentration of the radiation along a very narrow cone in the direction of their movement. The production of these relativistic electron bunches consists, firstly, on their generation by thermionic emission from a hot filament, followed by the acceleration using a linear accelerator (LINAC). A booster ring brings these electrons to their final kinetic energy and are finally introduced into the storage ring. A set of magnetic quadrupoles and sextupoles maintain the electrons focused, while the magnetic bends (magnetic dipoles) and the insertion devices (undulators and wigglers) modify the straight trajectory of the electrons, emitting radiation. The energy lost in these processes is recovered by a radio frequency cavity. The beamlines were experiments are done run off tangentially to the storage ring, along the axes of the insertion devices and tangentially at bending magnets.

Before the sample, a set of mirrors and monochromators of different classes are used to control de radiation characteristic that will be used during the measurement. More information about the operation, characteristics and possible experimental techniques used on of this large facilities can be found elsewhere [53,54].

In the present work three different facilities have been used, ESRF (European Synchrotron Radiation Facility, Grenoble, France), ALBA (Cerdanyola del Vallès, Spain) and ALS (Advanced Light Source, Berkeley, USA). The principle characteristics of these facilities are summarized on Table 2.6.

Storage ring specifications	**ESRF**	**ALBA**	**ALS**
Energy (GeV)	6	3	1.9
Current, top-up (mA)	300	250	500
Brilliance (photons/(s/mm^2 mrad^2 0.1% BW))	10^{21}	10^{18}	$3{\cdot}10^{18}$
Circunference radius (m)	844	269	197
Beamlines	44	8	44

Table 2.6 Main characteristics of the synchrotron facilities used in this research.

2.3.3.1 SpLine (ESRF, Grenoble, France)

SpLine is a beamline supported by the Spanish government (Collaborating Research Group) that started its operation in 2005. It is regulated by a contract between the Spanish Ministerio de Educación y Cultura, responsible for the beamline operation and its accessibility to the Spanish scientific community, and the ESRF. It is a hard X-ray line with two branches dedicated to X-ray absorption experiments (branch A) and high resolution X-ray diffraction (branch B), which operate in alternate mode [55]. In this work only branch B has been used for HAXPES measurements (see section 2.4.3). The main beamline parameters are displayed on Table 2.7. For more technical information see section 2.4.3.

2.3.3.2 CIRCE Line (ALBA, Cerdanyola del Vallès, Spain)

CIRCE beamline is dedicated to photoemission experiments in the range of soft X-rays (100-2000 eV). A couple of deflecting mirrors deflect the photons into one of the two endstations that form the beamline. The NAPP branch is dedicated to near ambient

pressure XPS and XAS for catalysis and surface science, while PEEM branch is dedicated to spectromicroscopy combining different techniques such as XMCD, XPEEM, LEEM or LEED in order to follow the evolution of early stages of growths, magnetic domains and surface chemical inhomogeneities [56]. Measurements from both endstations are present in this work. The main beamline parameters can be found in Table 2.8. For more technical information see section 2.4.2, 2.4.4 and 2.4.5.

Parameters	**SpLine, branch B**
Monochromator	Si (111) double crystal monochromator
Energy range (keV)	5-45
Flux (photons/s)	10^{13}
Energy resolution ΔE/E	$1.5 \cdot 10^{-4}$
Working pressure (mbar)	10^{-10} (analyser), 10^{-8} (chambers)
Focus size, hor. x vert. (μm)	300 x 100

Table 2.7 Main characteristics of SpLine beamline, branch A

Parameters	**CIRCE, NAPP**	**CIRCE, PEEM**
Monochromator	Variable angle plane grating monochromator	
Energy range (eV)	100-2000	
Flux (photons/s)	10^{13}	
Energy resolution ΔE/E	$1 \cdot 10^{-4}$	
Working pressure (mbar)	10^{-10} - 25	10^{-8}
Focus size, hor. x vert. (μm)	20 x 100	3.2 x 36

Table 2.8 Main characteristics of CIRCE beamline, NAPP and PEEM endstations.

2.3.3.3 11.0.2 APPES-II (ALS, Berkeley, USA)

Beamline 11.0.2 is dedicated to molecular environmental science. It has two different branches: the first one covers microscopy and imaging techniques (STXM and pictography), while the second one covers spectroscopy techniques such as XPS and XAS from ultra-high vacuum conditions to near ambient pressures (~10 mbar). During this work only the NAP-XPS branch was used. Actually, it has two different endstations for standard NAP-XPS (APXPS-1) measurements and a second one for wet spectroscopy (APXPS-2), each one with its own differentially pumped analyzer [57]. The results

presented in chapter 5 are from the second endstation. For more technical information, see section 2.4.4.

Parameters	11.0.2 - APXPS-2
Monochromator	Style plane-grating monochromator
Energy range (eV)	90-2000
Flux (photons/s)	10^{10}
Energy resolution ΔE/E	$3 \cdot 10^{-4}$
Working pressure (mbar)	10^{-6}
Focus size, hor. x vert. (μm)	200 x 60

Table 2.9 Main characteristics of 11.0.2 beamline, NAP-XPS branch

2.4 Deposition techniques

Three different metal oxides have been grown on graphitic substrates. The deposition technique used for each material depended on the final purpose of each single oxide/substrate system and on the physical and chemical properties of the source used for the deposition of each oxide. In this way, three different deposition techniques have been used. In the next lines a brief description of these techniques and the role played by them in this work will be presented.

2.4.1 Thermal evaporation

Thermal evaporation (also known as thermal vaporization) belongs to the group of Physical Vapor Deposition (PVD) techniques, defined by the fact that only physical processes take part on the substrate coating. Therefore, it consists on the formation of a vapor by heating the target material and the subsequent deposition of the evaporated material on the surface of the substrate. This process can be done under a reactive atmosphere, obtaining a coating of a different compound from the original target. The advantage of this deposition method lies on the low energy of the particles arriving to the surface, as atoms leave the heated target with thermal energies given by $\frac{3}{2}kT$, where k is the Boltzmann constant and T the absolute temperature [58], and thus, implying energies below 0.15 eV. The evaporation of the target material can take place after melting (gas/liquid interface) or by sublimation directly from the solid (gas/solid interface),

depending on the relation between meting point and vapor pressure. Precisely, the vapor pressure parameter is defined as the partial pressure at which equilibrium between the gas and solid or liquid phases is reached given a fixed temperature. The relationship between vapor pressure (P) and temperature (T) is described by the Antoine equation (which is derived from the well-known Clausius-Clayperon equation), where A, B and C are material dependent constants:

$$\log_{10} P = A - \frac{B}{C+T} \quad \text{(Eq. 2.1)}$$

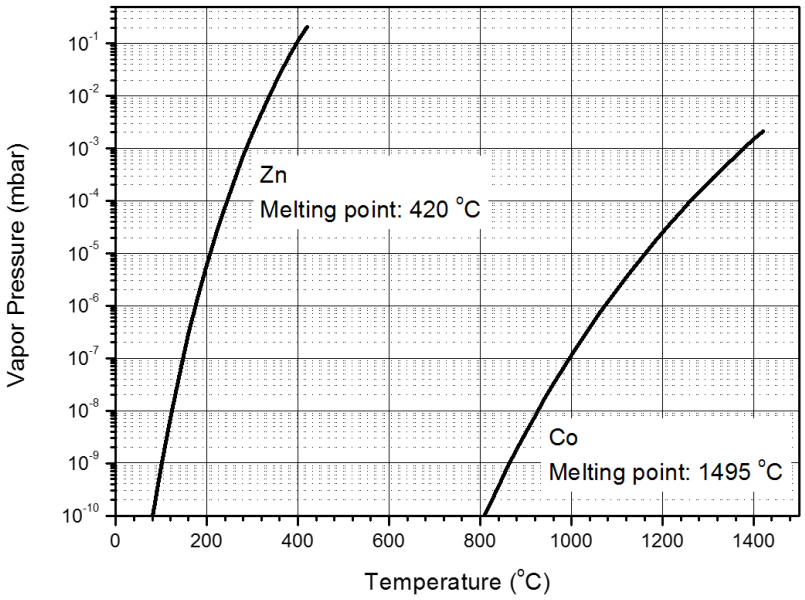

Figure 2.9 Cobalt and zinc vapor pressures

Regarding the experiments performed in this research, the two materials which have been evaporated using this technique under oxygen atmosphere in order to deposit their respective oxides were Co (P_{O2} 10^{-5} mbar) and Zn (P_{O2} 10^{-3} mbar). Figure 2.9 shows the vapor pressures as a function of temperature for both materials. As it can be seen, the vapor pressure is much higher for Zn than for Co given a certain temperature, so it has been much more difficult to control the evaporation rate of Zn. In fact, metallic Zn is considered a *vacuum poison* as its deposition on the chamber walls and elements will cause the contamination of the specimen under study if any part of the camber, included the sample, is heated. This contamination problem has been a limitation for applying thermal treatments to clean or re-oxidize the samples.

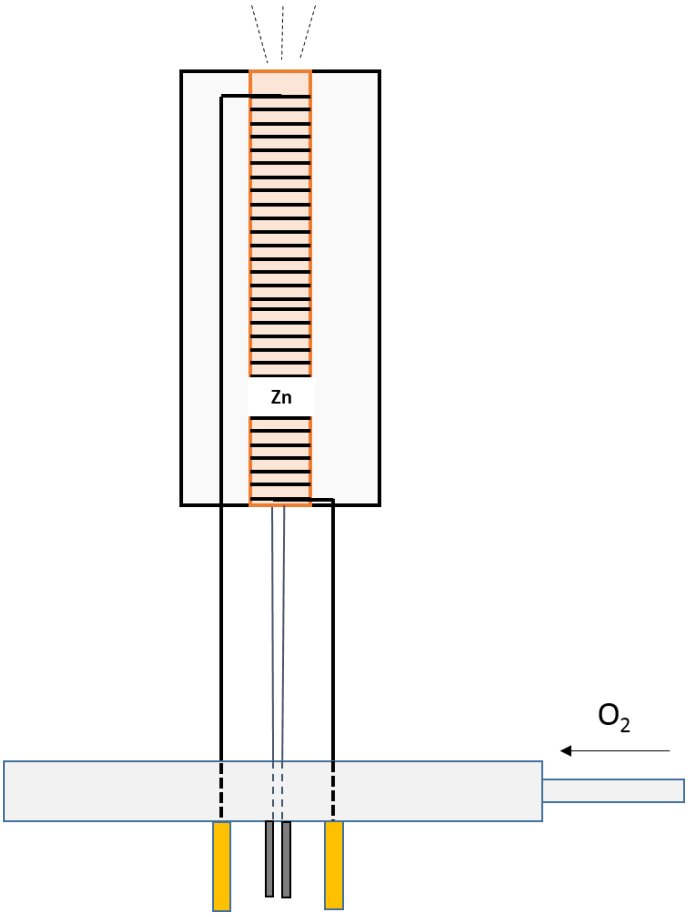

Figure 2.10 Basic scheme of the resistive heating evaporator.

For cobalt thermal evaporation a Co-wire has been used passing electric current directly through it (4A, 2.8V). The calibration of the deposition rate was done by directly comparing the XPS intensities obtained during the *in situ* growths with those reported in [59]. Zinc thermal evaporation has been carried out using an evaporator based on a Knudsen cell. The Zn-lumps were introduced on a ceramic crucible enclosed by a tungsten filament. A tantalum shield surrounds the ceramic to avoid heat losses and possible contamination due to tungsten sublimation. A C-type thermocouple (W-5% Rh vs. W-26% Rh) is situated at ceramic bottom in order to control de temperature. The oxygen was introduced by a gas line incorporated next to the evaporator flange. Once inside the chamber, the evaporator was situated at approximately 10 cm from the sample. Figure 2.10 shows a scheme of the evaporator. Finally, the calibration was done by successive evaporation attempts followed by *in situ* XPS measurements in order to determine the critical temperature at which ZnO deposition was reached and guarantee a very low evaporation rate. This process was repeated for both substrates used, HOPG and

graphene/Cu sheets, as the kinetic and morphological characteristics of the growth are different depending on them. The electric current used was (3.5-4 A, with 3.0-3.5 V).

The Au/Cr (300/30 Å) coating of the TEM SiN grids was done by thermal evaporation using the Denton Vacuum DV-502A system. A shutter allows the selection of the material to be deposited. During the deposition process the sample was heated at 300 °C.

2.4.2 e-beam evaporation

E-beam evaporation is just a variant of the PVD method explained in the previous point. In this case, the target material is heated by electron bombardment. The target material acts like the anode, receiving the electrons emitted by a thermionic-emitting filament and accelerated by a high voltage (several kV) established between target and filament. This technique allows local temperatures much higher than other approaches based on resistive heating, thus being very useful for the evaporation of refractive materials. Figure 2.11 shows a basic scheme of a typical e-beam evaporator.

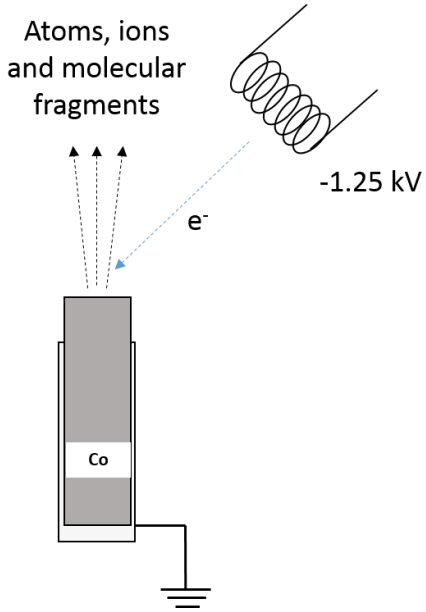

Figure 2.11 Basic scheme of the e-beam heating evaporator

In the present work a dual e-beam evaporator (e-flux 2, from Tectra) has been used at the Chambao chamber and CIRCE-NAPP endstation to evaporate metallic cobalt under reactive atmosphere of oxygen, just as described before. Nevertheless, the physical integrity of the filament depends on the pressure of the vacuum chamber, with an upper

limit situated at ~10^{-5} mbar. To overcome this issue, the oxygen gas outlet directly flows in the surroundings of the sample, in such a way that the local atmosphere around the sample surface is higher than the filament surroundings. In this way, very low coverages of CoO could be deposited on HOPG.

The instrument calibration was done in a similar way than for the resistive heating evaporator, that is, by gradually increasing the emission current of the filament and checking by *ex situ* XPS the deposition of CoO on HOPG. The reached deposition rate was very low. As the surface changes after atmosphere exposure, the CoO/HOPG samples where compared to CoO/HOPG growth previously by resistive heating PVD and measured before and after atmosphere exposure. The parameters used where 10 mA for current emission, 7A for filament current and 1.25 kV for voltage difference.

2.4.3 Atomic Layer Deposition (ALD)

The atomic layer deposition method belongs to the so called Chemical Vapor Deposition (CVD) group of deposition techniques [60]. They are characterized by the exposure of the substrate to volatile precursors, which react and/or decompose on the substrate surface to produce and deposit the desired compound. This process is done under high vacuum condition to guarantee very low levels of contamination.

The distinctive feature of the ALD in comparison to other CVD processes is that the reactant and the precursor used for the chemical reaction are never together in their gas phase [61]. This allow a very high control of the deposit, regarding its composition and thickness, achieving a layer by layer growth. In order to illustrate in depth the sequence of the chemical steps of the ALD process and its potential on controlling coatings of very low thicknesses, we will take as an example the Al_2O_3 deposition presented in Chapter 5. For this material, the organometallic precursor is TMA, which bounds to the hydroxyl groups of the surface liberating methane. The gas phase of the precursor guarantees a perfect wetting of the surface, while the restriction of bonding only to hydroxides groups allows the deposit of a single layer of precursor on the surface. After the exposure of the substrate to the TMA, this one and its residues are purged and immediately the sample is exposed to the oxidation reactant. In the case of Al_2O_3, oxygen plasma or water could be used as oxidants, although oxygen plasma gives better oxidation results, reason why it was used. Independently of the reactant, the oxidation process removes the reaming methyl groups by new hydroxyl moieties, affording a new hydroxyl

layer ready for the next cycle. Hence, the high control of the thickness lies on the guarantee of a deposition of only one layer per cycle and a complete coverage, provided that initially the surface has hydroxide groups which act as nucleation centers. Temperature also plays an importer role, obtaining better stoichiometric and crystalline results at higher temperatures. A scheme of the reaction process is shown in Figure 2.12.

In this work the Al_2O_3 deposition by ALD has been done by using TMA as precursor and oxygen plasma as reactant. In order to ensure an amorphous growth, the deposition was done at low temperature (40 °C). The ALD instrument used was an Oxford FlexAl -Plasma Enhanced from the Nanofabrication Facility of the Moeluclar Foundry. The device deposition thickness was already calibrated (Al_2O_3 with oxygen plasma 1 nm per seven cycles on SiO_2 waffers), although the nominal values were verified by *ex situ* XPS for different substrates. For more information of the ALD recipe see section 2.5.1.

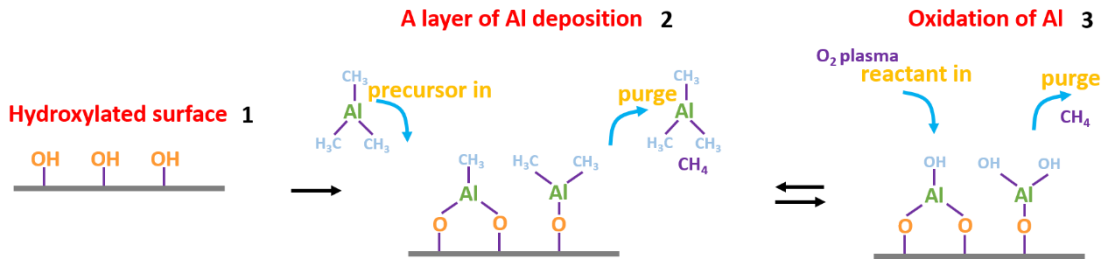

Figure 2.12 Basic scheme of the ALD process for Al_2O_3. Steps 2 and 3 constitute the complete deposition cycle, which is repeated successively.

2.5 Characterization techniques

A quick overview of the contents of this section allows to define the present research as a surface science work. Most of the used techniques focus their potential at the chemical, structural and morphological characterization of surfaces and interfaces. In the next lines an abbreviated description of the theoretical and practical fundamentals of each characterization technique will be presented, as well as a brief technical report of the experimental details. The main techniques used in this work are XPS (including technical variations) and confocal Raman spectroscopy. The rest of the techniques have been used as a support for the mean characterization.

2.5.1 X-Ray Photoelectron Spectroscopy (XPS)

X-Ray photoelectron spectroscopy (XPS) is mostly a chemical characterization technique based on the analysis of the photoemitted electrons when a sample is irradiated with X-rays. The low mean free path of the electrons before losing their energy by inelastic scattering with the rest of the solid turns out XPS into a surface technique. The development of the XPS goes back to the early decades of the XX century after the discovery of the photoelectric effect by Herzt in 1887. The first experience is this field was carried out by Moseley, Rawlinson and Robinson before the World War I. However, it would not be until the 1950s when Siegbahn could take the first XPS spectrum from a cleaved sodium chloride sample. He was granted the Nobel Prize in Physics in 1981 for his efforts on developing the XPS technique [62].

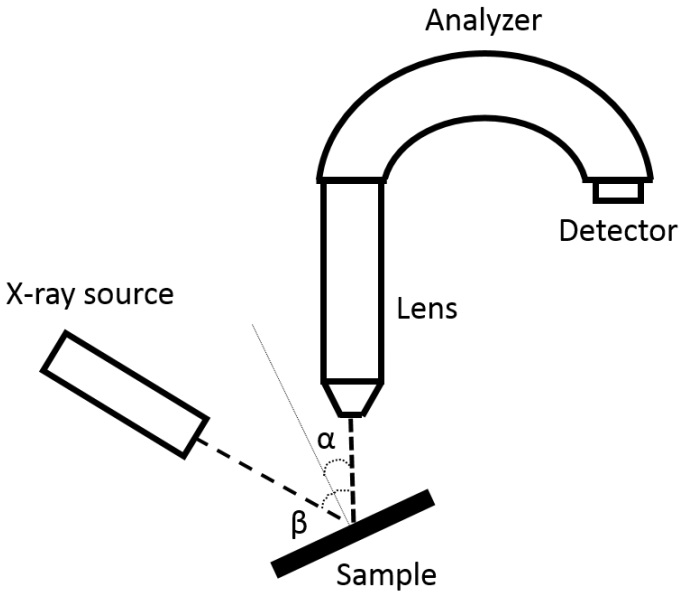

Figure 2.13 Scheme of the XPS experimental setup.

The typical experimental setup of a XPS device consist on an X-rays source that illuminates the sample and an electron analyzer. These last element need to fulfill three conditions: collimate and focus the photoemitted electrons from the sample surface, separate the electrons depending on their kinetic energy and finally, detect them. These three steps are achieved by a combination of electrostatic lens, a capacitor of a particular geometry and an electron detector, respectively. The separation path between sample and detector must be under UHV conditions, so the scatter probability of electrons due to gas

atoms and molecules becomes depreciable. A basic scheme of these structure is shown in Figure 2.13.

Regarding the general features of XPS [63], each photoemitted electron is going to leave the sample with a kinetic energy, E_k, defined by:

$$E_k = h\nu - E_B - \Phi \quad \text{(Eq. 2.2)}$$

where $h\nu$ is the energy of the photon, E_B the binding energy of the photoemitted electron and constant Φ the work function of the analyzer, being straightforward the conversion from kinetic to binding energy. The value of the binding energy depends, firstly, on the particular element and orbital, and secondly on the chemical environment (type of atoms and bonding to them). This is the reason why XPS technique is sensitive to chemical element differentiation and useful for the characterization of the chemical details of the elements that conform the solid. However, not all the peaks measured on an XPS spectrum are due to photoemission of electrons from a precise orbital [63,64]:

- Photoemission lines: these lines are referred directly to the core level electrons which are photoemitted by the X-rays and which has been briefly discussed above. The scheme of the basic XPS emission process is shown in Figure 2.14. In those non-s orbitals, the spin-orbital (S-O) coupling will induce a doublet structure of the photoemitted structure, where the intensity of each line will depend on the electronic population. For example, the Zn 2p contribution is split into Zn $2p_{3/2}$ and Zn $2p_{1/2}$, with an intensity ratio of 2:1 due to the electronic population (4 and 2 electrons, respectively). Besides, the total intensity of a certain energy level depends on the photoemission cross section, which also depends on the photon energy. The peak width (FWHM, full width at half of the maximum) is a convolution of three factors: the natural line width (i.e. the lifetime of the hole resulting from the photoionization process), the width of the used X-ray source and finally the instrumental contribution. These kind of peaks are usually symmetric, although different factor during the photoemission process can led to broadening and asymmetrical shapes.

- Multiplet splitting: these features appear after the photoemission of an s-type electron. The new unpaired electron left after these process can couple with other core level unpaired electrons and create several possible final state configurations and energies. This results in the asymmetrical splitting into several contributions of the photoemission line.

- Shake-up satellites: this type of lines occurs when the photoemission process does not lead to the formation of ions in the ground state, but in an excited state. In this case, the kinetic energy of the photoemitted electron is reduced, giving that energy to the excited atom.

- Shake-down satellites: is a situation similar to the last description. In this case the photoemitted electron transfers energy to a valence band electron that leaves also the solid. This effect turns into a broadening of the photoemission line.

- Plasmons: this is a third class of energy loss line. The emitted photoelectron can excite a collective resonance of the electrons of the solid known as plasmons. The energy quantification of these oscillations determines the appearance of a series of peaks of decreasing intensity equally spaced.

- X-Ray satellites lines: these low intensity lines are due to the non-monochromatic emission of the X-ray source and are usually ignored. Same effects as described before rule these lines.

- X-Ray ghost lines: as before, these low intensity lines are due to the non-monochromatic emission of the X-ray, but in this case because of the oxidation of the metallic anode.

- Auger lines: these lines are produced by electrons emitted from the solid after a non-radiative de-excitation process (see Figure 2.14). The hole left in the core shell after the photoemission is occupied by a new electron from an upper level. The energy difference can be emitted as a photon or directly transferred into a second electron of the same energy level, being emitted from the solid with that

kinetic energy. The Auger nomenclature refers to this three-electron process. For example, in the Auger transition LMM the first letter (L) indicates the core level from where the first electron is photoemitted, while the other two letters (MM) indicate the second shell from where the electrons move (one to the core shell hole and the other one to the outside of the solid). Therefore, the kinetic energy of Auger electron does not depend on the photon energy. In addition, the spectrum of this Auger transition is very complex, but very useful from a qualitative point of view in order to distinguish different oxidation states and compounds of the same element (see Figure 2.14 as an example).

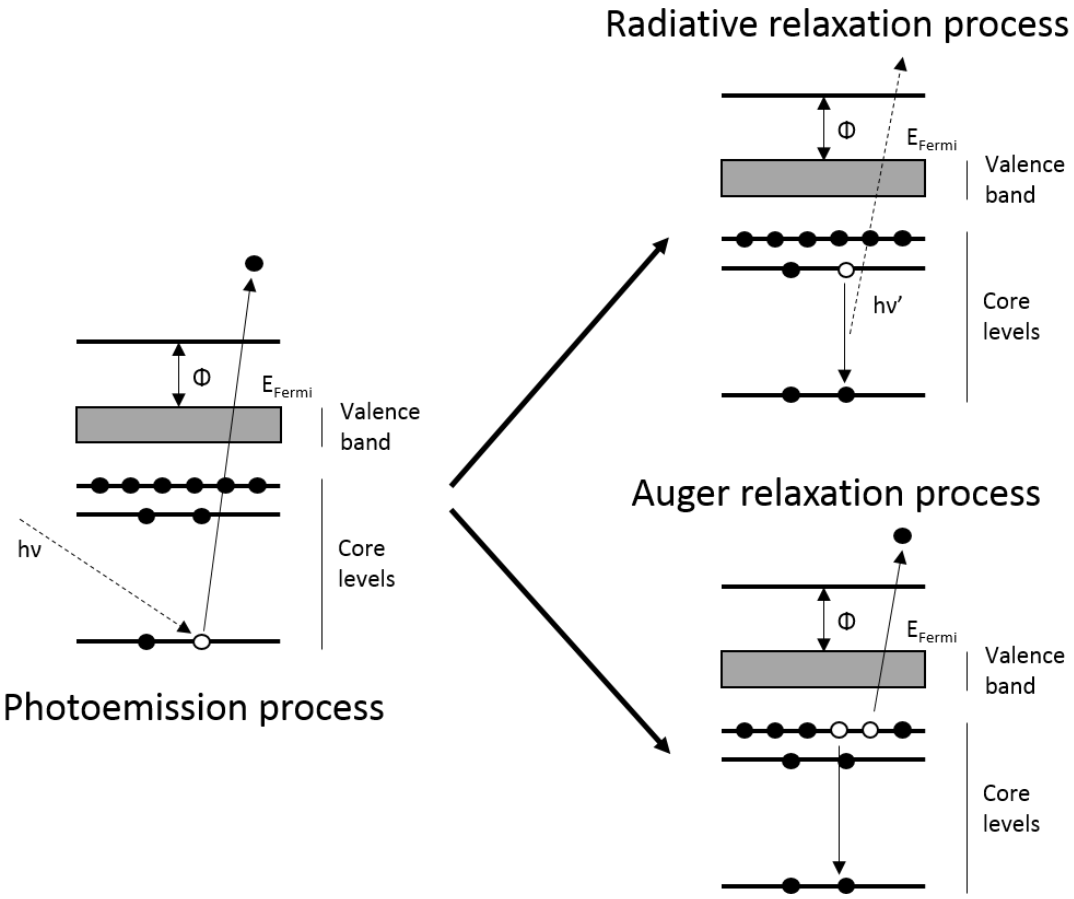

Figure 2.14 XPS emission process and two possible relaxation ways, by fluorescence (photon emission) or Auger process (Auger electron emission)**.**

At this point, it is important to emphasize the role of the initial and final states of the atom during the photoemission process. As it has been described previously, these relaxation processes, which can be inter or intra-atomic, determine the emergence of new features in the XPS spectra that modify the theoretical and expected energy level scheme

of atoms. Besides, initial states will depend on the chemical environment of the atom, and the combination of both, initial and final states, will determine the energy position and shape of the XPS contributions. Meanwhile, these states turn out especially important for the Auger contributions. First, because the shape of these contributions is especially sensitive to them. And in second place, both initial and final states can be easily inferred from the Wagner plot, which combines the plotting of the kinetic energy of the Auger electron with the binding energy of the corresponding emitted photoelectron [65,66].

In order to illustrate the utility of the Wagner plot we will use the example of Zn, which will be deeply discussed in Chapter 4. Nevertheless, the next lines are of general application. The Auger parameter is defined as the sum of the Auger kinetic energy and the photoemission binding energy:

$$\alpha' = E_k^F(L_3M_{45}M_{45}) + E_b^F(L_3). \qquad \text{(Eq. 2.3)}$$

This parameter is very sensitive to the local environment of the atoms since it strongly depends on the relaxation energy of the final state. As deduced elsewhere [63,66], the previous expression can be set as:

$$\alpha' = cte_{L_3M_{45}M_{45}} + 2\,R(L_3) \qquad \text{(Eq. 2.4)},$$

where $cte_{L_3M_{45}M_{45}}$ is a constant for each element and $R(L_3)$ is the relaxation energy of the core level L_3. Therefore, straight lines with slope +1 in the Wagner plot correspond to atoms with the same final state or, in other words, same relaxation energy. On the other hand, it can be also shown that [66]:

$$E_k^F = cte_{L_3M_{45}M_{45}} + \left[-2\left(E_{Mq} + \Phi\right) - 2KQ\right] - 3E_b^F \qquad \text{(Eq. 2.5)}.$$

where the term $\left[-2\left(E_{Mq} + \Phi\right) - 2KQ\right]$ is related to initial states. Accordingly, straight lines with slope +3 in the Wagner plot correspond to atoms with the same initial states.

One last clarification must be done concerning the probing depth of the analysis. As stated before, electrons must leave the sample without losing their energy in order to offer relevant chemical information. Therefore, the depth of the analysis is going to be

limited by the inelastic mean free path (IMFP) of the electrons, i.e. the distance that electrons can move through the solid without suffer any inelastic scattering process. This distance depends on many factors, although a rough approximation would distinguish between material parameters (density, type of atoms, valence electrons, energy gap…) and the kinetic energy of the photoemitted electron. In this way, the *Universal Curve* shown at Figure 2.15 and first published by Seah and Dench in 1979 [67], gives an overview of the IMPF behavior. This is extremely important as it opens the door to non-destructive depth profile measurements by changing the photon energy and consequently the kinetic energy of the photoelectron. Nevertheless, it could also give rise to difficulties in the analysis if only one photon energy is used, as measured photoelectron of different elements may come from different depths.

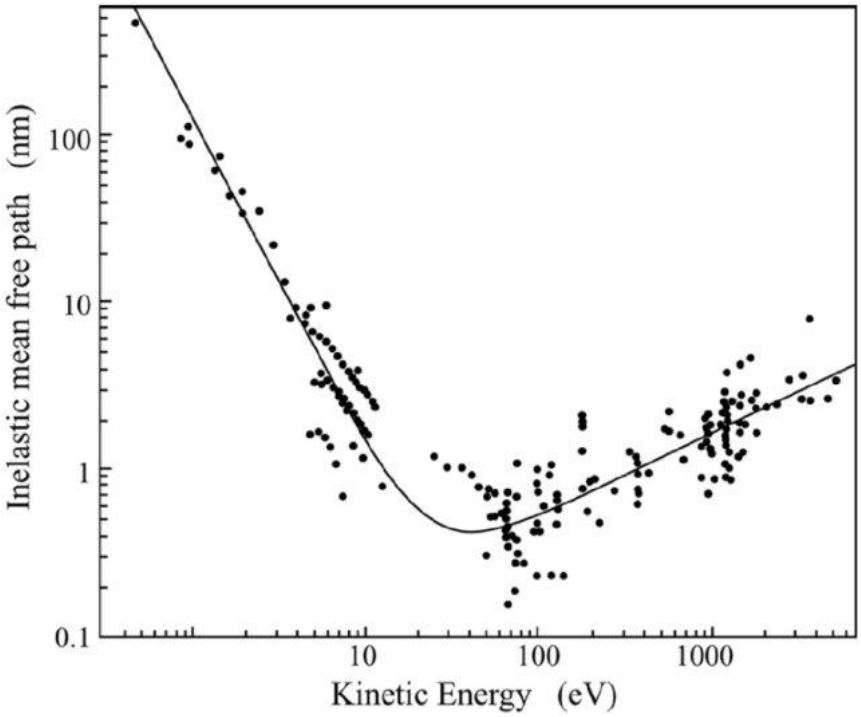

Figure 2.15 Inelastic mean free path curve Universal Curve. The original plot is from [67].

For more accurate IMPF values, in this work it has been managed the Tanuma, Powell, and Penn formula IMFP-TPP2M.[68]:

$$\lambda = \frac{E}{E_p^2\,[\beta\, Ln(\gamma E) - \left(\frac{C}{E}\right) + \left(\frac{D}{E^2}\right)]} \qquad \text{(Eq. 2.6)}$$

where λ is the IMFP and E is the electron energy. E_p (which is the free-electron plasmon) B, γ, C and D values depend on the material parameters, such as the energy gap, density, the number of valence electrons per atom (for elements) or molecule (for compounds) and finally the atomic or molecular weight.

2.5.1.1 Photoemission peak analysis

Inelastic background

In order to perform a qualitative analysis of the of the photoemission contributions several facts must be taken into account. In first place, the XPS spectra present a background due to the electrons which have lost energy during one or more inelastic processes. This is an accumulative background; more inelastic electrons are expected as the analyzed kinetic energy is reduced (meaning that electrons emitted from a deeper zone that have lost part of their energy are collected). Therefore, from the total intensity measured for a particular photoemission peak it has to be subtracted this inelastic background, which in fact can modify the real shape and energy position of the photoemission line. There are three different forms of background subtraction:

- Linear background: the simplest method for background substation. It consists on the drawn of a straight line between the initial and the final energies of the XPS contribution. Usually it is not a good choice and it is used in combination with the Shirley method.

- Shirley background: it can be considered the most popular method due to its easy computation, although significantly errors can be derived from its use [69]. It consists on an iterative method where the total amount of subtracted background at a particular point depends on the intensity value of the previous binding energy point. The basic equation of the background function S is [70]:

$$S_{S,i}(E) = k \int_{E}^{+\infty} dE' (j(E') - S_{S,i-1}(E')) \qquad \text{(Eq. 2.7)},$$

where j(E') is the measured intensity at energy E', and k is the difference between the intensity values at E_{min} and E_{max} used in the fit. The initial value $S_{S,0}$ is the one

corresponding to a constant background. It can be used in combination with the linear subtraction.

- Tougaard background: this is the most precise but also most complex method. It takes into account the extrinsic loss process that contribute to the background [71,72,73,74]. It can be shown that the primary spectrum, F(E), is given by:

$$F(E) = j(E) - \lambda(E) \int_E^\infty K(E, E' - E) j(E') dE' \qquad \text{(Eq. 2.8)}$$

,where K(E,T) is the differential inelastic scattering cross-section for a given energy loss T, λ(E) is the IMFP and j(E) is the measured total flux of emitted electrons of energy E. Now, K(E,T) can be calculated from dielectric response theory or experimentally obtained from electron energy loss measurements. In any case, K(E,T) can be replaced by a universal cross-section, simplifying Eq. 2.7:

$$F(E) \simeq j(E) - B \int_E^\infty \frac{E - E'}{[C + (E' - E)^2]^2} j(E') dE' \qquad \text{(Eq. 2.9)}$$

,where B ~ 2866 eV^2 and C ~ 1643 eV^2. In addition, by recalling B parameter value elastic contributions can also been considered [63].

Quantitative analysis

Once the inelastic background has been subtracted, the real shape of the peak can be analyzed. Two types of analysis can be distinguished regarding the level of treatment. In first place, the quantification approach allows to determine the concentration of each element, as well as an estimation of the amount of each material (in case of a multilayer surface). The qualitative analysis is a deeper treatment where the goal is the detailed chemical study of a certain XPS contribution. In this work the quantitative analysis has been applied for the calculation of the relative amount of metal/oxide compounds and for an estimation of the coverage in terms of equivalent monolayers (Eq-ML). In the next lines a brief introduction to the fundamentals of the different quantitative methods used in this work will be exposed:

- Atomic concentration: the intensity measured for a certain photoemission line depends on three factors which are only related to that specific energy level and atom: the cross-section for that atomic orbital and element, the number of atoms per unit of volume of the sample and finally the IMFP of those specific photoelectrons. Other factors could also determine the intensity, but they will depend on the experimental setup and they will be the same for all the samples and elements measured by that specific XPS analyzer. Therefore, giving an experimental setup, there exist for each element a constant, called atomic sensitivity factor (S), which can normalize the measured intensity (I) in order to compare the real amounts of each element that are presented on the sample. The relative atomic concentrations are given by [64]:

$$C_x = \frac{I_x/S_x}{\sum I_i/S_i} \quad \text{(Eq.2.10)}$$

This general expression assumes that the surface composition is homogenous. If as usually happens this is not the case, important estimation mistakes can be made.

- Factor analysis: is a multivariative statistical algorithm that has been widely used as a standard method of data handling in analytical chemistry, mainly in the analysis of Auger and core-level photoelectron spectra [75]. The basic idea is the capability to separate the different and overlapped contributions of a series of spectra, obtaining the relative amount of each contributions and its single shape. It is beyond the scope of this work to explain in detail the mathematical manipulation required, but an overview will be described in order to understand the data treatment. The method is based on the construction of a set of abstract eigenvalues (C^a, abstract concentrations) and eigenvectors (R^a, abstract spectra) from the data matrix, D. Then, a real significance must be given to these abstract components. The easiest way to do so is by the *target testing* method, where a set of known spectra or concentrations are needed. The final result will be a new set of eigenvalues and eigenvectors with the estimated spectra and concentrations of each component in which the initial series of spectra can be deconvoluted. A schematic overview of the process is presented in Figure 2.16.

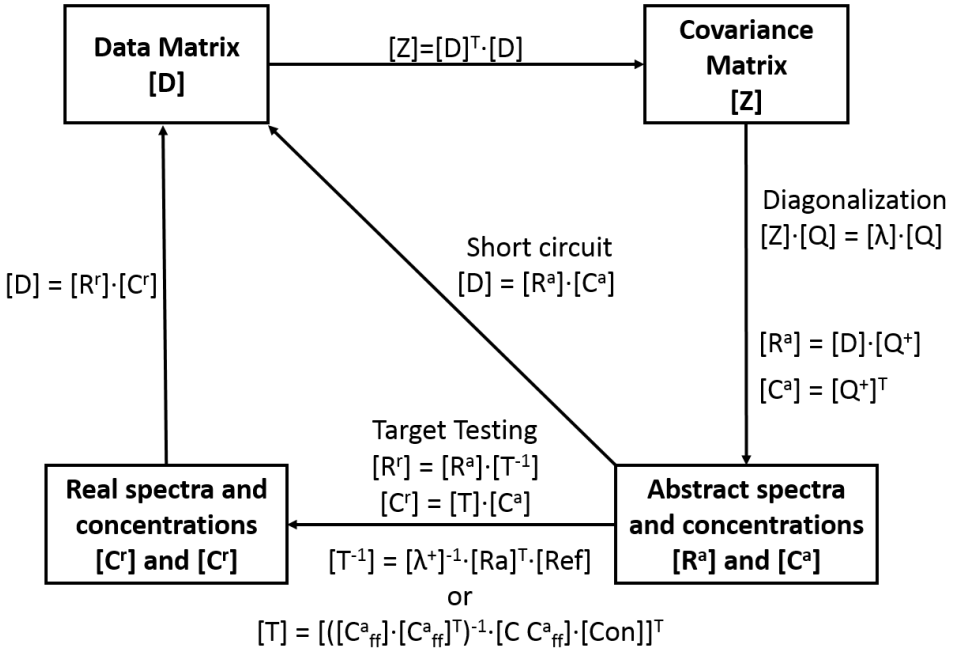

Figure 2.16 Basic scheme of the Factor Analysis methodology.

- Coverage estimation: the simplest way to estimate the coverage is to suppose a uniform and homogeneous layer across the complete measured area. Under this premise, the intensity of infinitesimal layer would be [63]:

$$dI = \Phi f D L n\, e^{\left(-\frac{x}{\lambda \cos(\alpha)}\right)} dx \quad \text{(Eq. 2.11)}$$

,where I is the measured intensity, Φ is the photoionization cross section of the orbital corresponding to that peak; f the photon flux, D is the detection efficiency of the analyzer; L is the correction factor for the angular anisotropy of the photoemission process; n is the number of atoms per volume unit; λ is the IMFP of the measured electrons; α is the angle between the path of the escaping electrons and the surface (also known as take-off angle, see Figure 2.14); and x is the depth from where the photoelectrons are emitted. In the simplest situation we measured an infinite material, so the total intensity of this bulk material is given by:

$$I_{Bulk} = \int_0^{\infty} \Phi f D L n\, e^{\left(-\frac{x}{\lambda \cos(\alpha)}\right)} dx = \Phi f D L n k \lambda \cos(\alpha) = I_{\infty} \qquad \text{(Eq. 2.12)}$$

If all the measurements have been taken at the same take off angle, then $\Phi\sigma nk\lambda\cos(\alpha) = I_\infty$ will be a constant for each material. A more complex situation would be a layer of thickness *d* over an infinite substrate. In this case, the intensity measured for both layer and substrate would be:

$$I_{layer} = \int_0^d \Phi\sigma nk\, e^{\left(-\frac{x}{\lambda_{layer}\cos(\alpha)}\right)} dx = I_\infty \left[1 - e^{-\frac{d}{\lambda_{layer}\cos(\alpha)}}\right] \quad \text{(Eq. 2.13)}$$

$$I_{subs} = \int_d^\infty \Phi\sigma nk\, e^{\left(-\frac{x}{\lambda_{subs}\cos(\alpha)}\right)} dx = I_\infty\, e^{-\frac{d}{\lambda_{subs}\cos(\alpha)}} \quad \text{(Eq. 2.14)}$$

In case that the substrate is only partially covered by a fraction Φ_L, the previous equations must be corrected to:

$$I_{layer} = \int_0^d \Phi\sigma nk\, e^{\left(-\frac{x}{\lambda_{layer}\cos(\alpha)}\right)} dx = \Phi_L I_\infty \left[1 - e^{-\frac{d}{\lambda_{layer}\cos(\alpha)}}\right] \quad \text{(Eq. 2.15)}$$

$$I_{subs} = \int_d^\infty \Phi\sigma nk\, e^{\left(-\frac{x}{\lambda_{subs}\cos(\alpha)}\right)} dx = I_\infty[1 - \Phi_L + \Phi_L\, e^{-\frac{d}{\lambda_{subs}\cos(\alpha)}}] \quad \text{(Eq. 2.16)}$$

From equations 2.12 and 2.13 the deposition rate can be estimated for a series of growth states on the same sample, as the thickness d is equal to the product of deposition rate (D) by time (t). Besides, the thickness is usually given in Eq-ML, being for CoO 2 Å, and for ZnO 2.6 Å per Eq-ML.

Qualitative analysis

The qualitative analysis is mainly a chemical analysis, and becomes one of the most important features of XPS measurements, despite the difficulties that can appear during the data treatment. The first issue is to determine the correct energy position of each contribution of the XPS spectra. In this way, conductor samples avoid this problem as long as the XPS equipment is correctly calibrated. On the other hand, insulator samples will charge due to the impossibility to compensate the emission of the electrons, given rise to a shift of all the spectral lines with a not fixed value from sample to sample. There are two ways to overcome this charge correction issue: by using an electron flood gun to

compensate the loss of electrons from the sample, or by using a specific contribution of known energy. For this last solution it is very common to use the C 1s of adventitious carbon, situated at 284.8 eV, for *ex situ* samples. In the case of *in situ* growths, well-known peaks from the substrates can be used for this purpose.

In second place, the shape of the photoemission lines is usually symmetric. As previously described, its intensity is going to depend on the number and localization of the specific atoms and the cross-section of the specific orbital, which also depends on the X-ray photon energy. However, different energy loss processes can modify this shape into different structures, from a slightly asymmetrical peak to a complex situation with various overlapped contributions. In general, each of these XPS contributions can be fitted as a combination of a Gaussian and Lorentzian symmetrical functions. The first term would take into account the contributions from the measurement process (x-ray line profile, Doppler and thermal broadening, and instrumental response), while the Lorentzian curve would simulate the natural lifetime width. There is not an analytical expression for the Gaussian-Lorentzian convolution. Despite, it is common to use a mathematical approximation, such as Gaussian-Lorentzian sums and products. In the case of asymmetrical contributions, there exists several approaches consisting on the use of Doniach-Sunjic functions, or just by the application of tail modifiers to the Gaussian-Lorentzian contribution, such as an exponential function with a piecewise condition. In this work the tails modifiers have been used in the case of asymmetrical peaks fitting. Equations 2.16, 2.17 and 2.18 display the functions used for XPS fitting.

$$G(E,\sigma) = \frac{e^{-(E-E_O)^2/(2\sigma^2)}}{\sigma\sqrt{2\pi}}, Gaussian\ function \qquad \text{(Eq. 2.17)}$$

$$L(E,\gamma) = \frac{\gamma}{\pi((E-E_O)^2+\gamma^2)}, Lorenztian\ function \qquad \text{(Eq. 2.18)}$$

$$T(E,s,k,\sigma) = \begin{cases} s\, e^{-k\frac{E-E_O}{\sigma}} & E \le E_o \\ 1 & E \ge E_o \end{cases} \qquad \text{(Eq. 2.19)}$$

2.5.1.2 Quantitative Analysis of Surfaces by Electron Spectroscopy (QUASES)

This type of analysis developed by S. Tougaard [71,72,73,74] is focused on the inelastic background in order to extract morphological information of the surface. The basic idea consists on the study of the energy loss of the background electrons in order to know where they come from. As it can be appreciated, it is a completely different

approach than previous approximations that supposed a homogeneous concentration of the different chemical elements among the surface, and in fact, the spectra shape can be completely modified depending on the origin of the emitted electrons, as shown in Figure 2.17.

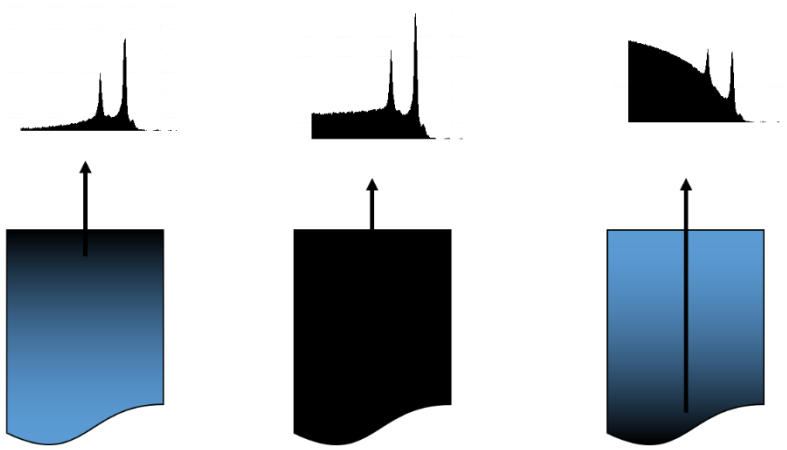

Figure 2.17 Influence of the atomic position and concentration on the inelastic background on XPS spectra.

The fundamental principles of QUASES analysis are the same than for the Tougaard background subtraction. The measured spectrum of emitted electrons, j(E,Ω), depends on the flux density of photoelectrons excited from a single atom, F(E_o,Ω), at energy E_o into a solid angle Ω, and also on the atomic concentration of those atoms, f(x) at a depth x. The multiple scattering events are included on the G function, which represents the energy distribution of an electron as a function of the path length x/cos(α) traveled thought the solid (where α is the take-off angle). Multiple scattering events are necessary as the XPS spectrum includes electrons that have moved along the solid a total distance of several IMFP In this way, j(E,Ω) is given by:

$$j(E,\Omega) = \int F(E_o\Omega)dE_o \int f(x)G\left(E_o, \frac{x}{\cos(\alpha)}, E\right)dx \qquad \text{(Eq. 2.20)}$$

As stated before, the differential inelastic electron scattering cross-section can be calculated from dielectric response theory or experimentally obtained from electron energy loss measurements. In addition, Eq. 2.19 can be solved for different concentrations profiles to calculate the primary excitation spectrum F(E,Ω). Therefore, through the use

of previousequations, F(E,Ω) could be obtained from the measured spectrum if f(x) is known, or vice versa, f(x) can be estimated if F(E,Ω) is already known.

The way to operate QUASES analysis needs first to measure a bulk sample of the compound from which the analysis is going to be done, i.e. the layer or substrate material (as the depth profile of the atomic concentration f(x) is known). From this measured spectrum the original primary excitation spectrum F(E,Ω) will be calculated. Once this data is known, from other measured spectra the concentration profile for each growth step can be calculated. In general, this kind of analysis is used in combination with other morphological characterization techniques such as AFM microscopy.

2.5.1.1 Experimental details

The XPS measurements shown in Chapters 3 and 4 were done at the CLAM 4-Caramon system of the GRIN group, at the Applied Physics Department of the Universidad Autónoma de Madrid, Spain, as described in section 2.3.1.1. The XPS experimental setup has a 9 channeltron hemispherical analyzer (model CLAM-4, ThermoVG Scientific). The X-ray twin anode source (model number: XR3E2) allows to use Mg K_α = 1253.6 eV and Al K_α = 1486.6 eV radiation alternatively to avoid overlapping of the main analyzed photoemission and Auger peaks. For survey spectra, an energy step of 0.5 eV and a pass energy of 50 eV was used, giving a resolution of 1.3 eV. For the rest of the regions the energy step was 0.1 eV and pass energy was set at 20 eV, giving an overall resolution of 0.9 - 1.0 eV respectively for each anode. The energy scale was calibrated by using the C 1s peak at 284.3 eV [76] for HOPG substrates and the Cu 2p 3/2 at 932.6 eV for G/Cu substrates [64].

Some XPS mapping measurements shown in Chapter 4 were performed at SCAI, Universidad de Málaga, Málaga, Spain by means of a PHI 5000 VersaProbe II analyzer. The X-ray source is a monochromatic Al Kα = 1486.6 eV emission with variable spot size ranging from 10 microns to 300 microns. It presents a lateral resolution of less than 10 μm and with a total energy resolution of 0.5 eV. The charge correction was carried out by an electron flood gun.

On the other hand, XPS measurements shown in Chapter 5 were done at the Imaging and Manipulation of Nanostructures Facility of the Molecular Foundry using a K-Alpha Plus XPS/UPS from Thermo Fischer Scientific. The X-ray source is a monochromatic Al K_α = 1486.6 eV emission with variable spot size ranging from 30

microns to 400 microns. For survey measurements the pass energy was set at 200 eV and the energy step at 1.0 eV. The rest of the regions were taken at a energy step of 0.1 eV and 50 eV for pass energy. The charge correction was carried out by an electron flood gun. A dual monoatomic and gas cluster ion source for depth profiling and sample cleaning was also installed in the analysis chamber (base pressure $\sim 10^{-10}$ mbar).

The spectra were fitted using the XPS Peak software, version 4.1, while the IMFPs for different energies were calculated by using the Tanuma, Powell, and Penn formula IMFP-TPP2M, contained in the software QUASES-IMFP-TPP2M. The inelastic peak shape analysis has been carried out by means of the QUASES software developed by S. Tougaard and F. Yubero. The plotting of all the spectra reported in this work have been done by OriginPro 8.0 software.

2.5.2 Photoemission Electron Microscopy (PEEM)

Photoemission electron microscopy (PEEM) uses the emitted electrons from a sample illuminated with X-ray radiation to display an image of the surface [77,78]. As all XPS based techniques, it is surface sensitive due to the reduced IMPF values of the emitted electrons. The local variations of the electron emission due to hν value and chemical composition produce the image contrast. Obviously, these electrons carry out chemical information of the surface, so actually a spectroscopic XPS mapping of the surface for different chemical elements can be performed if an energy filter is added to the analyzer, technique variation known as X-ray photoemission electron microscopy (XPEEM).

2.5.2.1 Experimental details

PEEM and XPEEM measurements were performed at PEEM endstation of CIRCE beamline, ALBA facility (Cerdanyola del Vallès, Spain). The microscope (Elmitec LEEM/PEEM III) can work in LEEM, LEED and PEEM (X-ray or ultraviolet) modes [79], although for measurements shown at Chapter 4 only XPEEM mode was used. The analysis chamber operates at UHV conditions. PEEM mode used for topography and work function contrast images handles a lateral resolution of ~10 nm. On the other hand, XPEEM mode presents a lateral resolution ~ 30 nm and a maximum energy resolution of 0.25 eV.

Pristine Graphene/Cu samples were measured by PEEM for topography and work function contrast images, and by XPEEM mode at different photon energies for the chemical study of the initial state of graphene sheets. The voltage difference between sample and detector (grounded) was set a 10 kV. The XPS regions under study were C 1s, O 1s and Cu 3d (valence band).

2.5.3 Hard X-Ray Photolectron Spectroscopy (HAXPES)

Hard X-ray photolectron spectroscopy is a variation of XPS where the energy of the photons is in the range of hard X-rays i.e. up to 15 keV, while commercial X-ray source emit at ~1 keV. Precisely, this higher hν allows an increment of the IMPF of about one order of magnitude. Besides, as the 90% of the photoelectrons emitted from the solid without any loss of energy come from a distance to the surface equivalent to $3\,\lambda\,cos(\alpha)$, the scanning depth of this technique moves from 2-3 nm for conventional XPS to 30-40 nm for HAXPES. The combination of this fact with the advantage of tunable X-ray radiation at synchrotron facilities allows the possibility to perform electronic and compositional non-destructive depth profiles [80]. However, this technique requires very long measurement times, as the photoemission cross-section drastically reduces for such high photon energies.

2.5.3.1 Experimental details

HAXPES measurements were performed at branch B of the Spanish SpLine beamline at the ESRF facility, Grenoble, France (see section 2.3.3.1). The analyzer is an electrostatic cylinder-sector (HV-CSA300), with a compact geometry and high transmission due to second order focusing. It is based on a cylinder sector with 90° deflection and 300 mm slit-to-slit distance and an entrance lens with 50 mm sample distance. The experimental setup can handle kinetic energies in the range of 15 keV to a few eV with the same analyzer setup and power supply, yielding a total resolution ΔE of 55 meV at hν of 15 keV and a pass energy of 10eV [81].

C 1s, O 1s and Co 2p contributions from a CoO monocrystal and *ex situ* CoO/HOPG samples of different thicknesses were measured at two different energies: 8 keV and 10 keV.

2.5.4 Near Ambient Pressure X-Ray Photoelectron Spectroscopy (NAP-XPS)

Near ambient pressure X-ray photoelectron spectroscopy is a variation of the conventional XPS technique. With less than 20 years, it is characterized by the high pressures at which XPS measurements can be performed. Although this technology can be extended to commercial XPS, it is mostly installed at synchrotron facilities. NAP-XPS allows the *in situ* study of different type of reactions, such as catalytic processes or thermal oxidations and reductions, at pressures up to ~30 mbar. This is achieved thanks to a differential pumping system that allows a pressure difference up to nine orders of magnitude between sample and detector [82,83]. The analysis chamber usually has installed several leak valves connected to different gas lines and a heating system for the *in situ* studies. For this reason, a moderate contamination of the chamber is expected. An X-ray window, usually a SiN membrane, separates the analysis chamber from the X-ray source in order to protect the optical branch from high pressures. Figure 2.18 shows a schematic representation of a typical HAP-XPS experimental system.

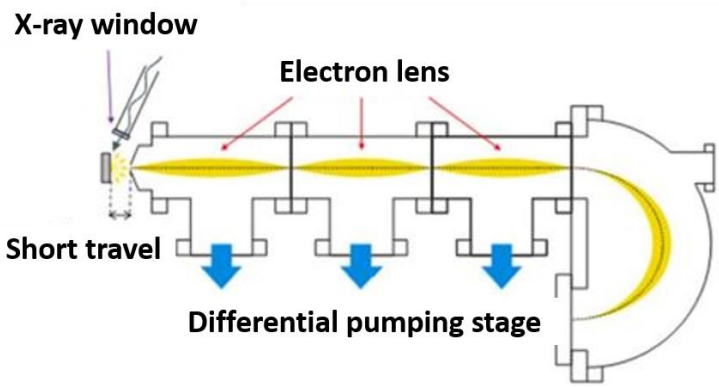

Figure 2.18 Basic scheme of the analysis station of a NAP-XPS system: X-ray window, short travel sample-aperture entrance, electron lens and differential pumping stage before the analyzer. Taken from [84].

2.5.4.1 Experimental details

NAP-XPS measurements have been done at two different synchrotron facilities. Chapter 3 discuss the *in situ* study of the CoO/HOPG gasification reaction performed at NAPP-XPS endstation of CIRCE beamline, ALBA facility, Cerdanyola del Vallès, Spain. The hemispherical analyzer (Phoibos NAP150 from SPECS) is connected to a differential

pumping system which allows a pressure range from UHV to 25 mbar. An overall ΔE of 0.2 eV was estimated at a photon energy of 500 eV, pass energy of 10 eV and 20 μm of exit slit. Samples can be heated up to ~700 °C by means of an infrared laser. In this experiment ~2 Eq-ML CoO/HOPG samples were grown *in situ* at the preparation chamber. After it, XPS measurements using a wide range of photon energies were performed at different O_2 pressures and temperatures to study the kinetic of the reaction. The C 1s, O 1s and Co 2p spectra were acquired.

The second NAP-XPS facility where NAP-XPS measurements were performed was APXPS-2 endstation of 11.0.2 beamline, ALS, Berkeley, USA. As before, the hemispherical analyzer (Phoibos NAP150, SPECS GmbH) is connected to the analysis chamber through a differential pumping system. The base pressure of the analysis chamber was 10^{-6} mbar. This endstation is especially designed for the installation of liquid and gas ultra-thin membranes to perform XPS measurements of that phases at very high pressures (in the order of ambient conditions) [85]. The reason why these type of experiments are done with a differentially pump station is the risk of rupture of the membrane. Chapter 5 will describe the testing experiment of a novel Al_2O_3 membrane performed at this beamline. O 1s, N 1s and Al 2p spectra were taken.

2.5.5 X-Ray Absorption Spectroscopy (XAS)

X-ray absorption spectroscopy (XAS) is a characterization technique that offers chemical and structural information at the short range of a certain chemical element of the sample [86,87]. As XPS, it is based on the photoelectric effect, but at a given photon energy range it measures the total absorption at each photon frequency, not only the emitted photoelectrons (remember that not all the photoelectrons arrive to the surface due to inelastic scattering events).

XAS had a parallel development with synchrotron facilities as they allow tunable photon energies. All XAS spectra have a common structure divided in two regions: XANES (X-ray absorption near-edge spectroscopy) and EXAFS (extended X-ray absorption fine structure). Near the binding energy of the core level the X-ray absorption increases sharply, known as the absorption edge. The XANES regions covers until ~50 eV above the absorption edge. The electron excited by this radiation ($E_{h\nu} \sim E_{BE}$) makes a transition between its core level and the unoccupied states of the atom. However, not all transitions are allowed, and in fact, the shape of this spectral is determined by the dipole

transition rules, which can be inferred from the Fermi Golden Rule of quantum theory. It is not the scope of this work to give a detail explanation of the calculus of this transition rules, but in first approximation (dipole approximation), the allowed transitions will be those where the orbital momentum changes by ±1 ($\Delta L=\pm1$ and $\Delta S=0$), and therefore the shape of the absorption spectrum will be the partial density of the empty states ($\Delta L=\pm1$) convoluted with a Lorentzian due to the finite lifetime of the hole at the core level. At a second level of approximation (quadrupole transition), weaker transitions with $\Delta L=\pm2$ are allowed. In any case, the whole picture is much more complex as the core-hole can actually affect the density of states, the unoccupied levels can be hybridized with other atoms (and thus permitting prohibited transitions) or due to structural distortions the crystal field can be modified leading to the splitting of the unoccupied orbitals. Therefore, XANES spectrum gives valuable chemical information about the sample.

Above 50 eV from the absorption edge starts the EXAFS spectra. In this case the photoelectrons have a high kinetic energy, what reduces the probability of multiple backscattering process and in fact the interaction with the surrounding atoms is going to be dominated by single backscattering processes. This allows the extraction of structural information about the type of atom under study but only in the near range, what among other features differentiated this technique from X-ray diffraction. In this work no EXAFS analysis is presented.

The real absorption spectrum can only be taken by a direct measurement of the photon flux that passes through the sample. However, in most of the cases this is not possible due to the thickness of the sample or because it is supported on a substrate opaque to X-ray radiation. Instead, different experimental approaches can be applied taking advantage from the fact that the core hole de-excitation gives rise to an avalanche of electrons, photons and even ions escaping from the surface. However, the probing depth of the analysis and some spectral features will depend on the decay products that are analyzed. The most common configurations are:

- Fluorescence yield: it studies the photons emitted by the sample. The main characteristic is that the fluorescent photon has a mean free path of the same order as the incoming X-ray, so it is a bulk measurement. Although in the most common configuration all the photons are measured without distinctions (total fluorescence

yield), it is also possible to measure the emitted photons as a function of their energy (partial fluorescence yield).

- Electron yield: in the case of total electron yield all the electrons emitted from the sample are measured, what can be done by measuring the current flowing to the sample if it is connected to earth, or by and electron detector (Channeltron). Very little is known about the probing depth of this configuration. The only work done for soft x-ray absorption gives values of the mean probing depth of about 4-5 nm, i.e. approximately the double as for XPS [88]. However, the measurements can also be done by differentiating the kinetic energies of the emitted electrons using an electron analyzer (partial electron yield). In this case, two options can be selected: selecting a window of the analyzed energy range at very low kinetic energy (5-15 eV) to collect only secondary electrons. This method is approximately equivalent to the above total yield method. However, it is also possible o select an energy range window to collect the Auger electrons from a determinate atom. In this case, the probing depth is slightly shorter due to the fact that secondary electrons are not collected.

- Ion yield: it measures the ion escaping from the top-layer of the sample, becoming a very surface sensitive approach.

2.5.5.1 Experimental details

XAS-XANES measurements were done at the NAPP-XPS endstation of CIRCE beambline, ALBA facility, Cerdanyola del Vallès, Spain. The configuration mode has been total electron yield measured by the drain current from the sample. C 1s, O 1s and Co 2p regions were measured on ~2 Eq-ML CoO/HOPG samples under different atmosphere and temperature conditions. All regions were normalized to the I_0 current measured from a gold reference sample in order to remove carbon and oxygen contamination features from the beamline optics.

Some XAS-XANES measurements reported on Chapter 3 were performed at BESSY II facility by our group previously to the present research. More experimental details can be found elsewhere [59].

2.5.6 Atomic Force Microscopy (AFM)

Atomic force microscopy belongs to the group of the scanning probe microscopies. Its operation consists on scanning the surface via a mechanical probe attached to a flexible cantilever, close enough to the surface in order to be affected by the interaction forces with the top-layer atoms of the sample, such as electrostatic repulsion, Van Der Waals forces or capillarity forces, among others. The tracking of the cantilever deformation allows to reproduce a map of the topography of the surface at the same time that some mechanical properties can be inferred from how the cantilever is affected by its interaction with the sample. In order to follow the deformation of the cantilever a laser is focus into its backside and the reflection is measured by a photoelectric sensor, so that deviations from the rest position can be traduced into useful information (see Figure 2.19). By fixing one parameter, for example tip-sample distance, a feedback loop enables the scan of a region by moving and controlling the probe over the sample with a piezoelectric system [89].

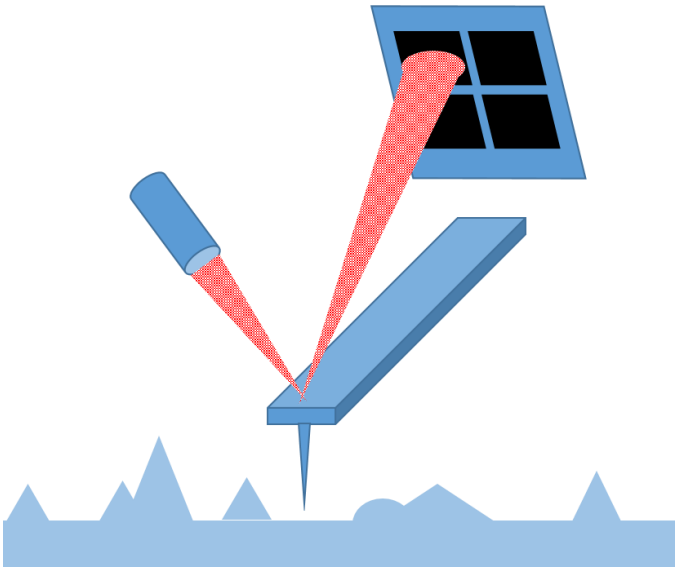

Figure 2.19 Scheme of the experimental setup of the cantilever, probe tip, laser and photoelectric sensor.

Depending on the parameter used in the feedback loop and the AFM configuration, different properties can be measured. Besides, different configuration modes could offer some advantages depending on the type of material measured.

2.5.6.1 Topography modes

Topography measurements are the base of AFM. For this purpose, several approaches have been developed, which can be divided into two categories depending if the static deflection of the cantilever is measured or if instead is tracked the dynamic oscillation of the cantilever. Different methods offer different interaction with the sample and also differences on the properties that can be study.

- Contact mode: this is the fastest mode. The deflection of the cantilever can be traduced directly into the topography of the sample. As no correction from the oscillation of the probe is required, it offers images with very high resolution. This mode runs the measurement always in the repulsion regime of the force-curve (see Figure 2.20 at section 2.4.6.2), so the tip is actually in touch with the sample. This fact implies that in addition to the normal forces applied between tip and sample lateral forces are experienced also by both, and the nature of the surface may affect the measurements (or even the surface can be modified by the tip).

- Oscillating modes: the main motivation of using this configuration is the benefits of the signal-to-noise ratio associated with the modulated signals. In this way topography images using a small tip-sample force can be taken. As the oscillation probe approaches to the surface, the frequency and amplitude changes due to the force interaction between tip and surface. As before, by controlling one of these parameters the topography of the sample can be measured. The main advantage is the low interaction between probe and sample, what can be very convenient for avoiding damage in soft materials.

- Intermittent contact mode (tapping mode): this is a variation of the oscillating mode. In this case the amplitude of the oscillation is high enough to enter in the contact regime and subsequently move far away from the sample. This technique involves large probe tip–sample forces, so it can be more destructive for both, probe and sample. However, this configuration allows to almost eliminate lateral forces and pass through the contamination layer of the sample. Changes on the phase of the cantilever in tapping mode can be useful to distinguish different materials, as these variations are strongly affected by the tip-sample interactions.

In fact, phase imaging is a measurement of the energy dissipation involved in the contact between tip and sample, which depends on adhesion and contact area. However, the contact area depends on the slope of the sample, and therefore the phase imaging has a topography component that can difficult the data interpretation. The majority of the AFM measurements presented in this work have been taken using the tapping mode.

2.5.6.2 Peak Force Quantitative Nanoscale Mechanical Characterization (QNM)

AFM is also capable to perform spectroscopic measurements regarding mechanical and electrochemical properties, taking advantage of the high resolution mapping of the AFM. In this way, force spectroscopy maintain the in plane axis fixed while the z axis (tip-sample distance) is ramped to measure the deflection of the tip as it approaches and retracts from the sample surface [89]. The force curves obtained at each point are similar to Figure 2.20. When the cantilever is far away from the surface no deflection is measured (A). As it approaches it feels the adhesion forces to the surface (B), which change into repulsion forces as it continues approaching to the sample. The maximum force (peak force) applied to the surface by the probe tip can be modulated in order to not disturb the surface (C). Once the tip starts to withdraw the force decreases until the maximum adhesion point (D), after what the tip comes off the sample and its deflection tends to zero (E).

Several mechanical properties can be inferred from these force-curves. Stiffness, deformation, dissipation and adhesion maps of the surface can be taken. In addition, some quantifiable properties such as elastic modulus can be calculated from the analysis.

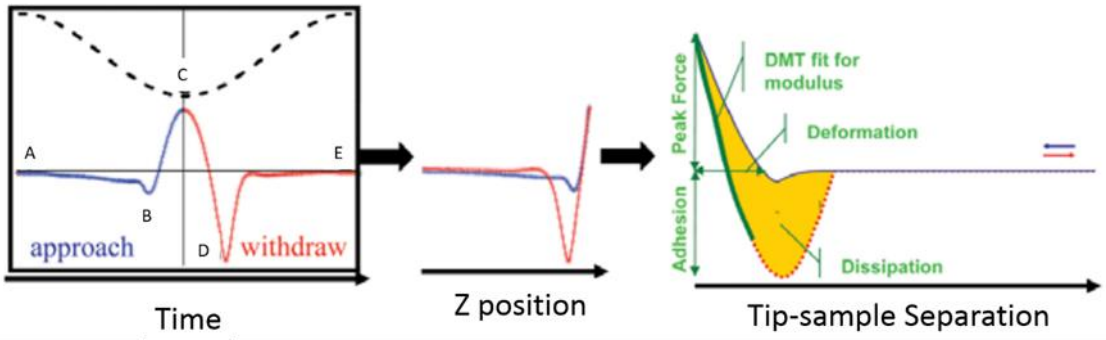

Figure 2.20 Force curves and information that can be obtained from them. Taken from [90].

2.5.6.3 Kelvin Probe Force Microscopy (KPFM)

Kelvin Probe Force microscopy (KPFM) is used to measure the work function of the surface if the probe-tip work function is already well calibrated [89]. If it is not the case, KPFM images will only show a contact potential difference (V_{CPD}) given by [91]:

$$V_{CPD} = (\Phi_{tip} - \Phi_{sample})/e \qquad \text{(Eq. 2.21)}$$

,where Φ are the tip and sample work functions. The principle of operation is simple. The electrostatic force between tip and sample is given by:

$$F_{electroestatic} = -\frac{1}{2}V^2\frac{dC}{dz} \qquad \text{(Eq. 2.22)}$$

,where C is the capacitance, z is the separation, and V is the voltage, each between tip and surface. Now, if there is no voltage difference between tip and sample the electrostatic force will be zero. Thus, a voltage vias (V_{bias}) composed by both a DC (V_{DC}) and AC (V_{AC}) terms will be applied to the tip:

$$V_{bias} = V_{DC} + V_{AC}\sin(\omega t) \qquad \text{(Eq. 2.23)}$$

The AC voltage is set to oscillate at the resonant frequency of the cantilever. Substituting Eq. 2.22 at 2.21 it can be demonstrated that if the V_{CPD} is not zero, then the electrostatic force will change as a function of sin(ωt):

$$F_{electroestatic} = F_{DC} + F_{\omega} + F_{2\omega},$$
$$where\ F_{\omega} = \frac{dC}{dz}[V_{DC} - V_{CPD}]V_{AC}\sin(\omega t) \qquad \text{(Eq. 2.24)}$$

This means that by a feedback loop the applied V_{DC} can be changed to minimize F_{ω} term, and therefore a map of the V_{CPD} can be performed.

2.5.6.4 Experimental details

AFM measurements shown at Chapters 3 and 4 regarding CoO/HOPG and ZnO/HOPG and G/Cu, respectively, were made in a Nanotec Cervantes Microscope with a Dulcinea electronic control unit at the ICMM, using Si tips from Nanosensors (PPP-NCHR and SSS-NCHR models, f~300 kHz, k~30N/m) and Si tips coated with Au nanoparticles, made by Yves Huttel (patent P201030712, current assignee CSIC). All the images were taken in tapping mode, and were processed with the WSxM software [92]. AFM images performed in combination with confocal Raman spectroscopy were taken with Witec ALPHA 300RA (see section 2.4.7.1). These AFM images were processed and analyzed with the software WiTec Project Plus 2.08

On the other hand, AFM and QNM measurements of the Al_2O_3 ultra-thin membranes shown in chapter 5 were taken at the Imaging and Manipulation of Nanostructures Facility of the Molecular Foundry with a Bruker Ikon 8 AFM. The images were taken also in tapping mode and were processes with the same WSxM software.

KPFM measurements were performed on re-oxidized ~2 Eq-ML CoO/HOPG samples Imaging and Manipulation of Nanostructures Facility of the Molecular Foundry using a Cypher VRS microscope at room temperature and nitrogen atmosphere. The images were processed and analyzed with the WSxM software.

2.5.7 Confocal micro-Raman Microscopy (CRM)

Raman spectroscopy is a technique used to measure vibrational, rotational, and other low-frequency modes of a certain material, which in fact represents a structural fingerprint. The fundamental principle of Raman spectroscopy can be classically deduced from the temporal dependence of the induced dipole moment of a molecule due to the effect of a periodic electric field. In this way, the induced dipole moment (μ(t)) can be written as:

$$\vec{\mu}(t) = \tilde{\alpha}\overrightarrow{E_o}\cos(\omega_o t) \qquad \text{(Eq. 2.25)}$$

,where $\overrightarrow{E_o}\cos(\omega_o t)$ is the external electric field of the incoming radiation and $\tilde{\alpha}$ is the molecular polarizability, which is physically related to the extent that the driving field is able to disturb the electron density of the sample out of its equilibrium configuration.

Nevertheless, the molecular polarizability is not a static parameter, but depends on the nuclear motion and the corresponding adiabatically adjust of the electronic density in order to minimize the energy of the system. Therefore, as it is shown elsewhere [93], the polarizability can be expanded into Taylor series around the equilibrium nuclear geometry Q_0, where Q represents the group of all individual normal modes q:

$$\alpha = \alpha(Q) = \alpha_o + \sum_{q=1}^{N}\left[\left(\frac{\partial\alpha}{\partial q}\right)_{q_o} \cdot q + \frac{1}{2}\left(\frac{\partial^2\alpha}{\partial q \partial q'}\right)_{q_o q'_o} \cdot q\, q' + O(q^3)\right] \qquad \text{(Eq. 2.26)}$$

Inserting equation 2.25 in 2.24 and applying a harmonic approximation it can be demonstrated that the induced diploe moment is given by:

$$\mu(t) = \alpha E_o \cos(\omega_o t) + \frac{1}{2}\left(\frac{\partial\alpha}{\partial q}\right)_{q_o} q_o E_o \cos\left[(\omega_o - \omega_q)t\right]$$
$$+\frac{1}{2}\left(\frac{\partial\alpha}{\partial q}\right)_{q_o} q_o E_o \cos\left[(\omega_o + \omega_q)\, t\right] \qquad \text{(Eq. 2.27)}$$

This last equation constitutes the theoretical base of the Raman spectroscopy, as the time-dependent induced dipole moment is a source of scattering radiation. The first term oscillates with the same frequency as the excitation radiation, and constitutes the elastic scattering known as Rayleigh scattering. The second term oscillates with the difference between the source and the molecular normal mode frequency, and therefore this radiation is red-shift. This component is known as Stokes scattering and constitute the typical Raman scattering spectrum. Finally, the third term is blue-shift and is identical to the previous one but with a reduced intensity due to the lowest population of these exited vibrational states.

Moreover, the classical selection rule that governs the Raman scattering process is given by $\left(\frac{\partial\alpha}{\partial q}\right)_{q_o} \neq 0$, i.e. Raman emission will be active if there are changes on the polarizability of a molecule in a given normal coordinate. Other factors that determine the Raman spectrum are the mass of the atoms and their chemical environment, including the bond strength of the molecule.

On the other hand, the experimental confocal Raman setup [93,94,95] consists on a point-like laser light source (focused with a lens or an objective onto a sample). The spatial extension of the focus spot on the sample is determined by the wavelength λ and the quality of the image formation. The image spot is then focused through the same (or a second) lens onto an aperture (pinhole) in front of a detector. There must exist a compromise in the aperture of the pinhole, the image is better as the pinhole dimensions decrease, but the Raman signal, which is thousand times lower than the Rayleigh emission, will be very tiny. This configuration enables the spectroscopic imaging of the sample with a lateral resolution of various hundreds of nanometers. In addition, the focus plane of the excitation laser on the sample will determine the probe depth of the analysis, and therefore also volumetric mappings can be achieved. Figure 2.21 shows a basic scheme of a confocal Raman microscope.

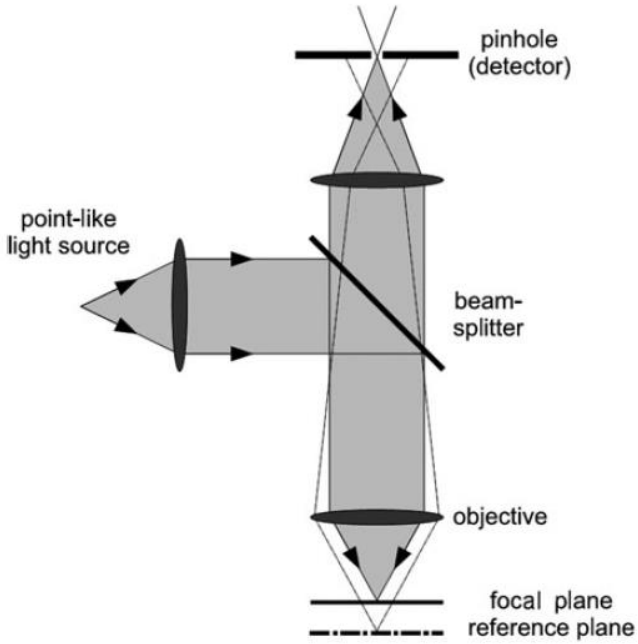

Figure 2.21 Basic scheme of the confocal Raman experimental set up. Taken from [93].

2.5.7.1 Experimental details

Raman spectra were taken at the ICV-CSIC with a confocal Raman microscope coupled with and AFM instrument (Witec ALPHA 300RA), with laser excitation at 532 nm and a 100x objective lens (NA = 0.9). The incident laser power was set in a range between 1 and 30 mW. The optical diffraction resolution was limited to about 200 nm laterally and 500 nm vertically while Raman spectral resolution of the system was down to 0.02 cm^{-1}. The samples were mounted in a piezo-driven scan platform having 4 nm

lateral and 0.5 nm vertical positioning accuracy, also equipped with an active vibration isolation system, active 0.7–1000 Hz. The images were processed and analyzed with the software WiTec Project Plus 2.08. In some spectra the fluorescence background from the Cu foil has been subtracted by a polynomial fit of degree 9.

2.5.8 Transmission Electron Microscopy (TEM)

Transmission electron microscopy (TEM) is an imaging technique based on the transmission through a thin sample (<100 nm) of an electron beam [96,97]. The image is formed by the interaction of the electrons with the electronic cloud of the sample atoms, where the low Broglie wavelength of the electrons allows the extremely high resolution of this technique. Besides, the diffraction of the incoming electron beam can be used to obtain structural information of the sample. Figure 2.22 shows a scheme of the microscope elements for imaging and diffraction configurations.

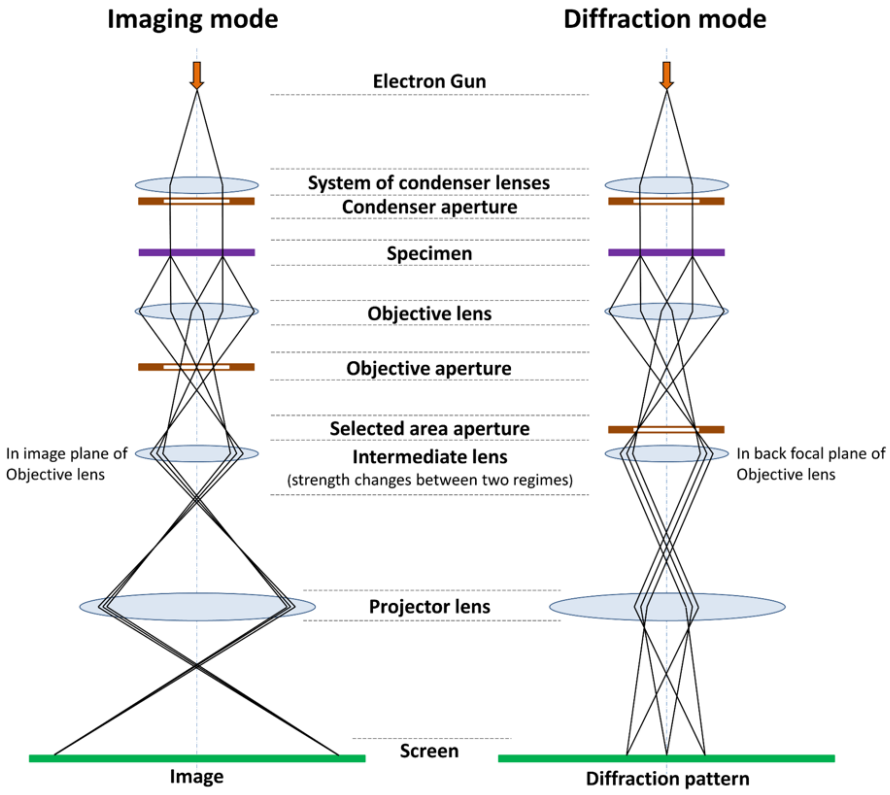

Figure 2.22 Basic scheme of the TEM elements on both imaging and diffraction modes. Taken from [98].

In addition TEM imaging is usually done in combination with other chemical techniques, such as energy dispersive X-ray (EDX) [99] or electron energy loss spectroscopy (EELS) [100]. In the case of EDX, the excited atoms due to the interaction with the electron beam can decay to the ground state emitting a particular fluorescence spectrum, which can provide a quantification of the composition of the sample. On the other hand, EELS technique studies the energy loss of the electrons of the TEM beam, which can be related with several inelastic process such as phonon excitations, inter- and intra-band transitions or plasmon excitations among others. If the electron-electron momentum transference conditions are adequate, then similar resolutions to XAS on transmission mode can be achieve [101]. In a similar way to XPS, EELS can be used just for elemental characterization or for deeper studies regarding the electronic structure of compounds.

2.5.8.1 Experimental details

TEM measurements were taken in two different facilities. In first place, TEM images, with their corresponding EDX and electron diffraction results shown in Chapter 4 were performed at SCAI, Universidad de Málaga, Málaga, Spain. The high resolution microscope was a FEI Talos F200X equipped with a FEG electron source of 200 keV, four simultaneous EDX detectors, EELS and four STEM (HAADF, DF1, DF2, BF) detectors for the collection of images, mapping composition and 3D topographies. The measured specimen was prepared from a ~3.5 Eq-ML ZnO/G/Cu sample at a SEM/FIB microscope Dual Beam Helios NanoLab 650 (FEI), see section 2.4.10.1 for more details.

In second place, the measurements shown in Chapter 5 were taken at the Imaging and Manipulation of Nanostructures Facility of the Molecular Foundry using a JEOL 2100-F 200 kV Field-Emission Analytical Transmission Electron Microscope. The instrument is equipped with an analytical pole piece, a high solid-angle EDX system for elemental X-ray analysis, a Gatan Tridiem spectrometer for energy-filtered imaging and spatially-resolved EELS, a HAADF (high-angle annular dark field) STEM detector, and several digital cameras.

2.5.9 Scanning Electron Microscopy (SEM)

Scanning electron microscopes (SEM) produce an image of the sample by a raster scan pattern of the surface with an electron beam [102]. The most common image

configuration uses secondary electrons that are emitted from the surface by different process involving inelastic scattering. As indicated on section 2.4.1, although the volume of the solid excited by the electron beam extends a depth from 100 nm to 5 μm depending on the material and energy of the beam, due to the low energy of these secondary electrons their IMFP limits the probing depth of the technique in the range of few nanometers. The amount of secondary electrons emitted from the sample depends on the topography among other material parameters.

On the other hand, backscattering electrons are high energy electrons coming from the electron beam that are elastically reflected by the sample. As the probability of backscattering electrons increases with the atomic number Z of the atoms that compose the sample, backscattered images gives a contrast image of the composition of the surface, but not a quantification. These types of images present o lower resolution than secondary electrons configuration.

Finally, as for the TEM measurements, the fluorescence route for atomic decay can also be measured by EDX detectors. As before, the depth of this analysis is much deeper and is considered a volume stoichiometry technique.

2.5.9.1 Experimental details

SEM images shown in Chapter 4 have been taken at two different localizations. In first place, the comparative study of the growth of ZnO on HOPG and G/Cu have been carried out with a Field Emission Gun-Scanning Electron Microscope Philips XL30 S-FEG at the SIdI facility of the Universidad Autónoma de Madrid. This microscope has a maximum resolution of 3.5 nm. The EDX measurements have been taken with the SEM Hitachi S-3000N, which has an ECON IV detector attached to it. The second SEM instrument is a Dual Beam Helios NanoLab 650 (FEI) from SCAI, Universidad de Málaga, Málaga, Spain. It has an electron field emission source ElstarTM XHR, with a beam energy range between 20-30 keV. It presents a resolution of 0.9 nm at 1 kV. Besides, it also has an ion source of gallium ElstarTM XHR for FIB analysis and manipulation.

SEM and EDX results described in Chapter 5 were done at the Imaging and Manipulation of Nanostructures Facility of the Molecular Foundry with a Zeiss Gemini Ultra-55 Analytical Field Emission SEM. It has a variable beam energy between 100 eV and 30 kV, with 1 nm resolution above 2 kV and several nm resolution at 100 eV.

2.6 Experimental methodology

The purpose of this section consists on a brief and detailed technical description of the treatments and processes performed in this work. In this way, section 2.5 is divided into three categories: deposition methodology, re-oxidation methodology and finally preparation methodology of free standing supports. For each case the chapters where these recipes have been used are indicated.

2.6.1 Deposition methodology

2.6.1.1 CoO deposition

CoO has been only deposited on HOPG substrates. Before being introduced inside the vacuum chamber, HOPG was cleaved at room conditions. As stated before, CoO deposition can be divided into two categories depending on the evaporation device:

- Thermal evaporation (cobalt wires): before using the Co wires for the first time since their contact with the atmosphere, they were outgassed by heating them using the working current under high vacuum condition, maintaining this situation until the pressure of the chamber dropped. Once the wires were cleaned, the evaporation was performed. The growth was done at room temperature. The steps for each evaporation were:

    1. Ensure initial pressure below 10^{-8} mbar.
    2. Position the sample in front of the evaporator, facing the opposite direction.
    3. Increase of the electric current until 4 A.
    4. After 20 minutes at that current value, open the O_2 leak valve until a final pressure of $2 \cdot 10^{-5}$ mbar.
    5. Rotation of the sample to face the evaporator. Evaporation time starts to count from this point.
    6. Once the desired evaporation time has been achieved, rotate the sample to the initial position.
    7. Decrease the electric current. Close O_2 leak valve is closed after two minutes.

These growths were done at the preparation chamber of CLAM 4-Camarón system. Subsequently, *in situ* XPS measurements were performed. One set of samples of ~0.5-4 eq-ML were then re-oxidized by method R1 (see 2.5.2) and measured by *ex situ* AFM. Other three samples of different thicknesses were measured again by *ex situ* XPS after 24 hours under atmospheric conditions. These same samples were then measured at the SpLine, branch B, by means of HAXPES.

- E-beam evaporation: the main difference to the previous one is the evaporation source. As before, the e-beam evaporator was outgassed after being in contact with the atmosphere by setting the evaporation parameters of electric current and voltage and waiting until the pressure dropped. The growth was done at room temperature. The steps of the evaporation process were:

    1. Ensure initial pressure below $5 \cdot 10^{-8}$ mbar
    2. Open O_2 leak valve until a chamber pressure of $9 \cdot 10^{-6}$ mbar. Sample facing the evaporator.
    3. Gradually increase the voltage difference until 1.25 kV.
    4. Gradually increase the filament current until 7 A.
    5. Gradually increase emission current until 10 mA.
    6. Evaporation time starts once the evaporator shutter is removed.
    7. Close the evaporator shutter once the desired evaporation time has been achieved.
    8. Decrease the emission current. After 2 minutes, O_2 leak valve is closed.
    9. Decrease filament current and high voltage.

    These growths were done at Chambao chamber, followed by *in situ* re-oxidation R1 (see 2.5.2) and *ex situ* AFM measurements; and at CIRCE-NAPP endstation for an *in situ* NAP-XPS study.

2.6.1.2 ZnO deposition

ZnO was deposited on HOPG and graphene/Cu substrates. HOPG was cleaved at room conditions before its introduction into the vacuum system, while G/Cu substrates were not thermally cleaned to avoid metallic zinc contamination. All ZnO growths were done by using the thermal evaporator described in section 2.3.1, which after every atmospheric contact was outgassed by heating it until work temperature was reached, maintaining this situation until the pressure of the chamber decreased. The growth was done at room temperature. The steps for the evaporation were:

1. Ensure initial pressure below 10^{-8} mbar.
2. Position sample. For HOPG substrate, sample positioned in front of the evaporator, facing the opposite direction. G/Cu substrate, sample situated in position 1 (see Figure 2.23).
3. Increase gradually the electric current until 3.5-4 A (HOPG and Grapene/Cu, respectively).
4. Once temperature reaches 330 °C, open O_2 leak valve until a final pressure of 10^{-3} mbar is stabilized.
5. Reposition sample. For HOPG substrates, rotation of the sample to face the evaporator. In the case of G/Cu substrate, in order to achieve the lowest deposition rate as possible, sample would be move to positions 1, 2 or 3 (from lower to higher deposition rates), as it is shown in Figure 2.13. Position 1 is away from the evaporator, position 2 is in front of the evaporator but in the opposite direction, and finally position 3 is facing the evaporation source. Evaporation time starts to count from this point (in case of position 1, from the moment at which O_2 leak vale is opened).
6. Once the desired evaporation time has been achieved, move the sample to the initial position. In the case of G/Cu samples situated at position 2 or 3, this implies to position 1. If the sample was at position 1, then O_2 leak valve is closed.
7. Decrease the electric current. Close O_2 leak valve after 2 minutes.

All these growths were done at CLAM 4-Camarón preparation chamber. Subsequently, *in situ* XPS measurements were performed. For a set of samples of representative thicknesses after *in situ* XPS measurements, *ex situ* confocal Raman microscopy, SEM and AFM measurements were performed. For a set of samples of 2 Eq-ML of ZnO on HOPG, *in situ* re-oxidation processes R1 and R2 were done for comparison with CoO/HOPG, measured by XPS, SEM and confocal Raman microscopy. 3,5 Eq-ML ZnO/G/Cu samples were *ex situ* measured by *ex situ* XPS-microscopy TEM and SEM-EDX. Finally, graphene/Cu pristine samples, previously measured by confocal Raman microscopy and PEEM, were used to grow ZnO by this method. Then, these samples were also measured with Raman spectroscopy.

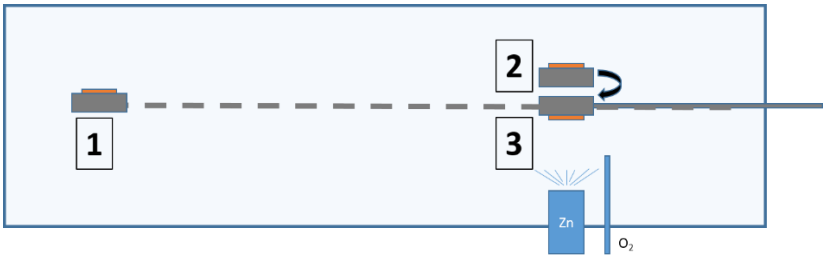

Figure 2.23 Position scheme of the G/Cu samples.

2.6.1.3 Al_2O_3 deposition

Al_2O_3 was deposited on different substrates: SiN, Au/SiN, G/SiN, G/Au/SiN, PMMA, free standing graphene, and Formvar. All these samples were grown by the ALD technique at 40°C and using oxygen plasma. The recipe of this process consist of:

1. Ensure initial pressure is below $5 \cdot 10^{-6}$ mbar
2. Pum 30 seconds and pre-heat at 40 °C for 2 minutes.
3. Cycle:
    a. TMA dose 0.02 seconds
    b. TMA purge 10 seconds
    c. Pre-plasma 0.1 seconds
    d. Plasma 2 seconds
    e. Post-plasma 0.5 seconds
4. Pump the growth chamber for 1 minute.

The samples growth by this technique were done at the cleanroom of the Molecular Foundry Nanofabrication facility. These samples were studied by XPS, SEM, AFM Raman spectroscopy and TEM. The final Al_2O_3 membranes were tested under realistic operando conditions at the 11.0.2 beamline of the ALS.

2.6.2 Re-oxidation methodology

CoO/HOPG and ZnO/HOPG samples were subjected to two different kind of thermal oxidation process, named before as R1 and R2:

- Re-oxidation process R1: the sample was heated up to 400 °C under ultra-high vacuum conditions and then exposed to O_2 for 1 hour maintaining that temperature.

    1. Initial pressure below 10^{-8} mbar.
    2. Position and align the sample, heater and pyrometer.
    3. Heat the sample under UHV to 400 °C
    4. Once the temperature is stabilized, open O_2 leak valve. Different pressures can be used depending on the experiment, from 10^{-5} mbar to 10^{-3} mbar.
    5. Stop heating after one hour.
    6. Close O_2 valve once the temperature is below 100 °C.

- Re-oxidation process R2: the samples were first exposed to O_2 and then heated up to 400 °C. After 1 hour under these conditions, the temperature was decreased.

    1. Initial pressure below 10^{-8} mbar.
    2. Position and align the sample, heater and pyrometer.
    3. Open O_2 leak valve. Different pressures can be used depending on the experiment, from 10^{-5} mbar to 10^{-3} mbar.
    4. Heat the sample under this pressure to 400 °C
    5. Stop heating after one hour of stabilized temperature.

6. . Close O2 valve once the temperature is below 100 °C.

2.6.3 Free standing supports preparation

This section refers to the preparation of the free standing supports used for the deposition of the Al_2O_3 membranes on chapter 5. The basic idea is to transfer the material that will serve as support for the Al_2O_3 deposition on the TEM SiN grid holes, in such a way that these holes will be cover by this *support* material. Therefore, two different approaches have been tried by using graphene and Formvar.

2.6.3.1 Free standing graphene

Two graphene transfer methods could be distinguish depending on the use of a polymer supportive layer (in our case PMMA) or by a free polymer method. The steps for each process are:

- Free polymer method:

1. Prepare sodium persulfate ($Na_2S_2O_8$) 0.5 mol/l in water.
2. Remove graphene from the backside of the copper foil by exposure to O_2/Ar (25/75%) plasma during 15 minutes.
3. Prepare a supportive Al adhesive foil frame consisting of ~2 mm width and a ~8 x 8 mm^2 hole, which is stuck on the graphene side of the copper foil.
4. Cu etching for ~4 hours with the sodium persulfate solution.
5. Transfer the graphene to deionized water (~4 hours) by a watch glass previously ultrasonic cleaned with isopropyl alcohol and with O_2/Ar (25/75%) plasma.
6. Gentle O_2/Ar (25/75%) plasma cleaning of the Au/Cr/SiN TEM grid.
7. An Au/Cr/SiN TEM grid is then used to lift the free standing graphene from water and is left to dry.

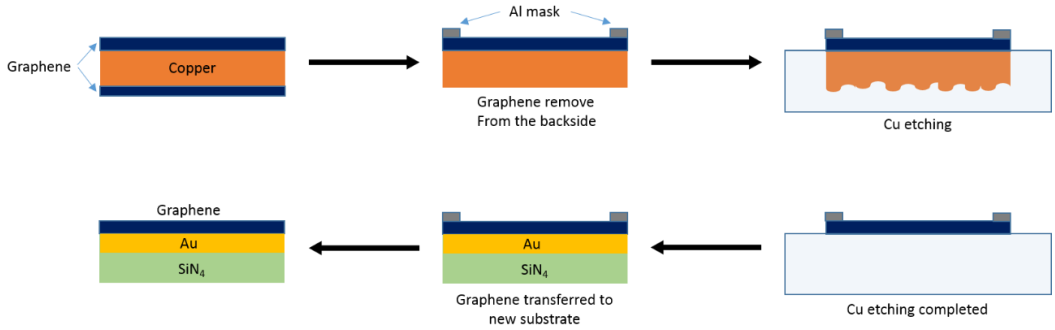

Figure 2.24 Basic scheme of the free polymer transfer method.

- PMMA supportive layer method:

1. Prepare sodium persulfate (Na2S2O8) 0.5 mol/l in water.
2. Remove graphene from the backside of the copper foil by exposure to O_2/Ar (25/75%) plasma during 15 minutes.
3. PMMA supportive layer preparation.
    i. PMMA spincoating (30 seconds, 3000 rpm) of PMMA solution on the graphene side of the copper foil.
    ii. PMMA layer cure at 120 °C for 15 minutes.
4. Cu etching for ~4 hours with the sodium persulfate solution.
5. Transfer the graphene to deionized water (~4 hours) by a watch glass previously ultrasonic cleaned with isopropyl alcohol and with O_2/Ar (25/75%) plasma.
6. Gentle O_2/Ar (25/75%) plasma cleaning of the Au/Cr/SiN TEM grid.
7. An Au/Cr/SiN TEM grid is then used to lift the free standing graphene from water and is left to dry.
8. Remove PMMA:
    i. 70 °C heating for 15 minutes to enhance adhesion.
    ii. Acetone soaking for 20 minutes (repeat twice)
    iii. Isopropyl alcohol soaking for 20 minutes.
    iv. Ethanol soaking for 20 minutes.

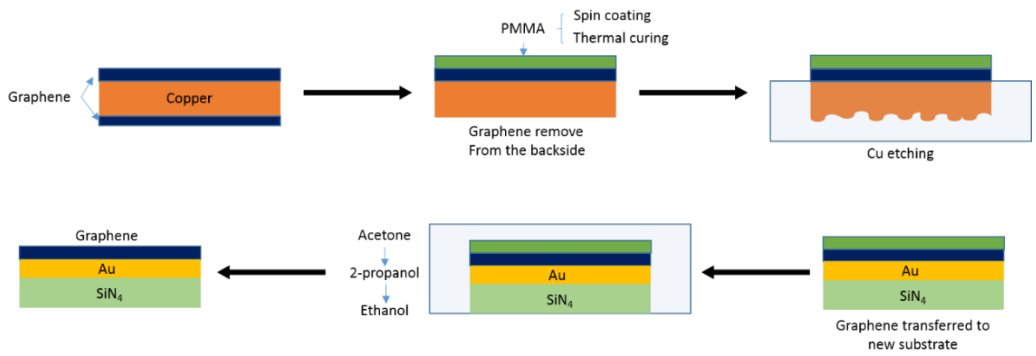

Figure 2.25 Basic scheme of the polymer supportive-layer transfer method.

After the Al_2O_3 growth the graphene could be removed by a gentle oxygen plasma etching.

2.6.3.2 Formvar

The Formvar free standing layer on TEM grids has been done following this steps:

1. Soak a glass microscope slide into Formvar solution for 20 seconds.
2. Dry in a vertical position for 5 minutes.
3. Cut with a blade the borders of the glass slide and the limit of the Formvar layer.
4. Very slow vertical immersion of the glass slide on a water container. The Formvar layers of both sides should be separated from the microscope slide floating on the water.
5. Clean the Au/Cr/SiN TEM grid with gentle O_2/Ar (25/75%) plasma.
6. An Au/Cr/SiN TEM grid is then used to lift the free standing Formvar from water and is left to dry.

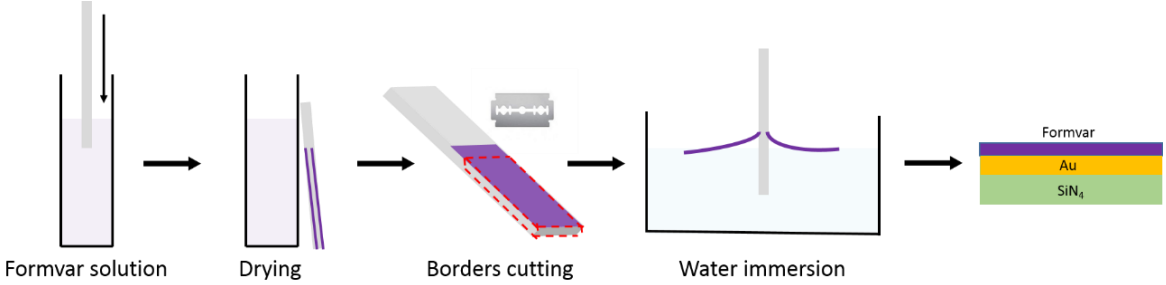

Figure 2.26 Basic scheme of the Formvar transfer method.

After the Al_2O_3 growth the Formvar could be removed by immersing the sample on chloroform.

Bibliography

[1] T. Takami; 2011; *Functional Cobal*t Oxides: *Fundamentals, Properties and Applications*; Singapore, Republic of Singapore; Pan Stanford Publishing

[2] B. Raveau, M. Seikh; 2012, *Cobalt Oxides: From Crystal Chemistry to Physics;* Weinheim, Germany; Wiley

[3] M. Chen, B. Hallstedt, J. L. Gauckler; "Thermodynamic assessment of the Co-O system"; *J. Phase Equilib.* 24, (2003); pp: 212-227; DOI: 10.1361/105497103770330514

[4] K. M. Nam, J. H. Shim. D.-W. Han, H. S. Kwon, Y.-M. Kang, Y. Li, H. Song, W. S. Seo, J. T. Park. "Syntheses and Characterization of Wurtzite CoO, Rocksalt CoO, and Spinel Co3O4 Nanocrystals: Their Interconversion and Tuning of Phase and Morphology". *Chem. Mater*., 22, (2010); pp: 4446-4454;DOI:

10.1021/cm101138h

[5] J. Dicarlo, A. Navrotsky; "Energetics of Cobalt (II) Oxide with the Zinc-Blende Structure". J. Am. Ceram. Soc., 76, (1993); pp: 2465-2467; DOI: 10.1111/j.1151-2916.1993.tb03967.x.

[6] Wikipedia Commons: spinel structure:

https://en.wikipedia.org/wiki/Cobalt(II,III)_oxide#/media/File:Cobalt(II,III)-oxide-unit-cell-2006-CM-perspective-3D-balls.png; and rocksalt structure:

https://en.wikipedia.org/wiki/Cubic_crystal_system#/media/File:NaCl_polyhedra.png

[7] J. Solé, L. Bausa, D. Jaque; 2005; *An Introduction to the Optical Spectroscopy of Inorganic Solids*, Weinheim, Germany; Wiley

[8] A. Awan, R. J. Lancashire; *Crystal Field Theory* (Chemwiki). Ed. by Davis University of California. URL:

http://chemwiki.ucdavis.edu/Inorganic_Chemistry/Crystal_Field_Theory/Crystal_Field_Theory.

[9] See: https://www.goodfellow.com

[10] See: https://www.hmw-hauner.de

[11] C. F. Klingshirn, B. K. Meyer ,A. Waag, A. Hoffmann, J. Geurts; 2010; *Zinc Oxide: From Fundamental Properties Towards Novel Applications*; Berlin, Germany; Springer

[12] Ü. Özgür, Ya. I. Alivov, C. Liu, A. Teke, M. A. Reshchikov, S. Doğan, V. Avrutin, S.-J. Cho, H. Morkoç; "A comprehensive review of ZnO materials and devices"; *J. Appl. Phys*. 98, (2005); pp: 041301; DOI: 10.1063/1.1992666

[13] T. Kogure, Y. Bando; "Formation of ZnO nanocrystallites on ZnS surfaces by electron beam irradiation"; *J. Electron Microsc*; 47, (1998); pp: 135-141; DOI: 10.1093/oxfordjournals.jmicro.a023570

[14] S.-K. Kim, S.-Y. Jeong, C.-R. Cho; "Structural reconstruction of hexagonal to cubic ZnO films on Pt/Ti/SiO_2/Si substrate by annealing"; *Appl. Phys. Lett*. 82, (2003); pp: 562 DOI: 10.1063/1.1536253

[15] C. H. Bates, W. B. White, R. Roy; "*New High-Pressure Polymorph of Zinc Oxide*"; *Science,* 137, (1962); pp: 993; DOI: 10.1126/science.137.3534.993

[16]Wikipedia Commons: wurtzite structure:

https://upload.wikimedia.org/wikipedia/commons/8/8e/Wurtzite_polyhedra.png; zinc-blende structure:

https://en.wikipedia.org/wiki/Zinc_sulfide#/media/File:Sphalerite-unit-cell-3D-balls.png ; and rocksalt structure:

https://en.wikipedia.org/wiki/Cubic_crystal_system#/media/File:NaCl_polyhedra.png

[17] P. Mikheeva, G. M. Zhidomirov, S. F. Ruzankin, S. A. Leontiev, V. G. Devyatov, S. V. Koshcheev, A. E. Cherkashin; "Modeling the photoelectron spectra of the valence O-2p band of Zinc Oxide by the Xα-scattered wave method"; *J. Struct. Chem*, 38, 5; (1997), pp 732-741; DOI: 10.1007/BF02763885

[18] S. A. Leontiev, S. V. Koshcheev, V. G. Devyatov, A. E. Cherkashin, and P. Mikheeva; "Detailed XPS and UPS studies of the band structure of Zinc Oxide"; *J. Struct. Chem*, 38, (1997); pp: 725-731; DOI: 10.1007/BF02763884

[19] N. Rössler, K. Kotsis, V. Staemmler; "Ab initio calculations for the Zn 2s and 2p core level binding energies in Zn oxo compounds and ZnO"; *Phys. Chem. Chem. Phys.*; 8, (2006); pp: 697-706; DOI: 10.1039/b512379h

[20] E. Dörre, H. Hübner; 1984, *Alumina: Processing, Properties, and Applications*, Berlin, Germany; Springer

[21] C. Dohmeier; D. Loos; H. Schnöckel; "Aluminum(I) and gallium(I) compounds: Syntheses, structures, and reactions". *Angewandte Chemie International Edition*. 35, (1996); pp: 129-149; DOI: 10.1002/anie.199601291

[22] D. C. Tyte; "Red ($B^2\Pi$–$A^2\sigma$) Band System of Aluminium Monoxide"; *Nature*, 202, (1964); pp: 383-384 ; DOI: 10.1038/202383a0

[23] K. Wefers; C. Misr; 1987. *Oxides and Hydroxides of Aluminum*. Alcoa Technical Paper No. 19, Revised; Alcoa Laboratories: Alcoa Center, PA

[24] J. Carlsson; S. Gorbatkin; D. Lubben; J. E. Greene; "Thermodynamics of the homogeneous and heterogeneous decomposition of trimethylaluminum, monomethylaluminum, and dimethylaluminumhydride: Effects of scavengers and ultraviolet-laser photolysis". *J. Vac. Sci. Technol*., B. 9, (1991); pp: 2759-2770; DOI: 10.1116/1.585642.

[25] L.G.Gosset, J.-F.Damlencourt, O.Renault, D.Rouchon, Ph. Holliger, A.Ermolieff, I.Trimaille, J.-J.Ganem, F.Martin, M.-N.Séméria; "Interface and material characterization of thin Al2O3 layers deposited by ALD using TMA/H2O"; *J. Non-Cryst. Solids*; 303, (2002); pp: 17-23; DOI: 10.1016/S0022-3093(02)00958-4

[26] α-Al_2O_3 structure: CrystalMaker Software Ltd., Begbroke Science Park, Building 5, Yarnton, OX5 1PF, UK; http://www.crystalmaker.com;

Timethylaluminum dimer:

https://en.wikipedia.org/wiki/Trimethylaluminium#/media/File:Trimethylaluminium-3D-balls.png

[27] Picture taken from: http://nanoprobes.aist-nt.com/apps/HOPG%20info.htm

[28] See: www.brukerafmprobes.com

[29] A. Das, S. Pisana, B. Chackraborty, S. Piscanec, S. K. Saha, U. V. Waghmare, K. S. Novoselov, H. R. Krishnamurthy, A. K. Geim, A. C. Ferrari, A. K. Sood. "Monitoring dopants by Raman scattering in an electrochemically top-gated graphene transistor"; *Nature Nanothecnology*; 3, (2008); pp: 210-215; DOI: 10.1038/nnano.2008.67

[30] J. E. Lee, G. Ahn, J. Shim, Y. S. Lee, S. Ryu; "Optical separation of mechanical strain from charge doping in graphene"; *Nature Communications*, 3, (2012); pp: 1024; DOI: 10.1038/ncomms2022

[31] G. Tsoukleri, J. Parthenios, K. Papagelis, R. Jalil, A. C. Ferrari, A. K. Geim, K. S. Novoselov, C. Galiotis; "Subjecting a Graphene Monolayer to Tension and Compression"; *Small*, 5, (2009); pp: 2397-2402; DOI: 10.1002/smll.200900802

[32] R. S. Weatherup, L. D'Arsié, A. Cabrero-Vilatela, S. Caneva, R. Blume, J. Robertson, R. Schloegl, S. Hofmann; "Long-Term Passivation of Strongly Interacting

Metals with Single-Layer Graphene"; *J. Am. Chem. Soc.*, 137, (2015); pp: 14358-14366; DOI: 10.1021/jacs.5b08729

[33] A. Dahal, M. Batzill; "Graphene–nickel interfaces: a review"; *Nanoscale*; 6, (2014); pp: 2548-2562; DOI: 10.1039/C3NR05279F

[34] P. R. Kidambi, B. C. Bayer, R. Blume, Z.-. Wang, C. Baehtz, R. S. Weatherup, M.-G. Willinger, R. Schloegl, S. Hofmann; "Observing Graphene Grow: Catalyst−Graphene Interactions during Scalable Graphene Growth on Polycrystalline Copper"; *Nano Lett*. 15, (2015); pp 917-922; DOI: 10.1021/nl5036463

[35] A. Grüneis, D. V. Vyalikh; "Tunable hybridization between electronic states of graphene and a metal surface"; *Phys. Rev. B*; 77, (2008); pp 193401; DOI: 10.1103/PhysRevB.77.193401

[36] J. S. Bunch, S. S.Verbridge, J. S. Alden, A. M. van der Zande, J. M. Parpia, H. G. Craighead, P. L. McEuen; "Impermeable Atomic Membranes from Graphene Sheets"; *Nano Lett*., 8, (2008); pp: 2458−2462. DOI: 10.1021/nl801457b

[37] P.R. Kidambi, B. C. Bayer, R. Blume, Z.-J. Wang, C. Baehtz,, R. S. Weatherup, M.-G. Willinger, R. Schlögl, S. Hofmann; "Observing Graphene Grow: Catalyst–Graphene Interactions during Scalable Graphene Growth on Polycrystalline Copper"; *Nano Lett.*, 13, (2013); pp: 4769−4778; DOI: 10.1021/nl4023572

[38] R. Blume, P. R. Kidambi, B. C. Bayer, R. S. Weatherup, Z.-J. Wang, G. Weinberg, M.-G. Willinger, M. Greiner, S. Hofmann, A. Knop-Gerickee, R. Schlögl; "The influence of intercalated oxygen on the properties of graphene on polycrystalline Cu under various environmental conditions"; *Phys. Chem. Chem. Phys*., 16, (2016); pp: 25989-26003; DOI: 10.1039/c4cp04025b

[39] Robert S. Weatherup, Baran Eren, Yibo Hao, Hendrik Bluhm, Miquel B. Salmerón; "Graphene Membranes for Atmospheric Pressure Photoelectron Spectroscopy"; *J. Phys. Chem. Lett*., 7; (2016); pp 1622−1627; DOI: 10.1021/acs.jpclett.6b00640

[40] Y. Zhang, L. Zhang, C. Zhou; "Review of Chemical Vapor Deposition of Graphene and Related Applications"; *Acc. Chem. Res*., 46, (2013), pp: 2329-2339; DOI: 10.1021/ar300203n

[41] A. Black, F. Jiménez, R. Bernardo-Gavito, S. Casado, D.Granados, A. Vázquez de Parga "Growth and characterization of 7,7,8,8-tetracyano-quinodimethane crystals on chemical vapor deposition graphene"; *J. Cryst. Growth* , 453, (2016), pp: 1-6; DOI: 10.1016/j.jcrysgro.2016.07.023

[42] See: https://www.graphenea.com/

[43] See: https://graphene-supermarket.com/

[44] See: https://www.acsmaterial.com

[45] See: https://www.sigmaaldrich.com

[46] See: http://microchem.com/

[47] See: https://www.norcada.com

[48] See: https://www.emsdiasum.com/microscopy/default.aspx

[49] See: https://www.thermocoax.com

[50] See: https://www.lbl.gov/

[51] See: http://stm.lbl.gov/Salmerón_group/new_php/index.php

[52] See: http://foundry.lbl.gov/

[53] P. Willmott, 2011, *An Introduction to Synchrotron Radiation*, Weinheim, Germany; Wiley

[54] A. C. Thomsom, D. Vaughan, 2001, eds. *X-Ray Data Booklet*

[55] See: http://www.esrf.eu/UsersAndScience/Experiments/CRG/BM25

[56] See: https://www.cells.es/en/beamlines/bl24-circe

[57] H. Bluhma, K. Andersson , T. Araki , K. Benzerara , G.E. Brownb,, J.J. Dynes, S. Ghosal M.K. Gilles N.-Ch. Hansen, J.C. Hemminger, A.P. Hitchcock G. Kettele, A.L.D. Kilcoyne, E. Kneedler, J.R. Lawrence, G.G. Leppard, J. Majzlam B.S. Mun, S.C.B. Myneni, A. Nilsson, H. Ogasawara, D.F. Ogletree, K. Pecherm, M. Salmeron, D.K. Shuh, B. Tonner, T. Tyliszczak, T. Warwick, T.H. Yoon; "Soft X-ray microscopy and spectroscopy at the molecular environmental science beamline at the Advanced Light Source"; *J. Electron. Spectrosc. Relat. Phenom,* 150, (2006); pp: 86-104; DOI: 10.1016/j.elspec.2005.07.005

[58] D. M. Mattow, 2010. "Chapter 6 - Vacuum Evaporation and Vacuum Deposition". *Handbookof Physical Vapor Deposition (PVD) Processing (Second Edition)*. Neatherlands, William Andrew Publishing, DOI:10.1016/B978-0-8155-2037-5.00006-X.

[59] D. Diaz-Fernández; 2015; Ph.D Thesis "*Study of the growth and interaction of cobalt oxides on graphite and oxides surfaces*"

[60] H. O. Pierson, "Chapter 2 – Fundamentals of Chemical Vapor Deposition " *Handbook of Chemical Vapor Deposition (CVD), Second Edition,* Neatherlands, William Andrew Publishing DOI: 10.1016/B978-081551432-9.50005-X

[61] R. L. Puurunen; "Surface chemistry of atomic layer deposition: A case study for the trimethylaluminum/water process"; *J. Appl. Phys.* 97, (2005); pp: 121301; DOI:10.1063/1.1940727

[62] K. Siegbahn, K. I. Edvarson, "β-Ray spectroscopy in the precision range of 1 : 1e6". *Nucl. Phys.*. 1, (1956); pp: 137-159. DOI:10.1016/S0029-5582(56)80022-9.

[63] D. Briggs, M. P. Seach, 1990, *Practical Surface Analysis. Volume 1. Auger and X-ray Photoelectron Spectroscopy, second edition;* Weinheim, Germany; Wiley

[64] J. F. Moulder, W. F. Stickle, P. E. Sobol, K. D. Bomben, 1992, *Handbook of X-ray Photoelectron Spectroscopy,* Eden Prairie, United States of America, Perkin-Elmer Corporation

[65] C.D. Wagner, A. Joshi, "The auger parameter, its utility and advantages: a review", *J. Electron Spectrosc. Relat. Phenom*., 47, (1988); pp 283-313; DOI: 10.1016/0368-2048(88)85018-7

[66] G. Moretti "The Wagner plot and the Auger parameter as tools to separate initial- and final-state contributions in X-ray photoemission spectroscopy", *Surf. Sci*., 618, (2013); pp: 3-11; DOI: 10.1016/j.susc.2013.09.009

[67] M. P. Seah, W. A. Dench, "Quantitative Electron Spectroscopy of Surfaces: A Standard Data Base for Electron Inelastic Mean Free Paths in Solids", *Surf. Interface Anal* 1, (1979); pp: 2-11; DOI: 10.1002/sia.740010103

[68] S. Tanuma, C. J. Powell, D. R. Penn, "Calculations of Electron Inelastic Mean Free Paths; V. Data for 14 Organic Compounds over the 50-2000 eV Range", *Surf. Interface Anal*, 21, (1993); pp: 165-176; DOI: 10.1002/sia.740210302

[69] S. Tougaard, B. Jorgensen. "Inelastic background intensities in XPS spectra", *Surf. Sci*. 143, (1984); pp.: 482–494; DOI: 10.1016/0039-6028(84)90554-5.

[70] J. Vágh, "The Shirley background revised". *J. Electron Spectrosc. Relat. Phenom*, 151, (2006); pp. 159–164; DOI: 10.1016/j.elspec.2005.12.002.

[71] S. Tougaard, "Quantitative analysis of the inelastic background in surface electron spectroscopy". ", *Surf. Interface Anal* 11, (1988); pp: 453–472; DOI: 10.1002/sia.740110902.

[72] S. Tougaard. "Formalism for quantitative surface analysis by electron spectroscopy". *J. Vac. Sci. Technol., A*, 8, (1990); pp: 2197-2203. DOI: 10.1116/1.577037.

[73] S. Tougaard, H. S. Hansen. "Non-destructive depth profiling through quantitative analysis of surface electron spectra". *Surf. Interface Anal* 14, (1989); pp: 730-738. DOI: 10.1002/sia.740141109.

[74] S. Tougaard. "Inelastic background correction and quantitative surface analysis". *J. Electron Spectrosc. Relat. Phenom,* 52, (1990); pp: 243-271; DOI: 10.1016/0368-2048(90)85022-2.

[75] E.R. Malinowski, D.G. Howery, 1991, *Factor Analysis in Chemistry, 2nd edition*; New York, United States of America; JohnWiley

[76] M. J. Webb, P.Palmgren, P. Pal, O. Karis, H. Grennberg, Carbon; *A simple method to produce almost perfect graphene on highly oriented pyrolytic graphite*, 49, (2011); pp: 3242-3249; DOI: 10.1016/j.carbon.2011.03.050

[77] Bauer, E. (2014). *Surface Microscopy with Low Energy Electrons*. New York, United States of America; Springer.

[78] E. Bauer ,"LEEM and UHV-PEEM: A retrospective"; *Ultramicroscopy*, 119, (2012); pp: 18-23; DOI: 10.1016/j.ultramic.2011.09.006

[79] Lucia Aballe, Michael Foerster, Eric Pellegrin, Josep Nicolas, Salvador Ferrer "The ALBA spectroscopic LEEM-PEEM experimental station: layout and performance", *J. Synchrotron Rad.*, 22, (2015); pp: 745-752; DOI: 10.1107/S1600577515003537

[80] J. Rubio-Zuazo, E. Martinez, P. Batude, L. Clavelier , A. Chabli, G.R. Castro, "Probing buried interfaces on Ge-based metal gate/high-k stacks by hard X-ray photoelectron spectroscopy" *Appl. Surf. Sci*., 257, (2011); pp: 3007-3013; DOI: 0.1016/j.apsusc.2010.10.108

[81] J. Rubio-Zuazo, M. Escher, M. Merkel, G.R. Castro, "High Voltage-Cylinder Sector Analyzer 300/15: A cylindrical sector analyzer for electron kinetic energies up to 15 keV", *Rev. Sci. Instrum*. 81, (2010); pp: 043304; DOI: 10.1063/1.3398441

[82] D. F. Ogletree, H. Bluhm, G. Lebedev, C. S. Fadley, Z. Hussain, M. Salmeron; "A differentially pumped electrostatic lens system for photoemission studies in the millibar range"; *Rev. Sci. Instrum*., 73, (2002); pp: 3872; DOI: 10.1063/1.1512336

[83] M. Salmeron, R. Schlögl; "Ambient Pressure Photoelectron Spectroscopy: A new tool for surface science and nanotechnology"; *Surf. Sci. Rep*; 63, (2008); pp: 169-199; DOI: 10.1016/j.surfrep.2008.01.001

[84] R. Toyoshima, H. Kondoh "*In situ* observations of catalytic surface reactions with soft x-rays under working conditions", *J. Phys.: Condens. Matter*, 27, (2015); pp: 083003; DOI: 10.1088/0953-8984/27/8/083003

[85] R. S. Weatherup, B. Eren, Y. Hao, H. Bluhm, M. B. Salmeron, "Graphene Membranes for Atmospheric Pressure Photoelectron Spectroscopy", *J. Phys. Chem. Lett*., 7, (2016); pp 1622-1627; DOI: 10.1021/acs.jpclett.6b00640

[86] F. de Groot, A. Kotani; 2008; *Core Level Spectroscopy of Solids*, Boca Ratón, United States of America; CRC Press

[87] G. Bunker, 2010, *Introduction to XAFS*, New York, United States of America, Cambridge

[88] M. Abbate, J. B. Goedkoop, F. M. F. De Groot, M. Grioni, J. C. Fuggle, S. Hofmann, H. Petersen, M. Sacchi; "Probing depth of soft x-ray absorption spectroscopy measured in total-electron-yield mode"; *Surf. Interface Anal*., 18, (1992); pp: 65-69; DOI: 10.1002/sia.740180111

[89] P. Eaton, P. West; 2010, *Atomic Force Microscopy*, New York, United States of America, Oxford University Press

[90] www.bruker.com;

http://www.cim.unipr.it/html/PeakForce-QNM_AFM_AN128.pdf

[91] D. Martinez-Martin, R. Longuinhos, J. G. Izquierdo, A. Marele, S. S. Alexandre, M. Jaafar, J. M. Gómez-Rodríguez, L. Bañares, J. M. Soler, J. Gomez-Herrero "Atmospheric contaminants on graphitic surfaces", *Carbon*; 61, (2013); pp: 33-39; DOI: 10.1016/j.carbon.2013.04.056

[92] I. Horcas, R. Fernández, J. M. Gómez-Rodríguez, J. Colchero, J. Gómez-Herrero, A. M. Baro, "WSXM: A software for scanning probe microscopy and a tool for nanotechnology". *Rev. Sci. Instrum*., 78, (2007); pp: 013705; DOI: 10.1063/1.2432410.

[93] T. Dieing, O. Hollricher, J. Toporski, 2010, *Confocal Raman Microscopy*; Berlin, Germany; Springer

[94] P. Vandenabeele, 2013, *Practical Raman Spectroscopy: An Introduction. Analytical techniques in the sciences*. Weinheim, Germany; Wiley

[95] A. Jorio, M. S. Dresselhaus, R. Saito, and G. Dresselhaus, 2011, *Raman Spectroscopy in Graphene Related Systems*. Weinheim, Germany; Wiley

[96] B. Fultz, J. Howe, 2007, *Transmission Electron Microscopy and Diffractometry of Materials*. Berlin, Germany; Springer

[97] D. B. Williams, C. B. Carter, 2009, *The Transmission Electron Microscope*, Berlin, Germany; Springer

[98] Wikipedia Commons: TEM schem:

https://en.wikipedia.org/wiki/Transmission_electron_microscopy#/media/File:Schematic_view_of_imaging_and_diffraction_modes_in_TEM..tif

[99] J. Goldstein, 2003, *Scanning Electron Microscopy and X-Ray Microanalysis*, Berlin, Germany; Springer

[100] R. F. Egerton, "Electron energy-loss spectroscopy in the TEM"; *Rep. Prog. Phys*, 72, (2008); pp: 016502; DOI: 10.1088/0034-4885/72/1/016502/meta

[101] J.Pflüger, J.Fink, G.Crecelius, K.P.Bohnen, H.Winter; "Electronic structure of unoccupied states of TiC, TiN, and VN by electron-energy-loss-spectroscopy"; *Solid State Commun*., 44, (1982); pp: 489-492; DOI: 10.1016/0038-1098(82)90130-2

[102] L. Reimer, 1998, *Scanning Electron Microscopy*, Berlin, Germany; Springer

Chapter 3

CoO on HOPG: carbon gasification reaction

"I must confess it was very unexpected and I am very startled at my metamorphosis into a chemist."

Ernest Rutherford

3.1 Introduction

This chapter will be dedicated to describe the study of the interface interaction between CoO and HOPG and, in particular, the carbon gasification reaction which take place within the re-oxidation of this system at low temperature (~400 °C). As stated in Chapter 1, cobalt is an essential catalytic element used in a wide variety of industrial processes. Although cobalt macroscopic behavior has been well described, the details of its atomic interaction with substrates and reactants is not fully understood [1]. Besides, the recent development of 2D materials, in particular graphene, has stimulated the attention of the scientific community paying attention to the interaction and effects of cobalt with carbon-based systems at the nanoscale. In this way, the combination of cobalt oxides with carbon-based materials gives rise to important properties [2], leading to excellent performances in applications such as catalysts, biochemical sensors and cathodes for Li-ion batteries. Another point of interest consists on the fabrication of nanostructures by patterning on graphene and graphite surfaces, which in fact has become a hot research topic due the multiple technological applications that these materials find in a wide range of fields [3,4,5,6]. For example, metallic Ni, Ag, Co and Fe nanoparticles have been used in this regard [7,8,9,10], being particularly useful those where the nano-channeling process can be controlled taking advantage of their magnetic behavior, such for cobalt in air conditions [11].

Previous work done in our group (Daniel Díaz-Fernández Ph.D. thesis) [12] and published in indexed international scientific journals, [13,14] described the early stages of growth of CoO on HOPG, and the interaction between them. One of the most surprising results was the capability to induce graphite nano-patterning at lower temperatures (~400 °C) than metallic cobalt nanoparticles (>600 ºC). A qualitative model of the process based

on the initial weakening of the graphite σ bonds was offered as explanation. Compared to Co nanoparticles, CoO initial deposition tends to oxidize and create defects on the uppermost layers of graphite, facilitating the later carbon gasification reaction. However, the inability to follow *in situ* the reaction process by conventional XPS has hindered its description and the comprehension of the role of each actor during the intermediate heating and oxygen exposure steps. In this Chapter, *in situ* NAP-XPS measurements at different temperatures and oxygen pressures will be presented trying to understand the details of this carbon gasification reaction.

In addition to nanochannels, the AFM measurements showed two more types of nanostructures as final products of this carbon gasification reaction: nanostrips and nanorings. This is not a complete surprise since both, carbon and cobalt based systems, have the ability to promote and lead to novel and exotic nanostructures. In fact, similar features can be found as early stages of growth of carbon nanotubes [15], metal nanorings promoted by carbon-based surfaces [16], Co superparamagnetic nanorings [17] or Co_3O_4 nanorings [18]. Due to their low dimensionality all these structures have attracted much attention because of their novel properties compared to bulk materials. Furthermore, self-assembles of organic and inorganic molecules forming nano-strips on graphitic samples have been the focus of a great number of publications in the last decades [19,20,21]. Through spectroscopic characterization techniques such as KPFM the nature of these nanostructures was also studied.

For a comprehensive reading it becomes necessary to introduce some measurements and results previously published in Díaz-Fernández Ph.D. memory [12]. In any case, the measurements shown here not original from the present thesis will be clearly indicated. Hence, the structure of the present chapter is divided into three sections. In first place, a brief summary of the growth model of CoO on HOPG will be described in order to introduce the wetting layer of CoO, which has a relevant role on the CoO-HOPG interaction and posterior re-oxidation process. In second place, section 3.3 will cover the CoO-HOPG interface interaction, which translates into the graphite upper layers oxidation and defects development. Although some results shown in section 3.3 have been previously reported [13], novel results from XPS, HAXPES and NAP-XPS measurements in combination with theoretical calculations of XPS and XAS Co 2p and O 1s spectra done by R.J.O. Mossanek and M. Abbate (Physics Department, Universidade Federal do Paraná, Curitiba, Brazil) will be described. Finally, the last section 3.4

constitutes the main heart of the present chapter and condense the main results obtained from the NAP-XPS *in situ* study of the carbon gasification reaction that takes place during the re-oxidation process of CoO on HOPG at ~400 °C, as described in section 2.6.2 for the re-oxidation process R1. A discussion of the chemical nature of the above-mentioned nanostrips and nanorings will close this section.

3.2 Model of growth of CoO on HOPG

CoO grows on HOPG following a Stranski–Krastanov growth mode, consisting on the formation of an initial CoO wetting layer followed by the growth of CoO islands. Figure 3.1 shows a representative AFM image where a dendritic CoO island has grown on it. The wetting layer has a thickness slightly larger than 4 Å, in agreement with the lattice constant of bulk CoO determined at 305 K (a = 4.2614 Å) [22]. These CoO deposits point out to a strong diffusion of the adsorbates along the HOPG surface towards the steps, allowing the formation of an ultrathin CoO wetting layer by auto assembling at the graphite terraces and the growth of dendritic structures on the steps. Once the terraces are filled up with the wetting layer new dendritic islands are able to grow on it.

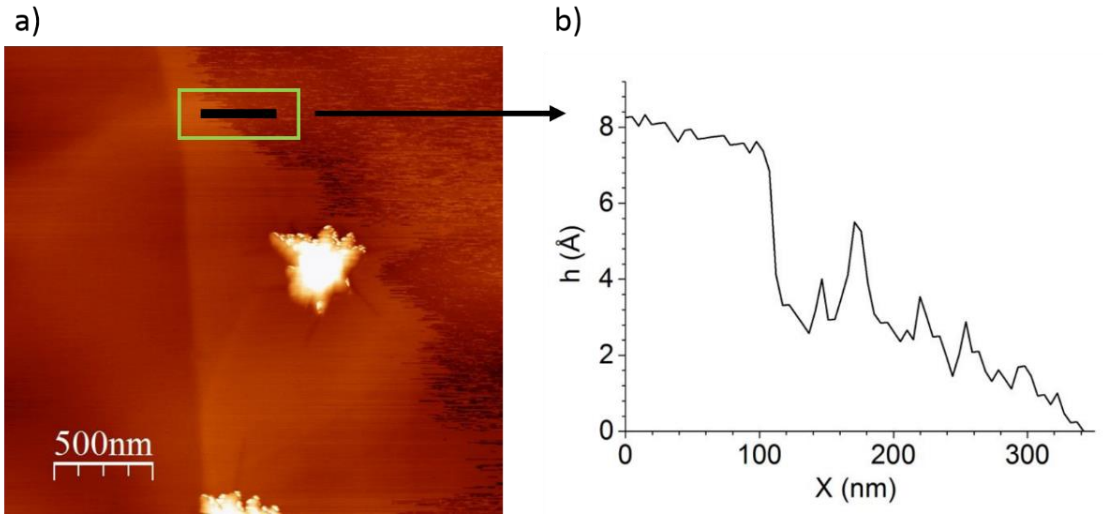

Figure 3.1 a) 2.5x2.5 μm^2 AFM image of the CoO/HOPG wetting layer; b) height profile of the wetting layer, as indicated. Both taken from [12].

This two-steps mode of growth as well as the morphology of the islands were also confirmed by the inelastic peak shape method implemented in the QUASES software.

The results of this analysis are depicted in Figure 3.2. The used model takes into account the presence of an initial CoO overlayer and the subsequent formation of islands on it. The most relevant result from this analysis is related to the calculated portion of wetting layer which is still uncovered by the CoO islands as a function of the amount of deposited material in equivalent monolayers (see Figure 3.2 a). As it can be seen, for a deposit of about 12 Eq-ML of CoO, the region of the wetting layer free of islands covers more than 50% of the surface. These results have also been compared to those obtained directly from the AFM images for each step of growth. The excellent agreement of the two techniques can be seen in Figure 3.2 b.

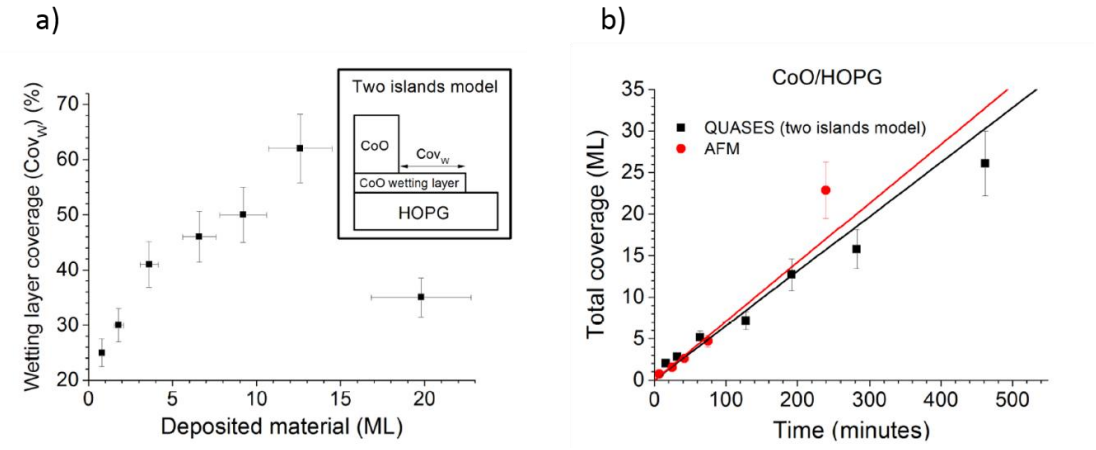

Figure 3.2 a) Percentage of uncovered wetting layer as a function of deposited material given by QUASES software; b) Comparison of the total amount of deposited material as a function of the growth time given by AFM (red dots) and QUASES software (black squares). Both taken from [12].

The importance of these results lies on the fact that in the early stages of growth (up to 12 Eq-ML), the interaction between CoO and HOPG is basically mediated by the wetting layer, as most of the surface is going to be covered by it and not by CoO islands. The AFM shows that these dendritic islands have an average height between 5-10 nm, while the IMFP through CoO matrix for electrons with kinetic energy of 1200 eV (typical C 1s electrons photoemitted using an Al anode) is about 20 Å. Therefore, the XPS signal from the substrate will basically come from free graphite and regions covered by only the wetting layer.

3.3 CoO-HOPG interaction

3.3.1 Analysis of the electronic structure of the CoO wetting layer

The electronic structure of the CoO wetting layer has been studied by means of XPS and XAS measurements taken at the Co 2p region. The measured spot size for both techniques ranged from tens to thousand microns, both cases much bigger than the size of CoO islands, and therefore the spectra will show an average of the contributions from both the wetting layer and the islands. However, as Figure 3.1 a shows, at the early stages of growth, the wetting layer will dominate the signal as for coverages lower than 12 Eq-ML, the spectra will basically give information regarding this wetting layer.

3.3.1.1 CoO XPS spectra

The CoO Co 2p spectrum has a complex structure. As it has been previously reported [23,24], the spectrum shows different structures such as multiplet splitting, charge transfer satellites and plasmon loss structures. However, all these factors are interrelated and strongly dependent on the chemical environment of the Co atoms. For this reason, a deeper study of these structures can give valuable information about the growth process of the CoO wetting layer. In this way, the top panel in Figure 3.3 a shows the theoretical calculation of the Co $2p_{3/2}$ XPS spectrum for CoO, which has been performed using cluster model calculations for a Co^{2+} ion in octahedral symmetry and high spin configuration using the standard parameters pdσ and 10Dq [23,25]. Moreover, these parameters are related to the grade of hybridization of the Co 3d-O 2p orbitals and crystal field, respectively, and have been lowered in order to simulate a loss of covalence (lower panels in Figure 3.3 a). This behavior could be related, for instance, to disorder or bi-dimensional character of the structure. In all cases, the spectra show a main line, a charge transfer satellite and a week multiplet peak located at 6 eV and 3 eV respectively from the main line. In Figure 3.3 b it is depicted the variation of pdσ and 10Dq parameters and how it affects to the intensity ratio between the satellite and the main line (I_{sat}/I_{main}), and the energy separation between both (ΔE_{sat}). As it can be seen, the reduction of CoO covalence is translated into an increase of the satellite intensity and a decrease on the energy separation between main and satellite contributions. Finally, Figure 3.3 c shows a selection of fitted Co 2p spectra, following the above mentioned three contributions, for a representative series of early stages of growth. The position and intensity of each peak

were left as free parameters and the agreement of the fittings to the experimental spectra was excellent in all cases.

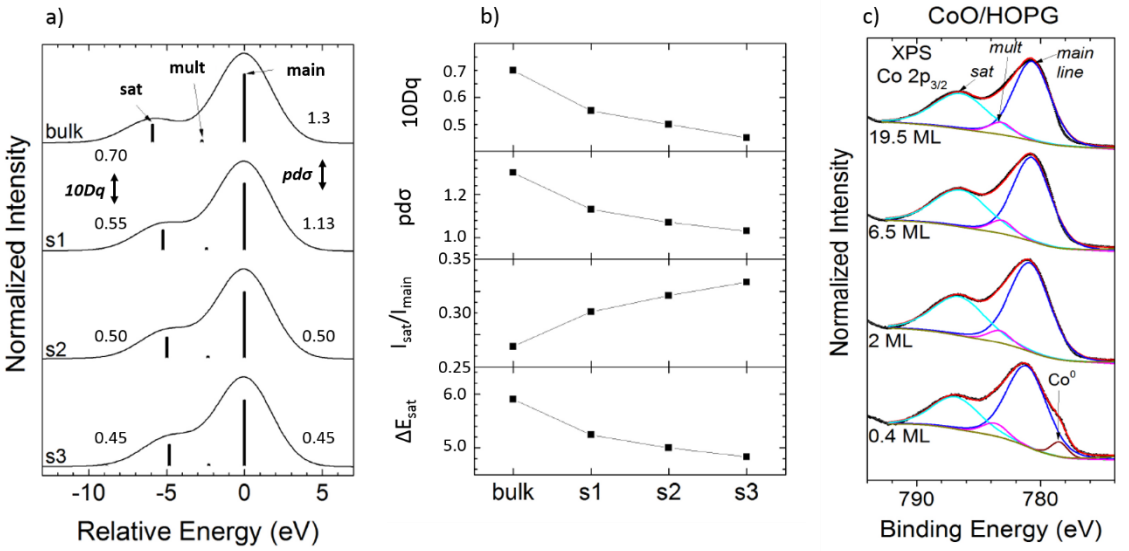

Figure 3.3 a) Cluster model calculations of the Co $2p_{3/2}$ XPS peak for different values of the pdσ and 10Dq parameters. b) Main line-satellite energy separation (ΔE_{sat}) and relative intensity (I_{sat}/I_{main}) for the different values of pdσ and 10Dq parameters. c) Fittings of the experimental Co 2p XPS spectra using the peaks given by the calculations. Figures taken from [12].

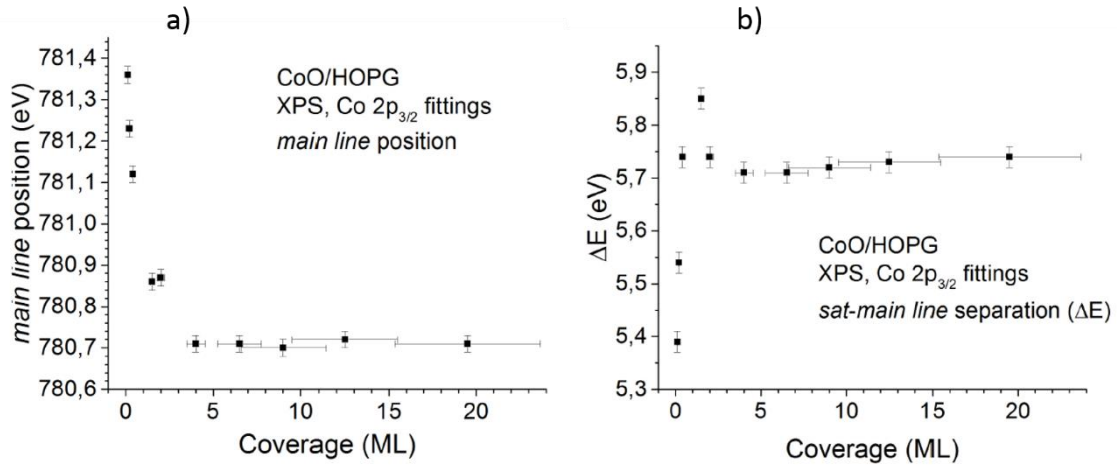

Figure 3.4 a) Binding energy position of the main line of the Co 2p XPS spectra as a function of the coverage. b) Main line-satellite energy separation (ΔE_{sat}) as a function of the coverage. Figures taken from [12].

The results obtained from the fittings regarding the main contribution position and the energy separation between this and the satellite line are shown in Figure 3.4 as a function of the amount of deposited material. Firstly, the main line position (see Figure 3.4 a decreases up to 0.7 eV for coverages lower than 2Eq-ML until being stabilized at normal bulk values (780.7 eV). This effect has been usually assigned to size effects in transition metal oxide ultra-thin films [26,27] and nanoparticles [28]. On the other hand, the energy separation, ΔE_{sat}, increases from 5.4 eV to 5.7 eV, corresponding again to the bulk value (Figure 3.4 b). As before, these lower values are obtained for coverages up to 2 Eq-ML, precisely when the CoO wetting layer is formed and dominates over the islands. Therefore, according to the previous calculations, this result seems to indicate a loss of covalence of the initial CoO wetting layer formed on the HOPG substrate.

- The x-ray core level photoemission calculations were performed using a standard cluster model. The cluster consisted of a $(CoO_6)^{-10}$ octahedron, which is solved within the configuration interaction method [25,29]. In this case, the ground state wave function is expanded in configurations beyond the simple ionic picture $|3d^n\rangle$, such as $|3d^{n+1}\mathrm{L}\rangle$, $|3d^{n+2}\mathrm{L}^2\rangle$, etc., where L denotes a hole in the ligand (oxygen) band. The main parameters of this model are the charge transfer energy (Δ = 5.5 eV), the d-d Coulomb repulsion energy (U = 5.2 eV), the p-d transfer integral (pdσ = 1.3 eV) and the crystal field (10Dq = 0.7 eV) [23,25]. The final state wave function is also obtained from the ground state by removing a core hole electron. The cluster model is solved with exact diagonalization and the spectral weight is found using the sudden approximation [30].

3.3.1.2 CoO XAS spectra

In order to confirm the bi-dimensional character of the initial wetting layer with respect to the bulk CoO, XAS measurements have been performed for two different CoO coverages, 2 Eq-ML and 20 Eq-ML. This technique shows a particular dependence on the photon polarization, and thus to the incident angle of the beam with respect to the sample surface. Besides, it provides a high sensitivity to the chemical environment of the ion, allowing a detailed study of anisotropic low-dimensional systems. Because of this, Co 2p and O 1s XAS spectra have been taken for these samples at two different incidence angle of the X-ray beam, i.e. normal and grazing incidence.

Firstly, Figure 3.5 a shows the experimental Co 2p XAS spectrum (dots) for the 20 Eq-ML CoO/HOPG case. This result was identical to previous bulk CoO spectra in the literature [31,32], presenting both the Co $2p_{3/2}$ and Co $2p_{1/2}$ edges due to spin-orbit split effects, while each edge is composed of different multiplet structures. Although the experiment was performed at different incident angles, the spectral shape resulted always similar, showing an isotropic character. The theoretical spectrum (continues line), also shown in Figure 3.5 a, reproduces well the energy position and relative intensities of all the features in the spectrum. This calculation was done by assuming a Co^{2+} ion in octahedral (O_h) symmetry and by computing the dipole transitions from 2p levels to empty 3d states. In this symmetry, the Co 3d levels are split, by the crystal field, into the t_{2g} and e_g states (see left panel of Figure 3.5), and so there would be no expected anisotropy between in-plane or out-of-plane states. Furthermore, Figure 3.5 b and c presents the Co 2p XAS spectra for the 2 ML CoO/HOPG sample, obtained respectively in the normal ($\theta = 0°$) and grazing ($\theta = 60°$) incidence conditions. Under normal incidence, in-plane states are excited by the photon electric field, whereas under grazing incidence, the out-of-plane states are potentially preferred. The two experimental spectra taken at these conditions are distinct from the other, as well as being different from the bulk one. The theoretical spectra shown in Figure 3.5 b and c is obtained assuming a Co^{2+} ion in tetragonal (D_{4h}) symmetry and by calculating the in-plane and out-of-plane dipole transitions from 2p levels to empty 3d states. Once again, it reproduces well the energy position and relative intensities of all the features in the spectrum. Now, in the tetragonal symmetry, the anisotropy arises due to the Co 3d levels being split into b_{1g}, e_g (in-plane), a_{1g} and b_{2g} (out-of-plane) states (see Figure 3d). It is worth mentioning that the CoO wetting layer spectra were reproduced with a smaller crystal field (10Dq = 0.5 eV) than in the CoO bulk case (10Dq = 0.9 eV) [33]. This is consistent with the effects of the loss of covalence observed in the Co 2p XPS spectra, as explained previously for Figures 3.3 and 3.4.

The same analysis has been performed on the O 1s edge. Figure 3.5 d depicts the XAS spectrum for the 20 ML CoO/HOPG system. The structures in the experimental spectrum are related to the empty O 2p band, covalently mixed to Co 3d and Co 4sp states, which are similar to previous bulk CoO results [34]. The corresponding Co 3d region of the experimental spectrum was also simulated as before using a Co^{2+} ion in octahedral symmetry, reproducing the energy position and relative intensities of the different features. As in the case of the Co 2p edge, this spectrum does not present any anisotropy.

On the other hand, Figures 3.5 e and f presents the O 1s XAS spectra for the 2 ML CoO/HOPG system, obtained respectively in the normal ($\theta = 0°$) and grazing ($\theta = 60°$) incidence conditions. The experimental data indicates an anisotropic electronic structure, outlined by the clear difference in the relative intensity of the structures in the Co 3d region of the spectra. The theoretical spectra, in this case, is also obtained by assuming a Co^{2+} ion in tetragonal (D_{4h}) symmetry and considering the in-plane and out-of-plane dipole transitions. Once again, it reproduces well the energy position and relative intensities of all the features in the spectrum.

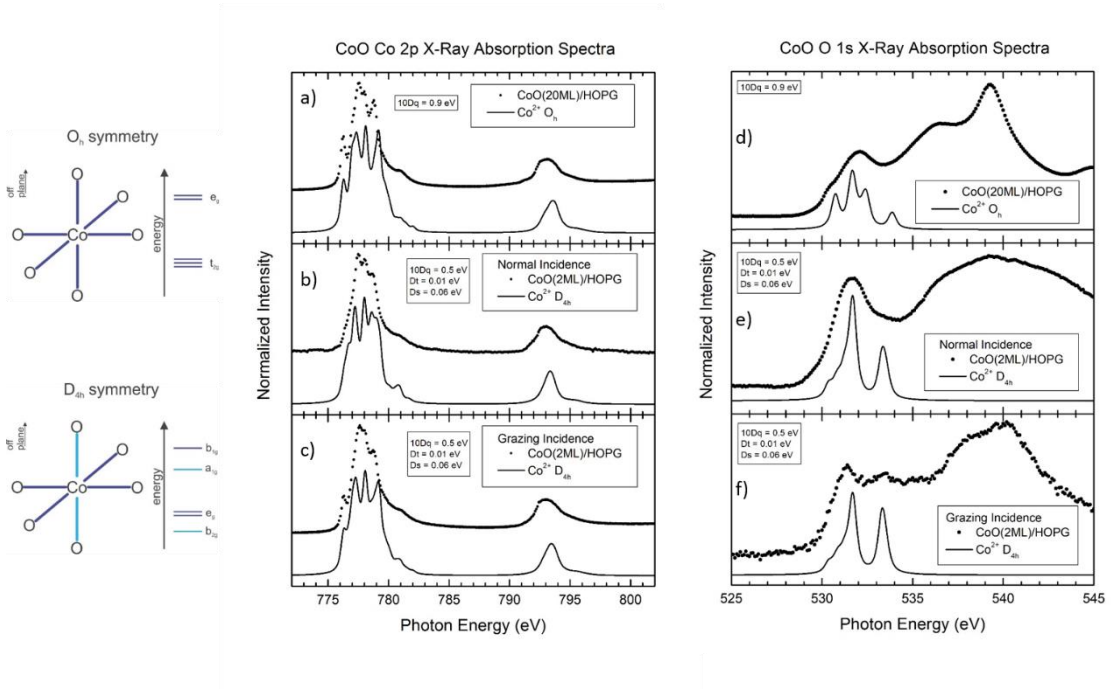

Figure 3.5 Experimental and calculated Co 2p and O 1s XAS spectra for: a) and d) 20 Eq-ML of CoO/HOPG. The spectrum has been calculated in octahedral Oh symmetry; b) and e) 2 Eq-ML of CoO/HOPG. The experimental spectrum has been taken at normal photon incidence and the spectra are calculated in D_{4h} symmetry; c) and f) 2 Eq-ML of CoO/HOPG. The experimental spectrum has been taken at grazing photon incidence and the spectrum is calculated in D_{4h} symmetry; Left panels indicate the corresponding atom arrangement for each symmetry. Experimental data taken from [12].

As a first conclusion, the X-ray photoemission and absorption results indicate that the electronic structure of the CoO wetting layer is quite different from the corresponding bulk compound. This initial layer not only presents a less covalent nature, but also a

highly anisotropic character in comparison to the bulk material. These effects are related to the low dimensionality of the wetting layer, as well as to the interaction with HOPG. In fact, it can help to explain why CoO grows in a Stranski–Krastanov model, as opposed to a layer-by layer or island mode. The electronic distortion of the wetting layer in contact with the graphite would prevent the growth of a new CoO layer, limiting the growth of CoO islands to punctual nucleation sites on it. Likewise, the formation of the wetting layer is closely linked to the interaction with the 2D structure of the HOPG substrate. In fact, only in the graphite steps, which can be considered as defects, CoO can grow forming dendritic islands in the very early stages of growth. As it will be discussed, this mode of growth, due to the interaction of the cobalt oxide with the HOPG substrate, is especially important and will significantly influence in the later re-oxidation process.

- The x-ray absorption simulations were done using full multiplet calculations [35,33]. The dipole transition energies and intensities are calculated with Slater integrals reduced to 80% of their atomic value to account for additional screening. In the case of Co 2p XAS, the calculation considers 2p -2p, 2p 3d and 3d-3d interactions, whereas for the case of O 1s XAS, the simulation can be done by switching off the 2p spin-orbit and the 2p-3d interaction. In the case of bulk calculations, these transitions are then projected into octahedral (O_h) symmetry with a crystal field parameter 10 Dq = 0.9 eV. In the case of the wetting layer calculations, these transitions are projected into tetragonal (D_{4h}) symmetry), with the crystal field parameters 10Dq = 0.5 eV, Dt = 0.01 eV and Ds = 0.06 eV. In all cases, the in-plane and out-of-plane contributions can be separated and/or weighted accordingly, depending on the incident angle of the XAS measurement.

3.3.2 The role of cobalt oxide on the creation of defects on HOPG

The behavior of the graphite substrate and its interaction with the as grown cobalt oxide has been studied by means of XAS, XPS, NAP-XPS and HAXPES measurements taken at the C 1s and O 1s region. As pointed out before, the spot size for all techniques oscillates from tens to thousand microns, therefore the results give an average of the contribution from free and in contact HOPG with CoO. However, the reader should remember that for the early stages of growth the wetting layer will dominate the signal as most part of the surface will be covered by it.

Taking advantage from its higher probing depth, XAS measurements were performed in order to study the effect of CoO deposition on HOPG as a function of the coverage. The C 1s XAS spectra of HOPG reflects the anisotropy of its electronic states showing the π* (off- plane) and σ* (in-plane) resonances [36]. By taking advantage of

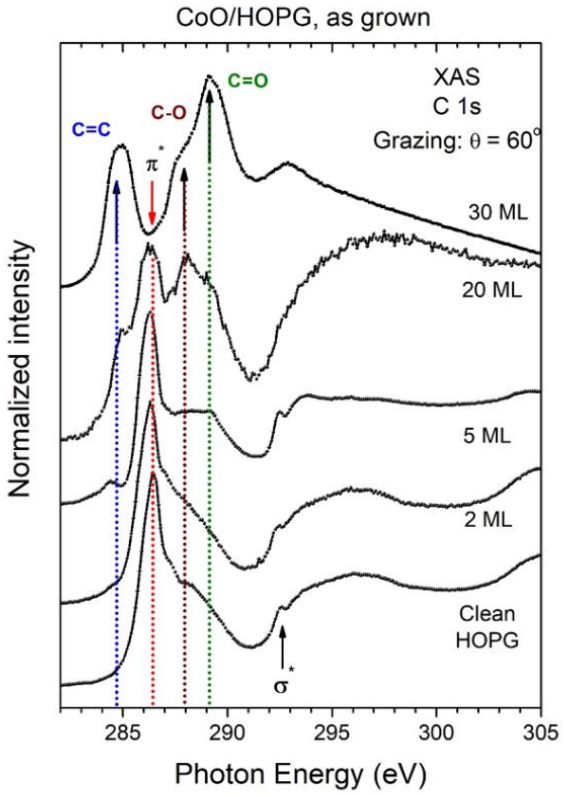

Figure 3.6 Experimental C 1s XAS spectra of the deposition of CoO on HOPG substrate for different coverages. Experimental data taken from [12].

the polarization of the synchrotron light beam, the absorption intensity of these π* and σ* states can be enhanced or reduced in the C 1s XAS spectrum by varying the photon incidence angle. Keeping this in mind, the C 1s region has been measured for different stages of growth and at a grazing incidence angle of θ = 60º (see Figure 3.6). This grazing angle allows to enhance the measurement of the off-plane graphitic bonds (π* states). The spectrum for a clean HOPG sample shows the typical asymmetric peak corresponding to the π* states with the maximum at 286 eV, while the σ* resonance appears as a weak structure starting at about 292.7 eV. When the deposited amount of CoO on the HOPG substrate increases, the spectra progressively change, emerging three new contributions around the energy range of the π* states. These three peaks resulted very clear in the last

growth stage (30 Eq-ML), where the π* states peak has been hidden. Focusing on the new contributions, the peak located at 289.2 eV is assigned to the formation of C=O bonds, whereas the peak located at 288.0 eV is assigned to C-O bonds, in agreement with the literature [37,38,39,40]. The peak located at 284.5 eV has been assigned to the appearance of broken graphitic rings, thus leading to the formation of localized C=C bonds as well as sp^3 defects on the HOPG surface. These results indicates that the CoO wetting layer deposition promoted both, the oxidation of the carbon atoms and the creation of defects at the HOPG surface. Finally, as the amount of deposited CoO increases, this effect is more pronounced.

3.3.2.1 HOPG behavior as a function of oxygen pressure

It is important to point out that multiple *in situ* experiments show that HOPG substrates remain unchanged under oxygen exposure in the range of 25-400 °C [41]. Nevertheless, as it has been previously discussed, deposition of CoO promotes graphite oxidation and the creation of defects. The bottom spectra of Figure 3.7 a shows the *in situ* XPS measurements for clean HOPG and 40 Eq-ML of CoO on HOPG. The C 1s spectrum for clean HOPG shows a single asymmetric peak centered at 284.3 eV, which is assigned to the contribution of carbon atoms bounded under sp^2 hybridization, as corresponds to graphite [42]. As it can be appreciated, once the CoO is deposited, only one new contribution at 285.0 eV related to graphite defects with sp^3 hybridization [43] clearly appeared, giving rise to a broadening of the C 1s peak. The absence of C-O and C=O contributions measured by XAS is due to the probing depth of XPS, much lower than for XAS. This means that the signal from this C 1s spectrum comes from the first surface monolayers of HOPG. However, after air exposure, i.e oxygen saturation of the sample, these carbon-oxygen contributions clearly increase. An attentive look to the top spectra of Figure 3.7 a (where the take-off angle has been varied from 0° to 40°) indicates that the graphite defects are mostly in the upper layers, whereas the C-O contribution is closer to the surface than C=O bonds.

In order to study the oxidation mechanism in more detail, the C 1s photoemission peak of an *in situ* sample of 2 Eq-ML CoO/HOPG has been submitted to oxidation under controlled oxygen atmospheres at room temperature (see Figure 3.7 b) in the CIRCE_NAPP beamline at the ALBA synchrotron. The spectra have been taken at a photon energy of 380 eV, so that the inelastic mean free path of the photoelectrons was

restricted to a few upper monolayers. The general behavior indicated that as oxygen exposure increases (pressure and time), two new peaks appears, one located at about 288 eV, assigned to C=O bonds, and the other one at 286 eV, assigned to C-O bonds [44,45]. These results confirmed those taken by XAS, but also demonstrated that the presence of the wetting layer makes possible the injection of oxygen to the HOPG surface. This is clearly seen in the spectra taken at an oxygen pressure of 1 mbar, where these two peaks continuously grow upon time with oxygen exposure. The inset of Figure 3.7 b, which shows an amplified detail of the energy region of the above peaks, also offers valuable information. The spectra taken at 10^{-3} mbar show that C=O bonds are firstly formed at the surface whereas C-O species start growing significantly at higher oxygen pressures (10^{-1} mbar). In comparison, C=O development was almost halted, possibly indicating that C=O was the first oxidation step, with a very short mean lifetime. This fact and its consequences will be discussed in section 3.4.1.4.

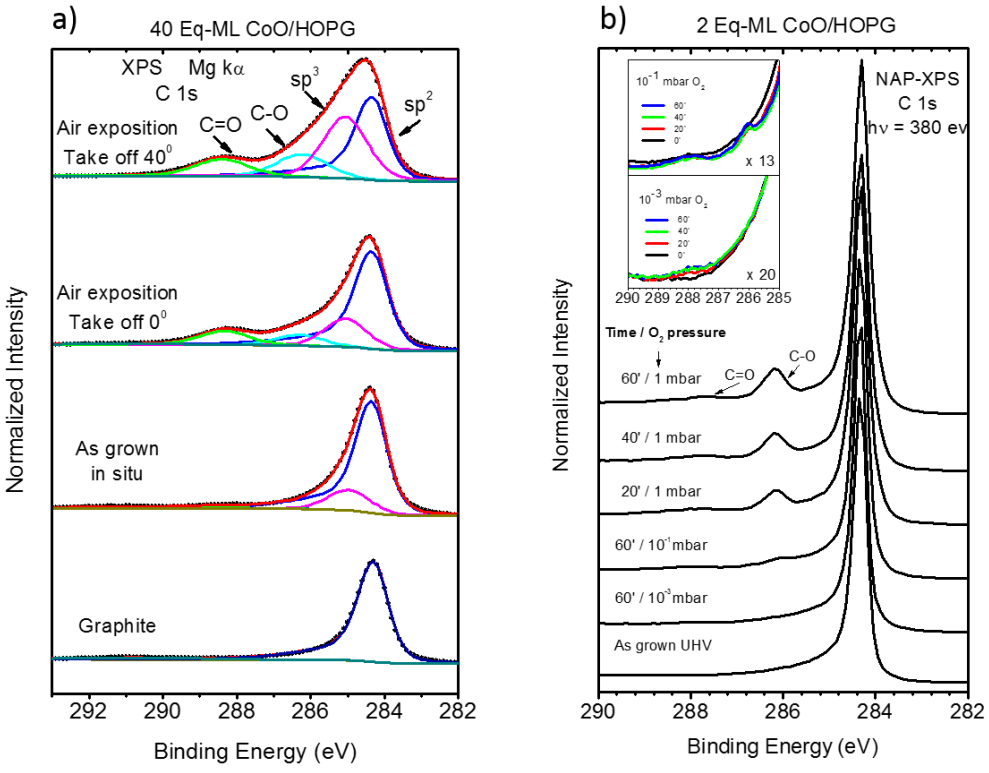

Figure 3.7 a) C 1s XPS spectra of clean HOPG substrate and a sample of 40 Eq-ML CoO/HOPG taken as grown *in situ* and after air exposition (superior panels). b) NAP-XPS C 1s spectra of 2 Eq-ML CoO/HOPG measured at different oxygen pressures as labelled. The inset shows a detail for very low oxygen pressures.

Summarizing, it has been demonstrated that CoO, and specially the wetting layer, acts as an "oxygen pump" into the HOPG substrate, being responsible for the creation of graphite defects and its subsequent oxidation. The mean probing depth of XAS is estimated to be about 50 Å [46] whereas for the photoemission spectra presented in Figure 3.7 b is reduced to 8 Å. In order to measure the HOPG signal below the CoO islands and to be able to estimate the thickness of these graphite oxidation layer, *ex situ* HAXPES measurements have been performed in the BM25 B beamline at ESRF. In this way, three samples were grown in our laboratory, containing 13, 25 and 40 equivalent Eq-ML of CoO have been measured *ex situ* using 10 keV photon energy. Therefore, the IMFP was estimated in the range of 115 Å to 173 Å, depending on the propagation medium, CoO or HOPG, respectively. Figure 3.8 shows the C 1s and O 1s spectra for these three samples, including in the O 1s plot a fourth spectrum from a CoO single crystal, just for comparison purposes. For the C 1s spectra in Figure 3.8 a, as the amount of CoO increases, the contributions from CO_x species and graphite defects also become bigger. This tendency can be appreciated in Figure 3.8 c, where the ratio between these contributions and the graphite sp^2 peak is plotted as a function of the CoO coverage.

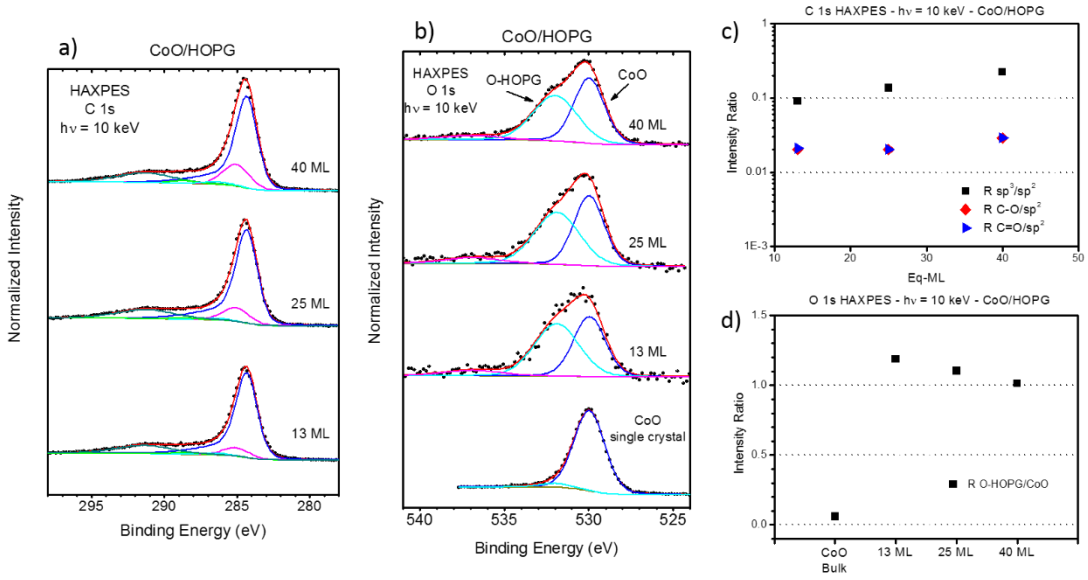

Figure 3.8 *Ex situ* C 1s (a) and O 1s (b) HAXPES spectra taken at 10 keV for three samples containing different coverages of CoO/HOPG. c) Ratios for C 1s contributions normalized to the main sp^2 peak as a function of the amount of material. d) $I_{O\text{-}HOPG}/I_{CoO}$ ratio as a function of the amount of material.

On the other hand, O 1s spectra are shown in Figure 3.8 b. As stated before, the oxidation process is supposed to be saturated after air exposure, thus the main two peaks appearing in the spectra at 530.0 eV and 531.9 eV are assigned to oxygen atoms from the CoO overlayer and oxygen atoms bounded to carbon atoms, respectively. The first peak agrees with that measured from the CoO single crystal sample. The second peak corresponds to oxygen atoms bounded to carbon atoms (labeled as O-HOPG), and conserves approximately its ratio with respect to that of CoO independently of the CoO coverage (see Figure 3.8 d). This indicates that the amount of oxidized HOPG is proportional to the CoO coverage, in agreement with the previous XAS measurements. Taking into account the thickness of the CoO equivalent layer and the fact that the oxidized HOPG layer lies below the last one, a simple approximation can be performed in order to estimate the thickness of the oxidized graphite layer from the O-HOPG and CoO contribution intensities of O 1s region shown in Figure 3.8 b. In this way, the theoretical intensities from the CoO and graphite oxide (HOPG-Ox) can be approximated as:

$$I_{CoO} = I_{CoO}^{\infty}\left[1 - e^{-\frac{d_{CoO}}{\lambda_{CoO}^{CoO}*cos\theta}}\right] \qquad \text{(Eq 3.1)}$$

$$I_{HOPG\_Ox} = I_{HOPG\_Ox}^{\infty}\left[1 - e^{-\frac{d_{HOPG\_Ox}}{\lambda_{HOPG\_Ox}^{HOPG\_Ox}*cos\theta}}\right] e^{-\frac{d_{CoO}}{\lambda_{HOPG\_Ox}^{CoO}*cos\theta}} \qquad \text{(Eq 3.2)}$$

,where λ_{CoO}^{CoO} is the IMFP of the CoO contribution at the CoO matrix, $\lambda_{HOPG\_Ox}^{HOPG\_Ox}$ the IMFP of the HOPG-Ox contribution at the oxidized graphite matrix and $\lambda_{HOPG\_Ox}^{CoO}$ the IMFP of the HOPG-Ox contribution at the CoO matrix. The explanation of the origin of these equations can be found in Chapter 2, section 2.5.1.1. By calculating the ratio $\frac{I_{HOPG\_Ox}}{I_{CoO}}$, all the factors that form part of I_{CoO}^{∞} and $I_{HOPG\_Ox}^{\infty}$ and depends on the electron kinetic energy and other parameters from the analyzer can be avoided as they are the same for both CoO and oxidized HOPG. Besides, the photon flux is obviously the same for both contributions and also the cross section and amount of oxygen atoms can be roughly approximated to be the same in both matrixes. Therefore, the new equation from where the thickness can be estimated from the XPS fitting of Figure 3.8 b is:

$$\frac{I_{HOPG\_Ox}}{I_{CoO}} = \frac{\left[1-e^{-\frac{d_{HOPG\_Ox}}{\lambda_H^H * cos\theta}}\right] e^{-\frac{d_{CoO}}{\lambda_H^C * cos\theta}} \lambda_H^H}{\left[1-e^{-\frac{d_C}{\lambda_C^C * cos\theta}}\right] \lambda_C^C} \quad \text{(Eq. 3.3)}$$

,where for hν = 10 keV, the IMPF are $\lambda_{HOPG\_Ox}^{HOPG\_Ox}(Ekin = 9468eV)$ ~ 17.3 nm, $\lambda_{HOPG-Ox}^{CoO}(Ekin = 9468eV)$ ~ 11.5 nm and $\lambda_C^C \sim \lambda_H^C$. Considering that the measurements were taken with an angle $\theta = 15°$, and that 13, 25 and 40 Eq-ML correspond to 2.6, 5 and 8 nm, respectively, the estimation of the oxidized graphite as a function of the CoO coverage is shown in Figure 3.9. Indeed, it can be seen the linear behavior of the thickness of the oxidized graphite layer with respect to the initial CoO layer thickness. The control of the thickness of the oxidized graphite layer could be interesting in different applications such as the production of graphene oxide layers.

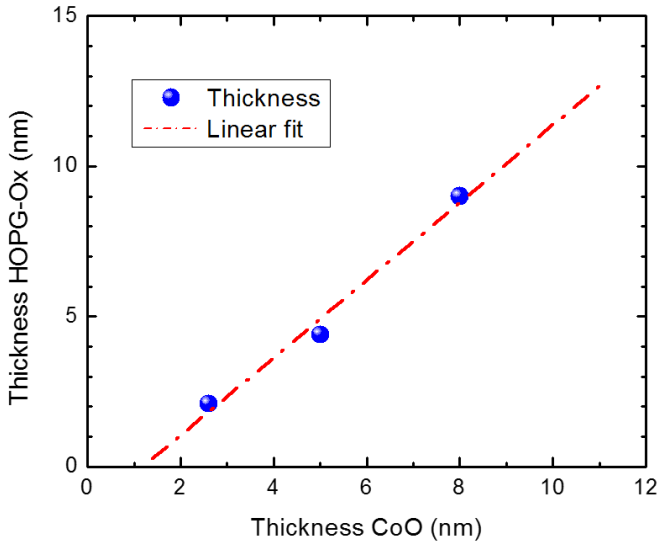

Figure 3.9 Thickness estimation of the oxidized graphite layer as a function of the CoO coverage as obtained from the intensities of the O 1s HAXPES spectra.

3.3.2.2 Cobalt oxide behavior as a function of oxygen pressure

Not only HOPG is altered by the presence of oxygen after CoO growth. In fact, the CoO layer is also affected. Figure 3.10 shows the NAP-XPS O 1s (a) and Co 2p spectra (b) at different oxygen pressures, from as grown to 1 mbar. Two different photon

energies have been used in each case to ensure that kinetic energies of the photoemitted electrons were the same for both regions and, therefore, the probing depth was equivalent. Therefore, black spectra are more surface sensitive (IMFP = 6 Å), while blue spectra come from a deeper region (IMFP = 14 Å). Regarding the O 1s spectra, as in Figure 3.8 b, two different contributions were measured at 530.0 eV and 532 eV, corresponding to CoO and O-HOPG. In the case of the as grown CoO, the contribution assigned to O-HOPG from the substrate does not correlate with the C 1s spectrum from Figure 3.7 b. Nevertheless, a small contribution from hydroxyls groups adsorbed on the surface of the transition metal oxide is expected [47], precisely at the same energy than O-HOPG species. However, due to the spectra evolution with oxygen pressure, these series of spectra just confirmed the previous results and the fact that HOPG becomes oxidized at the upper layers, in particular at the interface with CoO.

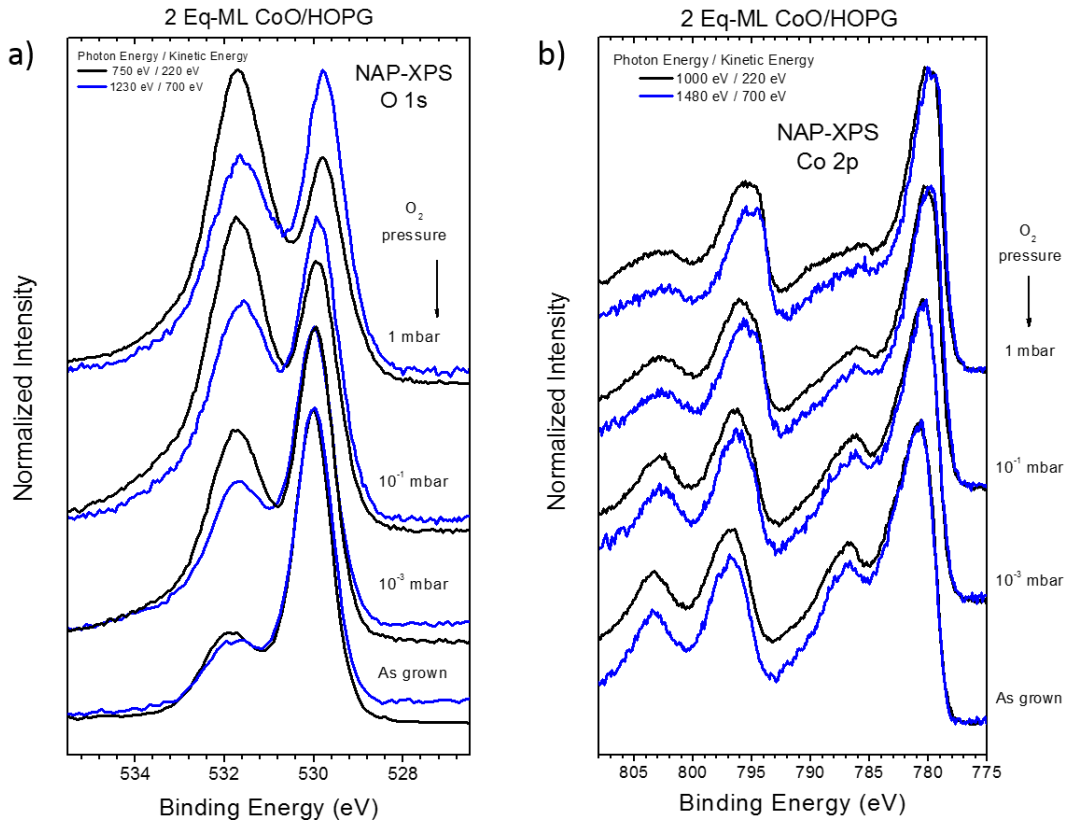

Figure 3.10 O 1s (a) and Co 2p (b) NAP-XPS measurements of 2 Eq-ML CoO/HOPG sample exposed to different O2 pressures during 1 hour.

On the other hand, the Co 2p spectra resulted more interesting as it offered information of how the CoO layer was modified by oxygen exposure. The XPS Co 2p

spectra show a transition from CoO to Co_3O_4 as a function of O_2 pressure. As stated before, the as grown CoO spectrum consists of a main line about 780 eV binding energy and a satellite at about 786 eV. However, after being exposed to 1 mbar the main line shifts by ~1 eV and two satellite weak peaks at ~786 and ~789 eV appear. Theoretical cluster model calculations for CoO and Co_3O_4 show these same features (see Figure 3.14 b), confirming the oxidation of Co^{2+} to Co^{2+}/Co^{3+} in the spinel structure. As it can be seen, the Co 2p spectra at each pressure resulted the same independently of the photon energy, indicating the complete transformation of the cobalt oxide in each step.

Figure 3.11 shows the XAS Co $L_{2,3}$ edge spectra at UHV conditions (a) and 1 mbar O_2 pressure (b) for two beam polarizations: 0 and $\pi/2$. As previously discussed in section 3.4.1.2, by taking advantage of the synchrotron light polarization the in-plane and off-plane Co-O bonds can be studied separately. In this case, XAS measurements performed at CIRCE beamline (ALBA facility) were done at two polarizations, 0 and $\pi/2$, which are equivalent to previous normal and grazing incidents, respectively. As before, Figure 3.11 a shows a strong anisotropy of the as grown Co $L_{2,3}$ spectra for both polarizations (indicating some sort of distortion on the Co coordination octahedron, as discussed in section 3.3.1.2). In the presence of 1 mbar of O_2 (see Figure 3.11 b) the spectral shape changes on going from typical CoO to Co_3O_4 spectrum [14]. In addition, the previous anisotropy is less clear, which could indicate a partial reconstruction of the cobalt oxide going from CoO to Co_3O_4 during the oxidation process.

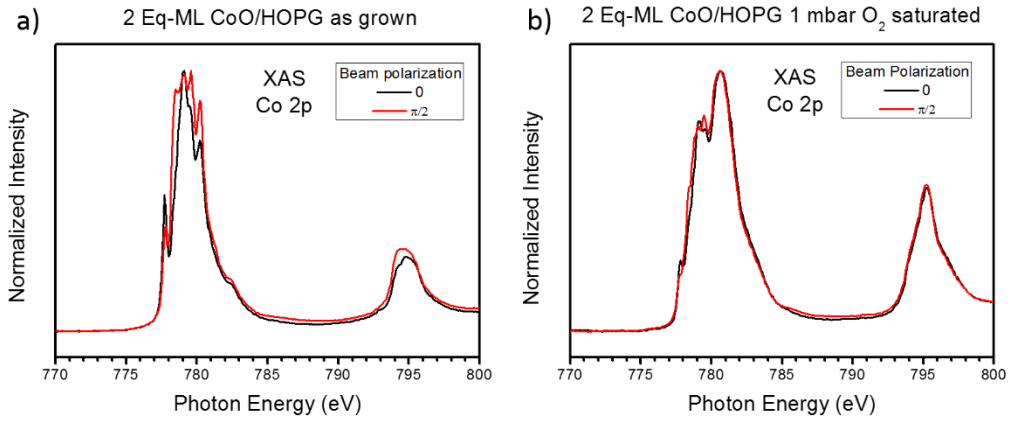

Figure 3.11 Co $L_{2,3}$ edge of as grown 2 Eq-ML CoO/HOPG sample at two beam polarizations: 0 and $\pi/2$. c) Co $L_{2,3}$ edge of 2 Eq-ML CoO/HOPG sample exposed for 1 hour to 1 mbar of O_2 at two beam polarizations: 0 and $\pi/2$.

3.4 Carbon gasification reaction induced by CoO re-oxidation on HOPG

3.4.1 Reduction and re-oxidation processes: a NAP-XPS *in situ* study

The carbon gasification reaction induced by the re-oxidation of the cobalt oxide has been studied by means of NAP-XPS. The spectra shown in the next lines belong to the same experiment than those plotted on Figures 3.7 b and 3.10. On the light of these measurements and as a final conclusion, a chemical model for this reaction will be proposed in sub-section 3.4.1.4.

3.4.1.1 Reduction process. Cobalt oxide and HOPG

As stated before, the re-oxidation process that give rise to the formation of nanochannels takes place after heating the CoO/HOPG sample at 400 °C in UHV conditions, followed by oxygen exposure at the same temperature. Two different O_2 pressures were used during l hour: 10^{-3} mbar (same pressure as reported previously in [14]) and 1 mbar.

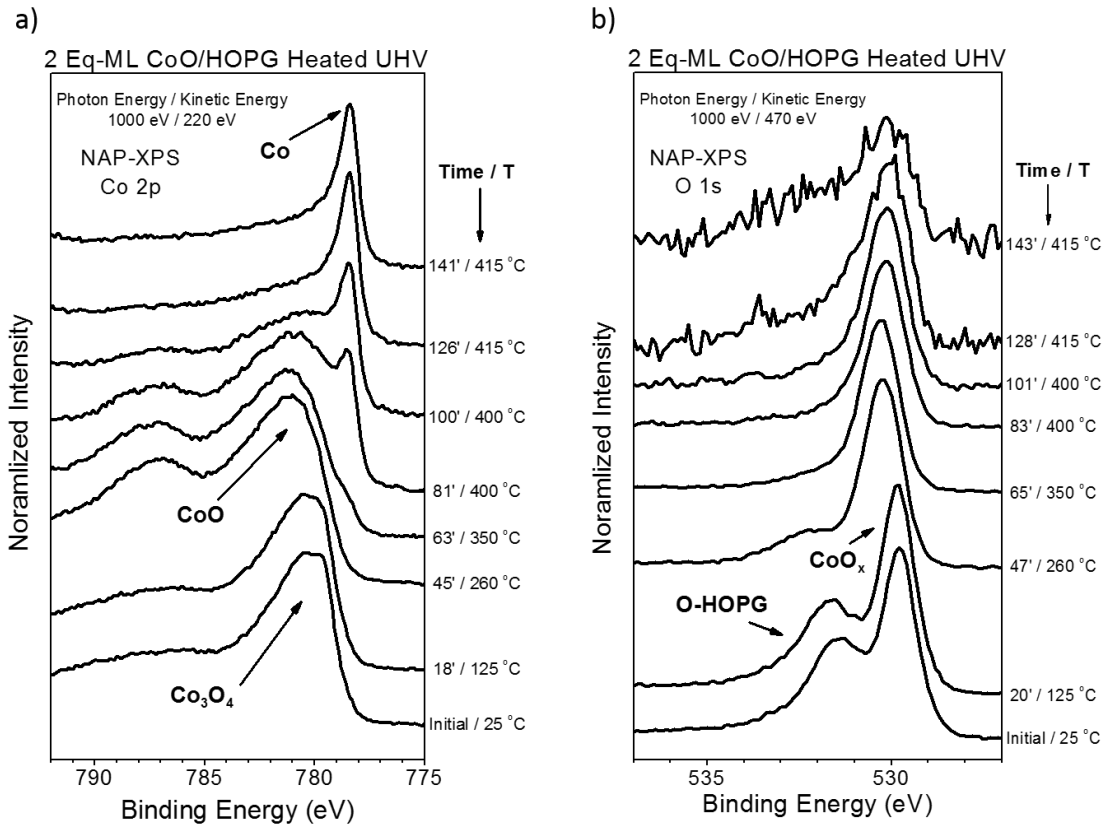

Figure 3.12 Co 2p (a) and O 1s (b) NAP-XPS measurements as a function of time of 2 Eq-ML CoO/HOPG sample heated at 415°C under UHV conditions.

The initial heating process induced the reduction of the cobalt oxide into metallic nanoparticles. Figures 3.12 a and b are referred to Co 2p and O 1s NAP-XPS spectra evolution with time and temperature, respectively. The Co 2p spectra show the gradual reduction of Co_3O_4 to CoO and then to metallic cobalt. On the other hand, the O-HOPG component of the O 1s spectra vanishes at temperatures lower than 400°C. It should be recalled that the starting point of this evolution is the 2 Eq-ML CoO/HOPG sample oxidized at room temperature, as shown in figure 3.10. In this way, the oxygen content of the sample is greater than that reported on [14], and therefore the time needed for the complete reduction has increased in comparison, from one to two hours. Furthermore, the actual heating system (with a slow heating ramp of ~5°/min) may be less quick than the one used previously, what can also induce a slower velocity of the reduction process.

By comparing Figures 3.10 and 3.12, the first remarkable fact is that the oxidation and reduction processes of the cobalt oxide layer are reversible, in agreement with previous works [48]. In second place, as it is shown in Figure 3.13 a, the initial anisotropy between both polarizations completely disappears, suggesting the extinction of the wetting layer in a clustering process to form new metallic Co nanoparticles. This result is also supported by previous AFM measurements shown in [14] just after the reduction process at UHV conditions.

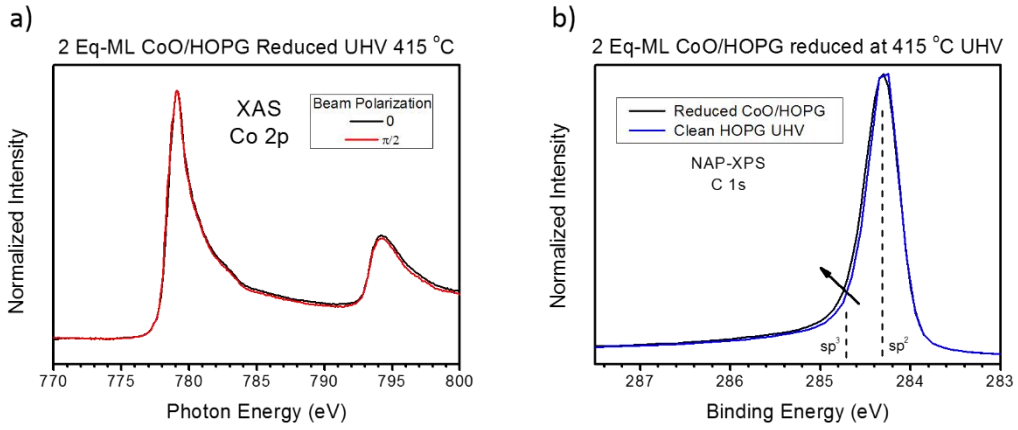

Figure 3.13 a) Co $L_{2,3}$ edge of 2 Eq-ML CoO/HOPG sample after reduction at 415 °C in UHV conditions at two beam polarizations: 0 and π/2. b) C 1s XPS measurement of clean and reduced HOPG.

It is also very interesting to remark the changes on the substrate. Figure 3.13 b shows the XPS spectra for the C 1s on clean HOPG and after the reduction. Although the

C-O and C=O contributions at 286 and 288 eV reported previously have disappeared, the main contribution corresponding to typical sp^2 hybridization at 284.3 eV widens at higher binding energies. The typical defects on graphite associated to a sp^3 hybridization translates into a contribution at ~285 eV [34], which fits very well to the signal widening observed. Therefore, it seems clear that the heating process in UHV removes the oxygen from the graphite, perturbing meanwhile the graphite lattice and being the cause of the development of defects, which translate in a different hybridization and coordination of the carbon atoms. Precisely, these defects verify the weakening hypothesis of the σ bonds of graphite due to the interaction with cobalt oxide [14], which acted as an initial "oxygen pump" for the graphite lattice.

3.4.1.2 Re-oxidation process: cobalt oxide

After the reduction process, the sample was exposed to oxygen at the same temperature (400 °C). In this step the kinetic is much faster than before. Changes on the oxidation state of cobalt are almost instantaneous (the first NAP-XPS spectrum for each pressure is completed just one minute after the opening of the oxygen valve). As shown in Figure 3.14 a, for 10^{-3} mbar the metallic cobalt is immediately re-oxidized to CoO and remains unchanged during the complete hour at that pressure. The picture is slightly different when the pressure was increased to 1 mbar. Again, the initial spectrum changed without transition to the characteristic shape of spinel cobalt oxide, as discussed above. Nevertheless, XAS Co $L_{2,3}$ spectra shown on reference [14] after the re-oxidation process showed that this state corresponded not to pure Co_3O_4, but a mixture with CoO (70/30%, Co_3O_4/CoO). This detail related to the mixed final state could be important in order to understand what happened during the entire process at this high pressure of oxygen, as it results more complex than for 10^{-3} mbar. Thus, the evolution of the Co $2p_{3/2}$ XPS spectra shows a variation of the relative intensities of the two characteristic satellites of the Co_3O_4 during the first ~20 minutes. After this time, the spectrum was stabilized in a mixture between Co_3O_4 and CoO. The CoO consists of Co^{2+} cations octahedrally coordinated on high spin configuration (Co^{2+} HS (O_h)). Regarding the spinel structure of Co_3O_4, it consists of Co^{2+} cations tetrahedrally coordinated in high spin configuration (Co^{2+} HS (T)) and Co^{3+} cations octahedrally coordinated in low spin configuration (Co^{3+} LS (O_h)), with a ratio of 1:2. Theoretical cluster model calculations [12] depicted on Figure 3.14 b show that the corresponding satellite for Co^{2+} HS (T) was situated at ~5.5 eV above the

main peak, whereas Co^{3+} LS (O_h) is situated at ~10 eV from the main contribution. These values matched the experimental relative positions measured in Figure 3.14 a, about 6 eV and 9 eV, respectively.

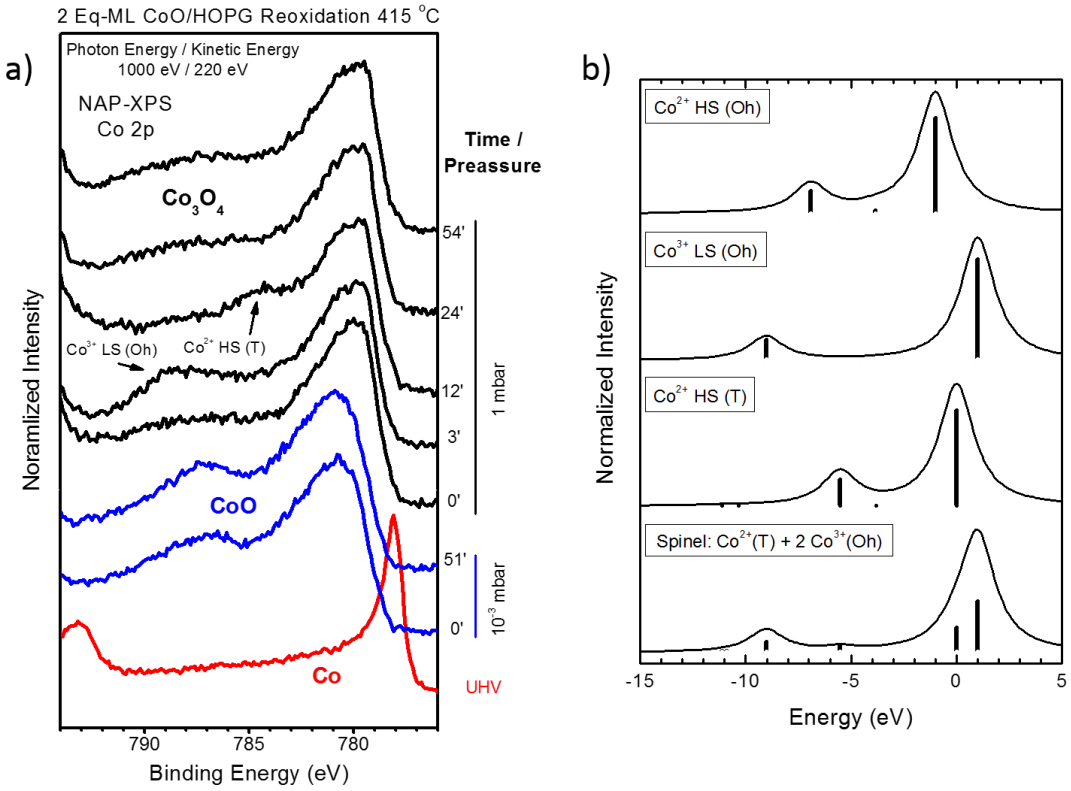

Figure 3.14 a) Co 2p NAP-XPS spectra as a function of O_2 pressure and time of 2 Eq-ML CoO/HOPG at 415°C. b) Cluster model calculations of Co 2p3/2 XPS peak for different Co ions at different symmetries as labelled. Taken from [12].

From the experimental point of view, J. van Elp et. al. [49] showed the transition between Co^{2+} HS (T) and Co^{3+} LS (O_h) states as a function of the lithium doping for some cobalt oxide derivatives (CoO, $Li_xCo_{1-x}O$ and $LiCoO_2$). In fact, in the case of $LiCoO_2$, Co-O interatomic distance is strongly reduced, resulting in a ligand field strong enough to stabilize a Co^{3+} low-spin ground state, which satellite dominates on the XPS Co 2p spectrum. Indeed, the relative position of these satellites from the main peaks agrees with the aforementioned calculations for CoO and Co_3O_4. These results point out that in the early stages of the CoO/HOPG re-oxidation at high oxygen pressures the relative amount of Co^{3+} and Co^{2+} varies.

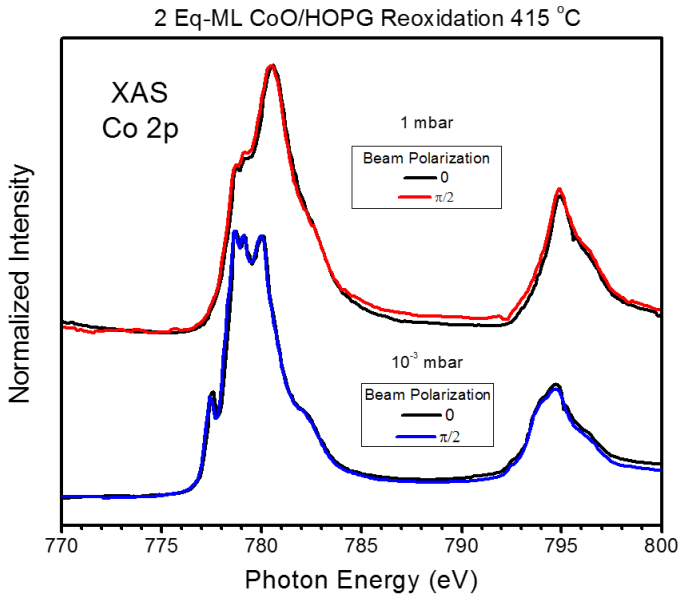

Figure 3.15 Co $L_{2,3}$ edge XAS measurements of 2 Eq-ML CoO/HOPG sample after the re-oxidation process at 415 °C for two different pressures (10^{-3} mbar and 1 mbar) at two beam polarizations: 0 and π/2.

On the other hand, the spinel structure is very common for many other metal atoms. A well-known spinel system due to its multiple applications is magnetite, the iron spinel Fe_3O_4. In this particular case, tetrahedral sites are occupied by Fe^{3+}, while octahedral sites are occupied by equal numbers of Fe^{2+} and Fe^{3+} in bulk Fe_3O_4. This spinel case is very interesting for the understanding of our cobalt oxides due to the fact that the proportion of octahedral Fe^{2+}/Fe^{3+} can be modified and these cations can be exchanged. Regarding magnetite nanoparticles, this ratio is shape [50] and size dependent [51]. In addition, plane surface termination also determines changes on the Fe^{2+}/Fe^{3+} ratio of total cations as compared to the bulk as it has been studied for the (001) terminated planes, which are mainly composed by octahedral Fe^{2+} and Fe^{3+} cations [52]. Although for Fe_3O_4 is relatively simple to satisfactorily explain the exchange between octahedral Fe^{2+} and Fe^{3+}, its behavior can be used to inspire a hypothesis for the current cobalt spinel issue. A possible explanation for the variation of the relative intensities of Co^{2+} HS (T) and Co^{3+} LS (O_h) satellites could be related with a resonance of the spinel structure between both states. It is already known that Co^{2+}/Co^{3+} oxidation states are able to interconvert with relatively weak variations in the oxidizing or reducing ambient conditions [53]. In addition, the close relationship between the rocksalt (CoO) and spinel oxygen sublattices and the ease with which cations can move between octahedral and tetrahedral sites,

especially at the surface [53], suggest a possible important exchange between both Co^{2+}/Co^{3+} states until equilibrium is reached (in the case of Co^{2+} including both octahedral and tetrahedral high spin configurations). It should be reminded that during the present re-oxidation process a strong carbon gasification reaction ruled by CoO_x (Co_3O_4/CoO mixture) nanoparticles is happening, where due to its low dimensionality the surface is maximized over the volume. Therefore, the two premises for Co^{2+}/Co^{3+} resonance -i.e. strong variations in oxidizing or reducing ambient conditions and high mobility of cations on the surface-, are fulfilled and can explain the relative intensity variations between both satellites of the Co_3O_4 spinel structure and also the presence of a small amount of CoO.

Finally, Figure 3.15 completes the study of the re-oxidation process of the cobalt oxide. As it can be appreciated in comparison with Figure 3.11, no anisotropy is shown by any spectra regarding the polarization of the synchrotron light at none of the oxygen pressures. In fact, this is consistent with the explanation offered to explain Figure 3.13 a, where the anisotropy was removed after the reduction to metallic cobalt due to a clustering process. During the re-oxidation this cobalt clusters would oxidize but with no morphological reconstruction of the initial wetting layer.

3.4.1.3 Re-oxidation process: HOPG

This section will be focus on the study of the effects on the HOPG substrate during the re-oxidation process, where essentially the carbon gasification reaction takes place. Figure 3.16 shows the C 1s NAP-XPS fitted spectra as a function of the oxygen pressure for a constant photon energy of 500 eV (a), while (b) plots the spectra as a function of the photon energy when the O_2 pressure is fixed at 1 mbar. The low photon energy of 500 eV in Figure 3.15 a ensures a very surface sensitive analysis (IMPF about 9.5Å). As it can be noticed, the presence of O_2 induces the development of defects on the graphite lattice (sp^3 contribution), although the signal of C-O and C=O is much lower than those shown in Figure 3.7 b for the same pressures at room temperature. This last circumstance can be explained by the rapid desorption of the products coming from the carbon gasification reaction, so the intermediate states currently bonded to the graphite surface have very tiny signal compared to the intensity of the main sp^2 peak.

On the other hand, important changes on the C 1s spectra can be found in Figure 3.16 b by varying the photon energy (IMPFs through cobalt oxide matrix of 6.8Å, 14.5Å

and 17.3Å for hν of 500 eV, 1000 eV and 1200 eV, respectively). As the probing depth is increased, the proportion of defects compared to the not perturbed graphite lattice signal has a very strong increase. This tendency points out that the graphite defects were developed essentially under the CoO_x clusters. This is in total agreement with previous published Raman spectroscopy measurements after the same re-oxidation process, where the defects increase all over the sample, but especially under the CoOx clusters [14]. In this manner, the rise on the sp^3 contribution in decrement of the graphite sp^2 peak for higher probing depths does not mean that the perturbation of the graphite lattice occurs at the bulk, but at the CoO_x/HOPG interface.

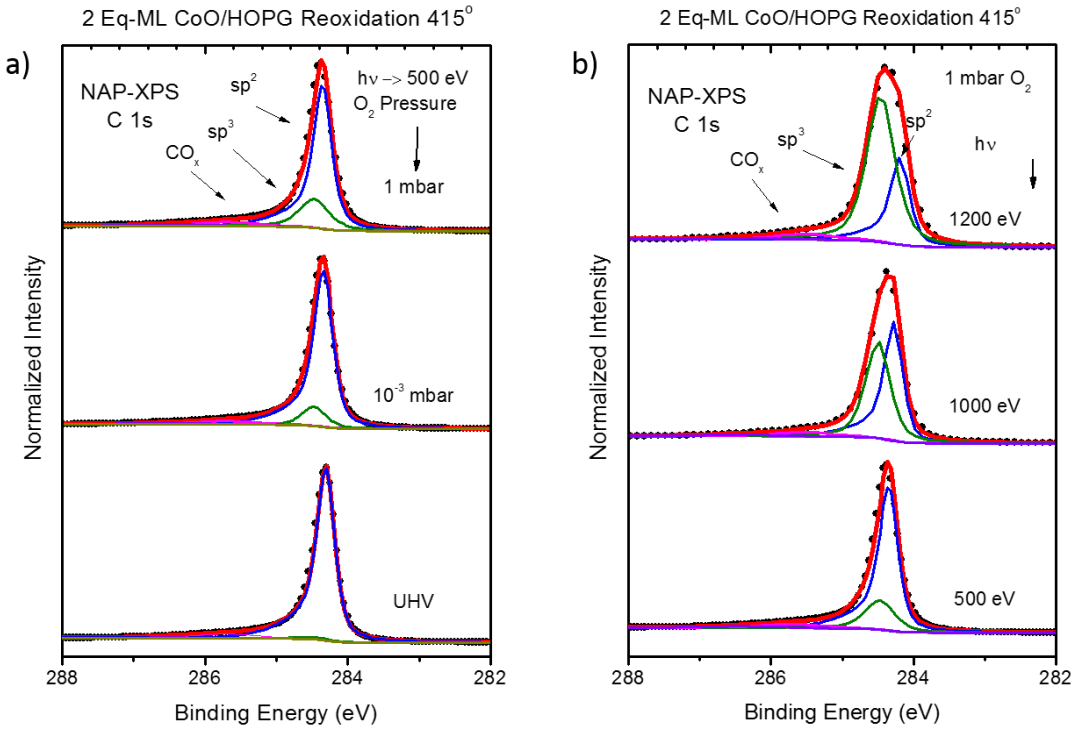

Figure 3.16 a) C 1s NAP-XPS measurements as a function of O_2 pressure of 2 Eq-ML CoO/HOPG at 415°C; b) C 1s NAP-XPS measurements with three different photon energies for 1 mbar of O_2 at 415°C.

The final products of the carbon gasification reaction (CO and CO_2 gases) could not be studied directly using the mass spectrometer of the analysis chamber of the BL24-CIRCE-NAPP endstation due to the high residual pressures of equivalent molecules. However, intermediate sates on the surface were investigated via O 1s NAP-XPS spectra

for different O_2 pressures. In any case, Figure 3.17 b shows, as supplementary information, the evolution with time of the CO, CO_2 and O_2 gases during the re-oxidation process performed at our laboratory during the re-oxidation process at a partial pressure of O_2 of 10^{-5} mbar [14]. As it can be appreciated, when the oxygen valve is open, the carbon gasification reaction starts and the partial pressure of CO significantly increases, while CO_2 slightly changes.

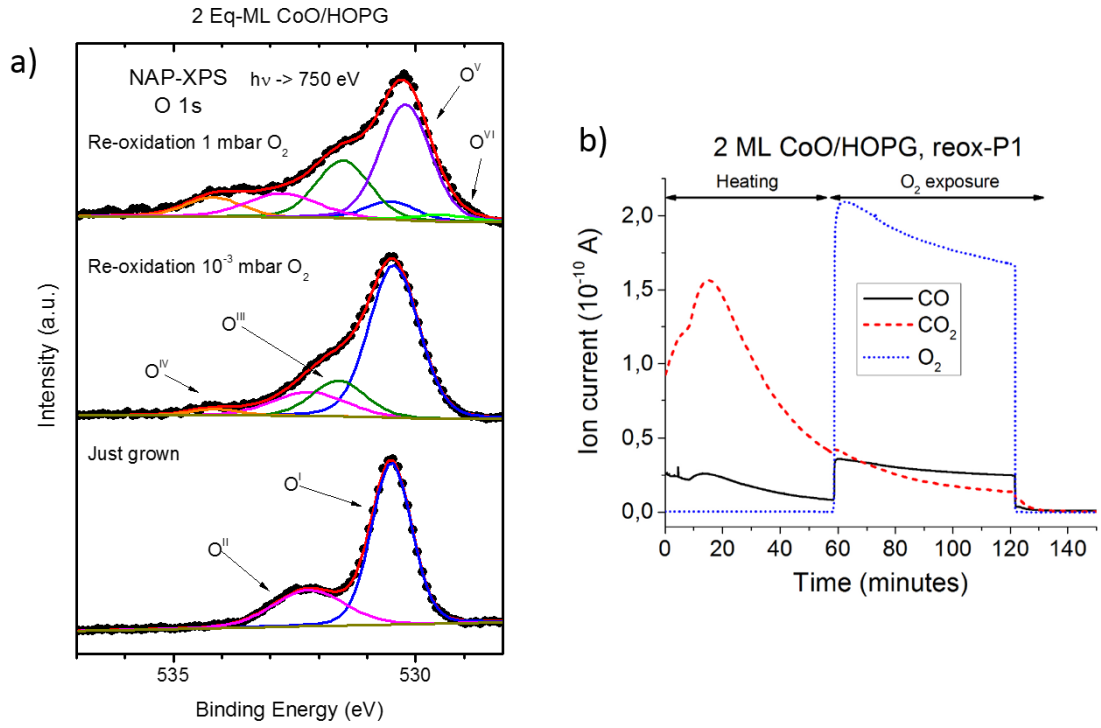

Figure 3.17 a) O 1s NAP-XPS measurements as a function of O_2 pressure of 2 ML CoO/HOPG at 415°C. Bottom: as grown CoO layer. b) Mass spectroscopy measurement as a function of time during the re-oxidation process for 10^{-5} mbar of O_2 at 400 °C [14].

Figure 3.17 a shows the O 1s spectra taken at a photon energy of 750 eV (IMPF 6.8Å). The initial as grown CoO has only two contributions: the main peak O^{I} at 530.5 eV, which is associated to the Cobalt oxide, and a second peak O^{II} at 532.3 eV, which is usually assigned on transition metal oxides to hydroxyls groups absorbed at the surface [38]. As it has been discussed previously, regarding the cobalt oxide, its re-oxidation at high pressures (1 mbar) leads to the mixture of CoO and Co_3O_4, whose contribution shifts to 530.2 eV, named as O^{V}. The spectra become more complicated as the O_2 pressure increases and the carbon gasification reaction takes place. Three more contributions

appear and increase their relative intensity with higher pressures, labelled as O^{III}, O^{IV} and O^{VI}. The first one at 531.6 eV could correspond to oxygen singly bonded to aliphatic carbon (C-O), and may correspond to an intermediate state where the carbon ring of the graphite lattice is broken [54,55]. The O^{IV} contribution is located at higher binding energy, 534.2 eV. Such high binding energies does not correspond to CO_x species, but with water molecules and/or different silicon compounds (SiO_x). Both contaminants should be taken into account due to the heating of different parts of the NAP-CIRCE chamber during the re-oxidation process. These may be contaminated by other experiments performed at the endstation. Finally, O^{VI} at 529.6 eV could correspond to oxygen doubly bonded to aromatic carbon (C=O) [45,46,56]. Its lower intensity and appearance only with high oxygen pressures could be explained as a previous stage of O^{III} with a very short mean time life. In addition, this behavior turns out in perfect harmony with the C-O and C=O species evolution of the C 1s spectra of Figure 3.7 b. The increase of both, graphite defects and oxygen intermediate states O^{III} and O^{VI} at the surface indicates an acceleration of the reaction kinetics with the increase of oxygen pressure.

3.4.1.4 The model of carbon gasification reaction

In the last sections XAS, XPS, HAXPES and NAP-XPS spectra of both graphite and cobalt oxides have been discussed in order to understand the nano-patterning process that take place during the carbon gasification reaction catalyzed by the initial CoO. It has been proved that the interaction between the initial deposit of CoO and HOPG leads to the oxidation of the HOPG substrate, in particular under oxygen atmosphere. In this way CoO acts as an oxygen pump into the graphite net. In parallel with the oxidation, the graphite also develops defects during this process, which means the conversion from typical sp^2 to sp^3 hybridization, with single C-C and C-H bonds, and also the possible formation of fixed double bonds C=C. The leading role of the initial CoO wetting layer lies on the percentage of surface covered by it in comparison to CoO clusters, and also on the fact that CoO oxidizes the substrate whatever its thickness is. This oxidation implies a weakness of the graphite structure, as evidenced by the broadness of the C 1s spectrum of the HOPG after the reduction process. This is precisely the reason that allows the subsequent carbon gasification reaction at lower temperatures once the oxygen is introduced. In this final step, again the re-oxidized cobalt oxide acts as an oxygen pump.

CO and CO_2 are liberated as final products, while the graphite develops more defects essentially under the CoO_x nanoclusters where the reaction takes place and intermediate C-O and C=O are formed in the substrate.

With this information we can propose a basic model of the observed carbon gasification reaction. In first place, the weakened graphite after the reduction process is characterized by the development of sp^3 defects, i.e. single bonded C-C and C-H. The graphitic aromatic ring was broken during the oxidation process of HOPG due to the presence of CoO, and although the reduction under UHV conditions eliminates the C-O and C=O species, it cannot recompose the broken aromatic rings. The chemical route regarding how the as deposited CoO oxidizes the HOPG and how the carbon gasification reaction takes place during the re-oxidation process at 400 °C is quite similar, although the kinetics of the second one is enhanced by 1) the higher temperature and 2) the weakened graphite because of the its broken rings due to the first oxidation of the substrate. In this way, first of all, the graphite rings break up by an hydrogenation process, which, as Figure 3.18 shows, could lead to three different scenarios, with triple (sp), double (sp^2) or single (sp^3) C-C bonding. Although the third case (yellow square corresponding to sp^3 hybridization, see Figure 3.18) optimizes the amount of C-H bonds, which were reported in Figure 3.6, is the double bonded C=C the one that could act as the door for the graphite oxidation. The first oxidation step consists on the development of C=O by the formation of carboxyl, ketone and aldehyde groups. All of them are intermediate steps, with a very short mean life time, as shown in Figure 3.7 b and 3.17 a, and imply sp^3 and C=O contributions at the C 1s and O 1s spectra (yellow square corresponding to sp^3 hybridization and green square corresponding to C=O contribution, see Figure 3.18). However, each of these groups can evolve in a different way. Regarding the carboxyls and ketones, the oxidation process can continue to primary and secondary alcohol, respectively, where aliphatic carbon (C-O) can be found (yellow square corresponding to sp^3 hybridization and blue square corresponding to C-O contribution, see Figure 3.18). On the other hand, the carboxyl and the aldehyde can progress to CO_2 and CO gases, respectively, leading in the graphite carbon bonded to hydrogen and/or OH^- groups (yellow square corresponding to sp^3 hybridization and blue square corresponding to C-O contribution, see Figure 3.18).

This chemical sequence can explain all the measured species from carbon and oxygen spectra, as well as the evolution of those with time and oxygen pressure,

spotlighting on the leading role of the initial CoO as oxidation agent of the HOPG. Precisely, this initial interaction between CoO and substrate is the key to understand how the graphitic rings initially break up, weakening the graphite network and being able to induce nano-patterning at lower temperatures than those previously reported for metallic nanoparticles.

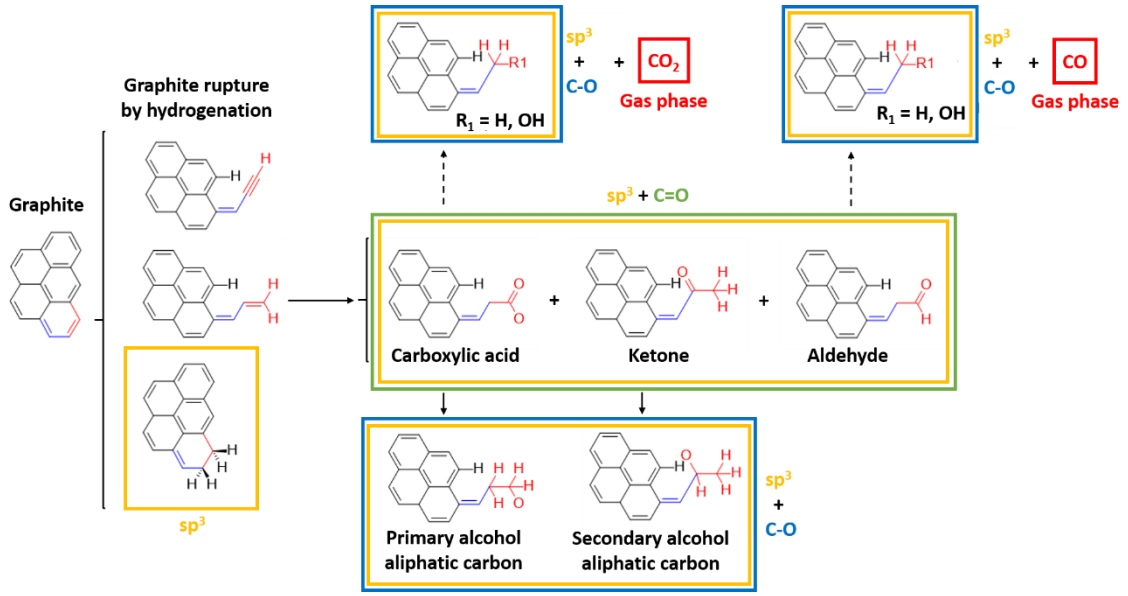

Figure 3.18 Proposed scheme of the carbon gasification reaction induced by Cobalt oxide nanoparticles on graphite via re-oxidation process R1.

3.4.2 Final nanostructures: an AFM-KPFM study

The carbon gasification reaction leads to three different kinds of nanostructures on the graphite surface which can be measured using AFM, as Figure 3.19 shows. In first place, nanochannels have been previously studied [12,14], and from the technological point of view they may be the most useful result of the carbon gasification reaction discussed above. In second place, nanorings and nanostrips have also been found on the HOPG surface. However, these nanostructures are much more evasive due to two constraining reasons:

- Its appearance was time dependent at room conditions. Figure 3.20 shows two images of the same re-oxidized CoO_x cluster. The images were taken in phase mode, at room temperature, under atmospheric conditions and with one hour of difference. As it can be appreciated, the number of nanorings was almost doubled.

The same effect was systematically observed with fresh samples, where initially this kind of nanostructures were absent but few hours later the sample was full of nanorings. As supplementary information it can be found an AMF video reporting the time-evolution of these nanostructures.

- These nanostructures tend to disappear under gentle energy flux, such as increasing temperature or electron and X-ray doses. This last circumstance has reduced the possibilities of chemical characterization, limiting the measurements to non-contact probe techniques at room temperature.

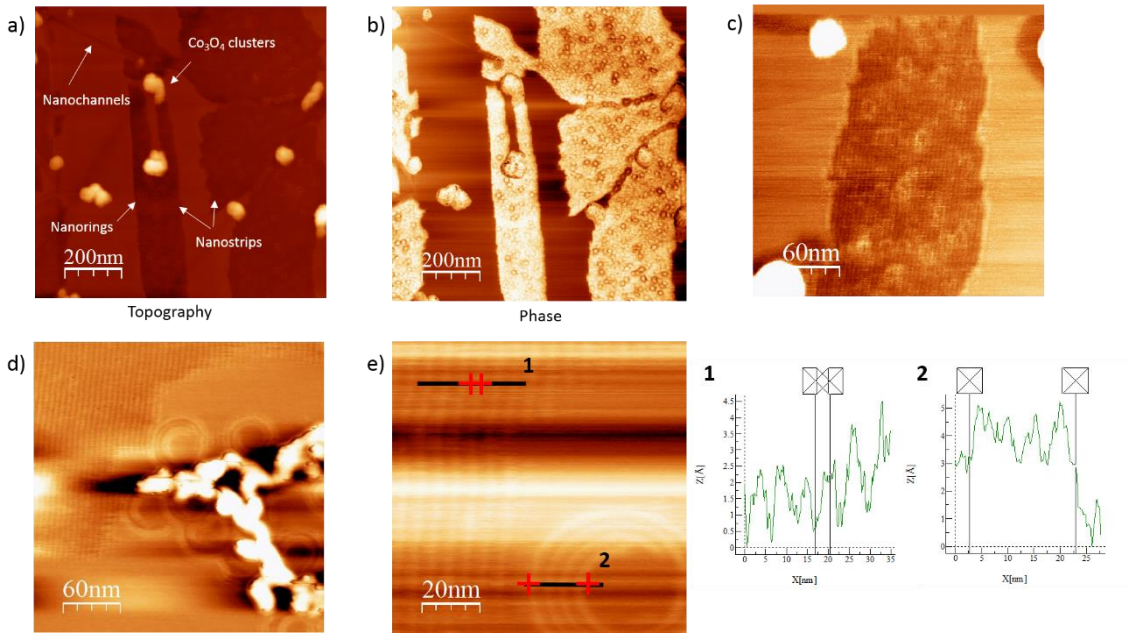

Figure 3.19 a) and b) topography and phase images, respectively, of 2 Eq-ML CoO/HOPG after re-oxidation process. CoO_x clusters, nanochannels, nanorings and nanostrips are shown. c) and d) details of nanorings and nanostrips on topography images; e) Topography detail of nanorings and nanostrips with their respective height profiles. d) and e) taken from [12].

Topography images show a broad range of nanorings dimensions, usually bigger as they are closer to CoO_x clusters. Under same growth conditions, the diameter of the nanorings for different re-oxidized samples varied from 41±2 nm to 25±2 and 13±2 nm. The height of individual rings was in the range 4-4.5 Å, while concentric rings (as Fig 3.19 e) are 1.5 Å high. This last value was the same than for the nanostrips, and could

correspond to an underestimation due to the big size of the tip in comparison to the small separation between nanostructures. In particular, the periodicity of both nanostrips and concentric nanorings is 5±0.5 nm. In most of the cases the nanorings were found to be in contact with the CoO_x nanoclusters (as in Figure 3.19 d or Figure 3.20). However, in some cases these structures can be found over regions covered by the nanostrips (as in Figures 3.18 a, b and c). Finally, these periodic strips are arranged along three directions rotationally separated by 120°.

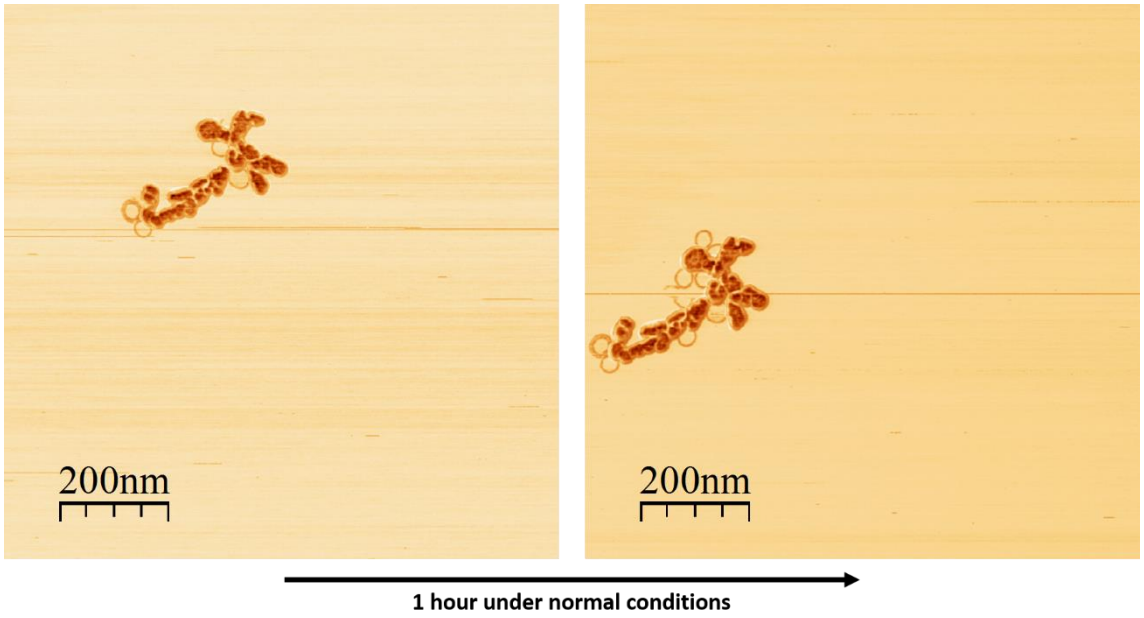

Figure 3.20 AFM measurements performed in *phase mode* of the same cluster at normal conditions with a lapse of 1 hour.

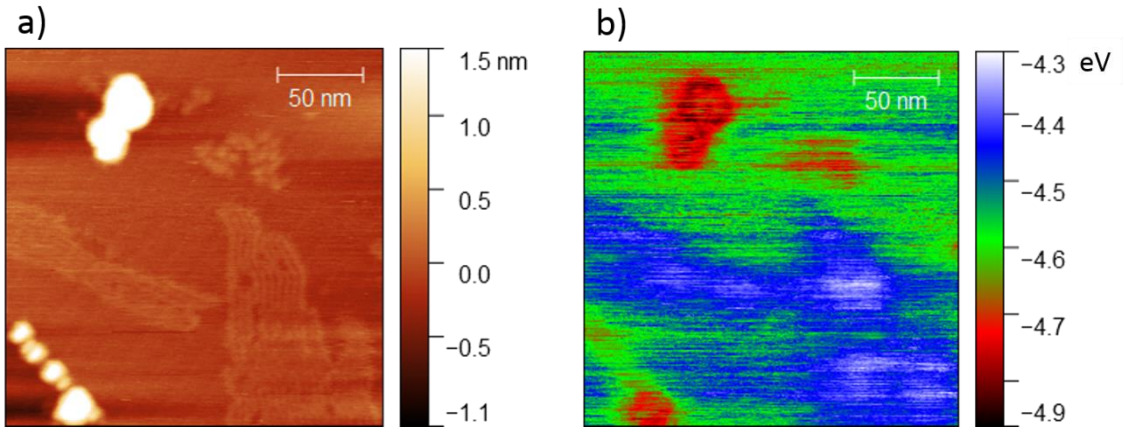

Figure 3.21 Topography (a) and work function map (b) of 2 Eq-ML CoO/HOPG after re-oxidation process R1.

The chemical nature of these structures is undetermined, but KPFM images show an important decrease of ~200 meV of the work function value for nanostrips in comparison to free HOPG surface. Figures 3.21 a and b show the topography and work function map, respectively, of a region with nanostrips, cobalt oxide clusters and free HOPG surface. Fixing the HOPG work function at 4.6 eV [57,58], the cobalt oxides clusters (composed in a 70% by Co_3O_4) show ~4.9 eV, in good agreement with other experiments [59]. Surface contamination of graphite with organic molecules after room conditions exposure leads to an increase of the work function [60], what could indicate a different origin of these nanostructures (not adventitious carbon). On the other hand, adsorption of different types of both organic [19,21,61] and inorganic molecules [20,62] on graphene and graphite substrates is thoroughly reported. Besides, similar dimensions and periodicities of ~4-7 nm for this kind of nanostrips can be found for self-assembled molecule chains, which can be aligned along the armchair axis of HOPG.

Therefore, given the lack of chemical data, exotic structures such as early stages of carbon nanotubes [15], metal nanorings promoted by carbon-based surfaces [16], Co superparamagnetic nanorings [17] or Co_3O_4 nanorings [18] cannot be discarded. However, the nanostrips work function is too low to be associated to carbon based arrangement as the carbon nanotubes or metallic or cobalt oxide structures. In the light of the KPFM results and similar reported AFM images on 2D materials such as graphene, it seems more plausible that these nanorings and nanostrips are self-assemble structures of organic and/or inorganic molecules present in the laboratory atmosphere. This could explain their time dependent appearance and their vanishing with gentle energy flow. In particular, the aforementioned development of defects in the graphite surface, and especially in the surroundings of the cobalt oxide clusters after the re-oxidation process, could lead to changes on hydrophobicity and reactivity of the HOPG surface. This could facilitate the adsorption of molecules and the curvature of the typical nanostrips where more HOPG defects can be found, i.e, near the CoO_x clusters, as it was shown by the C 1s spectra of Figure 3.15.

3.5 Conclusions

This chapter has summarized the main results regarding the *in situ* study of the carbon gasification reaction promoted by the re-oxidation of cobalt oxide on HOPG. As it was reported by our group in previous works, the most astonishing result was the nano-

patterning of the graphite surface at lower temperatures than for metallic nanoparticles. However, there was a lack on the understanding of what make this possible. In these pages, novel results regarding the electronic characterization of the CoO wetting layer and the *in situ* study of the carbon gasification reaction through NAP-XPS have been presented. It has been shown how the initial CoO is able to introduce oxygen on the HOPG structure, breaking the graphitic rings and introducing some defects: hence, moving from sp^2 to sp^3 hybridization. Although after the reduction process the C-O and C=O bonds induced by the initial CoO deposition disappeared, the broken graphitic rings have weakened the graphite network and therefore the carbon gasification reaction take place with quicker kinetics that for typical metallic nanoparticles. By means of these experiments the initial hypothesis related with the weakening of the HOPG σ bonds and consequent low temperature nano-pattering has been proved. On the other hand, the oxidation at room temperature from CoO to Co_3O_4 resulted a reversible process, although the re-oxidation at 400 °C of metallic Co leads to a not stable transition at high pressures, where the Co^{3+}/Co^{2+} ratio changes with time until the equilibrium is reached in a Co_3O_4/CoO mixture. This fact is due to 1) the size of the nanoparticles, i.e. surface is predominant over volume, and 2) the strong variations of the oxidation-reduction conditions during the carbon gasification reaction. Closing, two new final nanostructures have been studied as final products present on the HOPG surface after the re-oxidation process: nanorings and nanostrips. Although the main core of the study has been topographical, KPFM measurements point out that these two structures share a same origin, self-assemble structures of organic and/or inorganic molecules which are present in the laboratory atmosphere (these nanostructures were only visualized after air exposure). The chemical modification of the graphite surface due to the carbon gasification reaction could induce changes on the hydrophobicity and reactivity of the HOPG surface, facilitating the adsorption of molecules and the curvature of the typical nanostrips near the CoO_x clusters, where defects concentration increases.

Bibliography

[1] S. Shetty, R. A. van Santen; "CO dissociation on Ru and Co surfaces: The initial step in the Fischer-Tropsch synthesis"; *Catal. Today*; 171, (2011); pp: 168-173; DOI:10.1016/j.cattod.2011.04.006

[2] L. Zhi, Y.-S. Hu, B. E. Hamaoui, X. Wang, I. Lieberwirth, U. Kolb, J. Maier, K. Müllen; "Precursor-Controlled Formation of Novel Carbon/Metal and Carbon/Metal Oxide Nanocomposites"; *Adv. Mater*. 20, (2008); pp: 1727-1731; DOI: 10.1002/adma.200702654

[3] F. Schwierz; "Industry-compatible graphene transistors"; *Nature* 472, (2011); pp: 41-42; DOI: 10.1038/472041a

[4] E. W. Hill, A. Vijayaragahvan, K. Novoselov; "Graphene Sensors"; *IEEE Sensors Journal* 11, (2011); pp: 3161-3170; DOI: 10.1109/JSEN.2011.2167608

[5] Q. Bao, K. P. Loh; "Graphene Photonics, Plasmonics, and Broadband Optoelectronic Devices"; *ACS Nano*; 6, (2012); pp: 3677-3694; DOI: 10.1021/nn300989g

[6] R. Raccichini, A. Varzi, S. Passerini, B. Scrosati; "The role of graphene for electrochemical energy storage"; *Nature Materials*; 14, (2015); pp: 271-279; DOI: 10.1038/nmat4170

[7] L. Ci, Z Xu, L. Wang, W. Gao, F. Ding, K. F. Kelly, B. I. Yakobson; P. M. Ajayan; "Controlled nanocutting of graphene"; *Nano Res*; 1, (2008); pp: 1-116 DOI: 10.1007/s12274-008-8020-9

[8] N. Severin, S. Kirstein, I. M. Sokolov, J.P. Rabe; "Rapid Trench Channeling of Graphenes with Catalytic Silver Nanoparticles"; *Nano Lett* 9, (2009); pp: 457-461; DOI: 10.1021/nl8034509

[9] S. Konishi, W. Sugimoto, Y. Murakami, Y. Takasu.; "Catalytic creation of channels in the surface layers of highly oriented pyrolytic graphite by Cobalt nanoparticles"; *Carbon*, 44, (2006); pp: 2338-2340; DOI: 10.1016/j.carbon.2006.05.003

[10] S. S. Datta, D. R. Strachan, S. M. Khamis, A. T. Johnson; "Crystallographic Etching of Few-Layer Graphene"; Nano Lett, 8, (2008); pp: 1912-1917 DOI: 10.1021/nl080583r

[11] L. Bulut, R. H. Hurt; "A Magneto-catalytic Writing Technique for Etching Complex Channel Patterns into Graphenic Carbons"; *Adv Mater*, 22, (2010); pp: 337-341; DOI: 10.1002/adma.200901932

[12] D. Diaz-Fernandez; 2015; Ph.D Thesis "*Study of the growth and interaction of Cobalt oxides on graphite and oxides surfaces*"

[13] D. Díaz-Fernández, J.Méndez, O. Bomatí-Miguel, F. Yubero, R.J.O. Mossanek, M. Abbate,G. Domínguez-Cañizares, A. Gutiérrez, S. Tougaard, L. Soriano; " The growth of Cobalt oxides on HOPG and SiO2 surfaces: A comparative study"; *Surf Sci*; 624, (2014); pp: 145-153. DOI: 10.1016/j.susc.2014.02.007

[14] D. Díaz-Fernández, J. Méndez, A. del Campo, R.J.O. Mossanek, M. Abbate, M.A. Rodríguez, G. Domínguez-Cañizares, O Bomatí-Miguel, A. Gutiérre, L. Soriano.; "Nanopatterning on highly oriented pyrolytic graphite surfaces promoted by Cobalt oxides"; *Carbon*; 85, (2015); pp: 89-98. DOI: 10.1016/j.carbon.2014.12.049

[15] D. Takagi, Y. Homma, H. Hibino, S. Suzuki, Y. Kobayashi; "Single-Walled Carbon Nanotube Growth from Highly Activated Metal Nanoparticles"; *Nano Lett*; 6, (2006); pp: 2642-2645; DOI: 10.1021/nl061797g

[16] M. Liu, Y. Lu, W. Chen; "Electrocatalysts: PdAg Nanorings Supported on Graphene Nanosheets: Highly Methanol-Tolerant Cathode Electrocatalyst for Alkaline Fuel Cells"; *Adv. Funct. Mater*.; 23, (2013); pp: 1289:1296. DOI: 10.1002/adfm.201370050

[17] M. Marin-Almazo, D. Garcia-Gutierrez, X. Gao, J. L. Elechiguerra, V. A. Kusuma, W. M. Sampson, M. Miki-Yoshida, A. B. Dalton, R. Escudero, and M. Jose-Yacaman; "Cobalt-Based Superparamagnetic Nanorings"; *Nano Lett*.; 4, (2004); pp: 1365-1371. DOI: 10.1021/nl049464b

[18] X. Liu, Ran Yi, N. Zhang, R. Shi, X. Li, G. Qiu; "Cobalt Hydroxide Nanosheets and Their Thermal Decomposition to Cobalt Oxide Nanoring"; *Chem. Asian J*.; 3, (2008); pp: 732-738. DOI: 10.1002/asia.200700264

[19] S. Manne, H. E. Gaub; "Molecular Organization of Surfactants at Solid-Liquid Interfaces"; *Science* 270, (1995); pp: 1480-1482. DOI: 10.1126/science.270.5241.1480

[20] Y.-H. Lu, C.-W. Yang, I.-S. Hwang; "Atomic force microscopy study of nitrogen molecule self-assembly at the HOPG-water interface"; *Appl. Surf. Sci*. 304, (2014); pp: 56-64. DOI: 10.1016/j.apsusc.2014.03.084

[21] P. Gallagher, M. Lee, F. Amet, P. Maksymovych, J. Wang, S. Wang, X. Lu, G. Zhang, K. Watanabe, T. Taniguchi,D. Goldhaber-Gordon; "Switchable friction enabled by nanoscale self-assembly on graphene"; *Nat. Commun*. 7, (2016); pp: 10745. DOI: 10.1038/ncomms10745

[22] W. Jauch, M. Reehuis, H. J. Bleif, F. Kubanek; "Crystallographic symmetry and magnetic structure of CoO"; *Phys. Rev. B*, 64, (2001); pp: 052102; DOI: 10.1103/PhysRevB.64.052102

[23] A.E. Bocquet, T. Mizokawa, T. Saitoh, H. Namatame, A. Fujimori; "Electronic structure of 3d-transition-metal compounds by analysis of the 2p core-level photoemission spectra"; *Phys. Rev. B* 46, (1992); pp: 3771; DOI: 10.1103/PhysRevB.46.3771

[24] M.C. Biesinger, B.P. Payne, A.P. Grosvenor, L.W.M. Lau, A.R. Gerson, R.StC. Smart; "Resolving surface chemical states in XPS analysis of first row transition metals, oxides and hydroxides: Cr, Mn, Fe, Co and Ni"; *Appl. Surf. Sci*. 257, (2011); pp: 2717-2730; DOI: 10.1016/j.apsusc.2010.10.051

[25] G. van der Laan, C. Westra, C. Haas, G.A. Sawatzky; "Satellite structure in photoelectron and Auger spectra of copper dihalides"; *Phys. Rev. B*, 23, (1981); pp: 4369; DOI: 10.1103/PhysRevB.23.4369

[26] D. Díaz-Fernández, E. Salas, J. Méndez, R.J.O. Mossanek, M. Abbate, C. Morales, G. Domínguez-Cañizares, G.R. Castro, A. Gutiérrez, L. Soriano; "Ultra-thin CoO films grown on different oxide substrates: Size and support effects and chemical stability"; *J. Alloys Compd.*, 758, (2018); pp: 5-13. DOI: 10.1016/j.jallcom.2018.05.112

[27] J.P. Espinós, G. Lassaletta, A. Caballero, A. Fernáandez, A.R. Gonzáalez-Elipe,A. Stampfl, C. Morant, J.M. Sanz; "Synchrotron Photoemission Characterization of TiO2 Supported on SiO2"; *Langmuir*, 14, (1998); pp: 4908-4914. DOI: 10.1021/la980280k

[28] K. Borgohain, J.B. Singh, M.V. Rama Rao, T. Shripathi, S. Mahamuni; "Quantum size effects in CuO nanoparticles"; *Phys. Rev. B*, 61, (2000); pp: 11093. DOI: 10.1103/PhysRevB.61.11093

[29] A. Fujimori, F. Minami; "Valence-band photoemission and optical absorption in nickel compounds"; *Phys. Rev. B* 30, (1984); pp: 957-971. DOI: 10.1103/PhysRevB.30.957

[30] D. Alders, F. C. Voogt, T. Hibma, G. A. Sawatzky; "Nonlocal screening effects in 2p x-ray photoemission spectroscopy of NiO (100)"; *Phys. Rev. B* 54, (1996); pp: 7716-7719; DOI: 10.1103/PhysRevB.54.7716

[31] S. Ya. Istomin, O. A. Tyablikov, S. M. Kazakov, E. V. Antipov, A. I. Kurbakov, A. A. Tsirlin, de N. Hollmann, Y. Y. Chin, H.-J. Lin, C. T. Chen, A. Tanaka, L. H. Tjeng and Z. Hu "An unusual high-spin ground state of Co^{3+} in octahedral coordination

in brownmillerite-type cobalt oxide"; *Dalton Trans*., 44, (2015); pp: 10708-10713 DOI: 10.1039/c4dt03670k

[32] S. C. Wi, J.-S. Kang, J. H. Kim, S.-B. Cho, B. J. Kim, S. Yoon, B. J. Suh, S. W. Han, K. H. Kim, K. J. Kim, B. S. Kim, H. J. Song, H. J. Shin, J. H. Shim, B. I. Min "Electronic structure of $Zn_{1-x}Co_xO$ using photoemission and x-ray absorption spectroscopy"; *Appl. Phys. Lett.* 84, (2004); pp: 4233-4235; DOI: 10.1063/1.1756197

[33] F. M. F. de Groot, M. Abbate, J. van Elp, G. A. Sawatzky, Y. J. Ma, C. T. Chen and F. Sette; "Oxygen 1s and cobalt 2p X-ray absorption of cobalt oxides"; *J. Phys.: Condens. Matter* 5, (1993); pp: 2277-2288; DOI: 10.1088/0953-8984/5/14/023

[34] L. Soriano, M. Abbate, A. Fernández, A. R. González-Elipe, F. Sirotti, J. M. Sanz; "Oxidation State and Size Effects in CoO Nanoparticles"; *J. Phys. Chem. B*, 103, (1999); pp: 6676-6679; DOI: 10.1021/jp990423r

[35] K. Okada, A. Kotani; "Complementary Roles of Co 2 p X-Ray Absorption and Photoemission Spectra in CoO"; *J. Phys. Soc. Jpn.* 61, (1992); pp. 449-453; DOI: 10.1143/JPSJ.61.449

[36] D.A. Fischer, R.M. Wentzcovitch, R.G. Carr, A. Continnenza, A.J. Freeman; "Graphitic interlayer states: A carbon K near-edge x-ray-absorption fine-structure study"; *Phys. Rev. B*, 44, (1991); pp: 1427-1429. DOI: 10.1103/PhysRevB.44.1427

[37] Y. Kebukawa, M.E. Zolensky, A. L. D. Kilcoyne, Z. Rahman, P. Jenniskens, G.D. Cody; "Diamond xenolith and matrix organic matter in the Sutter's Mill meteorite measured by C-XANES"; *Meteoritics & Planetary Science*, 49, (2014); pp: 2095-2103; DOI: 10.1111/maps.12312

[38] G.D. Cody, E. Heying, C. M. O. Alexander, L.R. Nittler, A. L. D. Kilcoyne, S.A. Sandford, R.M. Stroud; "Establishing a molecular relationship between chondritic and cometary organic soids"; *Proc. Natl. Acad. Sci*., 108, (2011); pp: 19171-19176; DOI: 10.1073/pnas.1015913108

[39] H.-K. Jeong, L. Colakerol, M.H. Jin, P.A. Glans, K.E. Smith, Y.H. Lee; "Unoccupied electronic states in graphite oxides"; *Chem. Phys. Lett.*, 460, (2008); pp: 499-502. DOI: 10.1016/j.cplett.2008.06.042

[40] H.-K. Jeong, H.-J. Noh, J.-Y. Kim, M. H. Jin, C. Y. Park, Y. H. Lee; "X-ray absorption spectroscopy of graphite oxide"; *EPL*, 82, (2008); pp: 67004. DOI: 10.1209/0295-5075/82/67004

[41] D.C. Sorescu, K.D. Jordan, P. Avouris; "Theoretical Study of Oxygen Adsorption on Graphite and the (8,0) Single-walled Carbon Nanotube"; *J. Phys. Chem. B*, 105, (2001); pp: 11227-11232. DOI: 10.1021/jp0122979

[42] M.J. Webb, P. Palmgren, P. Pal, O. Karis, H. Grennberg; "A simple method to produce almost perfect graphene on highly oriented pyrolytic graphite"; *Carbon*, 49, (2011); pp: 3242-3249. DOI: 10.1016/j.carbon.2011.03.050

[43] B. Rousseau, H. Estrade-Szwarckopf, A.-L. Thoman, P. Brault; "Stable C-atom displacements on HOPG surface under plasma low-energy argon-ion bombardment"; *Appl. Phys. A*, 77, (2003); pp: 591-597. DOI: 10.1007/s00339-002-1538-x

[44] D. Yang, A. Velamakanni, G. Bozoklu, S. Park, M. Stoller , R.D. Piner, S. Stankovich, I. Jung, D.A. Field, C.A. Ventrice Jr., R.S. Ruoff; "Chemical analysis of graphene oxide films after heat and chemical treatments by X-ray photoelectron and Micro-Raman spectroscopy"; *Carbon*, 47, (2009); pp: 145-152. DOI: 10.1016/j.carbon.2008.09.045

[45] K. Haubner, J. Murawski, P. Olk, L. M. Eng, C. Ziegler, B. Adolphi, E. Jaehne; "The route to functional graphene oxide"; *Chem. Phys. Chem.*, 11, (2010); pp: 2131-2139. DOI: 10.1002/cphc.201000132.

[46] M. Abbate, J. B. Goedkoop, F. M. F. de Groot, M. Grionit, J. C. Fuggle, S. Hofmann, H. Petersen, M. Sacchi; "Probing Depth of Soft X-ray Absorption Spectroscopy Measured in Total-electron-yield Mode"; *Surf. Interface Anal.*, 18, (1992); pp: 65-69. DOI: 10.1002/sia.740180111

[47] J.-C. Dupin, D. Gonbeau, P. Vinatierb, A. Levasseur; "Systematic XPS studies of metal oxides, hydroxides and peroxides"; *Phys. Chem. Chem. Phys*. 2, (2000); pp: 1319-1324; DOI: 10.1039/a908800h

[48] M. Oku, Y. Sato; "*In situ* X-ray photoelectron spectroscopic study of the reversible phase transition between CoO and Co3O4 in oxygen of 10−3 Pa"; *Appl Surf Sci*., 55, (1992); pp 37-41. DOI: 10.1016/0169-4332(92)90378-B

[49] J. van Elp, J. L. Wieland, H. Eskes, P. Kuiper, G. A. Sawatzky, F. M. F. de Groot, T. S. Turner;" Electronic structure of CoO, Li-doped CoO, and $LiCoO_2$"; *Phys. Rev. B*, 44, (1991); pp: 6090-6103. DOI: 10.1103/PhysRevB.44.6090

[50] C.-H. Ho, C.-P. Tsai, C.-C. Chung, C.-Y. Tsai, F.-R.Chen, H.-J. Lin, C.-H. Lai; "Shape-Controlled Growth and Shape-Dependent Cation Site Occupancy of

Monodisperse Fe3O4 Nanoparticles"; *Chem. Mater*. 23, (2011); pp: 1753-1760. DOI: 10.1021/cm102758u

[51] J. Park, K. J. An, Y. S. Hwang, J. G. Park, H. J. Noh, J. Y. Kim, J. H. Park, N. M. Hwang, T. Hyeon; "Ultra-large-scale syntheses of monodisperse nanocrystals"; *Nat. Mater*. 3, (2004); pp: 891-895. DOI: 10.1038/nmat1251

[52] S. A. Chambers, S. A. Joyce; "Surface termination, composition and reconstruction of Fe_3O_4 (001) and γ-Fe_2O_3(001)"; *Surf. Sci.*, 420, (1999); pp: 111-122. DOI: 10.1016/S0039-6028(98)00657-8

[53] C. Sarah, E. M. Petitto, G. A. C Marsh, A. L. Marjorie; "Cobalt oxide surface chemistry: The interaction of CoO(1 0 0), Co_3O_4(1 1 0) and Co_3O_4(1 1 1) with oxygen and water"; *J. Mol. Catal. A-Chem.* 281, (2008); pp: 49-58; DOI: 10.1016/j.molcata.2007.08.023

[54] A. Ganguly, S. Sharma, P. Papakonstantinou, J. Hamilton; "Probing the Thermal Deoxygenation of Graphene Oxide Using High-Resolution *In situ* X-ray-Based Spectroscopies"; *Phys. Chem. C*, 115, (2011); pp: 17009-17019. DOI: 10.1021/jp203741y

[55] C. Hontoria-Lucas, A. J. Lopez-Peinado, J. D. Lopez-Gonzalez, M. L. Rojas-Cervantes, R. M. Martin-Aranda; "Study of oxygen-containing groups in a series of graphite oxides: Physical and chemical characterization"; *Carbon*; 33, (1995); pp: 1585. DOI: 10.1016/0008-6223(95)00120-3

[56] O. Akhavan; "The effect of heat treatment on formation of graphene thin films from graphene oxide nanosheets"; *Carbon*, 48, (2010); pp: 509 - 519. DOI: 10.1016/j.carbon.2009.09.069

[57] S. J. Sque, R. Jones, P. R. Briddon; "The transfer doping of graphite and graphene"; *Phys. Stat. Sol.* 204, (2007); pp: 3078-3084; DOI: 10.1002/pssa.200776313

[58] H. Hibino, H. Kageshima, M. Kotsugi, F. Maeda, F.-Z. Guo, Y. Watanabe; "Dependence of electronic properties of epitaxial few-layer graphene on the number of layers investigated by photoelectron emission microscopy"; *Phys. Rev. B*, 79, (2009); PP: 125437. DOI: 10.1103/PhysRevB.79.125437

[59] X. Wang, Q. Peng, W. Zhu, G. Lei; "High performance of inverted polymer solar cells with Cobalt oxide as hole-transporting layer"; *Semicond. Sci. Technol*. 30, (2015); pp: 055001. DOI: 10.1088/0268-1242/30/5/055001

[60] D. Martinez-Martin, R. Longuinhos, J. G. Izquierdo, A. Marele, S. S. Alexandre, M. Jaafar, J. M. Gómez-Rodriguez, L. Bañares, J. M. Soler, J. Gomez-Herrero; "Atmospheric contaminants on graphitic surfaces"; *Carbon*, 61, (2013); pp: 33-39. DOI: 10.1016/j.carbon.2013.04.056

[61] G. C. McGonigal, R. H. Bernhardt, D. J. Thomson; "Imaging alkane layers at the liquid/graphite interface with the scanning tunneling microscope"; *App. Phys. Lett*., 57, (1990); pp: 28-30. DOI: 10.1063/1.104234

[62] D. S. Wastl, F. Speck, E. Wutscher, M. Ostler, T. Seyller, F. J. Giessibl; "Observation of 4 nm Pitch Stripe Domains Formed by Exposing Graphene to Ambient Air"; *ACS Nano*, 7, (2013); pp: 10032-10037. DOI: 10.1021/nn403988y

Chapter 4

Interaction of ZnO with HOPG and CVD graphene

"Normal science, the puzzle-solving activity we have just examined, is a highly cumulative enterprise, eminently successful in its aim, the steady extension of the scope and precision of scientific knowledge."

Thomas Kuhn

4.1 Introduction

The present chapter summarizes the results regarding the growth of ZnO on two different graphitic substrates, HOPG and CVD graphene grown on polycrystalline copper. The chapter is divided into two parts, the first one regarding the HOPG and, subsequently, the graphene. Although the motivation of the study was driven on the interaction between the oxide and the graphene, the study on HOPG serves as a link to the previous CoO/HOPG research and of course, it has been performed for comparison purposes with the graphene case. The first monolayer of HOPG is atomically equivalent to that of graphene thus, differences on the ZnO growth between both substrates will be related to the number of stacking graphene sheets and interaction among them with the rest of the surface. While graphite can be though as a bulk graphene, for the case of graphene the most influential factor is going to be related to the electronic interaction between graphene atomic layer and the metallic substrate.

Both, ZnO and graphene are materials exhibiting unique physical and chemical properties, in particular, transparency and conductivity. Since its discovery in 2004 [1], graphene has been one of the most discussed topics on the first decades of the 21st century, and has meant a turning point on the study and application of 2D materials. In this sense, the very high ballistic transport distances of the order of the micron and the very large carrier mobility [2,3,4] combined with the absorption of only 2.3% of visible light [5], places graphene as an extraordinary candidate for new optoelectronic devices. In addition, graphene impermeability to most gases [6] makes it also a promising candidate for ultrathin passivation coating [7]. On the other hand, ZnO is a wide band gap semiconductor (3.3 eV) with a large exciton binding energy (60 meV) [8]. In addition,

high levels of charge carriers can be introduced into ZnO by heavy substitutional doping (n-type) while preserving good values of transparency. This converts ZnO in a very interesting transparent conducting oxide [9,10]. The combination of the properties of graphene and ZnO gives rise to the fabrication of devices used in many important technological applications such as in optoelectronics [11], sensors [12], lithium-ion batteries [13] and solar cells [14]. In general, the growth methods used in these technologies are performed at high temperatures (> 400 °C), and in fact, the local substrate temperature determines the type of nanostructure obtained [15].

However, this idealistic view of combining graphene and ZnO (or in general other materials) contrasts with the scarce number of real applications in industry and/or mass electronic devices. Without doubt, this frustrating fact is related to the difficulty to grow large areas of non-defective graphene, but also with the complexity of the interaction of graphene with other materials (substrates, multilayer systems) and/or media (gas, liquids) in contact with it, which leads to changes on the graphene properties.

In this sense, the substrate plays a very important role in the electronic properties shown by graphene by means of the strength on the bonding between both. According to Robert S. Weatherup et. al. [7] for the case of metals, depending on the position of the d valence band states respect to the Fermi level [16], two different interactions are reported. In the case of Ni, Co, Fe, or Pd, the strong hybridization between π graphene states and metal d states leads to the destruction of the linear dispersion of graphene at the K point, whereas for weak interaction, such as for Cu, Au, Ag, Pt, this linearity is preserved but charge transfer between metal and graphene normally shifts the Fermi level position, i.e. doping of graphene. For SiC (0001) substrate, a covalent bonding between the substrate and the first carbon layer will prevent the good electrical properties of graphene [17,18]. In all these cases, this interaction can be modulated or suppressed by controlled intercalation of metallic atoms at high temperatures [19,20], even at room temperature for alkaline elements [21,22], or by the formation of an oxidized layer between substrate and graphene [23].

The majority of the experimental and theoretical aforementioned studies regarding electronic properties of graphene, assume a very good environmental control without the influence of any kind of chemical species present in air, such as organic molecules, water or even just oxygen. This fact implies that the description of the last paragraph remains as a simplified view of the realistic properties of graphene. As it was previously discussed,

for some metals such as Ni or Co [7], graphene acts as a good passivation coating, inhibiting the intercalation of oxygen and water and preserving the metal from oxidation. This circumstance makes real the previous assumption of no environmental perturbation. However, a wide range of reports show how for copper substrates the exposure to air conditions can lead to oxygen and water intercalation [24,25] via the edges and defects of graphene, eventually giving rise in the long term to more metal oxidation in comparison to not graphene containing surfaces [26]. Furthermore, by increasing the humidity and/or temperature, this oxidation process of the copper substrate can be accelerated, leading to the formation of a few nm film of Cu_2O, which enables the electronic decoupling of the graphene from metal copper [27,28]. In this manner, two different but correlated factors can modify the graphene properties (and interaction) as a function of time: the substrate and the environment. The possibility of adding a third parameter able to also disturb the electronic structure of graphene, such the deposition of a thin film layer on the top of graphene, can make even more difficult to understand the full picture. Besides, the control of these three parameters and the understanding of the interrelations among them becomes essential for real graphene-based devices and other applications.

The fundamental interaction between ZnO and graphene started to be studied in the recent years. In particular, there is an increasing interest in obtaining a free-standing single ZnO monolayer [29] because it could preserve similar properties as graphene [30,31], due to quantum confinement effect [32]. To our knowledge, a single layer of ZnO has been grown by ALD [33]. Nevertheless, the strongly hydrophobic character of graphene makes difficult to grow semiconductor metal oxides, and forces to an initial functionalization of the graphene surface via UV/ozone treatment [33,34]. This kind of treatments can damage the graphene and modify its properties, what at the end of the day it is not recommendable, especially if the final device is looking for the combination and potential emergent properties of both, graphene and semiconductors metal oxides. Furthermore, as it was previously pointed out, the usual modes of growth of ZnO imply the use of high temperatures (> 400 °C). However, for industrial processing of devices, room temperature conditions are desirable in order to preserve other materials of the device (such as graphene), reduce diffusion between components and ultimately reduce costs.

On the basis of the previous discussion, the main motivation of the present chapter is the study of the early stages of growth of ZnO on graphene grown by CVD on

polycrystalline copper, but unlike previous investigations, taking into account the cross relationships and influences of graphene, substrate, environment and oxide thin film. For this reason, thermal evaporation of metal zinc under oxygen atmosphere (10^{-3} mbar) at room temperature has been chosen in order to ensure quasi-equilibrium growth conditions. However, and in spite of the interest on basic research regarding the early stages of growth and the interaction between both materials at the interface level, there exists a lack of studies performed by this method, which actually preserves the original substrate. One reason could be the contaminant character of zinc for ultra-high vacuum systems, due to its high vapor pressure. The growth of ZnO on HOPG has been also performed for obvious comparison purposes, paying special attention to the interaction and the interface formed between these materials. In addition, and related with the previous Chapter 3, the re-oxidation of ZnO/HOPG under different conditions has been investigated looking for catalytic behavior of the ZnO deposit, in a similar way to CoO.

This chapter is structured in two main blocs. First, in section 4.2 the interaction between ZnO and HOPG will be described. It is divided into two subsections, 4.2.1 dedicated to the study of the early stages of growth of the oxide on the HOPG and subsection 4.2.2 where the ZnO/HOPG re-oxidation is discussed. The early stages of growth will be quantitative and qualitative investigated from the chemical and morphological points of view using XPS, AFM and SEM measurements. In addition, the chemical interaction between both, oxide and substrate will be discussed in more detail. Regarding the re-oxidation process, it will be mainly studied through *in situ* XPS and *ex situ* Raman spectroscopy. The second bloc regarding the ZnO interaction with graphene on copper constitutes section 4.3. As before, section 4.3.1 summarizes the main results related to the early stages of growth of ZnO on this substrate, doing such chemical and morphological characterization by means of XPS, AFM and SEM measurements. The second subsection 4.3.2 presents the chemical and structural characterization of the as received graphene on polycrystalline copper studying how the nano and micrometric inhomogeneities of the substrate could influence on the later growth of ZnO. This study was carried out mainly by XPS, XPEEM and Raman spectroscopy, although some AFM and SEM measurements completed the characterization. Finally, this bloc is closed with the last subsection 4.3.3, where the interaction between ZnO, graphene and copper is discussed in terms of the electronic decoupling as a consequence of ZnO deposition. For comparison purposes, this electronic decoupling of graphene from the metallic substrate has been also induced by water immersion of the graphene/Cu sheet. This study has been

carried out basically by XPS, Raman spectroscopy and TEM-EDX measurements. Precisely, this last subsection condenses the discussion of the cross interaction between the ZnO deposit, graphene, copper and the chemical environment. A qualitative model of the chemical process which allows the electronic decoupling between graphene and copper through the ZnO deposition is suggested. Finally, the chapter is closed with a final section 4.4 of conclusions.

4.2 Interaction of ZnO with graphite

4.2.1 Early stages of growth of ZnO on HOPG substrates

This first section devoted to the growth of ZnO on HOPG summarizes the main results of the morphological and chemical characterization of the mode of growth was performed using *in situ* XPS and *ex situ* AFM and SEM measurements. The interaction between both oxide and graphite was deeply studied by XPS as a function of the coverage.

4.2.1.1 Quantitative chemical analysis

As stated previously in Chapter 2 "Experimental details", section 2.6.1.2, the chemical analysis was performed by successive evaporations of ZnO on the same HOPG substrate, being the sample analyzed *in situ* by XPS for each step. Figure 4.1 shows the XPS survey (a) and Zn LMM (b) spectra as a function of the coverage given in equivalent monolayers (Eq-ML). The survey spectra evolution reflects the expected behavior of a growth process. The clean substrate shows only regions referred to carbon from the graphite, highlighting the C 1s regions which well be later discussed in detail. Negligible traces of oxygen were measured after the graphite cleavage in air. The atomic sensibility factor of Zn 2p contribution is much larger than the one for C 1s (about 11 times). This implies a very strong signal for ZnO even for very low equivalent coverages. As it can be seen, just for 1.3 Eq-ML (this is just 3.4 Å) the Zn LMM Auger contribution from the ZnO has almost the same intensity than the C 1s contribution. A potential issue was the overlapping between the zinc Auger signal and the C 1s and O 1s contributions. However, by changing the X-ray source anode (Al or Mg) this issue could be overcome. For the largest coverages, only ZnO contributions were visible. At this moment the growth experiment was considered finished. On the other hand, Figure 4.1 b depicts the evolution of the Zn LMM Auger contribution with the coverage, which gives chemical information regarding the oxidation state of zinc, while the Zn 2p is almost the same for the metal and

oxide compounds. There is no variation in the spectra, remaining the same shape that corresponds to the presence of ZnO (metal Zn and ZnO reference spectra can be found in section 2.1.2.1). The only difference observed is the signal to noise ratio, as corresponds to the amount of material contributing to the XPS signal in each step

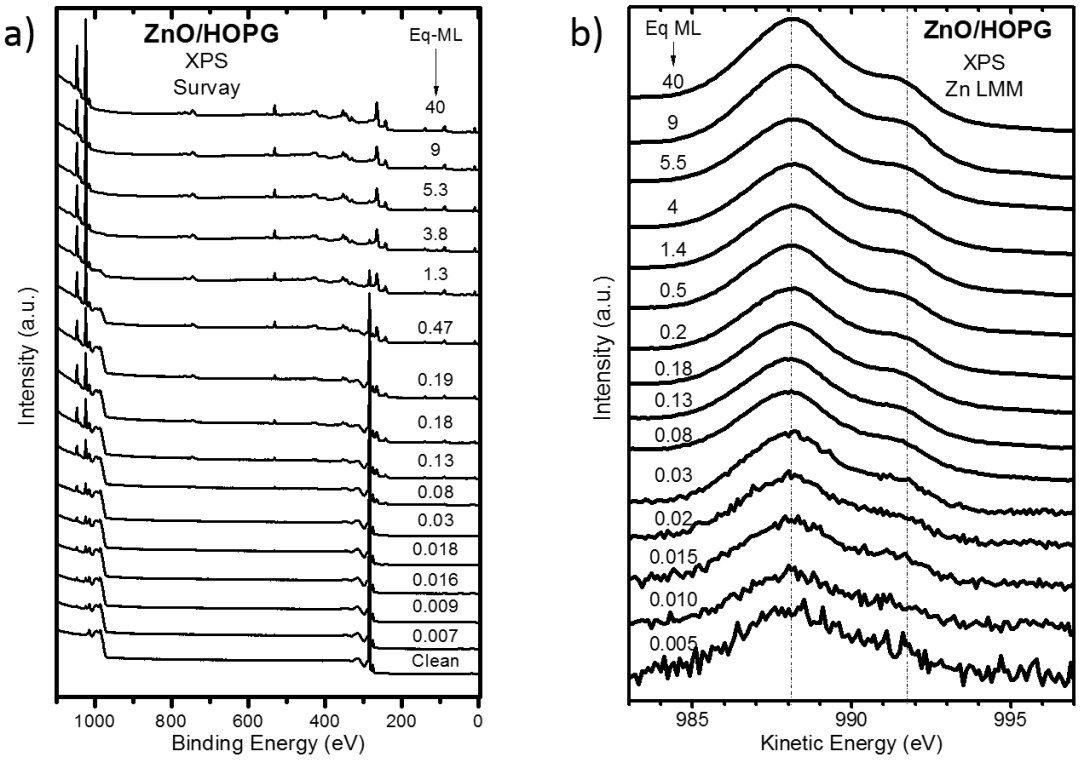

Figure 4.1 a) XPS survey spectra and b) Auger Zn LMM XPS spectra as a function of the coverage for the growth of ZnO on HOPG.

Intensities of the Zn $2p_{3/2}$ and C 1s peaks are represented in Figure 4.2 as a function of the evaporation time. The deposition rate was maintained constant and the XPS peak intensities shown in this figure follow the expected behavior according to an exponential growth mechanism, where the intensity of the deposited material is given by $I = I_o\left(1 - e^{-Dt/\lambda}\right)$ and the intensity of the substrate by $I = I_o e^{-Dt/\lambda}$, where I_o is the maximum intensity of a bulk reference sample of the material, D the deposition rate and λ is the inelastic electron mean free path [35]. The curves of the intensities roughly show two different rates of growth: a slow growth rate for the early stages governed by the nucleation process, and a much faster growth rate for the intermediates and final stages. An estimation of the growth rate using the XPS data is difficult and may be not realistic since it is known that the morphology of the deposits strongly influences the simple

quantitative analysis. However, values as 0.05 and 2.0 Eq-ML/min for both ranges of growth have been calculated using the previous formulas, showing impressive differences between both regimes. For these estimations, we have used values for the inelastic mean free path of $\lambda = 19.6$ Å for the C 1s peak through a ZnO matrix and $\lambda = 7.5$ Å for the Zn 2p peak through a ZnO matrix. These results are consistent with a slow growth of ZnO nucleation centers on the HOPG surface, followed by a rapid increase of the growth of ZnO when the coverage of the surface has significantly increased. Besides, these results were supported by AFM and SEM measurements. The saturation of the Zn 2p signal together with the disappearance of the C 1s signal are consistent with the growth of a ZnO thin films with a thickness larger than the three times inelastic mean free path of the elements (> 60Å), where the signal of the 95% of the elastic photoemitted electrons comes from.

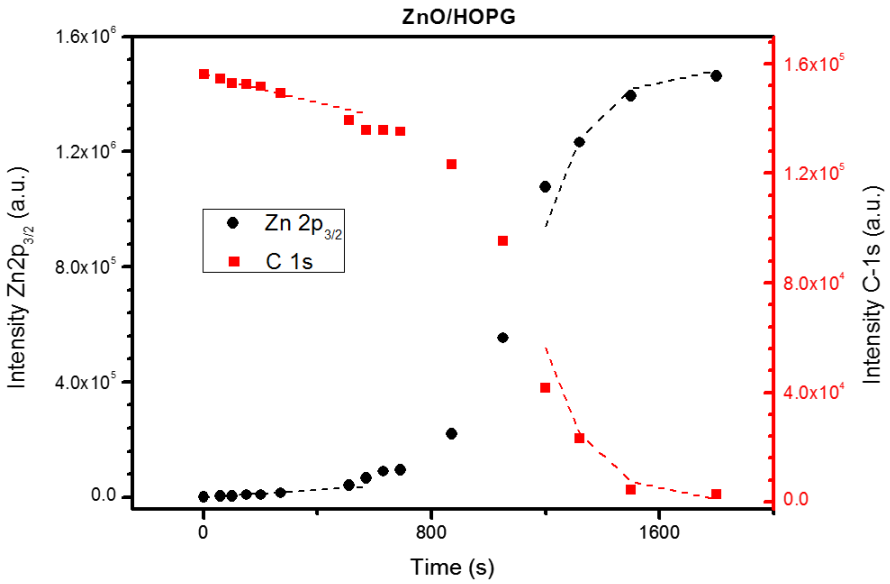

Figure 4.2 Evolution of the intensities of the Zn 2p 3/2 (black dots) and C 1s (red squares) as a function of the evaporation time for the growth of ZnO on HOPG.

Factor analysis (FA) with Target Testing procedure, as explained in section 2.5.1.1 of Chapter 2, has been used to estimate the relative quantity of metallic Zn and ZnO for each deposition step. The results of FA applied to the spectra of the deposits on HOPG are depicted in Figure 4.3. As main components, the experimental spectra of the reference Zn and ZnO samples have been proposed (Figure 4.3 a dots). The recalculated components (solid line) show an excellent agreement with the experimental spectra,

indicating the goodness of the proposed components. Figure 4.3 b shows the experimental (dots) and calculated (solid line) spectra for each step of growth, showing again good agreement. Figure 4.3 c shows the concentration of each component or, in other words, the relative amount of ZnO and metallic Zn in the sample. As shown, the concentrations for ZnO are approximately 1.0 for all coverages whereas for metallic Zn the corresponding values approach to zero, which indicates that Zn atoms are completely oxidized and ZnO is formed upon evaporation of metallic Zn in oxygen atmosphere on HOPG at room temperature.

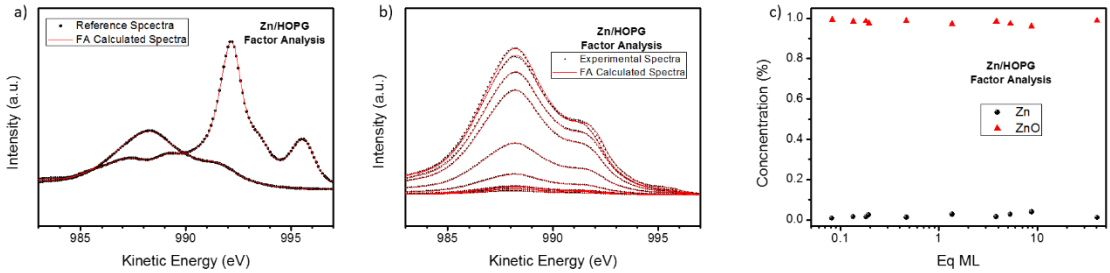

Figure 4.3 Results of factor analysis for the growth of ZnO/HOPG: a) proposed and calculated components used in factor analysis; b) fittings of the experimental spectra using a linear combination of the proposed components; c) concentration for each of the components as a function of the coverage.

4.2.1.2 Quantitative morphological analysis

The analysis of the morphology during the growth was performed through *ex situ* AFM and SEM measurements. To this end, several samples with different coverages were prepared. In this way, 30x30 μm^2 AFM images for different coverages of ZnO on HOPG are shown in Figure 4.4. ZnO forms big clusters (1-3 μm), preferably on the HOPG steps, keeping almost clean the terraces. Anyhow, some clusters also grow on the graphite terraces. Further coverages lead to the increase of the size (5 μm) of the clusters as well as the appearance of new nucleation centers on the terraces. Finally, for large coverages (>40 Eq-ML), coalescence of the clusters, forming a micro-structured ZnO film, is produced. Therefore, the way of growth followed the Volmer-Weber mode. The above results are consistent with a large diffusion of metallic Zn atoms throughout the HOPG surface with the formation of little nucleation centers, leading to a microstructure formed by micrometric clusters upon coalescence. In fact, this AFM conclusions are perfectly

coherent with the previous analysis regarding the evolution of the intensities of the Zn $2p^{3/2}$ and C 1s peaks with the deposition time.

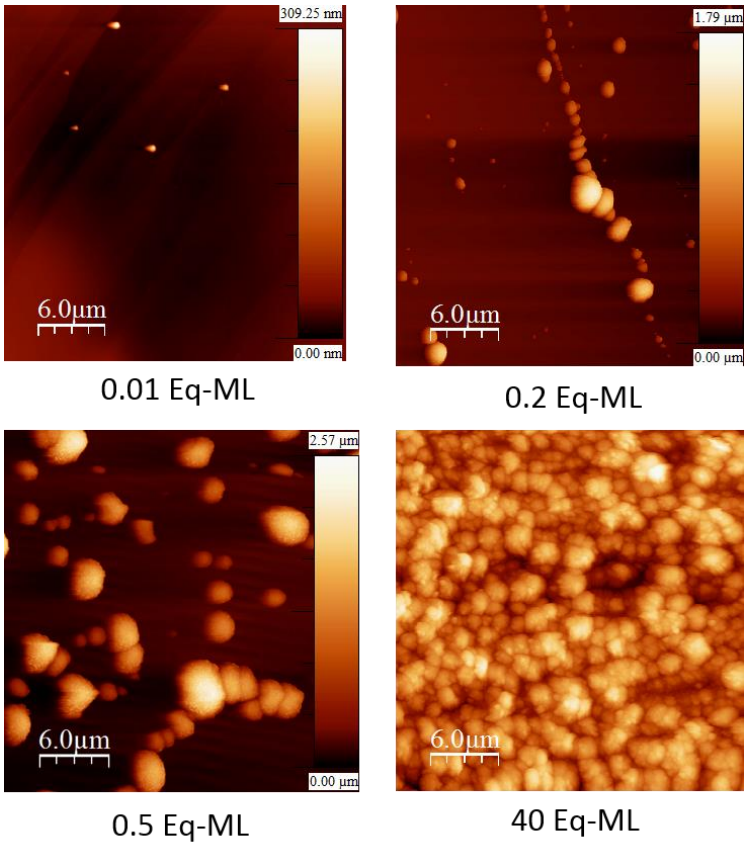

Figure 4.4 30x30 μm^2 AFM images for different stages of growth of ZnO on HOPG

On the other hand, SEM images are shown in Figure 4.5, matching completely the above AFM images. The preferential growth of the clusters on the steps is now much more evident. The SEM images give the same lateral sizes of the nanostructures as those given by AFM. Besides, Figure 4.6 shows images of the two types of nanostructures formed upon deposition of ZnO on HOPG: clusters (top images) and caterpillars (bottom images). The clusters are initially formed at the terraces and above some steps and show a radial growth from the nucleation center, clearly observed in the image of the bottom of the cluster in Figure 4.6 (right-top). In a different way caterpillars, which mainly grow on the HOPG steps, show a lateral growth from the step edge, as observed in Figure 4.6 (right-bottom). In fact, the shape of the bottom side of these nanostructures seems to have the mold of the step from where they have grown marked in its shape.

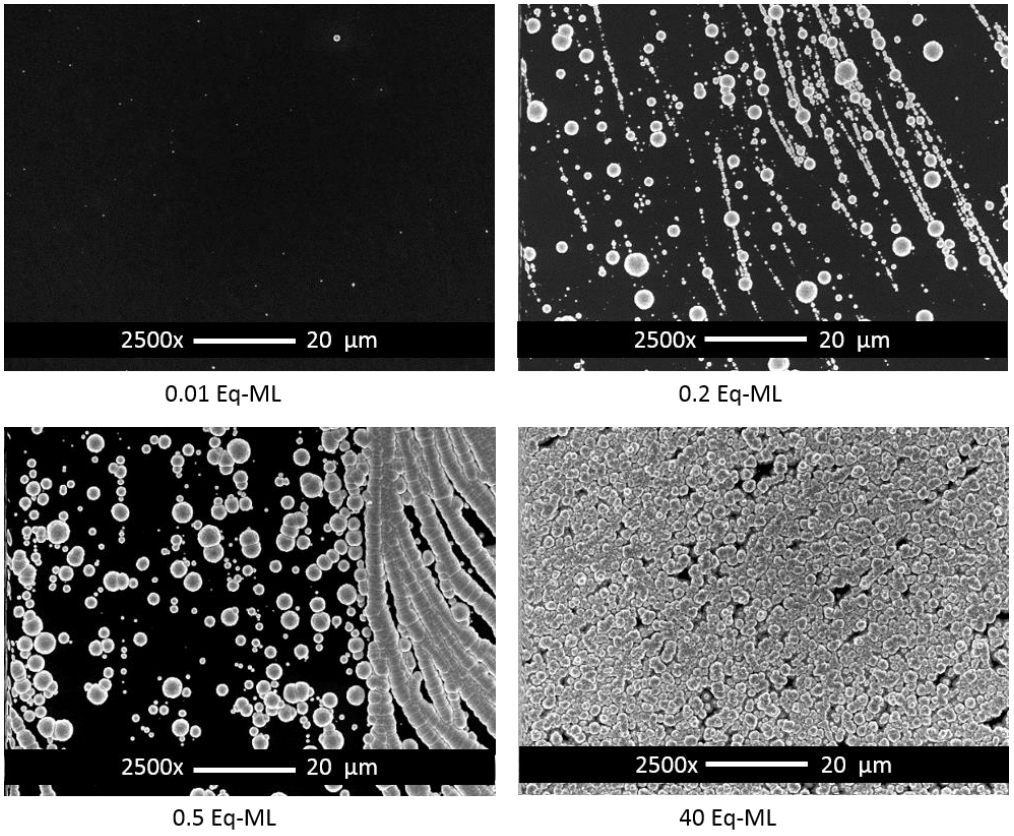

Figure 4.5 2500x magnification SEM images for different stages of growth of ZnO on HOPG.

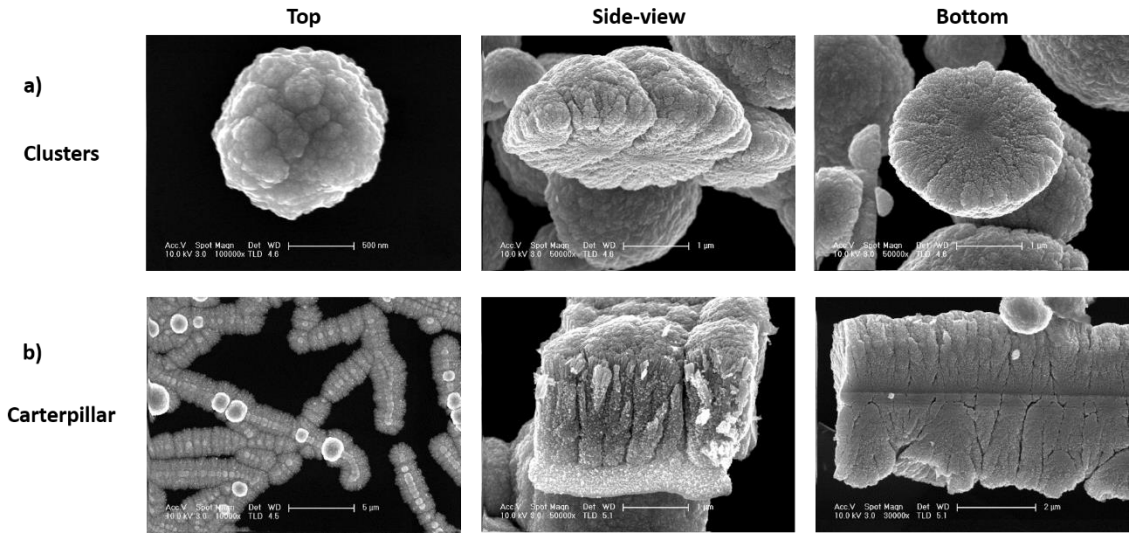

Figure 4.6 SEM images of the different ZnO nanostructures formed on the HOPG substrate: a) clusters; b) caterpillar-like.

Finally, an inelastic peak shape analysis of the XPS survey spectra has been performed by using QUASES software (see section 2.5.1.2 of Chapter 2). The results obtained by this method are usually represented by the variation of the height of the nanostructures as a function of the coverage, as shown in Figure 4.7. In this case, the "islands model" has been used by analyzing the Auger O KLL peak as measured with the Mg anode, assuming that all oxygen atoms in the sample are bonded to Zn, and thus forming ZnO. For this peak, the inelastic mean free path of the electrons is 12.6 Å. However, the nanostructures formed on HOPG, as seen by AFM, give height values of about 1 μm, which is up to thousands times larger than the inelastic mean free path of the photoelectrons. As consequence, the real height of the islands cannot be resolved by this method. However, the model agrees with the formation of islands, i.e. confirming a Volmer-Weber mode of growth. The arrow drawn in the top left corner of Figure 4.7 means that the growing islands are at least three times the value of the inelastic mean free path of the photoelectrons, as more than 90% of the measured photoemitted electrons come from this depth.

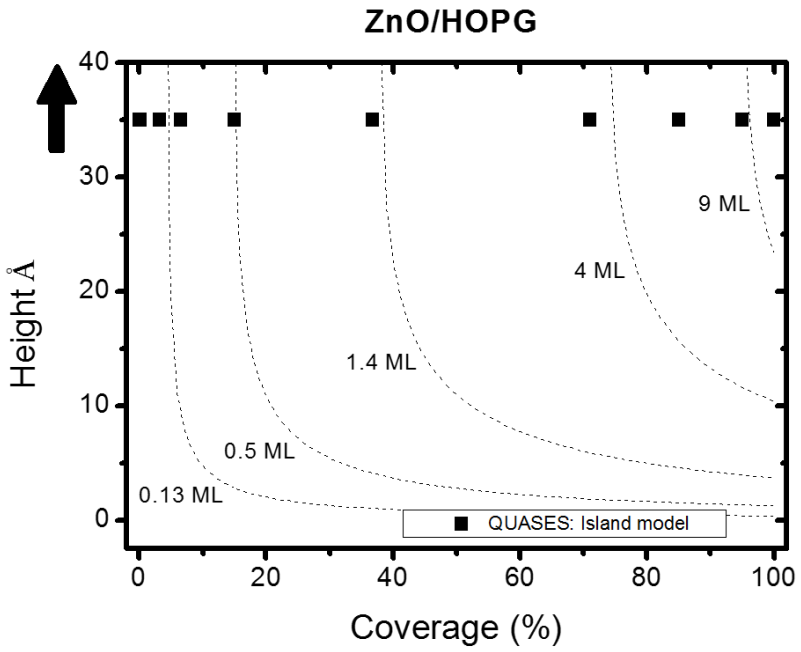

Figure 4.7 Results for the inelastic peak shape analysis for the growth of ZnO on HOPG.

4.2.1.3 Chemical analysis: ZnO/HOPG interaction

Now is time to discuss in more detail the chemical interaction between the ZnO and the substrate, which has been studied by *in situ* XPS measurements. Focusing in first

term on the deposited film, Figure 4.8 shows the XPS Zn $2p_{3/2}$ spectra as a function of deposition time and coverage. As it can be appreciated, the Zn $2p_{3/2}$ contribution is around

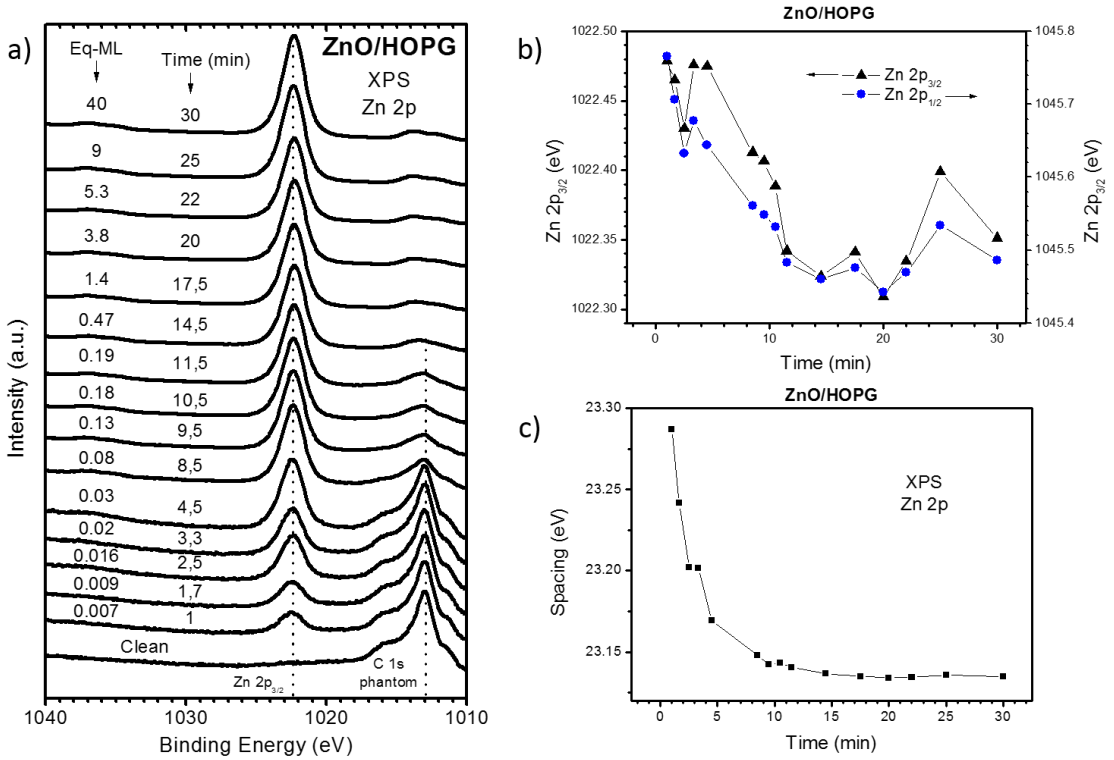

Figure 4.8 a) XPS Zn $2p_{3/2}$ spectra as a function of the coverage for the growth of ZnO on HOPG; b) Zn $2p_{3/2}$ and Zn $2p_{1/2}$ shifts as a function of deposition time; c) Zn 2p spin-orbital spacing (S-O) as a function of the deposition time.

1022.4 eV [36]. The phantom peak of the C 1s due to the oxidation of the magnesium anode initially dominates at an energy of ~1006 eV. The deposited ZnO has practically a perfect Zn/O composition rate of 1:1, as stated before by FA. However, some interesting features can be extracted from this region, as those shown on Figure 4.8 b and c for the energy shift of both Zn $2p_{3/2}$ and Zn $2p_{1/2}$ peaks and the energy spacing between both, i.e. the S-O interaction, respectively. As it can be appreciated, there is a tiny shift of about 0.2-0.3 eV to lower binding energies from the very first growth stages (lower than 0.2 Eq-ML). Besides, the energy separation between these two contributions clearly decrease 0.15 eV as a function of the deposition time, and thus as a function of the coverage and size of the ZnO clusters, until its stabilization at roughly 23.13 eV, which in fact is the value obtained from the ZnO reference sample (see section 2.1.2.1 of Chapter 2). These behaviors could be related to size effects of the ZnO clusters, as previously reported for

CoO on the previous chapter and other elements on different substrates [37,38,39]. Although the size of the ZnO structures shown in Figures 4.4 and 4.5 is enough to be considered as bulk, it is also true that structures smaller than 5 nm could be found for lower coverages than 0.2 Eq-ML, precisely when the nucleation process is more limited and less big clusters can be found. Therefore, these nanometric structures could influence on the Zn 2p spectrum for coverages lower than 0.2 Eq-ML.

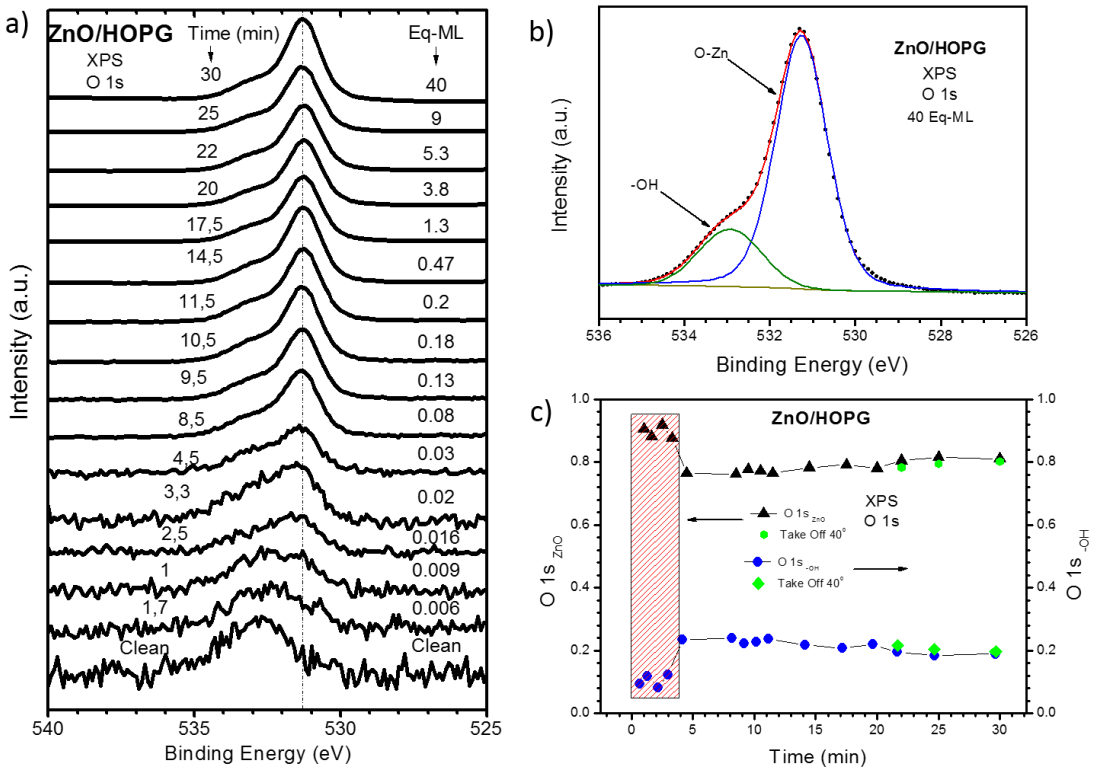

Figure 4.9 a) XPS O 1s spectra as a function of the coverage for the growth of ZnO on HOPG; b) XPS O 1s fitting for 40 Eq-ML of ZnO on HOPG; c) relative intensities of O-ZnO and defects/OH^- components as a function of the deposition time.

On the other hand, Figure 4.9 shows the XPS O 1s spectra as a function of the coverage. The clean HOPG substrate shows a very weak and depreciable peak at ~ 532.8 eV which is associated to absorbed oxygen on the graphite structure. In the case of bulk ZnO, as it is shown in Figure 4.9 b for the 40 Eq-ML coverage, the O 1s spectrum has two contributions. The main peak at 531.3 eV is associated to O-Zn bonds, while the shoulder at 533.0 eV can be associated to hydroxides groups [40,41] and defects related to oxygen atom vacancies in the matrix [42,43]. Figure 4.9 c depicts the relative weight

between these two contributions as a function of the deposition time. The values are gradually stabilized on 0.8 and 0.2 for the O-Zn and OH^- contributions, respectively, which is in agreement with the literature [40]. Two details of this last figure can be highlighted. Firstly, the last coverages were taken at two different take-off angles, increasing the relative amount of the OH^- contribution with the angle. This fact indicates its surface nature, in agreement with the reported termination of some ZnO facets, such as (0001) and (000-1), on OH^- groups for their thermodynamic stabilization [44]. Secondly, in the very early stages of growth (marked by the red striped box) the O-Zn contribution seems overestimated. The overlapping between the O-HOPG and OH^- made very difficult to obtain the correct fitting of this region at the very beginning.

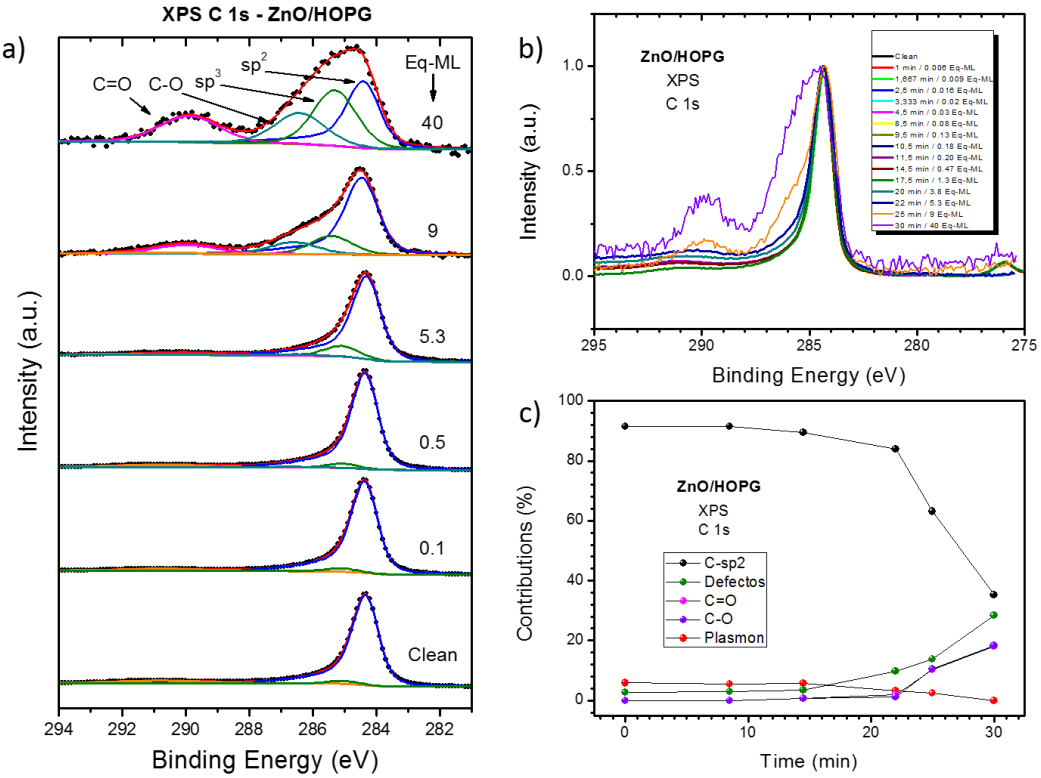

Figure 4.10 a) XPS C 1s fitted spectra as a function of the coverage for the growth of ZnO on HOPG; b) normalized XPS C 1s spectra as a function of the coverage and deposition time; c) relative intensities of the C 1s spectra components as a function of the deposition time.

Finally, XPS C 1s spectra are shown in Figures 4.10 a and b as a function of the coverage. Figure 4.10 a depicts a selection of fitted spectra for different ZnO coverages,

showing no negligible evolution of defects (sp^3 contribution [45]) and graphite oxides (C-O and C=O [46,47]) from the initial asymmetric peak corresponding to sp^2 hybridization [48]. Figure 4.10 b offers this same information by comparing the normalized shape of the C 1s peak for all the spectra of the series. Therefore, the deposition of ZnO induces the development of defects on the graphite substrates and its oxidation. Due to the large micrometric size of the ZnO clusters, the measured HOPG signal comes from the free surface, not from below the ZnO structures. Hence, in this case XPS is not the best technique for the study of the interface between oxide and substrate. The only worthy information we can obtain is the confirmation that, as for the case of cobalt, some kind of interaction was taking place between both materials that partially extends beyond the specific localization of the clusters. Most probably, the defects could be created while travelling the Zn adatoms throughout the HOPG substrate towards the steps or big clusters.

4.2.2 Re-oxidation process: ZnO/HOPG

For comparison purposes with CoO grown on HOPG, ZnO/HOPG samples of 0.2 Eq-ML coverage were submitted to different re-oxidation process, R1 and R2, as described in section 2.6.2 of Chapter 2. The aim was to study the interaction between the oxide and the graphitic substrate, and describe the morphological and chemical changes on both (ZnO deposits and substrate).

4.2.2.1 *In situ* study: XPS

In this re-oxidation experiment up to five ZnO/HOPG samples of 0.2 Eq-ML were used. Each of them were submitted to a specific treatment: as grown, exposed to oxygen at two different pressures for one hour (10^{-5} mbar and 10^{-3} mbar, same sample) at room temperature (RT), heated up to 400 ºC in UHV conditions for one hour and re-oxidized following R1 (heated up to 400 °C under UHV conditions and then exposed to O_2 for one hour after achieving that temperature) and R2 (exposed to O_2 and then heated up to 400 °C) recipes. For both R1 and R2 cases the oxygen pressure used was 10^{-5} mbar in order to be able to use the mass spectrometer of the preparation chamber.

Figure 4.11 a shows the Zn LMM Auger spectra after these six different treatments. As it can be seen, although for all cases the oxide spectrum dominates, the as grown and exposed to O_2 at RT samples present two features at ~992 and ~995 eV

characteristic of the metal, indicating the development of defects and oxygen vacancies during the growth, probably due to the use of lower oxygen pressure. However, these minor contributions disappear independently of the thermal treatment used. Figure 4.11 b shows the O 1s normalized spectra, including the one taken from ZnO powder reference. As it can be appreciated, after the thermal treatment the main peak is shifted 0.5 eV to lower binding energies. Nevertheless, the most striking effect consists on the intensity decrease of the shoulder associated to hydroxides or defects. In agreement with the previous discussion of the Zn LMM Auger spectra, it seems that the reduction of this shoulder can be associated to the decrease of the number of oxygen vacancies [43]. Finally, Figure 4.11 c shows the XPS C 1s spectra of the HOPG substrate. Unlike for the case of cobalt, no changes on the graphite are observed.

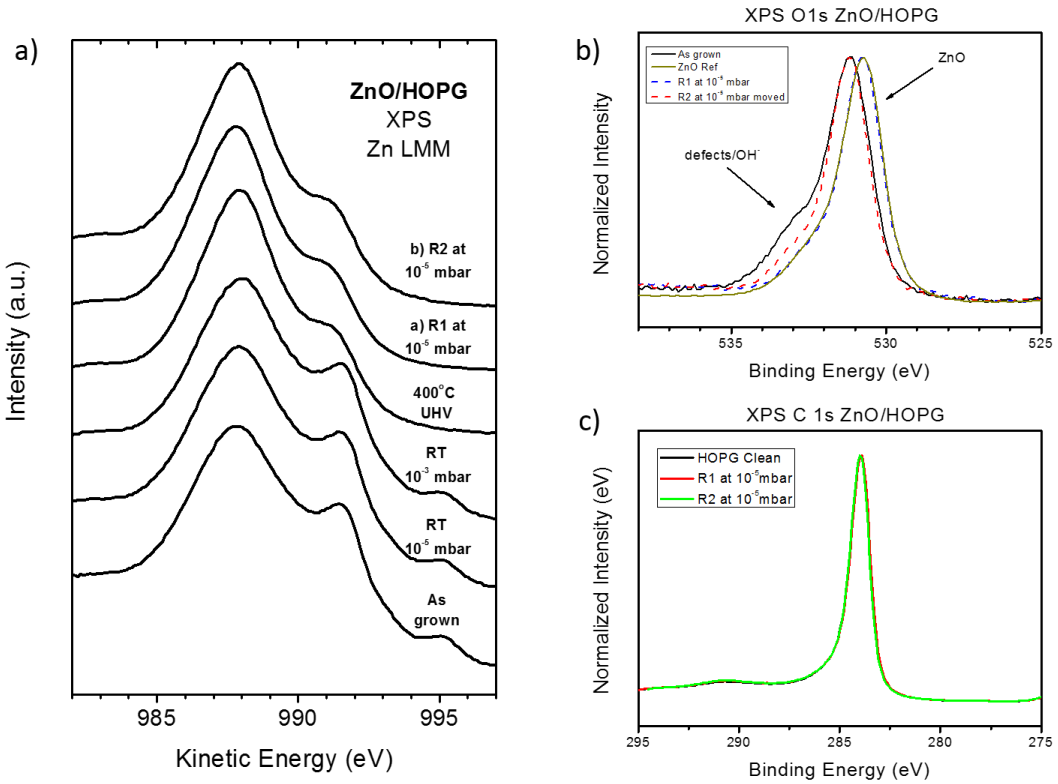

Figure 4.11 a) Auger Zn LMM XPS spectra as a function of the thermal treatment; b) normalized XPS O 1s spectra for as grown ZnO/HOPG sample and after different thermal treatments; c) normalized XPS C 1s spectra for clean HOPG and ZnO/HOPG sample after different thermal treatments.

Figure 4.12 shows the change in percentage of the amount of oxygen in comparison to the as grown samples, confirming that these thermal treatments imply a deeper oxidation of the ZnO together with the reduction of defects. Figure 4.12 b shows, as compared to the as grown samples, the Zn $2p_{3/2}$ and O 1s energy shifts and the S-O split of the Zn 2p contribution. Both contributions shift to lower binding energies, although the shift is greater for the Zn 2p (it is worthy to remark that C 1s contribution had no energy change). The S-O split also has a very similar behavior, reducing its value in a parallel way to the energy shift of the Zn $2p_{3/2}$ and O 1s contributions. As it was explained before, this change on the S-O split value can be associated to an increment on the size of the ZnO structures. Therefore, from the XPS analysis it can be inferred that the re-oxidation process implies a recrystallization of the ZnO, where the amount of oxygen vacancies is reduced and where the size of the ZnO is increased, possibly by an aggregation process.

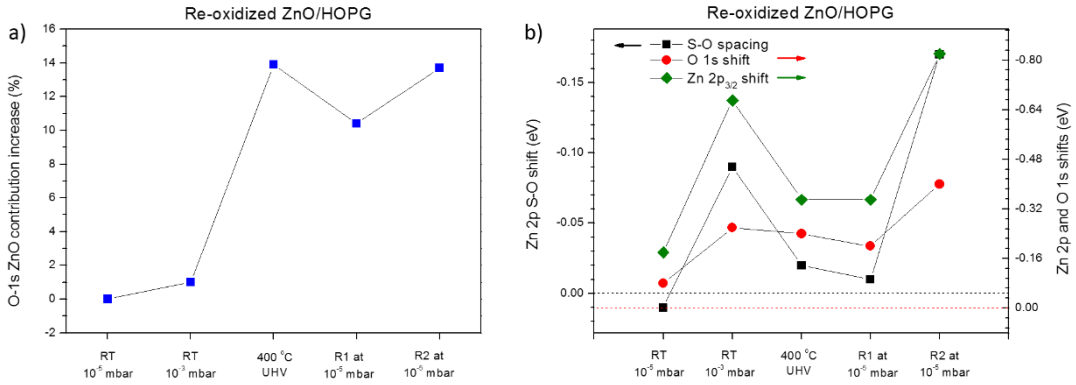

Figure 4.12 a) O-ZnO component increase of O 1s spectra as a function of the thermal treatment; b) S-O spacing (black square, left axis) and O 1s and Zn $2p_{3/2}$ shifts (right axis, red circle and green rhomb, respectively) as a function of the thermal treatment.

The mass spectrometry measurements performed during the three thermal treatments did not show any variation on the chamber residual gases that could be related to a carbon degasification reaction, as in the cobalt oxide case.

4.2.2.2 *Ex situ* study: Raman spectroscopy and SEM

Ex situ confocal Raman spectroscopy measurements were performed in these same samples. The advantage of this technique is that it can be used to analyze the

substrate under the ZnO and follow any kind of chemical and structural change on both the ZnO and the graphite. Figure 4.13 shows the Raman spectra for the sample exposed to O_2 at 10^{-3} mbar (which in fact, can be taken as the as grown sample) and the three samples submitted to different thermal treatments. Two different behaviors can be distinguished. Regarding the ZnO, the E_2^{low} at ~99 cm^{-1} is ascribed to Zn sublattice, E_2^{high} at ~439 cm^{-1} is associated to oxygen vibrations and E_1(LO) at ~590 cm^{-1} is strongly affected by defects as oxygen vacancies [49]. In this way, the sample with no thermal treatment presents a very broad band at 350-600 cm^{-1}, indicating a very amorphous growth and the existence of a great number of oxygen vacancies defects, confirming the previous XPS conclusions. On the other hand, after the thermal treatment this defect band

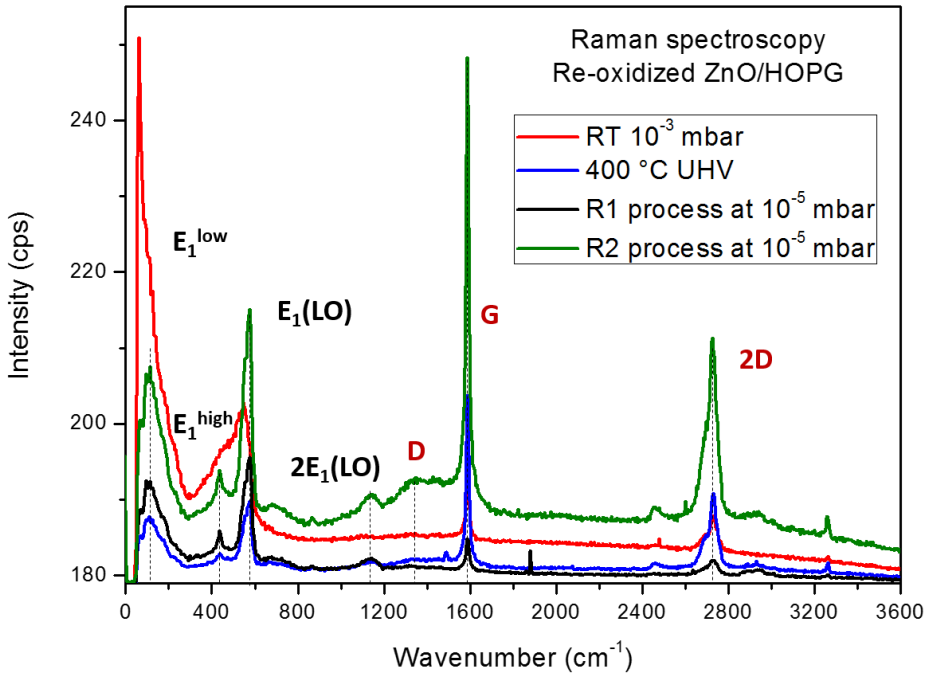

Figure 4.13 a) Average Raman spectra for each thermal treatment. Main ZnO bands (black color) and graphite bands (red color) are indicated.

decreases, being able to resolve separately the E_2^{high} and E_1(LO) contributions and appearing the second order $2E_1$(LO) peak at ~1145 cm^{-1}. Therefore, these thermal treatments induce a clear recrystallization on the ZnO clusters. Going to the substrate, the clean graphite Raman spectrum is defined by two main contributions, the G and 2D bands at ~1586 cm^{-1} and 2727 cm^{-1}, respectively [50]. The first one is associated to the doubly

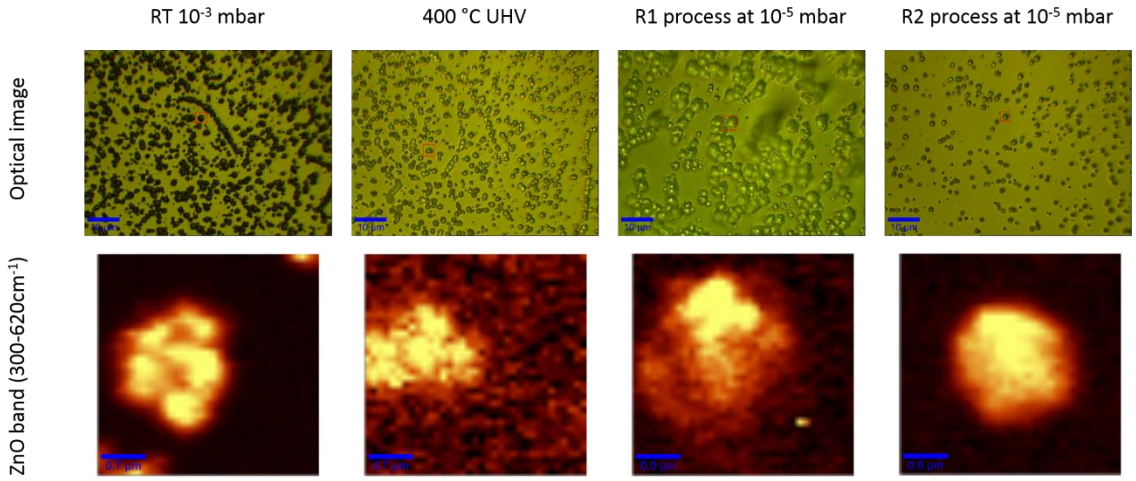

Figure 4.14 Top: optical images of ZnO clusters on HOPG after different thermal treatments. Red squares indicate the mapped area, depicted at the bottom for the intensity of the ZnO defect band (350-620 cm^{-1}).

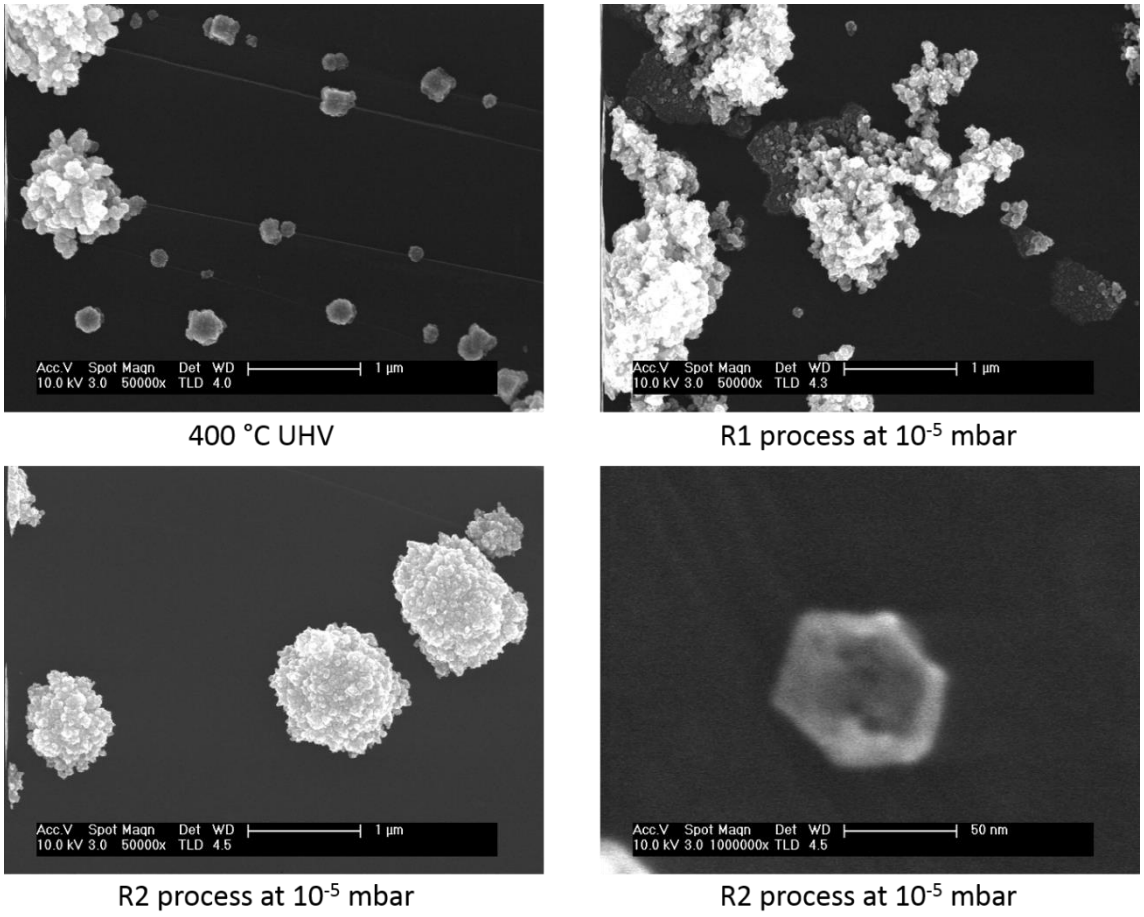

Figure 4.15 50000x magnification SEM images of ZnO clusters after different thermal treatments. Bottom right image shows a detail of R2 with 1.000.000x magnification.

degenerate zone center E_{2g} mode, while the 2D band is ascribed to the second order of zone-boundary phonons. As it can be seen, initially only these two bands are measured, and only after the R2 process (coinciding with the most crystalline ZnO) appears a broad contribution at ~1350 cm^{-1} that corresponds to the D band, which is associated with defects on the graphite. Therefore, by Raman spectroscopy seems clear that also the HOPG substrate suffers changes after these thermal changes.

Figures 4.14 and 4.15 shows optical and SEM images of ZnO clusters after the thermal treatments. The optical images show a clear modification of the clusters aspect, being more lightened after the thermal process, accordingly to the reduction on the number of defects and the corresponding increase of the expected transparency characteristic of the ZnO. The 50000x SEM images show clusters with more regular and hexagonal shapes after the recrystallization. In fact, ~50 nm hexagonal and flat clusters appear after these thermal treatments, as a pretty example of well crystallized ZnO.

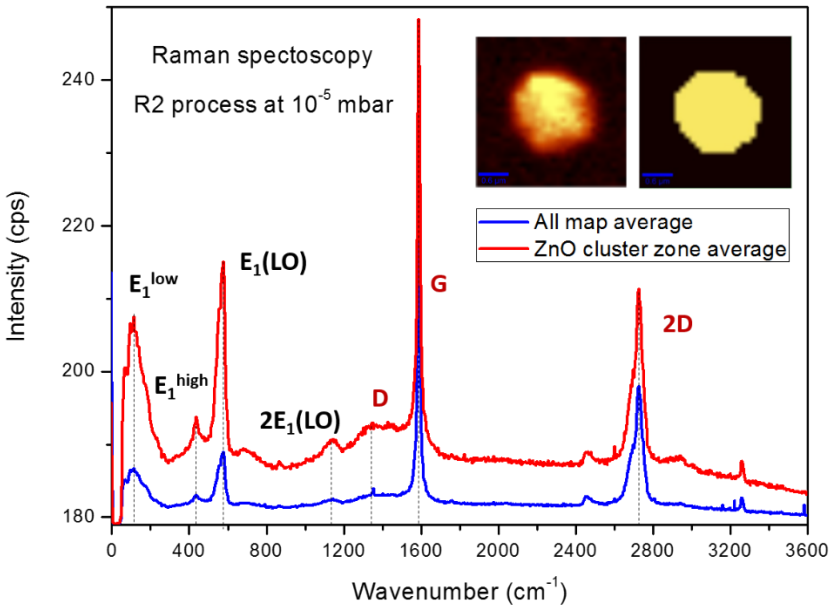

Figure 4.16 Averaged Raman spectra for R2 thermal treatment at 10^{-5} mbar for the complete mapped zone (blue) and averaged Raman spectra applying a mask only in the ZnO cluster area. Main ZnO bands (black color) and graphite bands (red color) are indicated.

Once proved that the HOPG substrate also suffers a modification, the next question are where and how it happens. Figure 4.16 shows two Raman spectra which correspond to

the same mapped area. The blue spectrum (bottom) shows the average of all the mapped area (shown in the left inset), whereas the red spectrum only shows the cluster area (right inset shows the mask used for this purpose). In addition to the evident increase of ZnO signal, the graphite D band corresponding to defects clearly amplifies under the cluster in comparison to the rest of the free HOPG surface. Therefore, the modification of the substrate only takes place at the interface between ZnO and HOPG, being almost invisible to XPS measurements at the early stages of growth. On the other hand, Figure 4.17 a shows a series of punctual Raman spectra taken with different laser power doses on a specific ZnO cluster of the as grown ZnO/HOPG sample. As it can be seen, for low powers (green, 0.5 W), there is no modification of the initial defective ZnO (the graphite bands are hidden by the ZnO). However, at LS35 (blue), the ZnO defects band is now resolved with two contributions (E_1^{high} and $E_1(LO)$), indicating that the recrystallization have taken place. At the same time, a very prominent D band appears, with two weak and

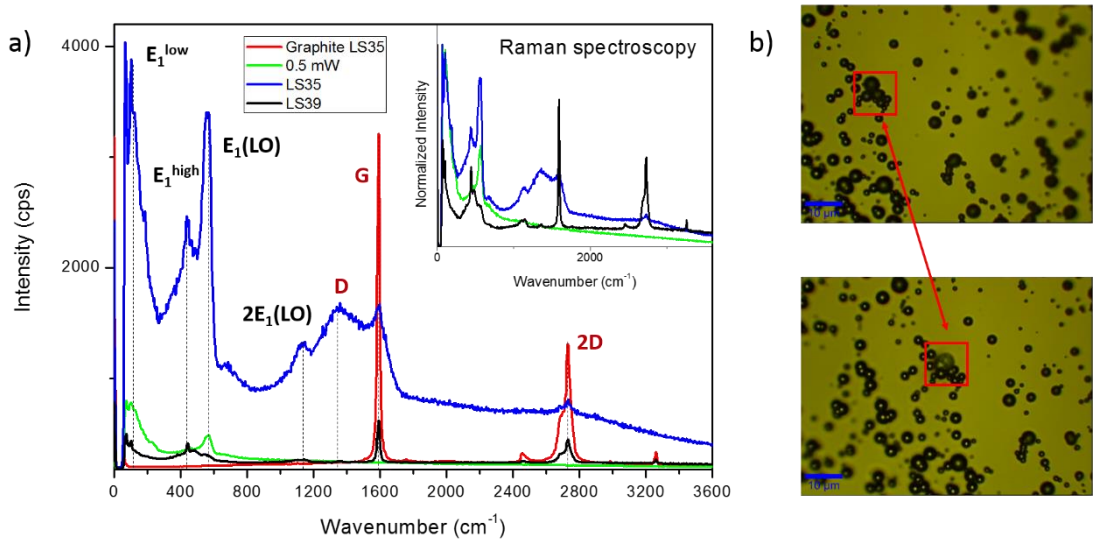

Figure 4.17 a) Averaged Raman spectra sample of as grown ZnO/HOPG at different laser powers. Red spectrum depicts clean HOPG of this same sample; b) optical images of the mapped area before (top) and after (bottom) the higher laser power LS39.

broad D and 2D bands. This picture is completely different for the free HOPG surface using this same power. The red spectrum shows the graphite outside the ZnO cluster, with no D band and a very strong and narrow G band. Consequently, there is no modification of graphite by this laser power, being the ZnO recrystallization induced by the thermal heating of the laser the cause of the graphite modification. Finally, if the power is

increased to LS39, the cluster is destroyed, decreasing the E_1(LO) ZnO defects bands and recovering the good quality graphite. Therefore, these experiments confirm that the graphite is really modified by the ZnO at the interface at the same time that the ZnO is recrystallized.

4.3 Interaction of ZnO with CVD graphene on polycrystalline copper

4.3.1 Early stages of growth of ZnO on CVD graphene on polycrystalline copper substrates

At this point, it starts the analysis of the growth of ZnO on CVD graphene on polycrystalline copper. This first section is dedicated to the chemical and morphological study of the early stages of growth, focusing mainly on the metal oxide. By means of *in situ* XPS the chemical interaction between both ZnO and graphene/Cu was investigated.

4.3.1.1 Quantitative chemical analysis

In the same way as for the growth of ZnO on HOPG, the study of the early stages of growth was performed by successive evaporation of ZnO on the same graphene/Cu sheet, analyzing the sample for each of these steps. Figure 4.18 a shows the XPS survey spectra as a function of the ZnO coverage. The pristine graphene reflects three elemental contributions. The most intense corresponds to copper, with two main regions: the Cu 2p (920-970 eV) and the Cu LMM (540-750 eV). In second place, the C 1s of graphene at ~284 eV, which is very weak in comparison to Cu signal due to the large difference between their atomic sensibility factors. Finally, unlike for HOPG, the O 1s contribution at ~531 eV is not depreciable, and it will be discussed in depth. Once ZnO deposition starts, the Zn 2p and Zn LMM Auger contributions start dominating the spectra. As before, the overlapping between the Zn Auger signal and the C 1s and O 1s contributions is overcome by changing between the Al or Mg X-ray source anodes. For the last coverages, only the ZnO contributions could be measured, point at which the experiment was finished. On the other hand, Figure 4.18 b shows the evolution of the Zn LMM Auger spectra. As it can be seen, the spectra corresponding to the early stages of growth are different than those of the final stages. From the comparison with the metallic Zn and ZnO reference spectra shown in Figure 2.4, it seems that the spectrum of the first one dominates on the early stages of growth whereas the final stages are dominated by ZnO.

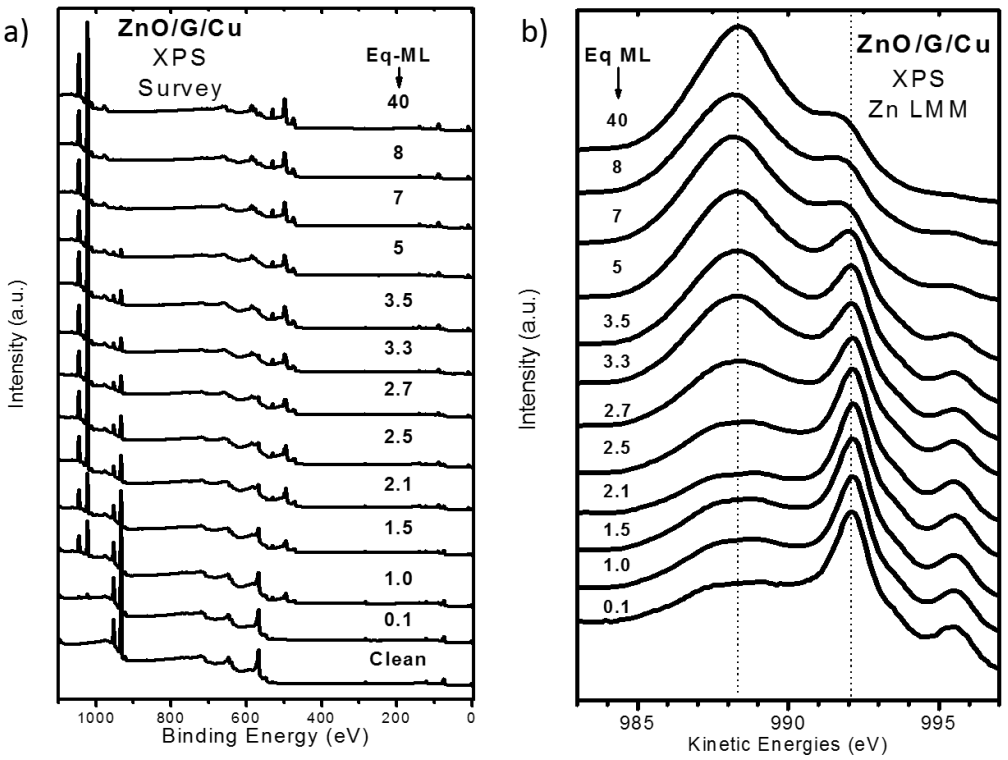

Figure 4.18 a) XPS survey spectra and b) Auger Zn LMM XPS spectra as a function of the coverage for the growth of ZnO on graphene on polycrystalline copper.

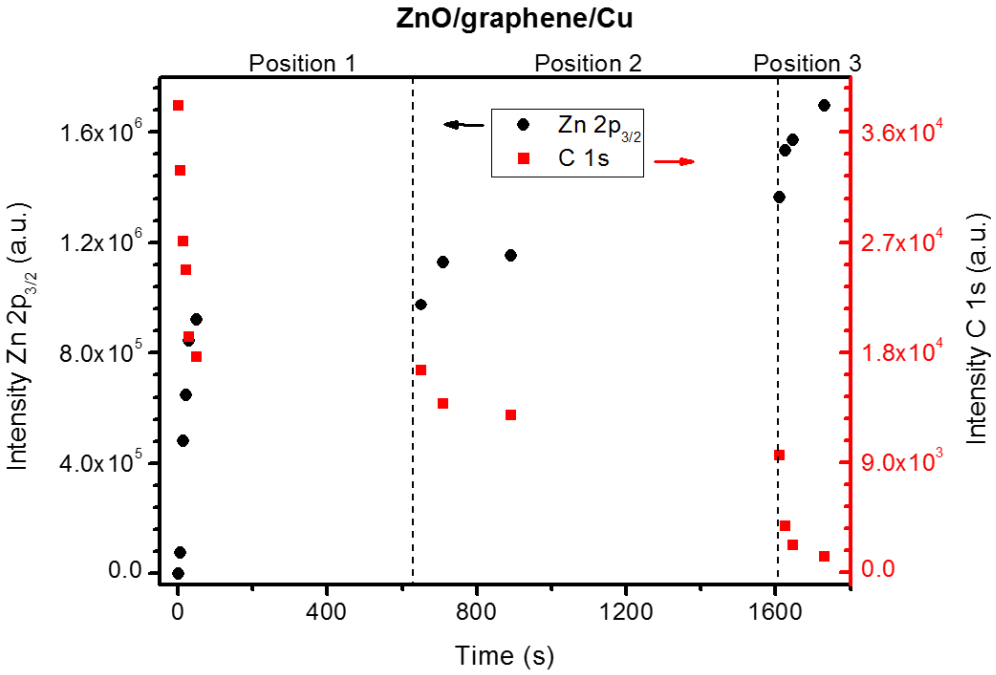

Figure 4.19 Evolution of the intensities of the Zn 2p 3/2 (black dots) and C 1s (red squares) as a function of the evaporation time for the growth of ZnO on graphene on polycrystalline copper.

The intensities from Zn $2p_{3/2}$ and C 1s contributions as a function of the coverage are depicted on Figure 4.19. As it was previously described in Chapter 2, section 2.6.1.2, three different relative positions between sample and evaporator were used in order to control the evaporation rate. In such a way, these three sample positions are clearly distinguishable and correspond to three different growth rates. The first stage is characterized by a very fast deposition rate, whereas for the second stage the change in intensity is minimal. The third stage leads to a complete coalescence of the film where the XPS signal of the C 1s peak disappears. In general, this behavior was different from the observed in the HOPG substrate. In the case of the graphene/Cu substrate we observe a very fast growth of nucleation centers whereas the deposition rate decreases when those nucleation centers have been created.

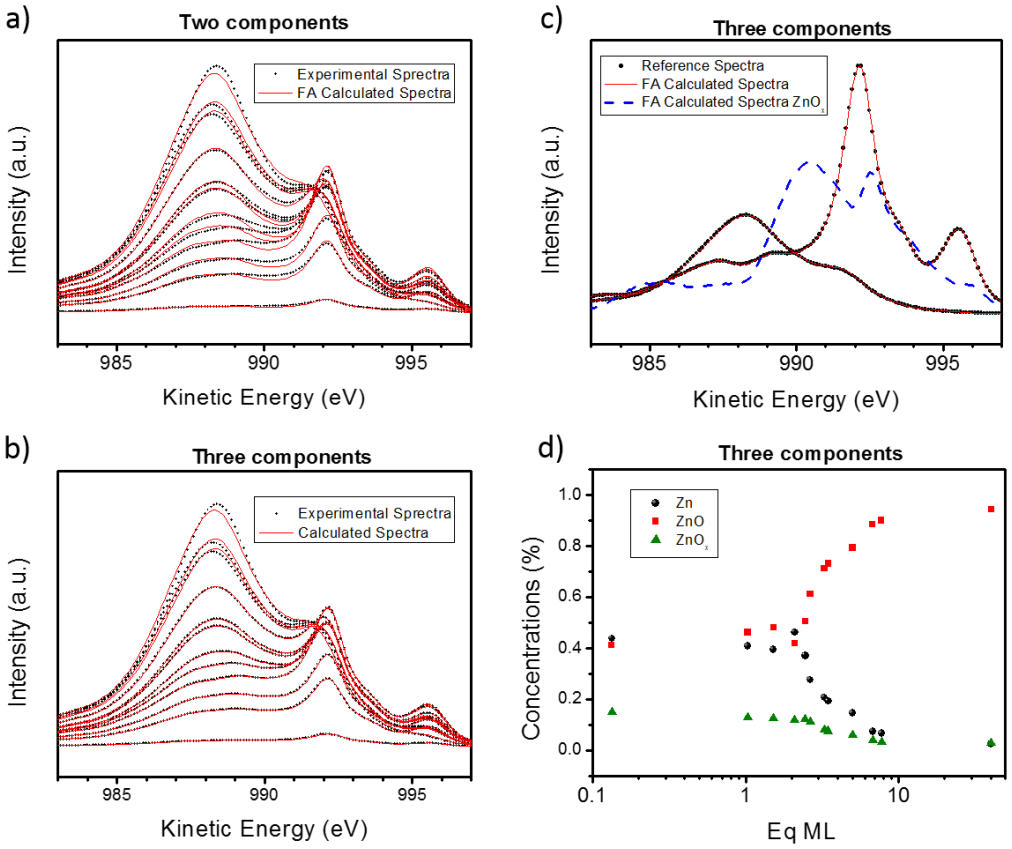

Figure 4.20 Results of factor analysis for the growth of ZnO/G/Cu: a) Fittings of the experimental spectra using a linear combination of the same components as in Figure 4.3 a. b) Fittings of the experimental spectra using a linear combination of the three components; c) Calculated components by factor analysis used in b. The new component is represented with dashed line. d) Concentration of each of the components as a function of the coverage.

Factor analysis has been applied to the Zn LMM spectra in order to study the amount of metallic Zn and ZnO present in each step. Figure 4.20 a shows the results obtained by using the same two reference spectra as for the HOPG case. In comparison, the results do not fit the experimental spectra to the same extent than those for the deposits on the HOPG substrate. The larger dispersion appears at the intermediate energy region defined in the spectra of the two main components. For this reason, the main component analysis has been recalculated allowing the presence of a third component on the basis of an estimation of the concentrations (Target Testing from estimated concentrations). Therefore, as shown in Figure 4.20 c, a third component (dashed-line) is needed to obtain the better fitting of the experimental spectra (see Figure 4.10 b). Figure 4.20 d shows the relative concentrations of these three components.

Our Laboratory	B.E. Zn 2p (eV)	K.E. Zn LMM (eV)	α (eV)	[-2(E_Mq+Φ)-KQ] (eV)
Zn	1021.9	992.1	2014.0	4057.8
ZnO_x	1022.2	990.5	2012.7 ± 0.2	4057.1 ± 0.5
ZnO	1021.9	988.3	2010.2	4054.0

Table 4.1 Binding energy (B.E.) of Zn 2p, kinetic energy (K.E.) of Zn LMM Auger transition, Auger parameter (α) and initial energy term [-2(E_{Mq}+Φ) - 2KQ] for the three components Zn, ZnO and ZnOx. BE and KE for the sub-oxide component are deduced from XPS measurements and FA calculations, respectively. Initial energy term is deduced from the $\boldsymbol{E_k^F = cte_{L_3M_{45}M_{45}} + \left[-2\left(E_{Mq} + \Phi\right) - 2KQ\right] - 3E_b^F}$ equation once KE and BE are known.

Regarding this third component, two different possibilities can be proposed: 1) interface contribution between ZnO/graphene; 2) Zinc sub-oxide as a transition between the metallic zinc and ZnO components. In order to clarify the origin of this third component, a Wagner plot for Zn atoms with different environments [51], including those of our Zn and ZnO reference samples as well as for the species corresponding to the new component appeared in the Factor analysis, labelled as ZnOx (solid circles), is depicted

in Figure 4.21 a. The Auger parameter for the Zn atoms is defined as: $\alpha' = E_k^F(L_3M_{45}M_{45}) + E_b^F(L_3)$, which is very sensitive to the local environment of the atoms since it strongly depends on the relaxation energy of the final state. The Auger parameter can be also set as $\alpha' = cte_{L_3M_{45}M_{45}} + 2\,R(L_3)$, and so straight lines with slope +1 in the Wagner plot correspond to atoms with the same final state or, in other words, same relaxation energy. On the other hand, the final states equation can be written as $E_k^F = cte_{L_3M_{45}M_{45}} + \left[-2\left(E_{Mq} + \Phi\right) - 2KQ\right] - 3E_b^F$, and hence straight lines with slope +3 in the Wagner plot correspond to atoms with the same initial states. It is necessary to point out that although this simplified picture is valid for core levels, in the case of ZnO, the participation of 3d states on the Auger transition could be ambiguous, as it hybridizes with about a 10% on the valence band [52,53]. However, due to this restricted hybridization it seems quite confident the validity of the equations associated to the Wagner plot and explained in section 2.4.1. The values of the kinetic energy of the Zn LMM Auger peak, the Zn $2p_{3/2}$ photoemission binding energy and the Auger parameter are given in Table 4.1. More details regarding the previous equations in Chapter 2, section 2.4.1.

According to the Zn Wagner plot, the initial state of the ZnO_x component resulted very similar to the metallic Zn and very different from that of ZnO. On the other hand, the final state of the ZnO_x shows a lower relaxation energy than for metallic Zn, suggesting a charge transfer from the Zn atoms. In Table 4.2 relative values of initial and final states between Zn, ZnO and ZnOx have been estimated. According to the above analysis we assign the new component appeared in the Factor analysis to ZnO_x sub-oxide at the ZnO/Zn interface, as reported elsewhere [54].

Δα(Zn ••• ZnOx)	1.34 ± 0.15 eV	**Δ[-2(E_Mq+Φ)-2KQ](Zn ••• ZnO_x)**	0.66 ± 0.45 eV
Δα(ZnOx ••• ZnO)	2.48 ± 0.15 eV	**Δ[-2(E_Mq+Φ)-2KQ](ZnO_x ••• ZnO)**	3.10 ± 0.45 eV
Δα(Zn ••• ZnO)	3.82 eV	**Δ[-2(E_Mq+Φ)-2KQ](Zn ••• ZnO)**	3.76 eV

Table 4.2 Relative values of Auger parameter and initial energy term between the three components Zn, ZnO and ZnO_x.

In order to confirm the real existence of this sub-oxide, fittings of the ZnO valence band have been performed, as any change on the Auger parameter must come from a variation of the Zn 3d level, since the core level Zn 2p has very little dependence on the oxidation state. To avoid the Cu 3d signal from the graphene/Cu substrate, different thick (>500 Å) samples have been grown containing different ZnO/Zn ratio on Si wafers by reactive thermal evaporation under different oxygen pressures from $2\cdot10^{-5}$ to $2\cdot10^{-3}$ mbar. It should be stressed that, for this study, the influence of the substrate is negligible, as we intend to verify whether the third component comes from the interaction at the ZnO/graphene/Cu or at the ZnO/Zn interfaces.

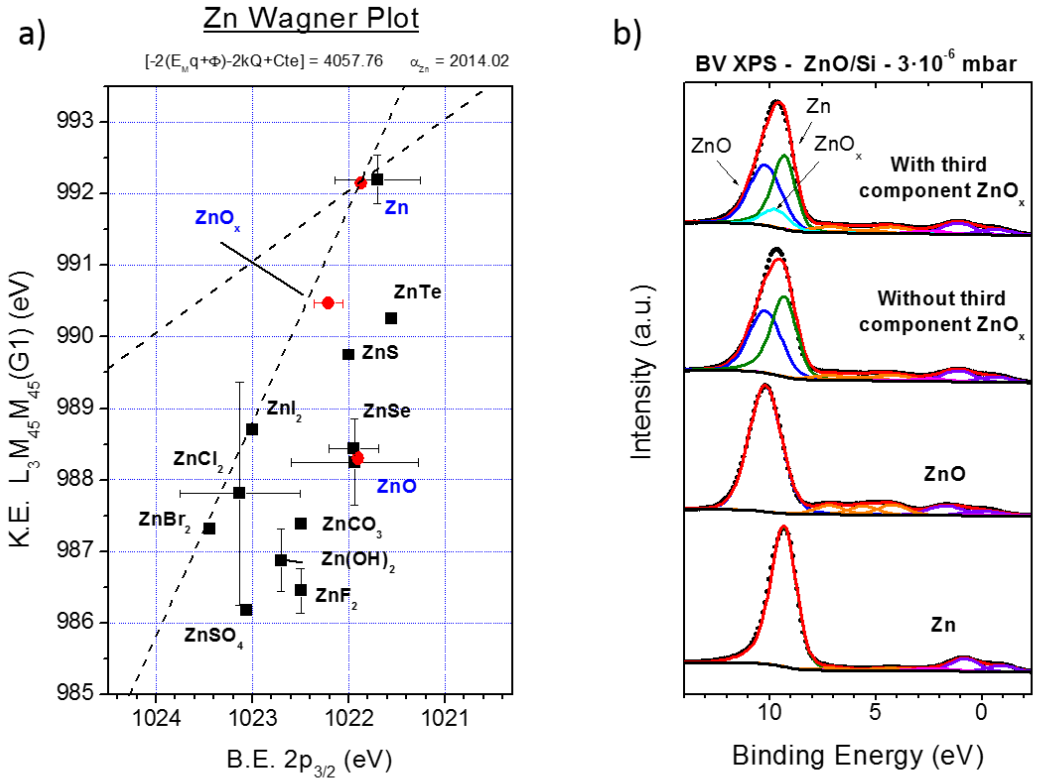

Figure 4.21 a) Wagner plot for different Zn compounds found in the literature (squares). The values obtained in this work for Zn, ZnO and ZnO_x are depicted as circles. b) Valence band fitting for ZnO/Si grown under low oxygen pressure, as labelled.

The valence band XPS spectrum, including the Zn 3d states, for a sample containing approximately 50% ZnO/Zn concentration ratio is shown in Figure 4.21 b. The fittings of the Zn 3d peak have been performed by using the curves taken from the ZnO and metallic Zn reference samples as shown in Figure 4.21 b (as labeled). A clear energy-

shift of 0.9 eV of the Zn 3d XPS peak between metal and oxide is reported in this work. However, the fitting of the experimental spectra is not well achieved without the use of a third component with an intermediate binding energy. In addition, the concentrations of these three components deduced by the fitting curves agree with those calculated by factor analysis of the Auger spectra. The analysis of the Zn 3d peaks confirms the initial hypothesis in which the third component was assigned to the $ZnO/ZnO_x/Zn$ interface and clears up the possible doubts regarding a mathematical artefact induced by the factor analysis method.

Once we have studied the new component, we go back to the results shown in Figure 4.20 d., where the concentrations of the three components are depicted. For the very early stages of growth (< 2 Eq-ML), no variations of the concentrations of the three species with coverage are observed. Furthermore, by tilting the sample with respect to the analyzer edge (not shown here), we observe an increase of the oxide component in detriment of the metallic component, indicating that metallic Zn and its associated ZnOx sub-oxide, are under ZnO. The graphene surface seems very avid of metallic Zn atoms, inhibiting its oxidation at the interface. In this picture, intercalation of metallic Zn between Graphene and the copper substrate is one possibility, as intercalation of other metals, even at room temperature, has already been observed [55,56]. In any case, the formation of both, ZnO/ZnO_x /graphene/Zn/Cu and ZnO/ZnO_x /Zn/graphene/Cu systems are consistent with the above results. Besides, this region of growth agrees with the fast growth obtained using the method 1 depicted in Figure 4.19, where the metallic Zn contribution follows the same behavior as those of ZnO accompanied by the ZnO_x sub-oxide (see Figure 4.20 d). In any case, reduction of ZnO to ZnO_x at the interface is expected as corresponds to the reducing character of both, graphene and Cu [54]. For further coverages, ZnO grows on the substrate hiding the signal from the other two Zn species (ZnO, ZnO_x) obtaining finally a stoichiometric ZnO thin film.

4.3.1.2 Quantitative morphological analysis

Following the same methodology than for the ZnO/HOPG growth, the morphological study of the ZnO/graphene/Cu system was carried out by means of *ex situ* AFM and SEM measurements. However, one first curiosity is shown in Figure 4.22, where optical images for samples with different coverages are shown. For the earlier stages of growth there is a difference on the color respect to the pristine graphene.

However, for further deposition the color changes to blue, violet and finally transparent (as it can be seen for the 40 Eq-ML sample). This changes are related with the light interferences with the thickness. However, taking into account the wide band gap of zinc oxide, it can also be related with changes on the morphology or with the composition of the films.

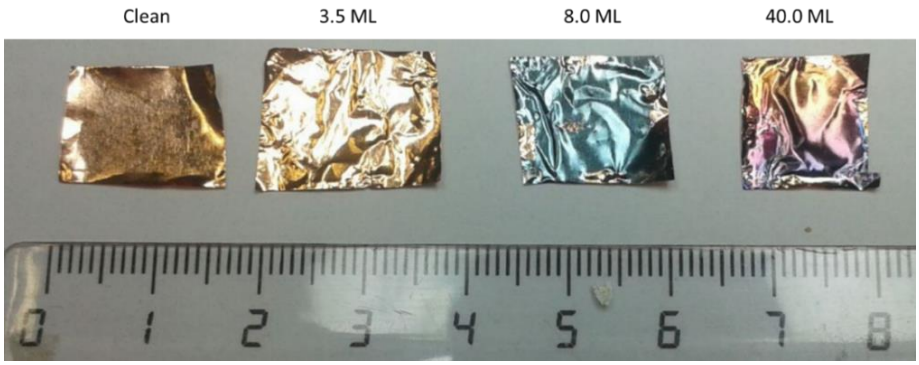

Figure 4.22 Optical images of ZnO/graphene/Cu samples with different coverages.

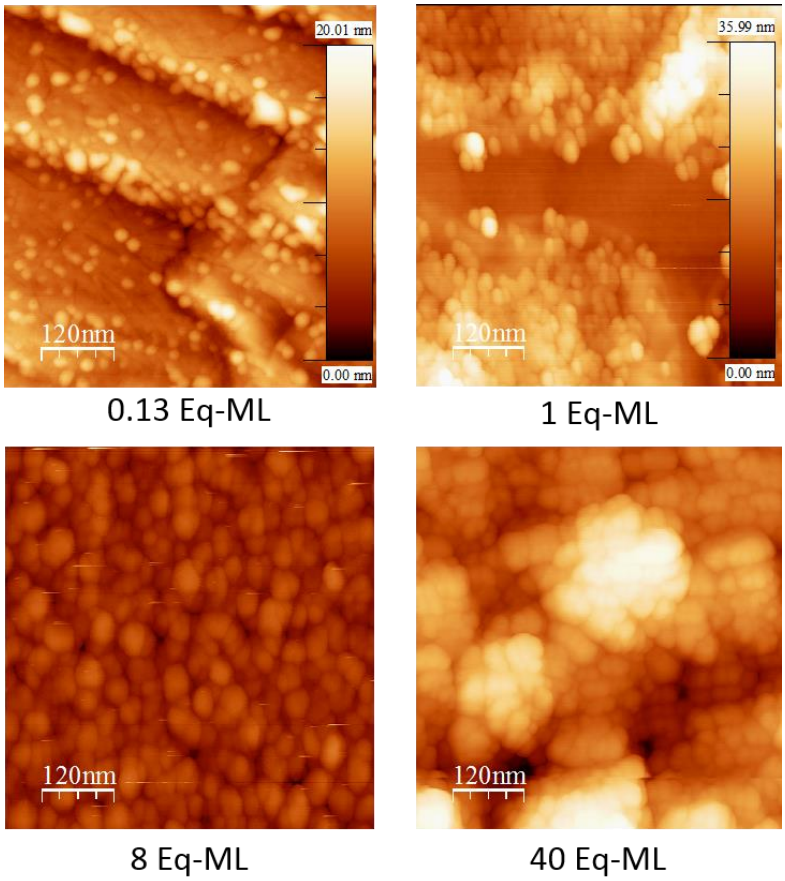

Figure 4.23 600x600 nm^2 images for different stages of growth of ZnO on graphene on polycrystalline copper.

Moving to the AFM images, Figure 4.23 shows 600x600 nm^2 images for different stages of growth of ZnO on graphene/Cu. The early stages of growth (0.1-1.0 Eq-ML) consist in the formation of very small clusters of 30 nm in size and about 20 nm in height. For further coverages, those small clusters slightly grow in size (up to 60 nm), finally forming aggregates of about 150-200 nm for large coverages (> 40 Eq-ML), coinciding with final transparent stage of Figure 4.22. The growth followed a Volmer-Weber model, but being the size of the initial clusters two orders of magnitude lower and the number of nucleation centers much larger than in the case of the HOPG substrate. On the other hand, SEM images with 100.000 x magnification show a very similar picture. The grain boundaries of the Cu substrate are clearly observed, whereas the size and distribution of the ZnO nanostructures are also in agreement with those observed in the AFM images.

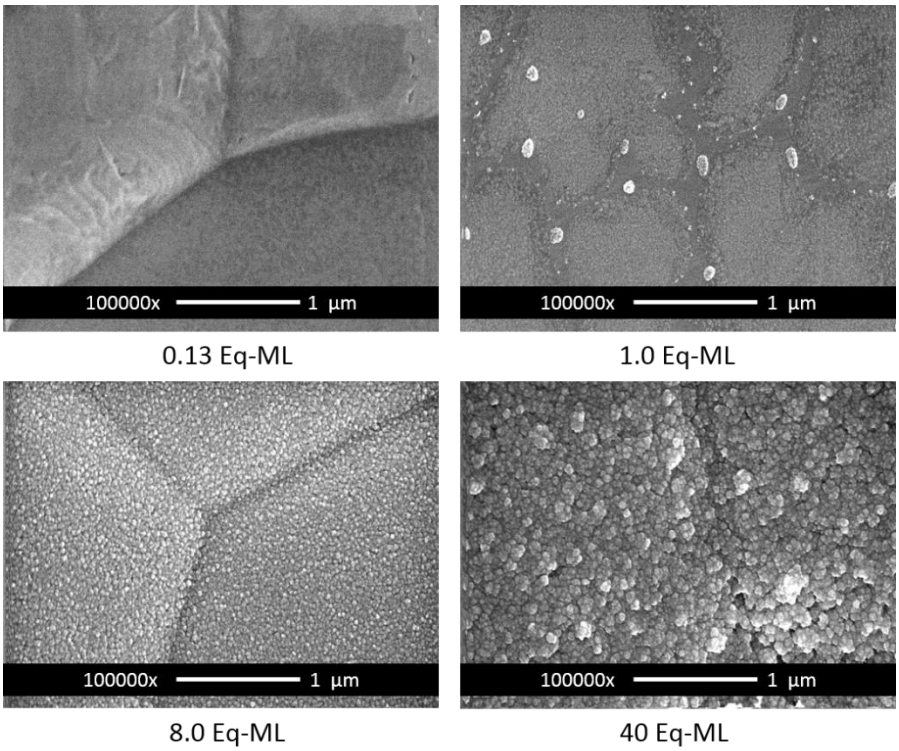

Figure 4.24 100000x magnification SEM images for different stages of growth of ZnO on graphene on polycrystalline copper.

Finally, by combining AFM and XPS measurements, inelastic peak shape analysis was performed in order to characterize the growth of ZnO on the graphene/Cu sheet. In this case, the C 1s XPS peak measured with the Al anode was used, giving an inelastic mean free path of 19.6 Å. The "buried layer" model was used within the QUASES

software. The results depicted in Figure 4.25 show three well different zones for low (0-2 Eq-ML), intermediate (2-5 Eq-ML) and final (5-10 Eq-ML) coverages. The first zone for low coverages indicates the growth of ZnO islands covering up to the 50% of the graphene surface with 2 nm height. This zone corresponds to the simultaneous deposition of metallic Zn and ZnO on the G/Cu substrate depicted in Figure 4.20 d, where the samples were grown using the method 1 (see Figure 2.23). The second zone, from 2 to 5 Eq-ML, shows a rapid increase of the islands height from 4 to 7 nm, then reaching the detection limit of the method whereas the total coverage is almost constant. This has been indicated by an arrow in Figure 4.25. Finally, the third zone is dominated by the signal saturation, indicating that the detection limit was reached. Coalescence is reached when approximately 9 Eq-ML were deposited.

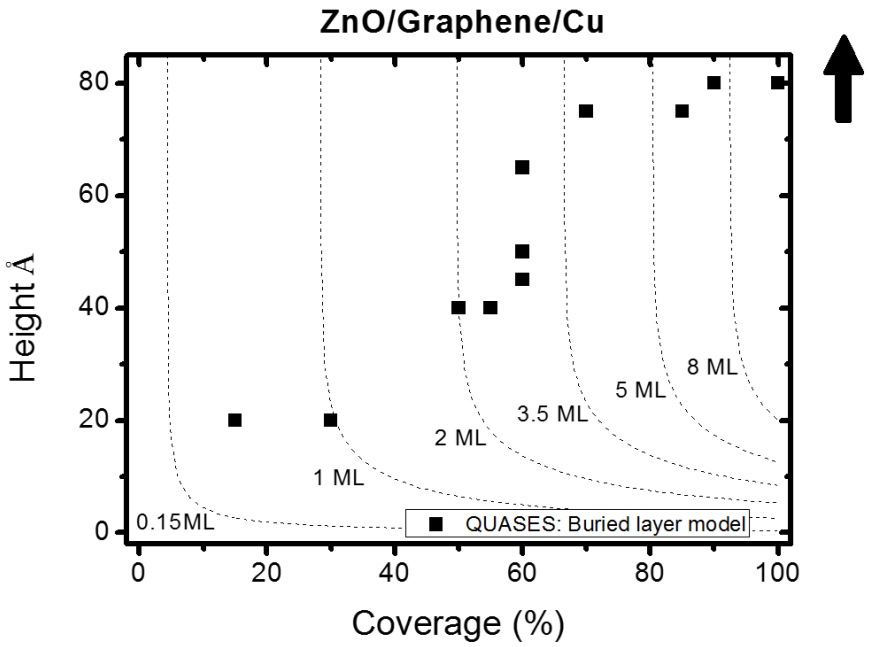

Figure 4.25 Results for the inelastic peak shape analysis for the growth of ZnO on graphene on polycrystalline copper.

According to the reported results, the following model of growth of ZnO on graphene/Cu substrates is proposed. The early stages of growth are characterized by a very fast deposition of roughly 50% metallic Zn and 50% of ZnO islands of about 2 nm in height and 30 nm in size. Independently from whether the Zn atoms intercalate between graphene and Cu or not, what is clearly observed is the large affinity of Zn atoms for the Graphene surface, then leading to the rapid formation of ZnO/Zn clusters. This will be

further discussed in the next pages, especially at section 4.3.3, where a chemical model of the growth and interaction between substrate, evaporated Zn and O_2 atmosphere is presented. In any case, as consequence of the high density of nucleation sites, the cluster size is in the nanoscale. Further stages are characterized by a lower deposition rate and the formation of a nanostructured ZnO thin film.

4.3.1.3 Chemical analysis: ZnO/graphene/Cu interaction

The interaction between ZnO, graphene and Cu was studied by means of *in situ* XPS measurements. The aim of this subsection is to work like an introduction, as a deeper discussion is presented on section 4.3.3 in the light of the previous 4.3.2 point dedicated to the characterization of pristine graphene and its qualitative influence on the posterior ZnO growth.

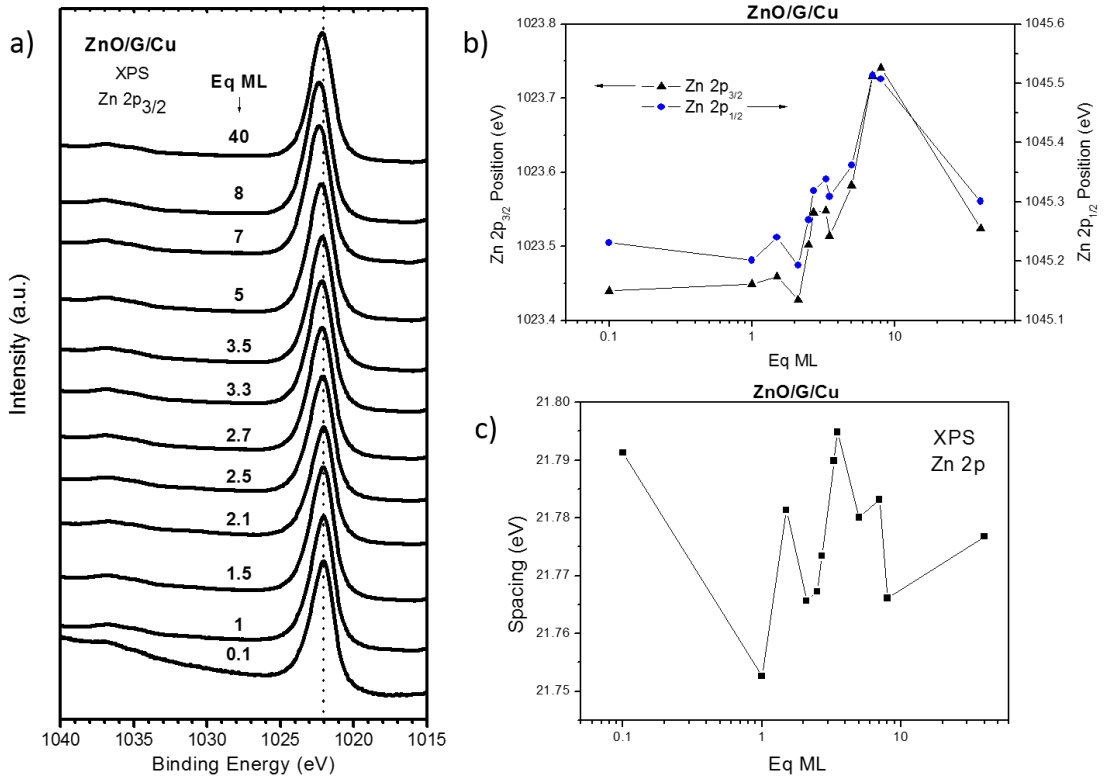

Figure 4.26 a) XPS Zn $2p_{3/2}$ spectra as a function of the coverage for the growth of ZnO on graphene on polycrystalline copper; b) Zn $2p_{3/2}$ and Zn $2p_{1/2}$ shifts as a function of the ZnO coverage; c) Zn 2p spin-orbit spacing (S-O) as a function of the ZnO coverage.

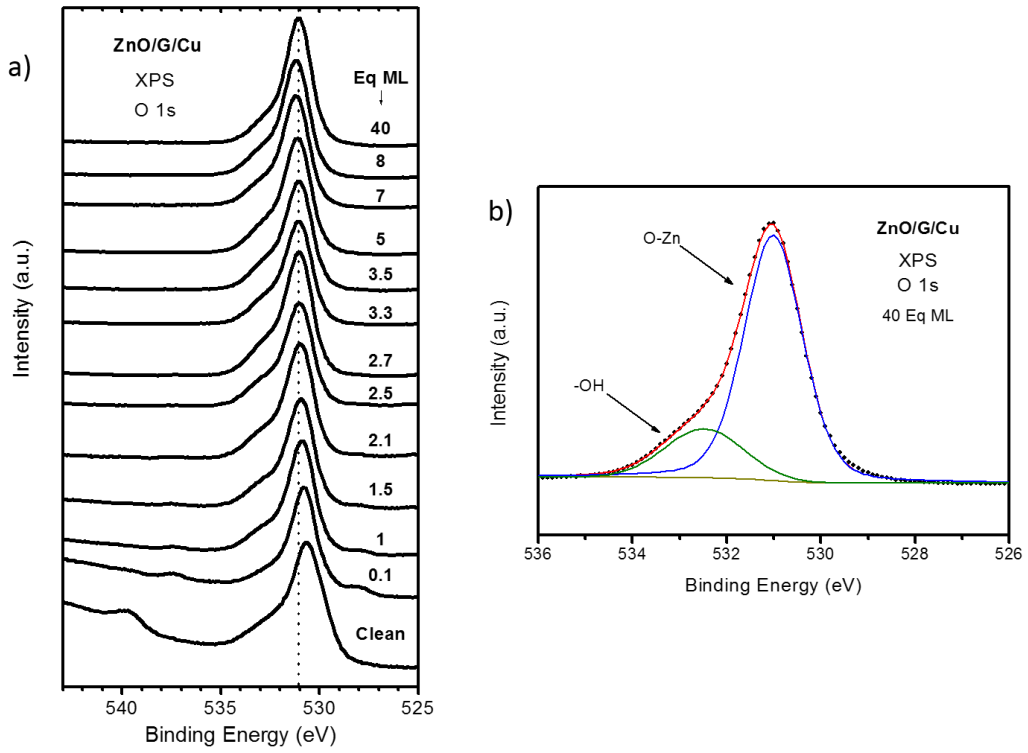

Figure 4.27 a) XPS O 1s spectra as a function of the coverage for the growth of ZnO on HOPG; b) XPS O 1s fitting for 40 Eq-ML of ZnO on graphene on polycrystalline copper.

Figure 4.26 shows the XPS Zn $2p_{3/2}$ spectra as a function of the coverage. Despite the fact that for the early stages of growth, metallic and Zn oxide live together in the sample, unlike the Zn LMM Auger region the Zn 2p spectra do not report changes (section 2.1.2.1). However, an attentive look into the energy position and the spacing between the Zn $2p_{3/2}$ and Zn $2p_{1/2}$ shows some interesting features in comparison to the ZnO/HOPG system. For example, Zn $2p_{3/2}$ peak was shifted ~1.3 eV to higher binding energies while only ~0.3 eV for the Zn $2p_{½}$ contribution, being both values almost constant for all ZnO coverages. Therefore, the S-O spacing was reduced about 1 eV. The reason of this important difference could be related to the scale of the morphology of the ZnO structures and the variation of the composition of the early stages of growth. This could be the reason why for the last coverage (40 Eq-ML), the Zn 2p energy positions starts to decrease (see Figure 4.26 b), although the bulk values reported for the micrometric clusters grown on the HOPG were not yet achieved. On the other hand, metallic Zn 2p was slightly shifted 0.7 eV to lower binding energies, and hence a gradually increase of ZnO in the initial Zn/ZnO measured mixture could explain the gradually shift to higher binding energies of the Zn 2p while preserving the S-O spacing (Figure 4.26 c). Although it is true that Zn 2p

is not the most appropriated region for a chemical analysis of this element in comparison to the Auger emission, it is also worthy to study in detail some aspects, as they could confirm the previous conclusions and draw a coherent picture.

Figure 4.27 shows the XPS O 1s spectra as a function of the ZnO equivalent thickness. Once the ZnO was deposited, the qualitative shape corresponds to typical ZnO (as it can be checked out by the O 1s fitting of Figure 4.27 b). As previously, for the last stages of growth, where the measured signal comes entirely from the ZnO, the relative ratio between the Zn-O and OH/defects contributions is 0.8/0.2. Nevertheless, an interesting point is that initially the sample has not a negligible component of oxygen, with an initial main peak slightly shifted to lower binding energies that corresponds to Cu-O bonds. This will be extensively discussed on section 4.3.2.

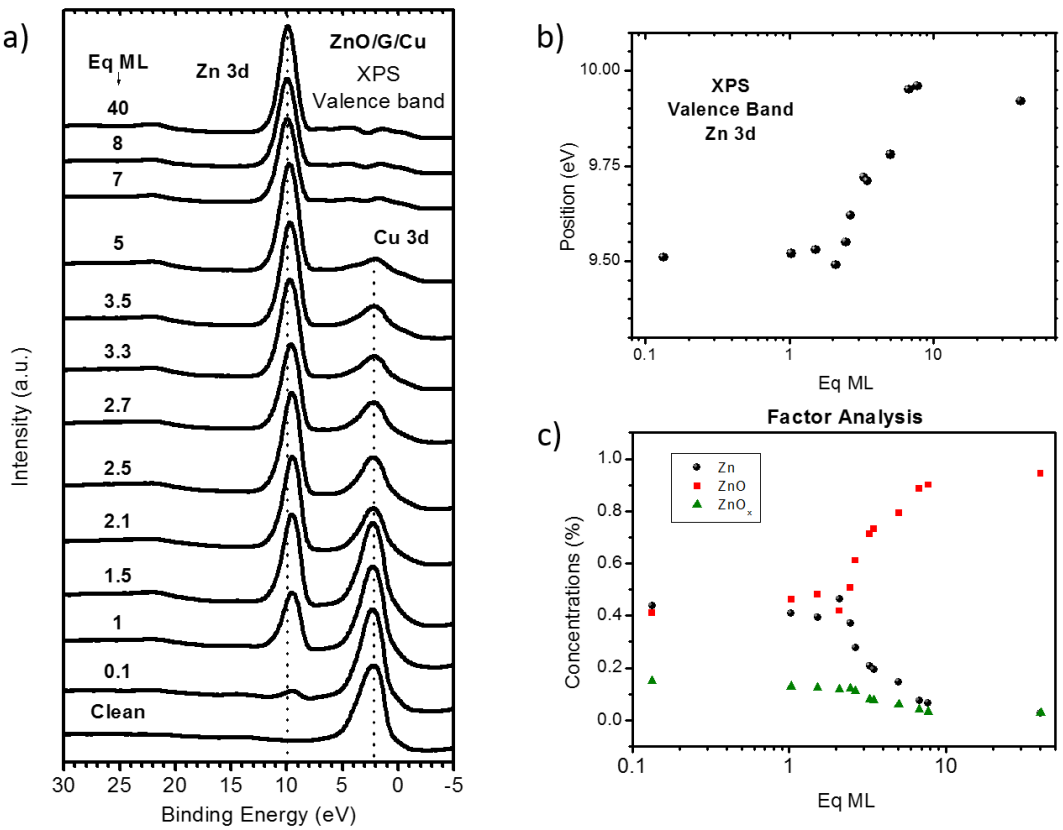

Figure 4.28 a) XPS Zn 3d spectra as a function of the coverage for the growth of ZnO on graphene on polycrystalline copper; b) Zn 3d binding energy as a function of the ZnO coverage; c) Taken from Figure 4.20 d: concentration of each of the factor analysis components as a function of the coverage.

Regarding the valence band, initially only the Cu 3d appears at ~2.3 eV, whereas the Zn 3d peak at ~10 eV appears as a function of the coverage, finally dominating the spectrum. More in detail, Figure 4.28 represents the energy position of the Zn 3d peak as a function of the coverage, with a clear total shift of 0.5 eV to higher binding energies and a stabilization of the value around 10 eV, in agreement with the reference spectra shown in Figure 2.4. In fact, this shift is parallel to the tendency shown by the composition of the film inferred from the factor analysis calculation (see Figure 4.28 c), closing once again the discussion regarding Figures 4.20 and 4.21.

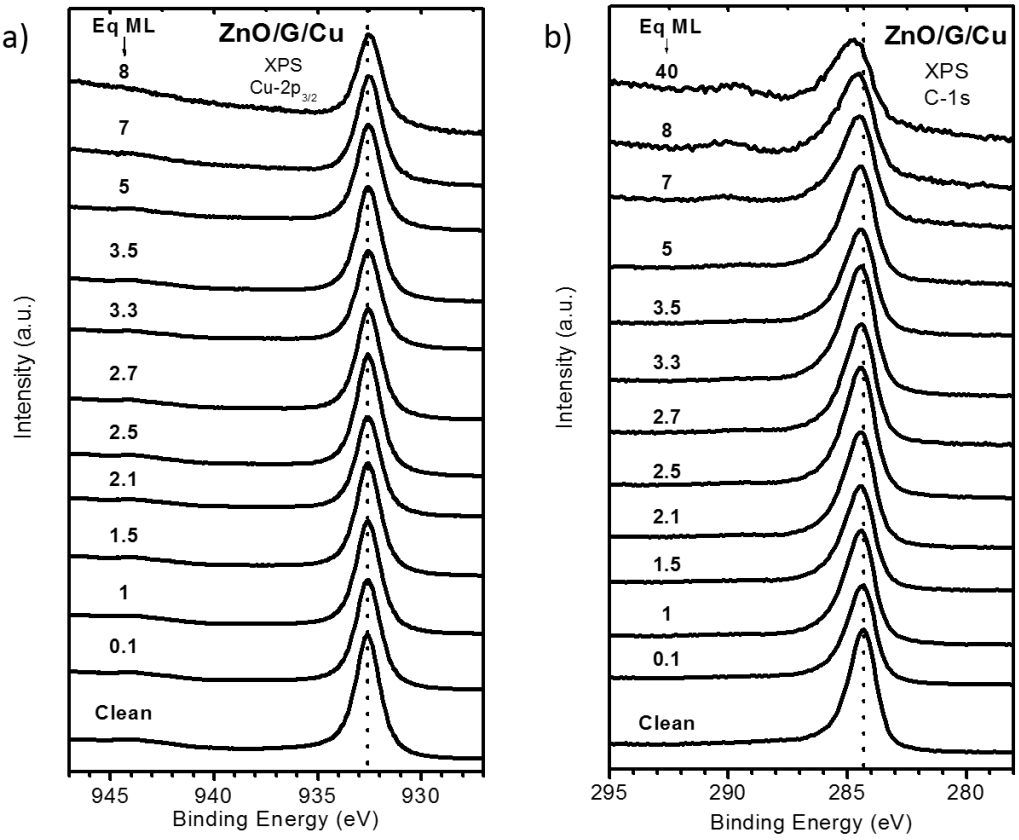

Figure 4.29 a) XPS Cu $2p_{3/2}$ spectra as a function of the coverage for the growth of ZnO on graphene on polycrystalline copper; b) XPS C 1s spectra as a function of the coverage for the growth of ZnO on graphene on polycrystalline copper.

Regarding the contributions from the substrate, Figure 4.29 shows the XPS Cu $2p_{3/2}$ (a) and C 1s (b) spectra as a function of the coverage. Although in next sections 4.3.2 and 4.3.3 both, the clean substrate and its modification by the ZnO deposit, will be discussed, in these raw spectra we can see some interesting features. First of all, the Cu

$2p_{3/2}$ did not change in energy position and width. In addition, the absence of strong shake up satellites discarded the presence of CuO (Cu^{2+}), and limits the oxidation state of Cu to Cu^0 or Cu^+, as both states share almost the same spectrum. On the other hand, the C 1s spectra remains almost with the same qualitative shape, although there is a slight shift to higher binding energies and a development of C-O and C=O bonds.

4.3.2 Initial chemical state of graphene

This section will deal with the chemical and structural characterization of the as received graphene/Cu sheets which have been used as substrates for the ZnO growth. The chemical characterization has been carried out by different XPS systems, moving from large spots (1 cm^2, giving an average measured of the whole sample) to progressive smaller analyzed areas (hundreds microns and nanometers). In this way, local chemical inhomogeneities can be correlated to the inhomogeneities seen in the previous ZnO growth. These XPS measurements were combined with Raman spectroscopy mappings, letting us the correlation between graphene defects, mechanical strain and graphene-Cu electronic coupling with the initial chemical state of Cu, graphene and chemical species intercalated between graphene and Cu.

4.3.2.1 Initial structural and chemical characterization of graphene

The study of the initial chemical and structural state of graphene has become necessary in the light of the observed differences on the ZnO growth for the different graphene/Cu samples grown by CVD with the same equipment and experimental protocol. For instance, Figure 4.30 shows the x5 optical images of two different 1x1 cm^2 graphene/Cu samples which come from the same 2x3 cm^2 sheet. Hence, both have been grown at the same time. Nevertheless, evident differences can be appreciated between the two samples. Although both show a similar distribution of Cu grains, around the same shapes and sizes, the color contrast inside each image between different Cu grains is completely different. In this way, left image shows a very strong contrast perfectly delimited by the grain frontiers, while in the right picture these differences among grains are not so clear (although in some of them this contrast can also be distinguished). Therefore, from these optical images two different types of inhomogeneities can be expected: 1) based on the centimeter scale differences between graphene/Cu samples; 2)

based on the micrometric-nanometric order local differences between Cu grains and the graphene grown on them.

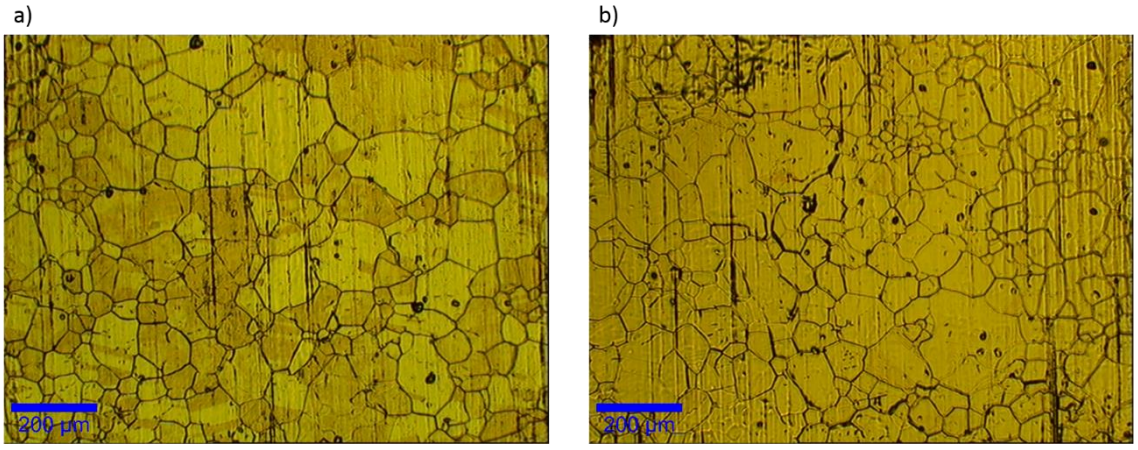

Figure 4.30 x5 magnification optical images of graphene on polycrystalline copper substrates for two different series of CVD growth.

The starting point of the discussion will be the chemical variations between different clean samples. First of all, the reader should remember that this graphene/Cu samples were used *as received* with no cleaning treatment (thermal or ion gun) in order to avoid graphene damage or Zn contamination. As stated previously, this allows to study a three-face problem (graphene- intercalated chemical species- Cu). Taking this in mind, Figure 4.31 shows two representative XPS C 1s and O 1s spectra taken with the CLAM4-Camaron system, which due to its large spot size (around 1 cm^2) gives an average information of the whole graphene/Cu sample. Although each sample had a unique XPS spectra, in particular regarding the O 1s region, the spectra shown in Figure 4.31 are useful to explain the kind of features seen on the complete series of samples (up to 12). The fitting of the initial graphene C 1s spectrum (see Figure 4.31 a) was very similar to the one performed on the HOPG substrate on Chapter 3. It shows a main peak at ~284.4 eV, basically dominated by the carbon atoms bonded on the graphene net by typical sp^2 hybridization [57]. The fitting has been performed using symmetric Gaussian-Lorentzian functions, as indicated elsewhere [58,59], although other authors use asymmetric functions [25,60]. The asymmetry of the graphene peak at higher binding energies has been related to the developing of defects, i.e. the appearance of a new contribution at ~285.5 eV corresponding to sp^3 hybridization. Finally, two more contributions related to C-O and C=O bonds at 286.3 eV and 288.1 eV can be found [58,59]. More complex was

the O 1s spectrum (see Figure 4.31 b), where up to five different contributions can be distinguished (labeled as O_1-O_5). The prominent structure is formed by two main contributions: O_2 at ~530.2 eV corresponding to oxidized copper (Cu_2O) [61], and O_3 at ~531.5 eV which could be related to a wide variety of possible species such as $Cu(OH)_x$, CO_x or H_2O [25,59,62]. These two contributions appear always, although the relative intensities between O_2 and O_3 varies depending on the graphene/Cu samples. The behavior of O_1, O_4 and O_5 contributions is different: they are less intense and not always appear. In general, (with only one exception corresponding to the O 1s spectra shown here), if O_5 is present, then O_4 and O_1 are negligible, and *vice versa*. In this way, the literature indicates different possibilities for these contributions: O_1 at ~527.5 eV could correspond to CO [63] and/or oxygen molecules [64] adsorbed on metal surfaces, O_4 at ~537.0 eV to adsorbed oxygen molecules on carbon surfaces [65], CO adsorbed on metallic surfaces [66] and/or water [67]; and finally O_5 at ~539.5 eV is said to come from oxygen molecules intercalated on the graphite planes [65] and/or water [67]. Therefore, these three contributions can be related to chemical species (O_2, H_2O, CO_x) intercalated between graphene and Cu, with different grades of interactions and bonds in the system C-O-Cu. In fact, the exposure of CVD graphene grown on polycrystalline copper to air implies the immediately intercalation of different types of molecules that can modify the electronic coupling between graphene and Cu [24,25] and, after longer periods of time, the oxidation of the cupper substrates due to galvanic corrosion, where the graphene acts as the cathode [26,27]. However, there is a lack on the study of this type of species, on how they are distributed within the sheet surface, about the chemical interaction between them and the graphene and Cu, and finally how they can influence in the posterior growth of other compounds.

As indicated previously, not all the samples share the same spectra. Figure 4.32 summarizes the fitting results for the C 1s (a) and O 1s (b) spectra in terms of the relative percentage among the different contributions on each region. As it can be appreciated, the C 1s spectra do not present significant variations, dominating the sp^2 contribution in the range of 75-58% and with a low amount of defects or carbon/oxygen bonds. On the other hand, relative percentages of the O 1s contributions have a large dispersion. In general terms, two tendencies could be distinguished. Firstly, the O_2 and O_3 contributions dominate in all cases, although their relative amounts suffer important variations, indicating different grades of Cu oxidation and surface contamination. Secondly, the O_5

contribution is inversely related to O_4 and O_1 contributions, indicating different chemical intercalated species.

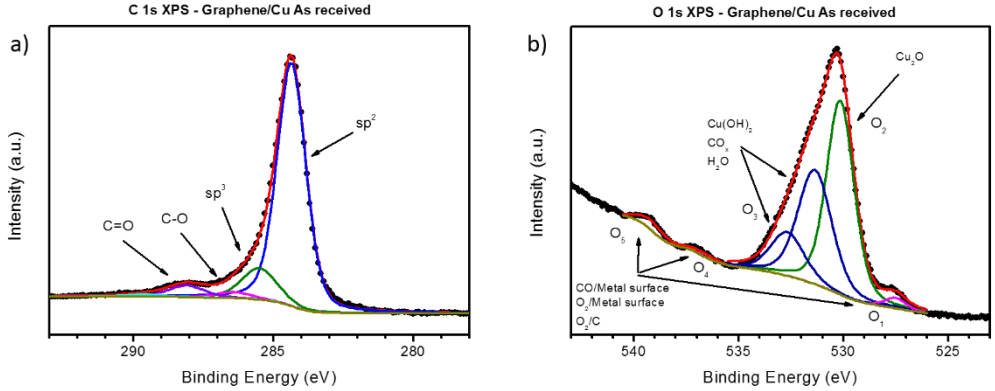

Figure 4.31 a) Characteristic XPS C 1s spectrum of as received CVD graphene on polycrystalline copper; b) characteristic XPS O 1s spectrum of as received CVD graphene on polycrystalline copper.

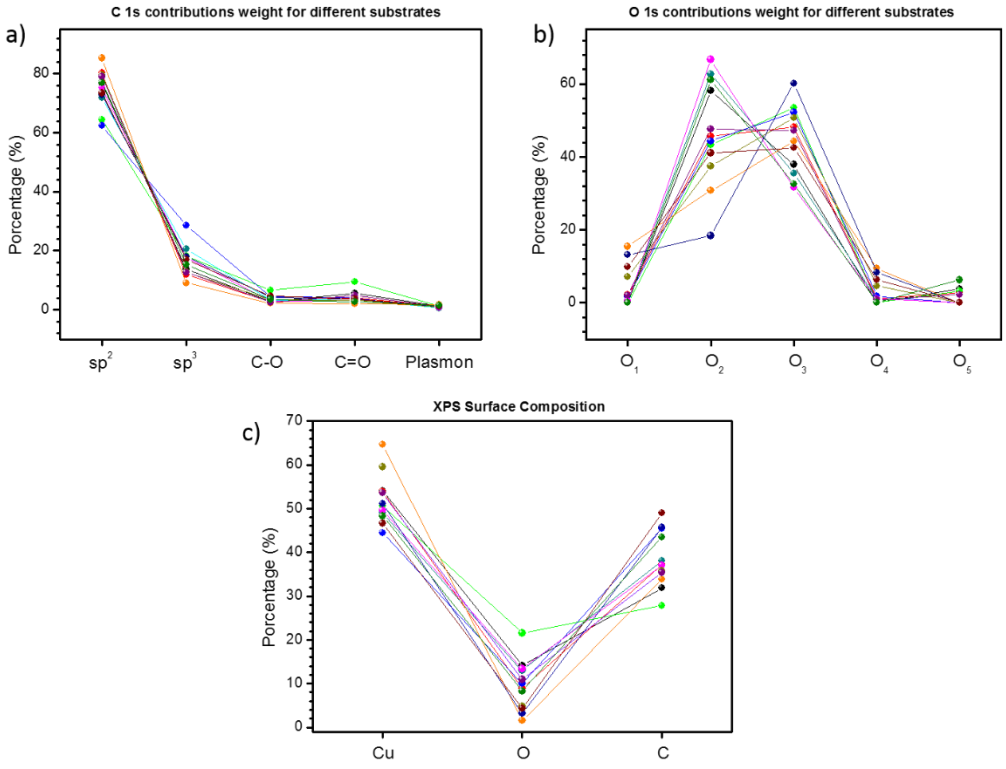

Figure 4.32 a) Percentages of the C 1s contributions after fittings, as in Figure 4.31 a, for a set of as received samples of graphene on copper; b) Percentages of the O 1s contributions after fittings, as in Figure 4.31 b, for a set of as received samples of graphene on copper; c) Surface composition of as-received graphene on copper substrates.

By comparing in Figure 4.32 c the surface concentrations of C, Cu and O, it is confirmed the disparity on the initial chemical state of the graphene/Cu samples due to initial surface contamination after exposure to air, involving the intercalation of different kind of chemical species that modify the oxidation state of Cu and its interaction with graphene. However, the C 1s analysis shows a graphene of good quality that seems really reproducible except for punctual exceptions.

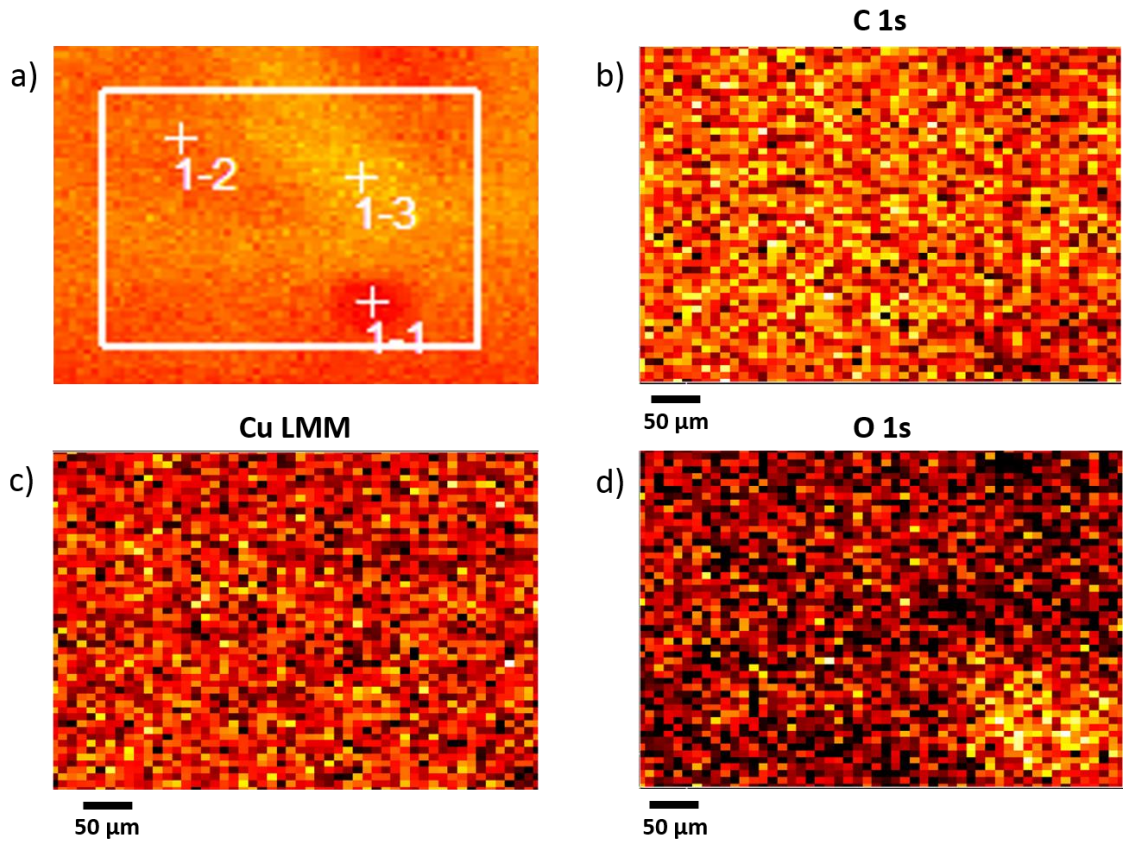

Figure 4.33 a) Image of secondary electrons of graphene on polycrystalline copper. The white square corresponds to the area mapped by XPS in Figures 4.33 b), c) and d) for C 1s, Cu LMM and O 1s regions, respectively. Points 1-1, 1-2 and 1-3 correspond to punctual spectra of Figure 4.34 figure (zones 1, 2 and 3, respectively).

The next step consists in the study of the micrometric inhomogeneities. Figures 4.33 and 4.34 show the XPS measurements performed at SCAI, Universidad de Málaga. The spatial resolution of this XPS instrument was about 10 µm, being able to distinguish differences among the Cu grains. In this way, Figure 4.33 a shows an image of secondary electrons of a clean graphene/Cu sample, where regions with different intensity can be

appreciated, indicating compositional differences. Besides, Figures 4.33 b, c and d correspond to the XPS intensity mapping of the C 1s, Cu LMM and O 1s regions, respectively. No difference can be appreciated for the first two regions, but a really intense spot appears for the O 1s mapping. Taking three individual spectra (positions shown in Figure 4.33 a), the chemical nature of this inhomogeneity is revealed. While the C 1s, Cu LMM and Cu 2p spectra are equivalent for these three coordinates, the O 1s spectra show remarkable differences between the spectrum taken at the right bottom corner (position 1-1) and the other two. In this way, the amount of oxidized Cu is slightly higher, although the relevant increase is associated to the $Cu(OH)_x$ contribution (O_3). In addition, in this regions appears O_5 contribution together with O_1 and O_4 (in the other two spectra only these last peaks appear, not O_5). Therefore, by these measurements it can be confirmed that: 1) graphene has been grown along all the surface with a very good and homogenous quality (at least with the present spatial resolution); 2) there are local inhomogeneities, with the typical Cu grain size, which are related to the oxidation state of Cu and the type and amount of intercalated species.

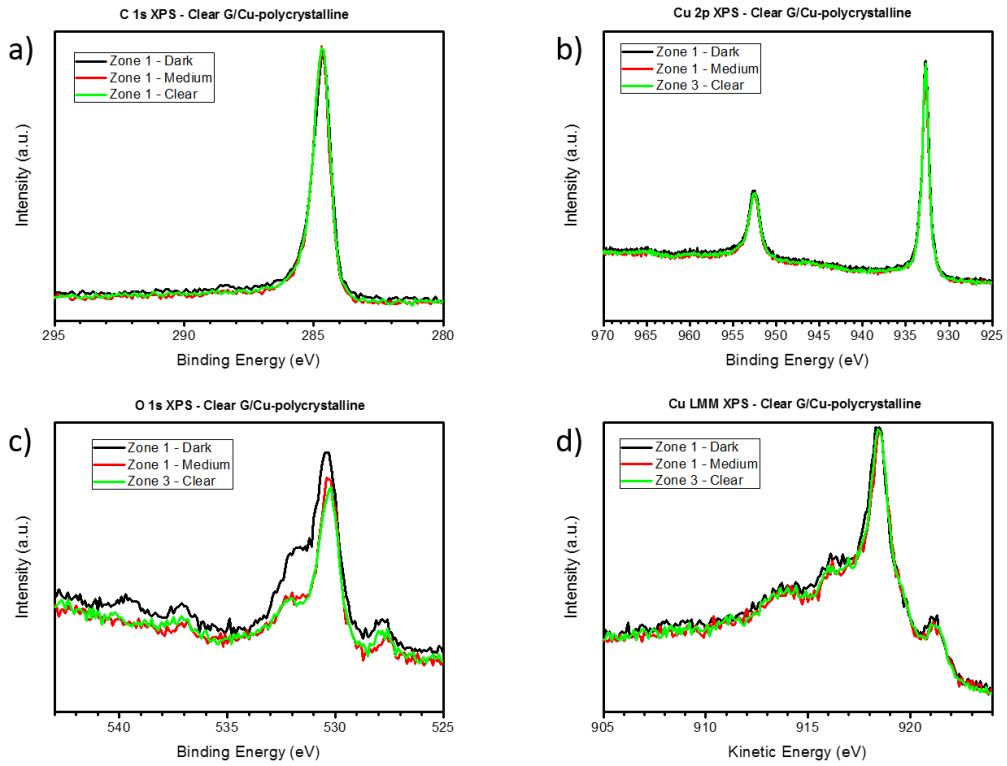

Figure 4.34 a) C 1s spectra of as-received CVD graphene on polycrystalline copper at three different positions as indicated in Figure 4.33 a. The same for Cu 2p, O 1s and Cu LMM regions in b), c) and d), respectively.

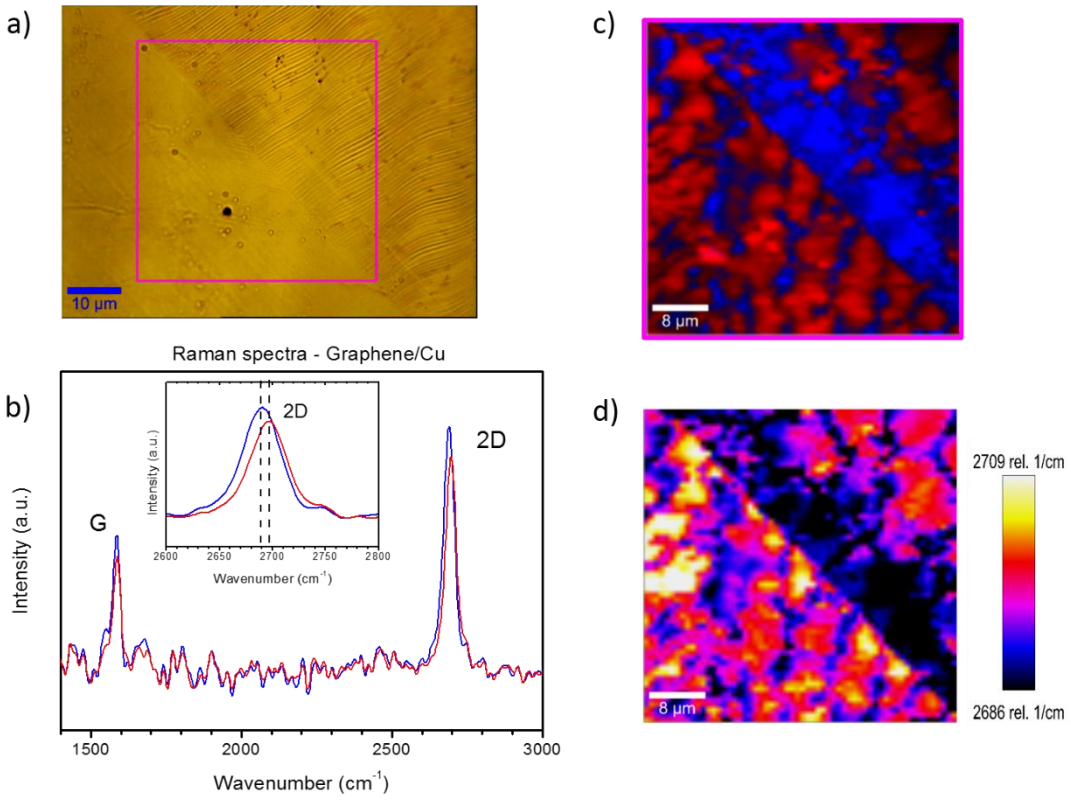

Figure 4.35 a) x100 magnification optical image of as received CVD graphene on polycrystalline copper. Magenta square corresponds to the Raman mapped area; b) averaged Raman spectra of blue and red zones. Inset: 2D band zoom; c) Raman mapping with red and blue colors corresponding to the previous average spectra; d) 2D band shift of the mapped area.

A further investigation of the initial chemical state of the as received graphene/Cu sheets and its homogeneities was done by combination of confocal Raman spectroscopy and XPEEM mappings at the same positions (with ~200 nm and ~30 nm of lateral resolution, respectively). In first place, Figure 4.35 shows the Raman measurements performed inside the magenta square of the optical image (a). As it can be seen, there exists a clear diagonal frontier from top left to bottom right corner, existing difference in the color but also in the roughness between both grains. Raman mapping (b) shows a graphene of good quality, with a spectrum where no D band is measured and the 2D/G ratio is about 2, indicating graphene monolayer [68]. However, the averaged spectra are different at both sides of the frontier (blue and red spectra (b) and areas (c)). The blue spectrum (corresponding to the right side) is slightly more intense than the red one, while the 2D band presents a shift of about 10 cm^{-1} to lower wavenumbers (see Figure 4.35 c).

These features wee respectively related to a change on the electronic coupling with the metallic substrate and a reduction of the graphene strain [27]. More detailed analysis of this behavior can be found in section 4.3.3. Finally, no variations on the energy position regarding the G band are appreciated, indicating the absence of modification of the graphene doping.

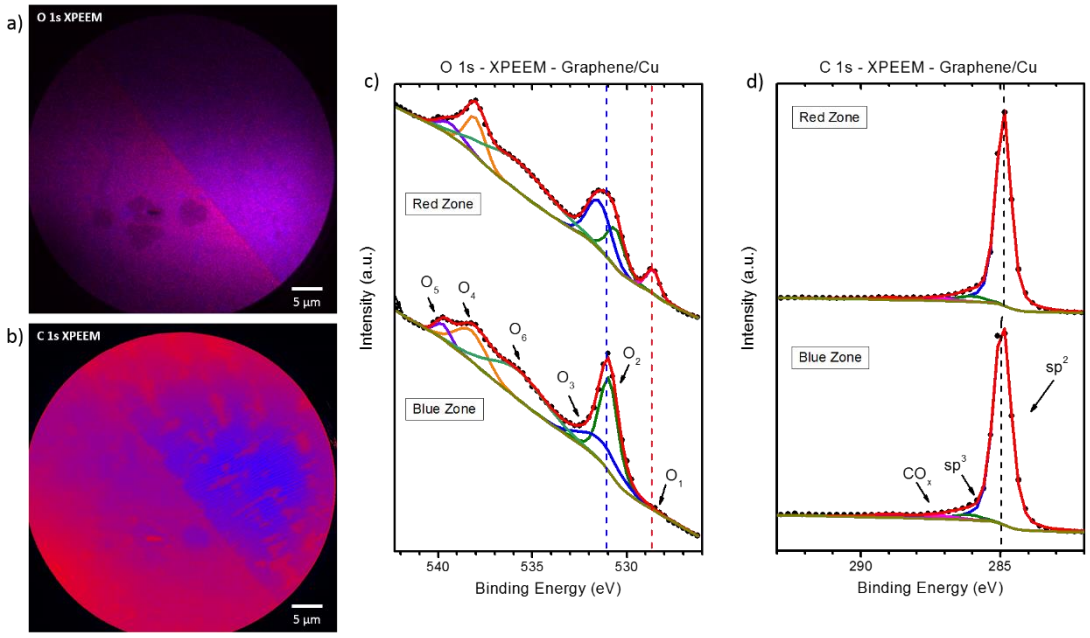

Figure 4.36 a) XPEEM image regarding the O 1s region of as-received CVD graphene on polycrystalline copper; b) XPEEM image regarding the C 1s region of the same zone as before; c) and d) average C 1s and O 1s spectra, respectively, for blue and red areas in a) and b). The measured area was the same as that previously measured by Raman in Figure 4.35.

On the other hand, Figure 4.36 shows the XPEEM mappings and spectra of the O 1s and C 1s regions performed at the same position than the previous Raman measurement. As before, the average spectra at both Cu grains are colored as blue (right) and red (left). The frontier is again clear, indicating chemical differences between both sides. As it can be expected from previous results, the most important differences were found on the O 1s spectra. In addition to the previous O_1-O_5 contributions, a new one labelled as O_6 was necessary in order to correctly fit the spectra. However, its presence and nature is not fully understood. Firstly, it is comparatively broader than the other components, what could indicate a convolution of signals from different chemical

species. In second place, it could be overestimated due to a not perfect background removal. Hence, this O_6 will not be further discussed as it does not offer any special variation between both red and blue areas and that it was not measured by other XPS systems. Therefore, regarding the O_1-O_5 contributions, there are some interesting differences. The blue zone, where the graphene was slightly decoupled from the Cu substrate, presents an increase on the oxidation of Cu (O_2 contribution) while the intercalated species are not so intense, or simply negligible, as O_1. On the other hand, the red area presents the opposite situation, with more intercalated species, less oxidation of the Cu surface and a larger electronic coupling between graphene and Cu. Therefore, it seems plausible that the oxidation of Cu occurs after the intercalation of H_2O and CO_x species, is such a way that after these species oxidize the metal, they vanish from the O 1s spectra. Besides, the oxidation of the Cu substrates promotes the electronic decoupling of graphene [27], drawing a coherent picture of the system graphene/Cu exposed to air. Regarding the C 1s spectra, the sp^2 hybridization dominated, being very low the amount of defects represented by the sp^3 contribution. The only difference between red and blue regions was that for the first case the peak was slightly shifted to higher binding energies. This feature is related to the electronic decoupling of graphene from the Cu and will be discussed in future sections.

In order to study the chemical state of Cu and the thickness of the oxidized layer, XPEEM measurements of the Cu 3d regions at different photon energies were performed. Cu 2p and Cu LMM regions, which may offer more clearly chemical information of the oxidation state better than the valence band, could not be measured due to technical limitations of the beamline regarding the maximum photon energy available and the analyzer specifications. In any case, Figure 4.37 a shows the averaged Cu 3d spectra for the red and blue areas at three different photon energies, from top to bottom, 135 eV, 350 eV and 600 eV (with IMFPs of 3.9 Å, 7.5 Å and 11.45 Å, respectively). For comparison purposes, Figure 4.37 b shows the valence band region of Cu, Cu_2O and CuO taken at the CLAM4-Camaron system with the Al anode. From the reference spectra, the Cu 3d peak position for the metallic Cu^0 and the Cu^{2+} is around 3.15 eV, while the Cu^{1+} is shifted to ~2.80 eV. These positions are indicated in Figure 4.37 a by blue/green and red dashed lines, respectively. Before the discussion, it should be taking into account that the valence band is very sensitive to changes on the photon energy due to the fact that the Cu 3d states are hybridized with the O 2p. Therefore, differences on the hybridization grade and on how the cross section of these orbitals depend with the photon energy can induce changes

on the shape of this region, which are not related to a change on the oxidation state of copper. Thus, these data must be discussed in a qualitative way. The red zone shows an expected behavior with the photon energy, moving the maximum of the peak from the expected Cu_2O position to metallic (the absence of the satellite structure at 10 eV characteristic of the CuO allows to discard this oxide), being this Cu oxidized layer very thin, for sure lower than 1 nm. On the other hand, the explanation seems more difficult for the blue zone. Contrary to what it would be expected, the maximum of the peak shifts to lower binding energies, indicating a greater oxidation below the surface. Nevertheless, this kind of sub-surface oxides are reported in the literature [69].

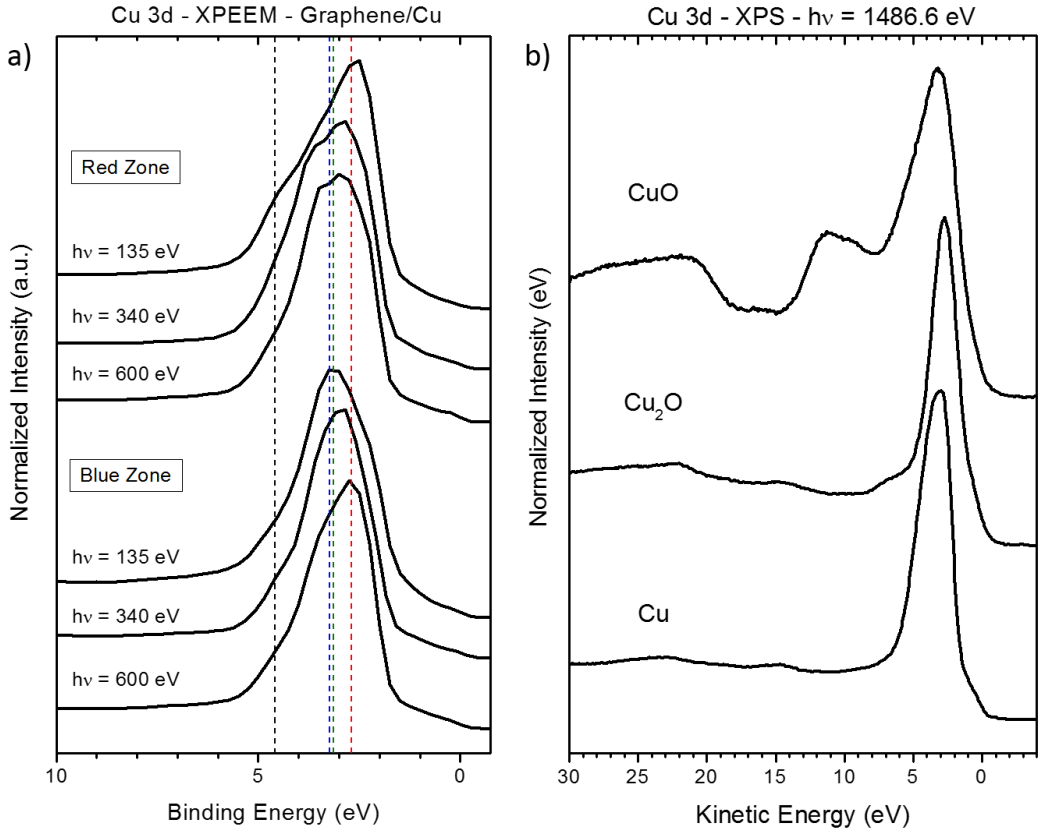

Figure 4.37 a) Average of the copper valence band region for red and blue zones of Figure 4.36 at different photon energies; b) Copper valence band region for metallic (Cu^0) and copper oxides (Cu^{1+} and Cu^{2+}).

The same Raman and XPEEM measurements were performed in a second position of the same graphene/Cu sample, as shown in Figures 4.38 and 4.39. In this case the mapped area is inside a Cu grain, where two parallel and straight lines delimit a vertical

rectangle in the center of the optical image (Figure 4.38 a). Two different Raman average spectra are depicted in Figure 4.38 b. The red one corresponds to monolayer graphene, the intensity ratio 2D/G < 2 as well as the change of the shape of the 2D band of the blue spectrum indicates that it corresponded to multilayer graphene. In fact, as it can be seen from Figure 4.38 c, the vertical rectangle drawn in the Cu grain is the area where graphene has grown in a more defective way, i.e. multilayer.

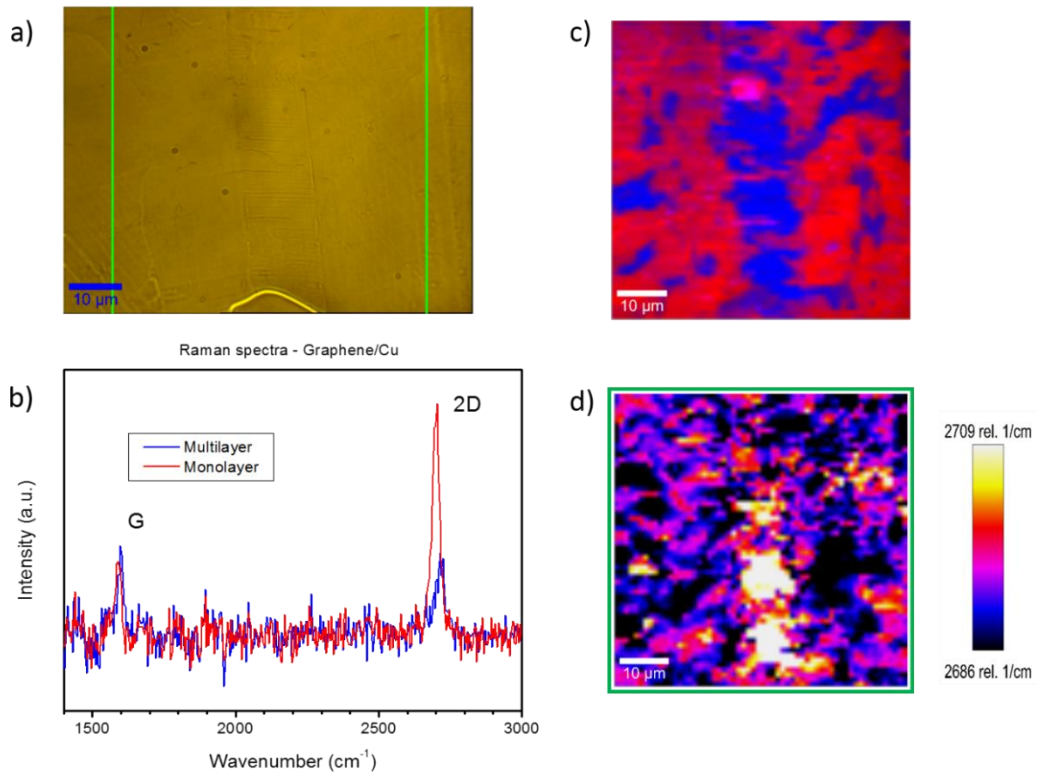

Figure 4.38 a) x100 magnification optical image of as received CVD graphene on polycrystalline copper. Green square corresponds to the Raman mapped area; b) average Raman spectra of blue and red zones. Inset: 2D band zoom; b) Raman mapping with red and blue colors corresponding to the previous average spectra; d) 2D band shift of the mapped area.

XPEEM measurements for the O 1s and C 1s regions shown in Figure 4.39 also confirm the Raman measurements. Better laterally resolved than before, the C 1s mapping (see Figure 4.39 b) shows three zones along the previous rectangle that are multilayer graphene. Considering the C 1s spectra, it is very clear how these multilayer areas have broadened the main peak, including a development of defects. The widened of the sp^2 contribution can be explained in terms of the interaction between different stacked

graphene layers, so each of them, although all are characterized by sp^2 hybridization, contribute in a slightly different energy position, broadening the main peak. On the other hand, the oxidation of Cu is much less effective under these multilayer graphene, as it can be seen in Figure 4.39 c, although there are intercalated species. This could be related to the role of graphene as cathode in the galvanic corrosion of Cu, so in the multilayer system this behavior is blocked.

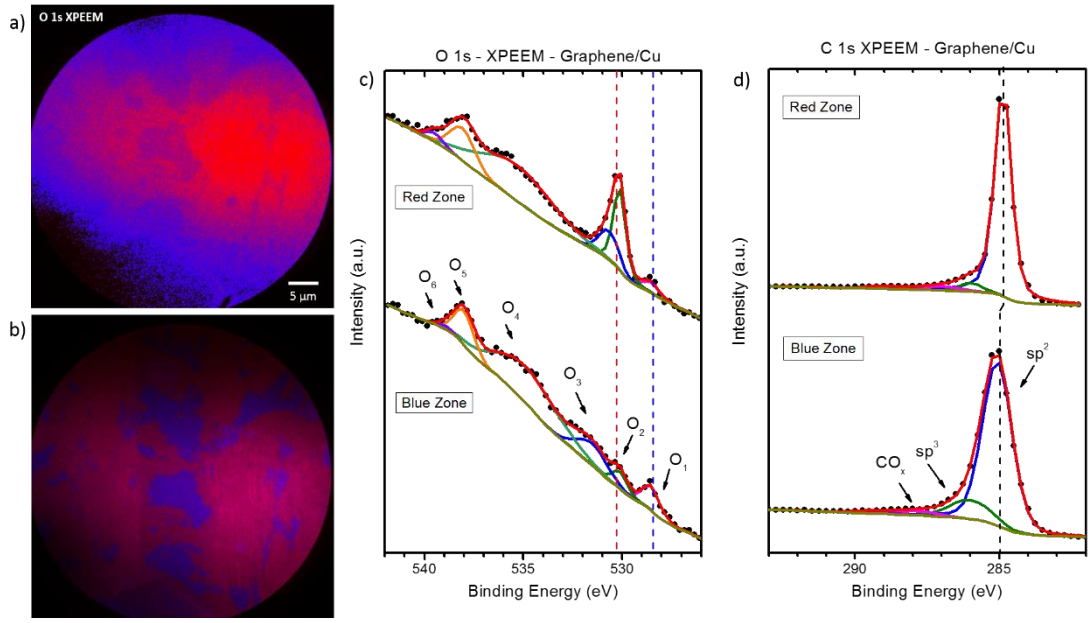

Figure 4.39 a) XPEEM image regarding O 1s region of as-received CVD graphene on polycrystalline copper; b) XPEEM image regarding C 1s region of the same zone as before; c) and d) average C 1s and O 1s spectra, respectively, for blue and red areas of 4.36 a and b figures.

There are some reports describing differences on the growth of graphene by CVD on Cu regarding the crystallographic direction and the topography of the Cu metallic surface. In this way, nucleation rate and growth velocity, and so the size of graphene domains and the amount of defects, may depend on the crystallographic direction [58]. It has been demonstrated that multilayer graphene typically grows on the Cu ridges, while monolayer graphene does in the trenches [70,71]. As the intercalation of chemical species between graphene and copper, and consequently the oxidation of the metallic substrate, depend on the number and distribution of graphene defects [24,25,26], the polycrystalline nature of the Cu sheet may be the base of the chemical inhomogeneities reported until this point.

4.3.2.2 Influence of the initial graphene inhomogeneities on the subsequent growth of ZnO

In previous subsection the initial chemical and structural sate of the graphene/Cu substrates has been discussed, concluding that although graphene has good quality and covers completely the sheet, there exists initial inhomogeneities mainly related to the chemical species intercalated between graphene and Cu, affecting to the oxidation of the latter and the electronic coupling between both. Next pages will deal with the ZnO growth and how it is affected by these local differences. The explanation is divided into four points: the two first are devoted to the characterization of the ZnO growth on graphene/Cu using *in situ* XPS and *ex situ* Raman spectroscopies, showing that the oxide growth is effectively affected. On the other hand, it will be discussed how modifying the substrate state, the ZnO growth characteristics could be modified and controlled. Finally, the role of Cu without graphene in the ZnO deposition is discussed.

- ***In situ* growth: an XPS study**

Figures 4.40 and 4.41 show two series of simultaneous ZnO deposition up to 3.5 Eq-ML on three 1x1 cm^2 graphene/Cu substrates performed at the CLAM4-Camaron system. Each of these two trios came from the same graphene/Cu sheet, and the deposition methodology (time and temperature) was the same. Therefore, two level of differences are expected: 1) comparing the two series, as they have been grown by CVD in two different moments, the graphene/Cu sheet is expected to show differences between them, what can translate in differences in the ZnO growth; 2) comparing the three samples for each series, as the growth is simultaneous, difference on the growth of ZnO can only be related to substrate influences. In this way, series of Figure 4.40 shows a graphene with a low rate of carbon-oxygen bonds and at the same time a low amount of defects, with the exception of substrate 1. Regarding the O 1s spectra, the main contribution is due to the Cu_2O, while for the intercalated species O_5 is negligible. Again, only in substrate 1 the O_3 contribution in larger, possibly indicating more surface contamination, in correlation with the greater number of defects. On the other hand, the second series depicted in Figure 4.41 shows more carbon-oxygen bods in the C 1s spectra, in any case with a low number of defects. As before, in the case of the O 1s spectra, the Cu_2O contributions dominates, but the most important difference with the previous series is that now (except for substrate 3) from the intercalated contributions only O_5 appears.

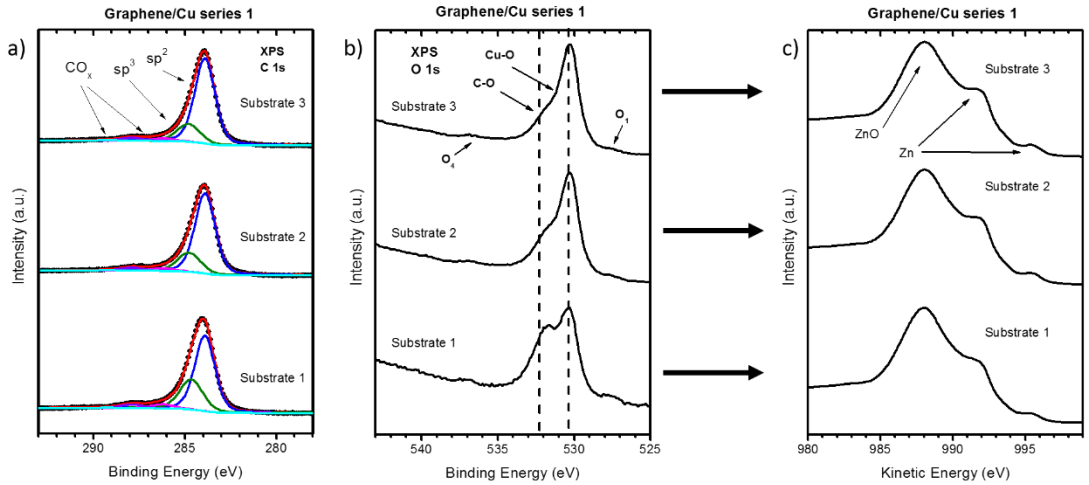

Figure 4.40 Series 1 of CVD graphene on polycrystalline copper. a) XPS fitting of C 1s region of as-received graphene; XPS O 1s region of as-received graphene; d) Zn LMM region after ZnO deposition. ZnO deposition was performed simultaneously on the three substrates of series 1.

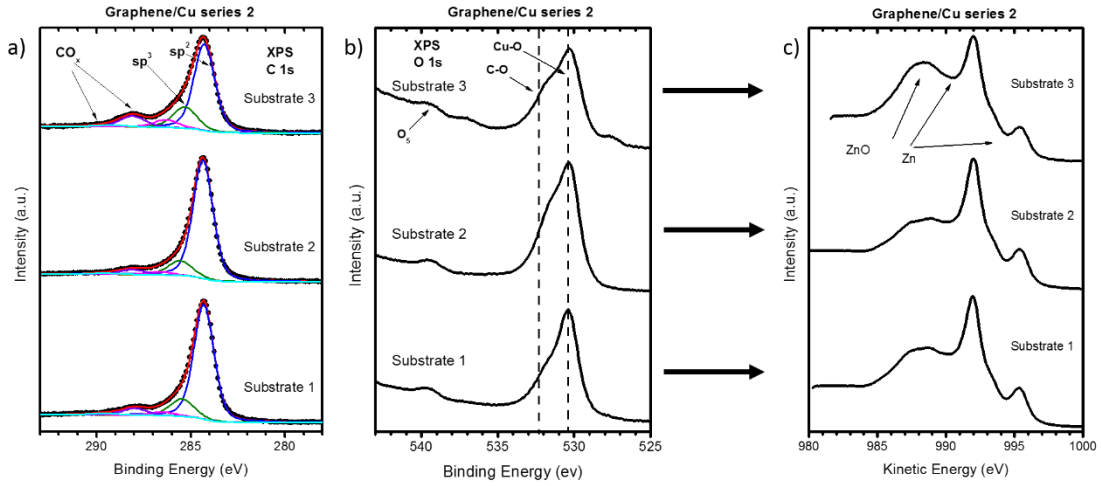

Figure 4.41 Series 2 of CVD graphene on polycrystalline copper. a) XPS fitting of C 1s region of as-received graphene; XPS O 1s region of as-received graphene; d) Zn LMM region after ZnO deposition. ZnO deposition was performed simultaneously on the three substrates of series 2.

As stated before, the ZnO growth can be chemically well characterized by measuring the Zn LMM Auger region, as shown in plot c of both Figures 4.40 and 4.41. Interesting results are obtained. Between both series, the Zn/ZnO ratio is completely

different, dominating the oxide state (Zn^{2+}) on series 1 and the metallic Zn on series 2. On the other hand, there are also differences between substrates of the same series. For example, in series 2 substrate 3 (where not only O_5 contribution, but also O_1 and O_4 appear), the amount of ZnO increases. Therefore, from these results in addition to more growths of ZnO on individual graphene/Cu substrates using the same deposition methodology but not shown here, several interrelationships can be inferred, confirming the influence of the chemical initial state of graphene/Cu, especially regarding the intercalated species (taking into account these facts, on subsection 4.3.3.3 is proposed a detailed chemical path of the ZnO/Zn growth on graphene/Cu):

- As O_3 increases compared to O_2, then the ZnO growth is slower, allowing a greater oxidation of Zn.
- In addition to the previous point, if O_1 and O_4 appear, then the growth is also slower and ZnO dominates.
- If O_5 dominates, then the growth is quicker and the metallic state dominates.
- No reciprocity between the C 1s spectrum of graphene and the ZnO growth could be inferred.

- ***Ex situ* Raman characterization**

This point is devoted to the *ex situ* Raman characterization of 3.5 Eq-ML of ZnO grown on graphene/Cu. This coverage has been selected because it allows the simultaneous measurement of both graphene and ZnO, as for lower deposits the ZnO bands are invisible whereas for greater coverages the graphene signal is hidden by the oxide. Figures 4.42, 4.43 and 4.44 show the measurements performed on three different samples, being 4.43 and 4.44 from substrate 1 and 3 of series 1 and 2, respectively. So, starting with Figure 4.42, the optical image (a) shows the frontier between two Cu grains. The Raman mapping was performed inside the red box. The average spectrum is depicted in Figure 4.42 b, where the band defects of ZnO (red) is very intense, while the 2D (blue) band has low intensity due to the high electronic coupling with Cu. Besides, Figures 4.42 c and d show the intensity of these two bands, being very clear the frontier between the two grains. In fact, in the darker grain the graphene 2D intensity is larger but also the ZnO signal (on the contrary, it would be expected that if the amount of ZnO is greater, then the signal from the substrate should be less intense). Therefore, the greater intensity of

the 2D band is related with a reduction on the electronic coupling with Cu (as previously analyzed for clean graphene/Cu substrates), what induces an increase on the ZnO deposition. Figure 4.42 e shows the AFM image of this same position. A white dashed line has been drawn along the frontier in order serve as an eye guide. The number and size of clusters is greater on the left side, with an average roughness of 8.3 nm in this area, in comparison with the other side, where the roughness is 7.5 nm. Hence, there are local inhomogeneities on the growth of ZnO which seem to follow the previous inhomogeneities observed on the graphene/Cu sheets.

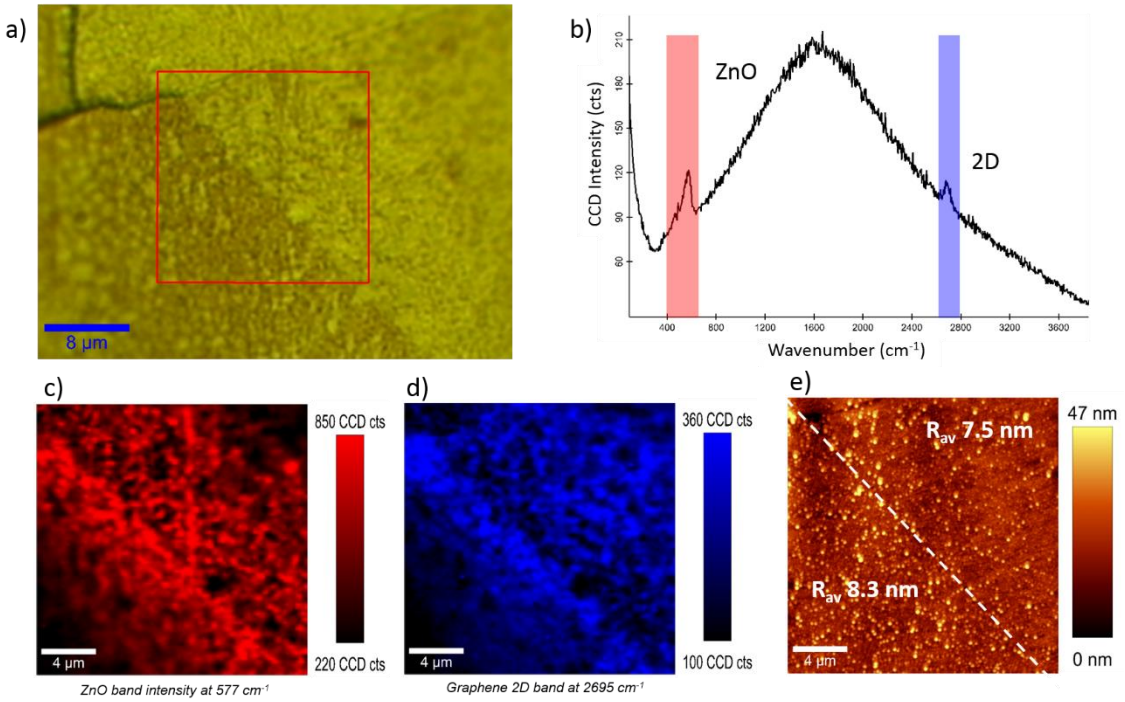

Figure 4.42 a) x100 magnification optical image of a sample with 3.5 Eq-ML of ZnO on graphene on copper; b) average Raman spectrum of the red square area of Figure 4.42a. In red ZnO band, in blue 2D graphene band; c) ZnO and d) 2D bands intensities of the same mapped area; e) AFM topography image of the same mapped area, where R_{av} indicates average roughness.

Figure 4.43 shows similar results to the previous 4.42 images. In this case the initial substrate was carefully characterized by means of XPS (see Figure 4.40) and after the growth by XPS and Raman spectroscopies and AFM measurements. In this way, the graphene/Cu Raman mapping shows areas where no signal from graphene are measured (b), corresponding in the optical image (a) to the clear zones. In addition, two different

spectra regarding the graphene have been obtained: monolayer graphene with an intense D band, indicating the developing of defects after the ZnO deposition (red), and graphene oxide, where the 2D ban is vanished and D and G bands are broadened [72]. Previous XPS and XPEEM measurements confirmed that graphene was grown over the whole Cu sheet, so the absence of Raman signal in the clear zones must be explained in terms of electronic coupling with the Cu. Taking a look to the ZnO band of defects on (c), there is clearly more deposition on the darker zones, i.e., where the graphene or graphene oxide is decoupled from the metallic substrate (as proposed in the discussion of Figure 4.42). The difference between the graphene and the graphene oxide regarding the intensity of the ZnO band is due to the focus of the microscope, not to differences on the deposition, as it was confirmed by AFM measurements. In this way, Figures 4.43 e-h show by AFM the ZnO growth variation between coupled and decoupled graphene areas. In fact, a step of around 20 nm between both zones has been measures in (h).

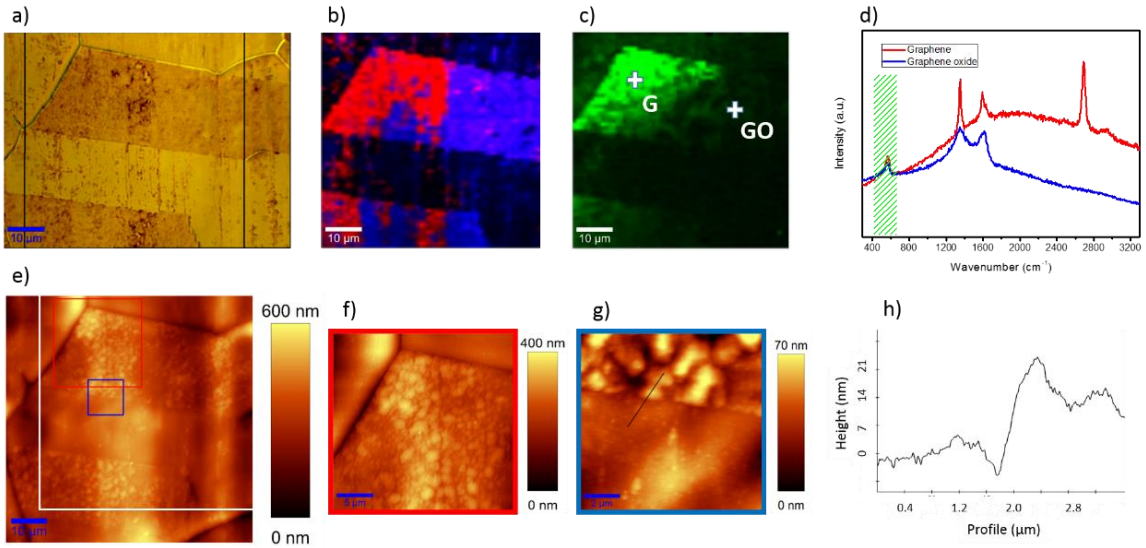

Figure 4.43 a) x100 magnification optical image of a sample with 3.5 Eq-ML of ZnO on graphene on copper. Black square corresponds to area mapped by Raman spectroscopy; b) and c) Raman mappings of graphene and ZnO, respectively; d) Raman spectra of the crosses depicted on figure c, G (red) and GO (blue). In green ZnO band shown in figure c. e) AFM topography image of figure a. White square corresponds to the mapped area. Red and blue squares correspond to AFM topography images f) and g). Figure h) present the AFM profile depicted in figure g.

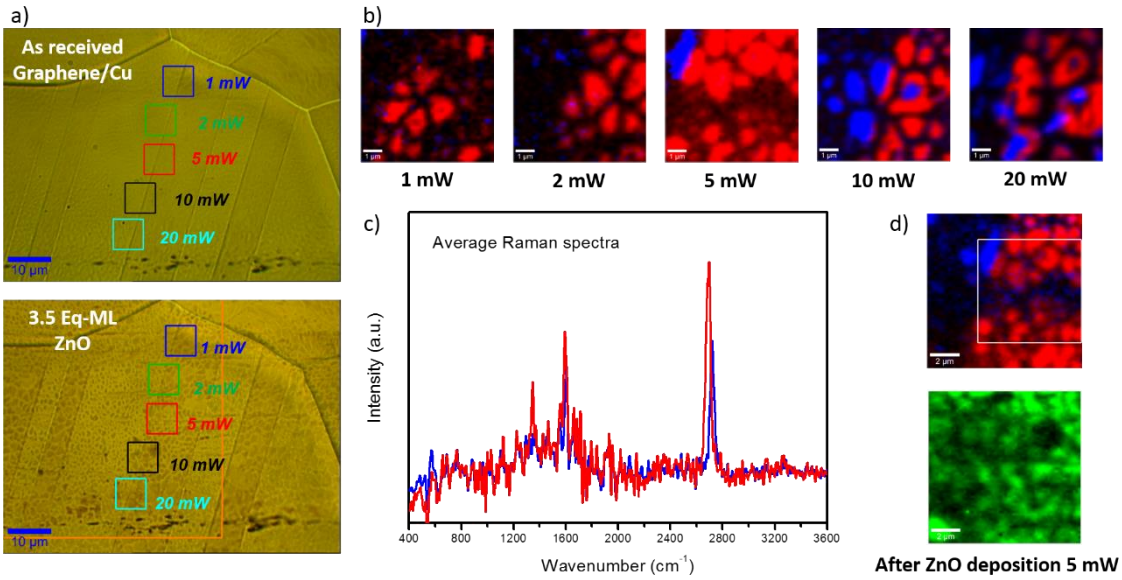

Figure 4.44 a) x100 magnification optical image before (top) and after (bottom) deposition of 3.5 Eq-ML of ZnO. Each square corresponds to the mapped area at a particular laser power, as indicated; b) Raman mappings at different laser power; c) Raman spectra corresponding to blue and red areas from the mappings; d) 5 mW mapping after ZnO deposition, in green ZnO band intensity.

Whereas XPS measurements are not destructive, confocal Raman spectroscopy focuses a lot of power in a localized position, existing a high risk of heating and modifying the sample, or even burning it out. In order to discard possible influences from the laser power on the measurements of clean graphene/Cu sheets or later ZnO/graphene/Cu samples, Figure 4.44 shows the results of the experiment performed on substrate 3 of series 2 of Figure 4.41, where the same positions were measured before and after ZnO deposition with different laser powers. Figure 4.44 a shows before (top) and after (bottom) optical images, with the colored squares indicating the mapped areas at different powers. Regarding the graphene spectra, no difference where reported using different laser powers, and after the ZnO deposition no important differences could be seen beyond a small development of defects. Figures in 4.44 b show the Raman mapping of clean graphene/Cu, performed along the straight line which seems to delimit different Cu domains in the optical image. As previously discussed, two averaged Raman spectra were obtained (see Figure 4.44 c), again following the same pattern: the red one is a more decoupled graphene, more intense and with the 2D band shifted to lower wavenumbers due to a reduction of graphene strain. From the mappings shown in (b), it is clear that

these two spectra are related to the different domains of Cu. In fact, some of these measured "graphene islands" were disposed at both sides of the Cu domains, showing these two different spectra (for example, in the 5 and 10 mW mappings this behavior is evident). As before, the areas where no graphene was measured was due to a very strong electronic coupling between graphene and Cu.

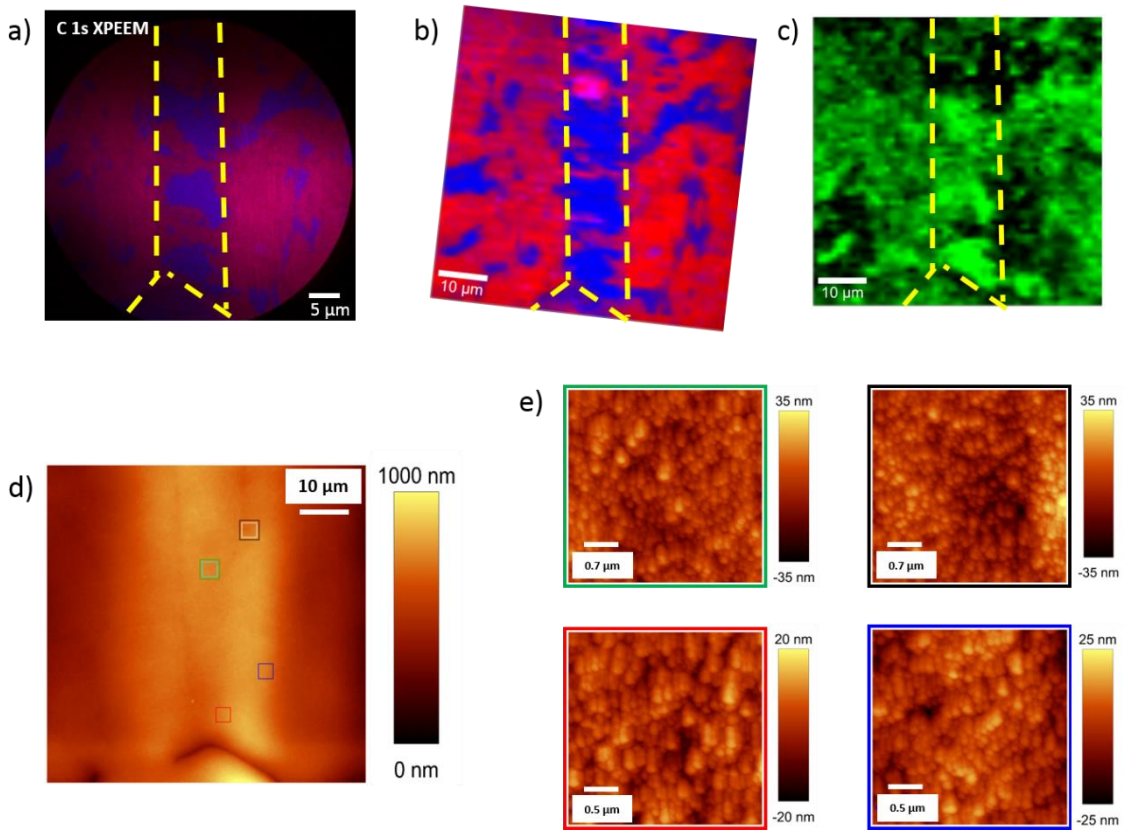

Figure 4.45 a) Taken from Figure 4.39, XPEEM image regarding C 1s region; b) Taken from Figure 4.38, Raman mapping of the same area with monolayer (red) and bilayer (blue) areas; c) Raman mapping of the ZnO band intensity after oxide deposition; d) AFM topography image of the same mapped area. The green, black, red and blue squares correspond to AFM images of figure e), corresponding to left top, right top, left bottom and right bottom, respectively.

Finally, once the ZnO was deposited, although the graphene did not show any change, ZnO was burned out and destroyed with laser powers greater than 5 mW (not shown here). However, Figure 4.44 d shows the intensity mappings of both graphene 2D band (for both average spectra) and ZnO defects band. In this case, no correlation between the measured graphene islands and the growth of ZnO could be measured. However, from

Figure 4.41 c it is known that this deposit has a large amount of metallic Zn, which is invisible to Raman spectroscopy. Therefore, the correlation between initial graphene state and local growth of ZnO may be hindered by the presence of metal Zn, as no information regarding its position can be inferred from these measurements.

Finally, Figure 4.45 shows the results of the last experiment, in which the initial graphene/Cu substrate was completely characterized by means of XPEEM (a) and Raman (b) mappings, and afterwards, the ZnO growth was performed and then the same position was measured by Raman spectroscopy. The initial state was previously discussed in Figures 4.38 and 4.39. Figure 4.45 c shows the ZnO defects band (green), and as it can be appreciated, there is more signal in the areas where multilayer graphene was grown. This fact confirmed a clear influence of the initial chemical and structural state of graphene on the later growth of ZnO. This issue is very important as it may difficult the controlled growth of interesting metal oxides, leading to differences on both, morphological (size of clusters, roughness, thickness) and chemical (composition, metallization, defects) fields. Finally, the AFM images of Figures 4.45 d and e do not offer any especial new result. The deposit in this area of the sample was sadly greater than 3.5 Eq-ML (being unable to measure the graphene Raman spectra), and so the ZnO clusters were very similar independently of the measured area. Therefore, as it would be expected, the differences on the growth of ZnO by the influence of the substrate are really important in the early stages of growth and not so much for thicker deposits.

- **Control of the ZnO growth by modifying the initial graphene**

At this point, if the local state of the graphene/Cu substrate determines the growth characteristics of ZnO, then the modification of the substrate would be able to control de growth of the oxide. This idea has been attempted by artificially uncouple the graphene from the metallic sheet, and subsequently growing ZnO simultaneously on both coupled and decoupled graphene/Cu substrates. The decoupling has been reached by water immersion of the sample during 12 hours, allowing the formation of a thin layer of Cu_2O between metallic Cu and graphene, and thus ceasing the electronic interaction between metal and graphene [27]. More information about this procedure and further consequences on both, graphene and Cu, is presented and discussed in section 4.3.3. Figure 4.46 shows the XPS C 1s (a), O 1s (b) and Cu LMM Auger (c) regions of these two substrates: substrate 1 refers to the as received graphene/Cu sheet taken as reference

and substrate 2 the as received graphene/Cu sheet before and after being decoupled. Both sheets were growth from the same polycrystalline Cu sheet during the same CVD process. As these C 1s spectra show, both as received substrates are nearly equivalent: with a main C 1s peak at the typical energy position of sp^2 hybridization, with low number of defects and carbon-oxygen bonds. Also the oxygen spectra are quite similar, dominating the Cu_2O peak and with only the O_1 and O_4 contributions from intercalated species. Concerning the Cu LMM spectra, the metallic state clearly dominates, being only residual the oxide species. However, this picture changes after the decoupling treatment. The C 1s spectra widens out and suffers an energy shift to higher binding energies related to the decoupling of graphene. Due to the oxidation of copper, both O 1s and Cu LMM are modified, increasing the Cu-O contribution and vanishing the peaks from intercalated species in the first case, and showing a mixture between Cu^0 and Cu^{1+} spectra in the Auger region of Cu. Therefore, even preserving the graphene quality, the substrate has evidently changed. Raman spectrum referred to the electronic decoupling is also shown in Figure 4.53.

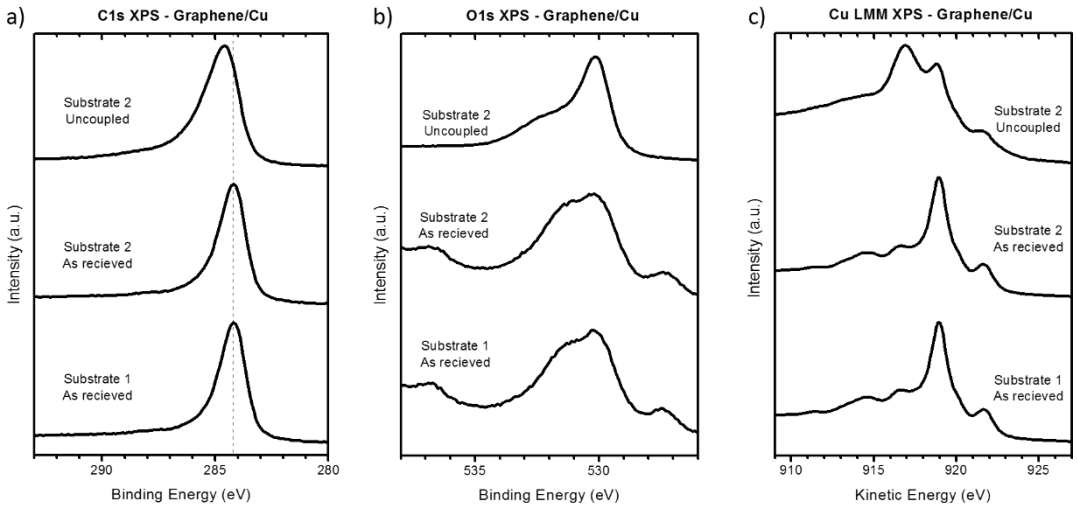

Figure 4.46 In all cases, from bottom to top, as received graphene/Cu substrate (control sample), graphene/Cu substrate as- received and same sample after graphene decoupling by water immersion. a) XPS C 1s region spectra; b) XPS O 1s region spectra; c) XPS Cu LMM region spectra.

The ZnO growth was performed simultaneously on both substrates and measured *in situ* by XPS in the CLAM4-Camaron system. As Figure 4.47 shows, there are

differences on the surface concentrations of zinc, oxygen, carbon and copper. Regarding the ZnO growth, after performing the evaporation in position 1 (M1, see section 2.5.1.2 of Chapter 2), there was almost no deposition of ZnO on the decoupled graphene in comparison to the control sheet, dominating ZnO over metallic Zn. Further deposition on stage 3 (M3), almost cover completely the sample, although again the deposition rate is lower for the decoupled graphene. Therefore, even if there are not important quantitative differences, it seems clear that the growth rate has been modified by externally changing the chemical state of the substrate.

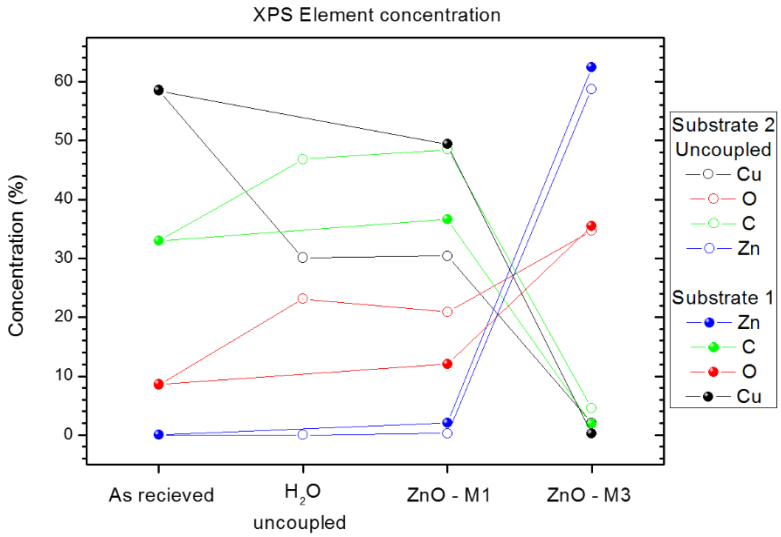

Figure 4.47 Surface composition for the two graphene/Cu substrates (control -1- and decoupled graphene -2-) at different stages of growth of ZnO. Both depositions where performed simultaneously.

Nevertheless, the most impressive results are related with changes on the morphology of the ZnO deposit. Figure 4.48 shows the SEM images of ZnO grown on coupled graphene/Cu (a) and on decoupled graphene/Cu (b). The size of the clusters in the second case increases almost a 100%, from ~34 to ~63 nm. This fact could indicate a change on the early stages of growth, being able a less number of nucleation sites on the decoupled graphene. Besides, the ZnO oxide film is not uniform and compact in the decoupled substrate, as some holes between clusters can be appreciated. Figures 4.49 a, b and c constitute a detail of the ZnO growth on the decoupled substrate at the frontier

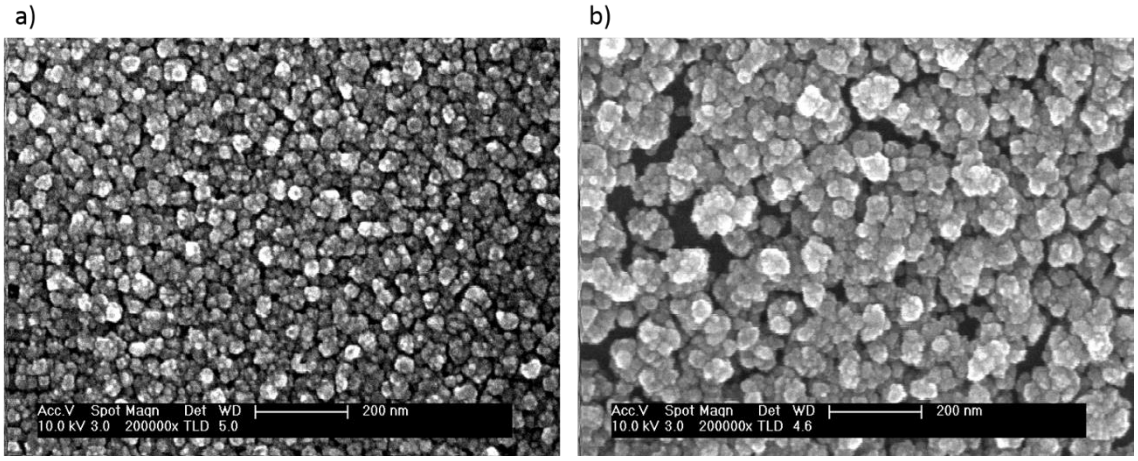

Figure 4.48 x200000 magnification SEM images of a) ZnO on coupled graphene/Cu substrate (control) and b) ZnO on decoupled graphene/Cu by initial water immersion. Both depositions where performed simultaneously.

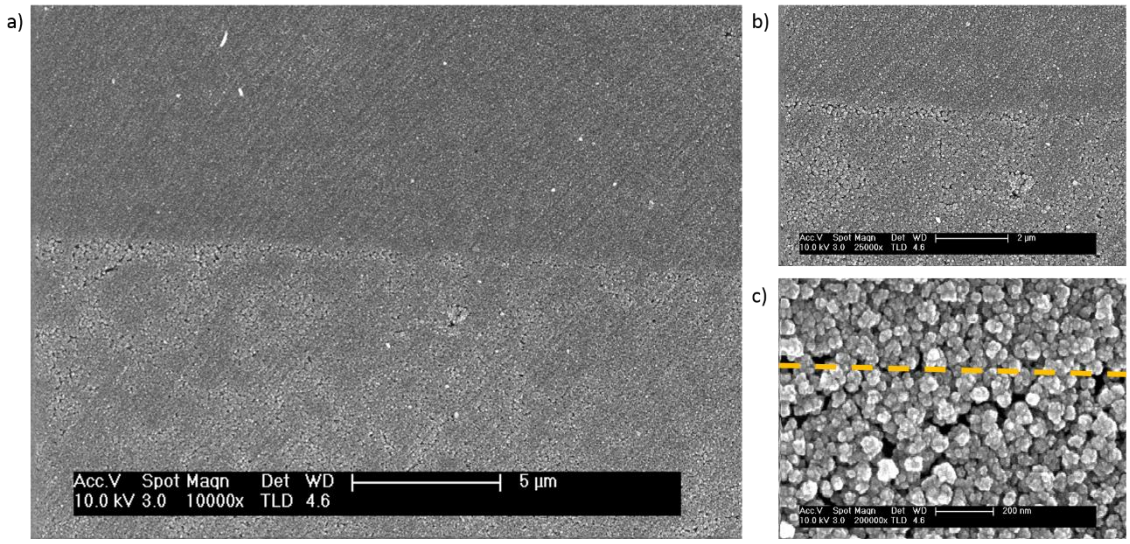

Figure 4.49 a) x10000 magnification SEM image of ZnO deposited on decoupled graphene/Cu by initial water immersion. Two regions are clearly differentiated corresponding to wet graphene (bottom) and dry graphene (top). b) and c) x25000 and x200000 magnification SEM images, respectively, of the same frontier area.

between the immersed side (bottom) and the graphene/Cu kept outside the water. Figure 4.49 a perfectly shows the mechanized roughness of Cu sheets (diagonals from left bottom corner to right top corner). In addition, the frontier between *wet* (bottom) and *dry* (top) graphene can be clearly appreciated. Figure 4.49 c shows that although the clusters have the same size at both sides, the thin film is compact on the dry side. This could indicate that the graphene breaks up in smaller domains during the immersion treatment,

leading to a fragmentation of the ZnO film as this initial defects could slow down the nucleation process at those sites.

With this experiment it was demonstrated that the initial graphene/Cu state influences and determines the ZnO growth characteristics. These can also be controlled by the modification of the initial nature of the graphene. Therefore, the initial issue regarding local inhomogeneities due to the polycrystalline nature of the Cu sheet and the later inhomogeneous growth of graphene may turn to a reversible problem. This opens a new path in the study of the growth of different kind of compounds on graphene, including of course ZnO, on dealing with applied devices.

- **Influence of other parameters on the growth: the chemical state of copper**

Until now the graphene/Cu substrate has been considered as a unique system, although the electronic interaction between both elements can be modulated and the oxidation state of the metallic sheet can be altered by the cathode role of graphene and the presence of different intercalated species between graphene and Cu. However, it has not been discussed separately the influence on the ZnO growth of graphene and Cu, and which of them plays the key role.

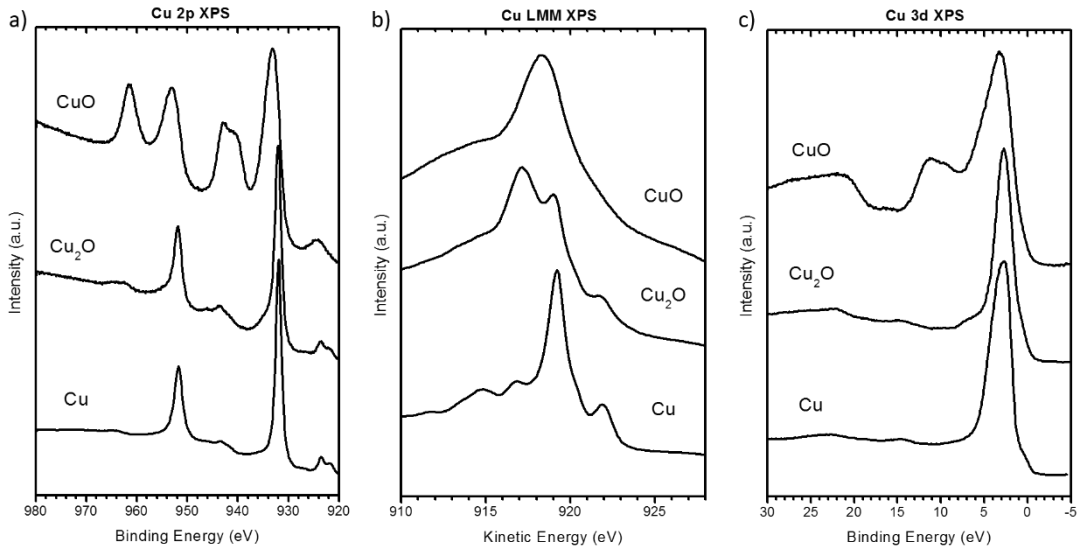

Figure 4.50 In all cases, from bottom to top as labelled, metallic Cu, Cu_2O and CuO a) XPS Cu 2p region spectra; b) XPS Cu LMM region spectra; c) XPS Cu valence band region spectra (Cu 3d).

As the possibility to manage free standing graphene (as in Chapter 5) is complicated due to technical and timing limitations at the in-house facility, the easiest solution was to dealt with free-graphene Cu sheet substrates with different oxidation sates. In this way, Cu sheets were oxidized by immersion on deionized water for seven hours (Cu_2O) and hydrogen peroxide for four days (CuO), while metallic Cu substrate was cleaned by Ar^+ sputtering. The XPS Cu 2p, Cu LMM and Cu 3d regions are plotted on Figure 4.50 for these three substrates. As stated before, the Cu 2p and Cu 3d regions shows a clear difference for the Cu^{2+} oxidation state, with a broadened and a shift to higher binding energies of the main peak and the appearance of shake up satellites. However, the differences between the Cu^0 and Cu^{1+} states are very subtle. Therefore, Cu LMM Auger region is the best choice to follow the oxidation state of Cu. As it can be seen from Figure 4.50 b, good grades of metal and CuO are easily obtained. However, the Cu_2O substrate has a little amount metallic Cu, being a mixture between the Cu^0 and the Cu^{+1} oxidation state. However, the oxide is at the surface, so at the end it will impact the early stages of growth of ZnO.

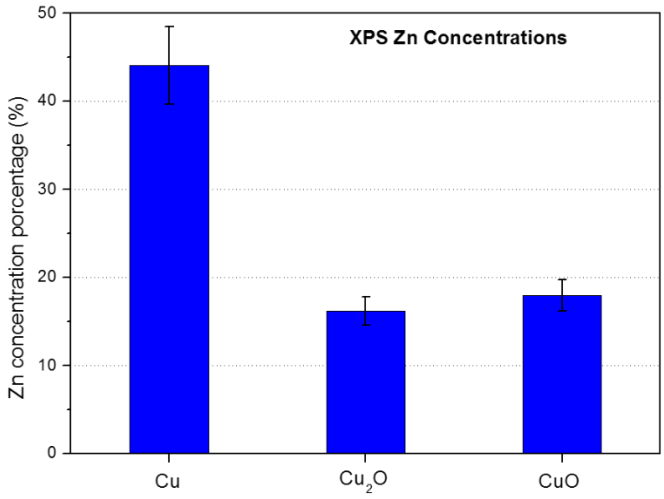

Figure 4.51 Zn surface concentration measured by XPS after simultaneous deposition of ZnO on metallic Cu, Cu_2O and CuO substrates.

After the surface characterization, the same deposition methodology (time, oxygen pressure and temperature) was used for the three substrates. Figures 4.51 and 4.52 show the Zn surface concentration measured by XPS and the XPS Zn LMM Auger spectra, respectively. In the case of metallic Cu substrate, the deposition was very fast,

with a high component of metallic Zn, as the Auger region shows. Although it is true that the time exposed to oxygen atmosphere has been the same for the three cases and that the faster deposition rate on this substrate may lead to an oxygen deficiency during the ZnO growth, it is also well-known that metallic copper acts as a reducing agent during the growth of ultra-thin metal oxides films, as for example reported for NiO [73]. On the other hand, the amount of Zn deposited for the Cu_2O and CuO substrates is quite similar, whereas for CuO, zinc is completely oxidized in comparison to the Cu_2O substrate, where a small amount of metallic Zn is found. In this way, the presence of metallic zinc is inversely proportional to the oxidation grade of the Cu substrate. Therefore, in the absence of graphene, the oxidation state of Cu determines the growth rate and chemical composition ratio Zn/ZnO.

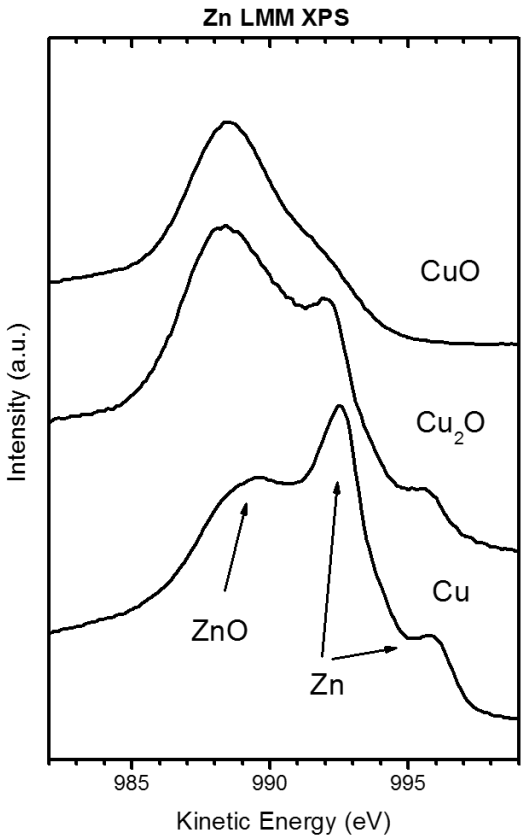

Figure 4.52 XPS Zn LMM spectra after simultaneous deposition of ZnO on metallic Cu, Cu_2O and CuO substrates.

However, previous experiments performed on graphene/Cu substrates showed that, while the Cu had basically the same metallic state (with residual contributions from Cu_2O), differences on the growth rate and chemical composition of the ZnO film were

also reported and could be associated to the presence of intercalated species such as CO, O_2, H_2O or other type of CO_x molecules present in the atmosphere. Therefore, Cu does not have the key role on the graphene/Cu system. Instead, it is a complex system where the cross relations between graphene, polycrystalline Cu and intercalated species determine the later growth of the metal oxide. Meanwhile, the graphene growth (in terms of number of nucleation sites, growth velocity and amount of defects) depends on the initial characteristics of the polycrystalline Cu, what at the end will determine the intercalation possibilities of different chemical species and the subsequently oxidation of the upper layers of the Cu substrate. Therefore, the key to deeply understand the growth behavior of ZnO consists in the whole graphene/intercalated-species/Cu system.

4.3.3 ZnO/graphene interaction and graphene electronic decoupling

This section is devoted to the interaction between ZnO and graphene, specifically regarding the electronic decoupling from the Cu substrate induced by the growth of ZnO. For the sake of clarity, some of the next figures have been already presented in previous sections of the present chapter, but they are necessary in the current discussion. In fact, this last part will also deal with the interaction between ZnO and the complete graphene/intercalated-species/Cu system, so it is closely linked to previous section 4.3.2.

4.3.3.1 The decoupling of Graphene from copper by water

In the last years several methods have been proposed to detach graphene from Cu substrates avoiding the destruction of the metallic sheet or the polymer residues. Ruizhe Wu et.al. work [27] reported an easy method to achieve this goal by immersion of the graphene/Cu sheet in deionized water, inducing the oxidation of the Cu surface and the intercalation of water by galvanic corrosion. As above mentioned, the final stage of this process consists on the electronic decoupling of graphene from the metallic substrate due to the formation of a nanometric layer of Cu_2O. This is just the acceleration of the natural process of corrosion and oxidation of copper due to the action of graphene and ambient humidity [24,25,26]. Figure 4.53 a shows a schematic representation of the electrochemical reaction proposed by Ruizhe Wu et. al. [27], where starting from the graphene boundaries, this acts as cathode and drives the oxygen reduction reaction forming hydroxides, while copper acts as the anode and provides electrons. These

hydroxides diffuse through the decoupled graphene/Cu interface and react with the copper ions forming Cu2O, eventually decoupling the entire graphene.

Figures 4.53 b and c summarize the main results obtained following the same aforementioned method, which has been successfully reproduced. As previously reported, for the Raman spectroscopy spectra (see Fig 4.53 b), the decoupled graphene shows two differences respect to the as received graphene/Cu. First, the intensity of the 2D band increased by a factor of 10, which was directly related with the cease of the electronic coupling between graphene and copper [74,75] due to the reduction of the electromagnetic screening from copper substrate. In addition, the 2D band shifts to lower wavenumber while the G band almost maintains its position. As G and 2D bands were more sensitive to doping and strain changes [76,77,78] respectively, this shift is indicating a significant reduction of the strain. This relaxation was induced by the formation of the copper oxide interlayer, which elevated the graphene and released the strain accumulated on the graphene during the final cooling stage of the CVD process due to differences on thermal expansion coefficients between graphene and Cu.

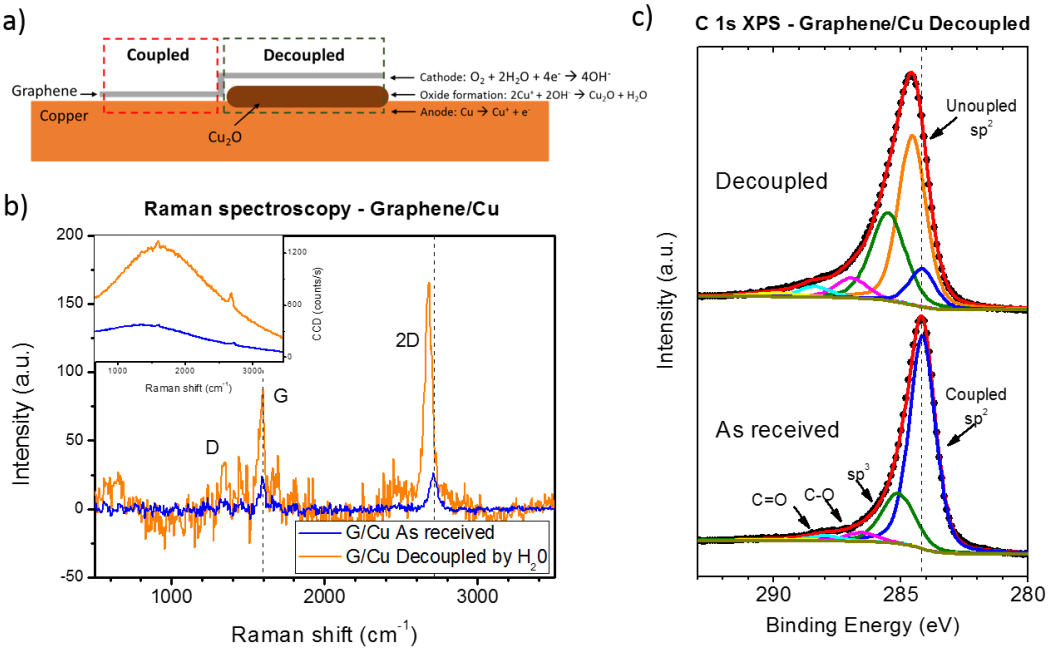

Figure 4.53 Graphene decoupling by water intercalation. a) Schematic representation of the galvanic corrosion on water driven by graphene; b) Raman spectra of as received graphene and decoupled graphene; c) XPS spectra of as received graphene and decoupled graphene.

Furthermore, XPS measurements were also sensible to this decoupling. Figure 4.53 c shows the C 1s region before and after the electronic decoupling, with a shift of 0.45 eV to higher binding energies for the last case. This can be explained in terms of coupled and decoupled contributions. For the as received graphene, the coupled sp^2 contribution at ~284.2 eV dominates the spectrum, with smaller contributions coming from defects (sp^3 at ~285.1 eV) and carbon-oxygen bonds (C-O and C=O at ~286.5 and ~288.0 eV, respectively). On the other hand, the decoupled graphene shows a broadening of the C 1s peak, related with the development of defects and carbon-oxygen bond, but also with the coexistence of two sp^2 contributions, one as before coupled at ~284.2 eV and a second and more intense decoupled contribution situated at ~284.6 eV. This shift of 0.45 eV recalls the reported changes on the C 1s spectrum for the as grown and air exposed graphene [25]. In this case, the shift to lower energies after air exposure (which is the case of our as received graphene) was interpreted due to oxygen intercalation between graphene and Cu. However, evidently the present shift does not mean the return to previous conditions. Graphene C 1s shifts are extremely complex and depend on many variables, such as work functions (doping) and chemical interaction between different species. In accordance with the Raman interpretation, the formation of Cu_2O interlayer would cause the electronic isolation of graphene from the copper substrate with the corresponding change on its inter-atomic relaxation energy.

The previous results will serve as a reference to compare the effects of ZnO deposition on the system graphene/Cu, as both Raman and XPS techniques are sensible to changes on graphene/Cu electronic coupling and can be used to follow mechanical, electronic and chemical changes on graphene.

4.3.3.2 The decoupling of Graphene from copper by ZnO

The chemistry and morphology of the early stages of growth of ZnO on graphene on copper have been previously discussed in section 4.3.1. As stated previously, the ZnO deposition follows a Volmer-Weber mode growth. In particular, until 2 equivalent monolayers (Eq-ML) the growth is characterized by a very fast growth of islands of about 2 nm height covering up the 50% of the surface (see Figure 4.25). These islands were composed by a similar amount of metallic zinc and ZnO, being located the oxide over the metal (see Figure 4.20 c). In second place, from 2 to 5 Eq-ML the growth shows a rapid increase on the height of the islands from 40 Å to 70 Å, reaching the detection limit of

the inelastic peak shape analysis while the total coverage is almost constant, although the height measured by AFM is about several tens of nanometers. At the same time the amount of metallic zinc starts to decrease as new ZnO grows over it. Finally, the third zone of Figure 4.25 is dominated by the saturation of the signal indicating that the limit of detection is reached once the coalescence throughout the whole surface is completed.

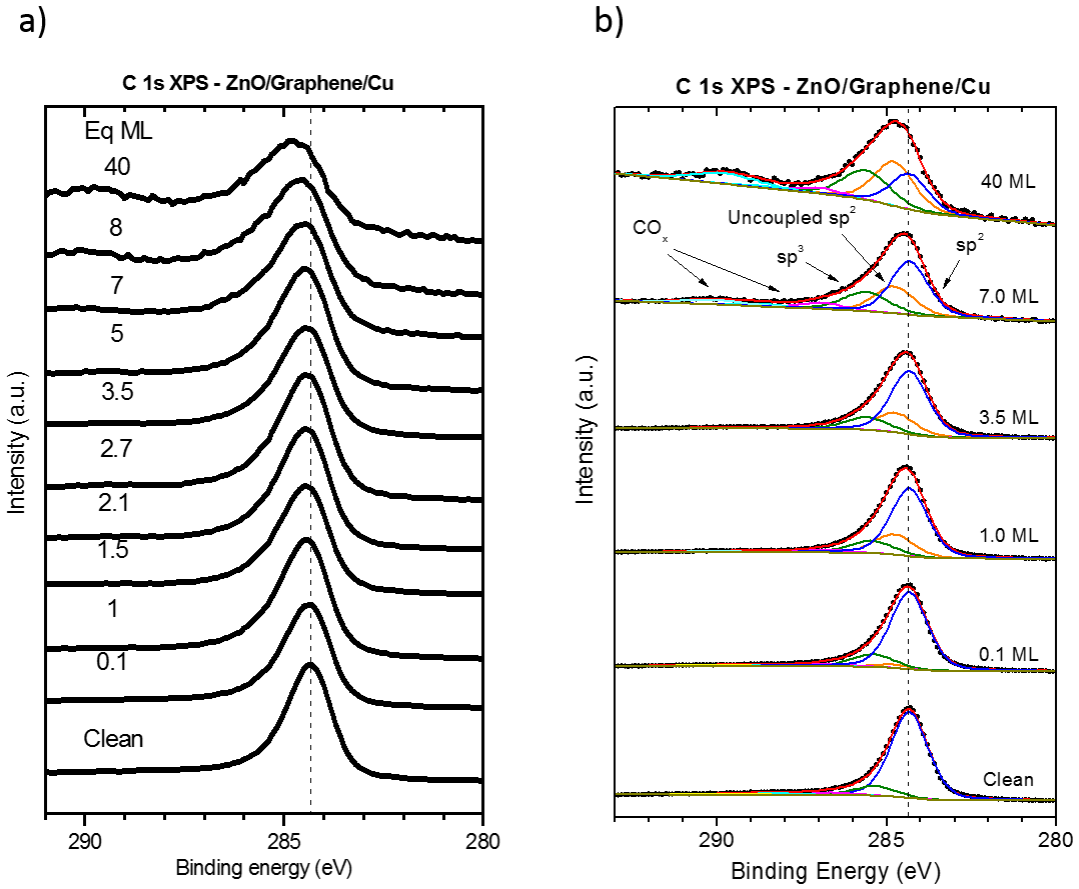

Figure 4.54 a) C 1s XPS spectra as a function of the ZnO coverage on graphene on polycrystalline copper. b) C 1s XPS spectra fitting for some selected stages of growth.

Figure 4.54 a shows the *in situ* XPS evolution of the C 1s region with ZnO coverage. With respect to the clean substrate, a slight shift of about 0.1-0.2 eV to higher binding energies can be observed. Figure 4.54 b presents the fitting of some selected stages of growth, where the same contributions as for Figure 4.53 c have been used. The shift can be explained in the same way as before as a result of the decoupled graphene, although the coupled sp^2 component remains the dominant and the shift is lower. This fact can be explained in relation with the growth mode (see Figure 4.55). The C 1s peak

position mostly changes until 2 Eq-ML, as long as large areas of the surface are covered by very thin ZnO. Once the covering is stopped at 50%, no newer areas are covered until 5 Eq-ML, and subsequently, no more graphene could be decoupled by the ZnO action. This behavior can be perfectly appreciated in Figure 4.55. The surface sensitivity of the XPS technique also plays an important role, as the height of ZnO islands grows and buries the carbon signal of the graphene which is decoupled under the ZnO, limiting the C 1s measured essentially to not covered graphene (and therefore coupled with copper substrate). For very large coverages (~40 Eq-ML), the shift increases to 0.3 eV due to the gradual development of graphene defects (labelled as sp3).

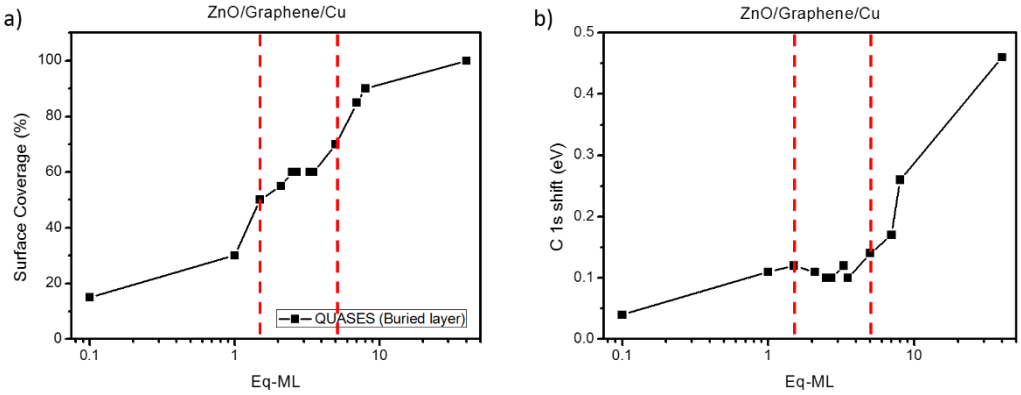

Figure 4.55 a) Percentage of the surface coverage of Graphene on copper substrate as a function of the deposited ZnO; b) XPS C 1s shift as a function of the deposited ZnO.

The decoupling hypothesis is confirmed by *ex situ* Raman spectroscopy measurements for a set of samples with 3.5 Eq-ML. Figure 4.56 a shows the optical image of the as received clean graphene/Cu substrate (substrate and its Raman mapping (left and right, respectively). As before, copper boundaries can be easily observed, delimiting zones with different coloring (dark and clear green), which correspond to areas where the 2D and G bands can be easily measured or where the graphene bands intensity is very low, respectively (see Fig 4.56 right). The range of intensities reported for the 2D band can be interpreted in terms of slight differences on the electronic coupling between graphene and copper due to the characteristics works functions of the different crystallographic facets of the metal [79], and also because of the different concentration of the aforementioned intercalated species. In addition, as in the case of Figure 4.43, two qualities of graphene were found: monolayer graphene with a 2D/G ratio of ~2 (red) and

graphene oxide (blue), where the 2D band disappear and the G and D bands intensities increase. After ZnO deposition, again optical images and Raman mappings were taken in the same area. Figure 4.56 b shows the same clear and dark optical regions and also qualitatively the same graphene spectra for the monolayer graphene and graphene oxide zones. However, an impressive enhancement of the intensity is measured for the D, G and 2D bands (see Figure 4.56 c). As established before, this increment on the 2D band is related with the electronic decoupling of graphene from copper. Besides, the Raman mapping of the intensity of the ZnO defects band shows how the oxide tends to grow on the initial optical dark zones, i.e. at the initial graphene less electronically coupled with the substrate. This behavior was also previously indicated in section 4.3.2.

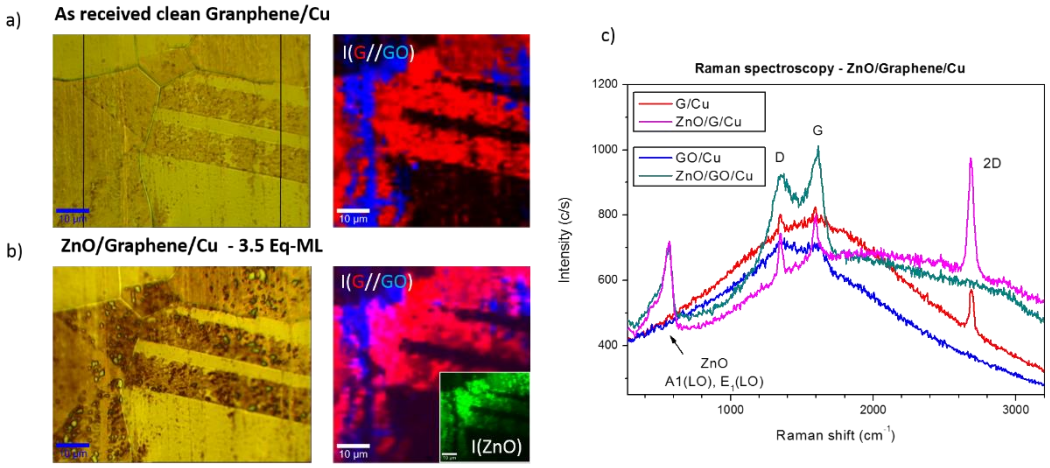

Figure 4.56 a) Optical image (left) and *ex situ* Raman mapping (right) showing monolayer graphene (2D band intensity, red) and graphene oxide (G band intensity, blue) from as received graphene/Cu; b) Optical image (left) and *ex situ* Raman mapping (right) showing monolayer graphene (2D band intensity, red) and graphene oxide (G band intensity, blue) after a deposition of 3.5 Eq-ML of ZnO. Inset: Raman mapping showing ZnO distribution (defects band, green); c) Individual spectra before and after ZnO deposition on both monolayer graphene and graphene oxide.

More in detail, Figure 4.57 shows AFM and local Raman measurements in which the relation between decoupled graphene and ZnO is clarified. Figures 4.57 a, b, and c show the Raman mapping after the deposition of ZnO referred to the 2D (red, monolayer graphene), G (blue, graphene oxide) and ZnO defects band (green), respectively, where b and c are a zoom from the square drawn on Figure 4.57 a. There exists a direct

relationship between graphene and ZnO mappings (b and c), where the maxima intensities for both are located in the same places. In fact, AFM measurement confirms two important data (see Figure 4.57 d). In first place, the initial areas where the 2D intensity was much less intense for the as received graphene is still very flat after the ZnO deposition, and second, the ZnO clusters of the central strip correspond to the positions where the Raman intensities are higher. Furthermore, Figure 4.57 e shows three individual spectra on three selected positions (1, ZnO cluster on the central strip; 2, on the central strip outside a ZnO cluster; 3, outside the central strip). As a general rule, it can be established that the more often presence of ZnO implies a deeper electronic decoupling of the graphene, with an increment of the 2D band and also the shift to lower wavenumber due to strain relief (as previously discussed for graphene decoupled with water).

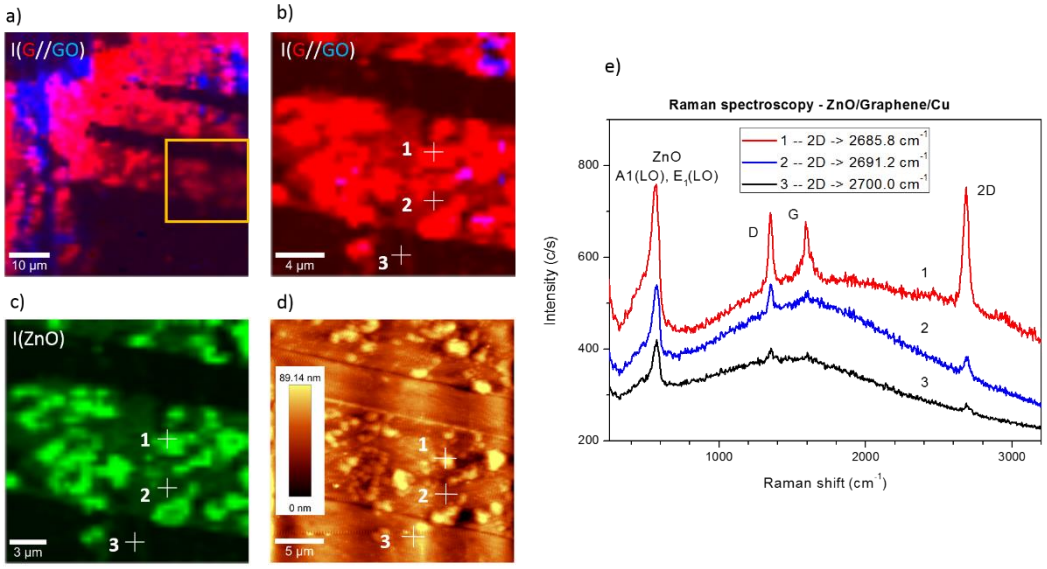

Figure 4.57 a) Raman mapping showing monolayer graphene (2D band intensity, red) and graphene oxide (G band intensity, blue) of the same sample shown in Figure 4.56 b (after ZnO deposition). b) Zoom mapping from (a) square. c) Zoom mapping from (a) showing ZnO distribution (defects band, green). d) AFM images from (a) square area. e) Individual spectra from points labeled at (b), (c) and (d) images.

Besides, Figure 4.58 shows the *in situ* XPS measurements of the C 1s region before and after the ZnO deposition, closing the demonstration of the electronic decoupling of graphene induced by the ZnO deposition. These *in situ* XPS measurements

discard an *ex situ* process driven by the exposure to air and limit the chemical and physical process to only four elements: copper substrates, graphene, initial oxygen and water intercalation and ZnO growth.

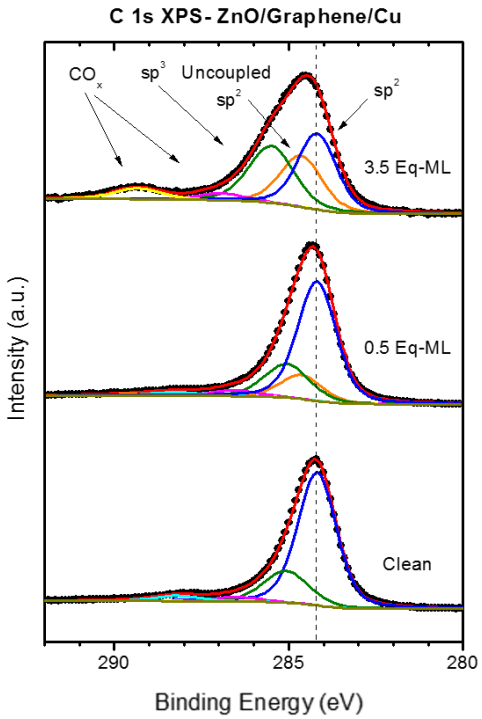

Figure 4.58 C1s *in situ* XPS spectra fitting for the sample shown on Figures X3 and X4 with a ZnO coverage of 3.5 Eq-ML on graphene on polycrystalline copper.

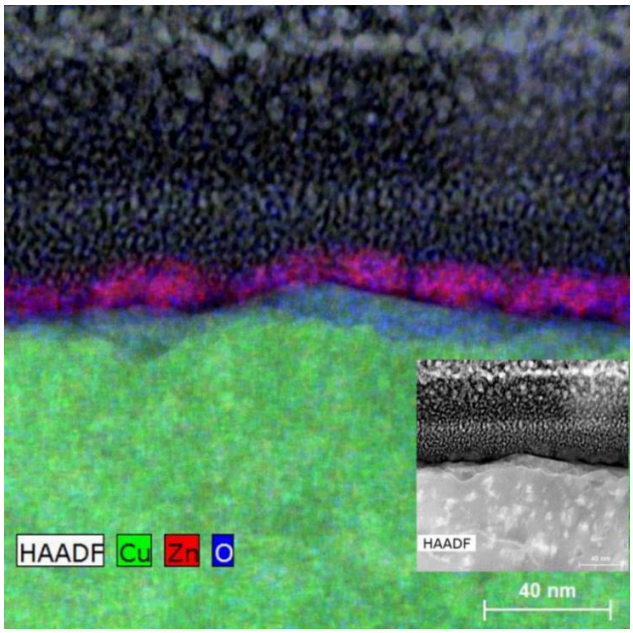

Figure 4.59 TEM profile image and EDX chemical mapping of the same 3.5 Eq-ML ZnO/G/Cu sample shown in previous Figures.

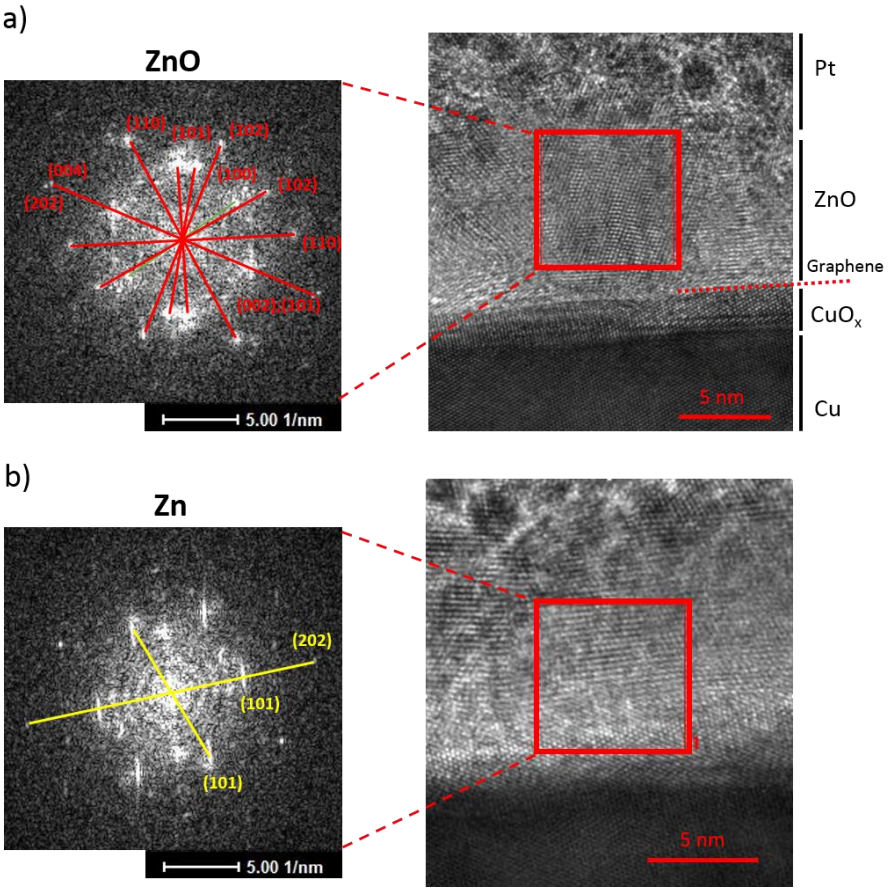

Figure 4.60 Same sample as in Figure 4.59: a) Diffraction pattern of ZnO layer; b) Diffraction pattern of Zn/ZnO cluster.

As last step, TEM imaging and EDX mapping allowed to study the depth profile and the role of the copper substrate in the same decoupled samples. In this sense, as it has been described no changes on the copper signal could be previously reported by Raman or XPS. As it has been already discussed, the Cu 2p region is not distinguishable for the metal or Cu_2O species, only for the Cu-LMM Auger transition. Nevertheless, the Zn and Cu Auger transitions overlap, what makes very difficult to follow any chemical change on the copper as it was done for zinc and carbon. In any case, Figure 4.59 shows the EDX chemical mapping overprinted on the TEM image of the profile, where four different layers can be distinguished from top to bottom: Pt (from the FIB attack to create the lamella); ZnO (red-blue); copper oxide (green-blue); and copper (green). The appearance of a thin layer of ~10nm of CuO_x is extremely enlightening, as it allows to connect the previous electronic decoupling of graphene by water with the same process driven by the ZnO, but with the difference that no liquid water is present (only the limited initial amount of intercalated water). In this way, ZnO seems to be the promoter of the oxidation of the

metallic substrate, which ceases the electronic coupling with graphene. On the other hand, Figures 4.60 a and b show the diffraction patterns of two different regions of the ZnO layer. Both, the metallic zinc and the oxide can be found in different ratios, with regions where the metallic contribution is thicker and dominates, always closer to the graphene/Cu, in accordance with the XPS results. Finally, these TEM measurements were not conclusive to determine the valance of the copper on the CuO_x layer. However, taking into account that no changes on the Cu 2p region were measured, that for water immersion the oxide created was Cu_2O, and finally that XPEEM results shown on Figures 4.36, 4.37, 4.39 pointed out to the absence of CuO, it seems that the most plausible option is the formation of Cu_2O.

4.3.3.3 ZnO and intercalated oxygen and water: the route for the decoupling

In the previous paragraphs it has been shown how the formation of a nanometric layer of possibly Cu_2O on the top of the copper sheet can electronically decouple the graphene from the metal, enhancing the intensity of the graphene Raman bands, shifting the C 1s region to higher energies and relaxing its strain. Besides, the formation of this oxide layer has been reached by two different routes. In the case of graphene/Cu immersion on water, the galvanic corrosion reaction is well established, where graphene acts as the cathode (see Figure 4.53 a). On the other hand, the decoupling by ZnO deposition seems to be more complex as up to eight different chemical species are present (copper, graphene, intercalated oxygen, water and organic molecules, oxygen gas and metallic zinc from the evaporation source and finally ZnO and metallic zinc on the surface of the sample). In the next lines we will propose a chemical pathway for the formation of the copper oxide layer based in the water immersion case and in complete agreement with the rest of the reported results concerning the ZnO growth on graphene/Cu sheets.

Air exposure induce intercalation of water and oxygen (among other chemical species) between graphene and copper. However, this process is not homogeneous over the entire sample, as depends on graphene edges and defects and also on the exposure time. Although graphene passivizes the metal surface slowing down the oxidation velocity of the surface, at the same time graphene plays a role as cathode in the described galvanic corrosion reaction, leading to the formation of a layer of copper oxide after time enough. In this way, the as received graphene/Cu samples have been exposed to air between its growth process and the posterior growth of ZnO and therefore present

intercalated oxygen and water. The initial amount of these species was not the same in all samples and regions, and combined with the various crystallographic facets of copper, slightly different electronic couplings between copper and graphene can be measured. Controlled exposure to oxygen gas at 10^{-3} mbar has no effect on the as received graphene. Ultimately, the initial state of graphene is not a fixed picture, but depends on the time exposure to air and on the initial quality of graphene. For instance, graphene/Cu samples used just after its CVD growth present less intercalated species and no decoupling can be reported after the ZnO deposition, so the presence of these chemical species is indispensable. Figure 4.61 a shows a scheme of this situation.

On the other hand, reactive thermal evaporation implies two new players. Metal Zinc is evaporated under molecular oxygen atmosphere (10^{-3} mbar), and it remains an open discussion if the oxide is formed initially in a gas phase and then it is deposited on the substrate or instead the metal is firstly deposited and subsequently is oxidized. In addition, it is true that the substrate can play an important role in first stages of growth depending on its chemical reducing and oxidizing behavior, as discussed previously for the different oxidation states of Cu. In the present case, a mixture of metal zinc and ZnO was first deposited, being the metal under the oxide and in contact with the graphene. As stated above, the lonely presence of 10^{-3} mbar of molecular oxygen does not induce any change on graphene for any sample, but if zinc is also present, then the graphene decoupling took place. With this discussion we would like to highlight the decisive role of zinc.

Regarding specifically the interrelation between copper, intercalated species, graphene and metal zinc, we focus on the work function of the two metals and graphene in order to describe the possible charge transference between them. It is well known that the Fermi level position are equal for conductor materials in contact, caused by electron transference from the material with smaller work function to the other. In the case of graphene, this does not mean the immediate p or n doping since chemical interactions between graphene and substrate are also determinant [80], and therefore the crossover between both doping states is established at 5.4 eV, much higher than the expected 4.5 eV value related with the graphene work function. In this way, both copper and zinc have work functions below 5.4 eV, so electron transference from them to graphene is expected. However, zinc has a slightly lower work function than copper (~4.3 eV [81,82] and ~4.5 eV [79], respectively), facilitating the charge transference to graphene and accelerating

the cathodic reaction where hydroxides are promoted from intercalated oxygen and H_2O molecules. Besides, three more factors can complement this explanation: 1) metal nanoclusters tend to lose electrons and ionized [83], 2) the reducing chemical nature of copper, which tends to reduce the oxides in contact with it and becoming itself oxidized, and 3) zinc 3d orbitals are completely full, what induce less reactivity with oxygen molecules and allows the presence of metal Zn even with such high pressures, two orders of magnitude higher than for other oxides, such as Co or Ni, using the same technique [84,85]. Thus, the metallic zinc deposited on graphene only become oxidized once the oxidation process of copper has finished because all the intercalated species have been consumed (see Figure 4.61 b). Under this description, depending on the initial amount of intercalated species and the initial state of graphene (local work function values of graphene and copper and the initial electronic coupling between them), then the thicknesses of the metal zinc deposit and the copper oxide layer can vary. This is shown in Figure 4.61 b.

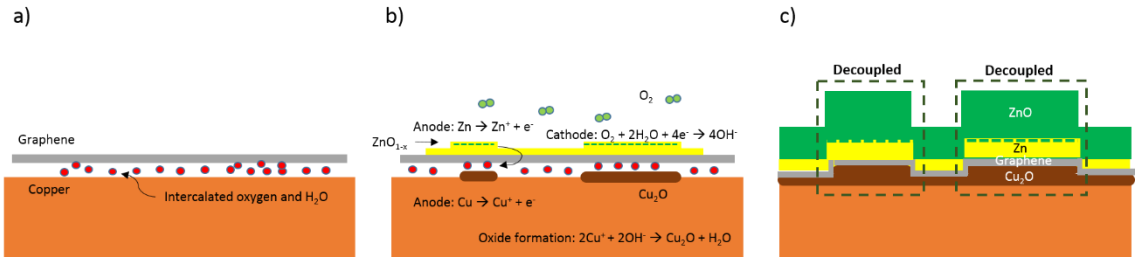

Figure 4.61 Schematic representation of the graphene decoupling process by ZnO deposition. a) Initial state of graphene; b) metal zinc deposition and copper oxidation; c) final state with decoupled graphene from the copper substrate.

Finally, ZnO growth on metallic zinc is much easier than on copper or graphene due to the mismatch between ZnO and these other surfaces, and because metal zinc tends to oxidize once the reaction is finished and charge transfer only involves the very first layers of zinc in contact with graphene. In this way, O_2 gas will partially oxidize the upper most layers of metal zinc forming a suboxide ZnO_{1-x}, which acts as seed for the posterior growth of ZnO. The difference on the roughness shown by the AFM measurement in Figure 4.57 d can be now well understood. Also the direct relation between the size of ZnO clusters and the graphene decoupling can be fulfilled by this explanation, as the

copper oxide layer is expected to be thicker under a cluster. This last step of the process is presented on Figure 4.61 c.

In order to close the discussion of section 4.3 devoted to the ZnO growth on graphene/Cu sheets, the QUASES results presented on Figure 4.25 can also be explained. The initial rapid coverage of the graphene by ZnO/Zn is related with the deposition of metallic zinc atoms and their high diffusivity along the graphene surface where more intercalated species can be found, what at the end is related with the opportunity of enhancing the oxidation reaction of copper. In this way, once these sites, where metal zinc has been deposited, are completely occupied, then ZnO starts to grow on them forming the inhomogeneities reported in Figures 4.56 and 4.57, among others. This explains the second phase on the QUASES diagram, where the height of the deposited islands increases but not the coverage. Only for longer depositions times all the surface is completely covered.

4.4 Conclusions

This chapter summarizes the main results regarding the growth of ZnO on graphitic substrates, such as HOPG and graphene grown by CVD on polycrystalline Cu. It is divided into two main blocks referred to each of the substrates, and in fact, although the deposition on HOPG has been performed for comparison purposes with the graphene/Cu sheets, both growths could be treated separately.

In regard of the mode of growth of ZnO, although the first atomic layer of both substrates are identical, the presented results indicate that the growth of ZnO on HOPG and graphene/Cu substrates is completely different. The early stages of growth of ZnO on the HOPG substrate consist in the deposition of micrometric ZnO clusters at the HOPG steps and point defects at the terraces with a large diffusion rate of the Zn atoms. The oxidation of Zinc atoms was complete, forming ZnO clusters. Besides, the final stages of the growth gave a microstructured ZnO thin film. However, the growth on the graphene/Cu sheets consisted in the deposition of Zn atoms on the graphene/Cu surface, remaining metallic, followed by the growth of many ZnO small clusters and leading to the formation of a sub-oxide (ZnO_x) at the ZnO/Zn interface, forming a ZnO/ZnOx/Zn/graphene/Cu structure. In this picture, the early deposition of the Zn atoms on the graphene layer seems to act as nucleation centers of ZnO, leading to a nanostructured ZnO thin film. In comparing the growth on both substrates, the role of

graphene seems crucial to create such nucleation centers. The different electronic structure and the corresponding interaction with other materials of graphene with respect to HOPG has been once again evidenced in these experiments.

Focusing on the thermal treatments performed on the Zn/HOPG substrates, three main conclusions could be reached. Firstly, with regard to the ZnO clusters, the thermal treatments lead to a recrystallization of the oxide, with a decrease of defects associated to oxygen vacancies, as both XPS and Raman spectra show. Secondly, the interaction between ZnO and HOPG could be measured by means of Raman spectroscopy, resulting on the oxidation of the graphite in the interface with the ZnO. However, the third conclusion points out that, in spite of the previous result, no useful catalytic behavior of ZnO on HOPG could be reported, as nano-channeling or carbon gasification of graphite described in Chapter 3 for the CoO/HOPG system after the re-oxidation process.

Moving to the ZnO growth on the graphene/Cu system and the interaction between them, it has been shown how the cross relation between the copper substrate, intercalated oxygen, organic and water molecules due to air exposure and graphene determine the whole picture. It is proposed that the deposited ZnO/Zn initial layer probably induces, by electron transference to graphene from metallic zinc, the electronic decoupling of graphene from the metallic substrate. The presence of zinc accelerates the galvanic corrosion of copper by the formation of hydroxides from the initial intercalated water and oxygen molecules. This reaction, which is essentially the same than for graphene/Cu immersed on water (also discussed in the text adding to the previously reported Raman spectra the XPS measurements), leads to the formation of a complex interface formed by $ZnO/ZnO_{1-x}/Zn/graphene/Cu_2O/Cu$. The electronic decoupling of graphene from copper depends essentially on two factors: the time which the as received graphene/Cu sheet is exposed to air before the ZnO deposition and the presence of zinc evaporated from metallic zinc under O_2 atmosphere.

Precisely, the initial chemical and structural state of the as received graphene/Cu sheets is extremely critic on the subsequently growth of ZnO. Meanwhile the growth characteristics of the oxide (in terms of nucleation, deposition and compositional rates) depend on the initial electronic coupling of graphene with Cu, this last condition already depends on the number of graphene defects, the chemical species intercalated between graphene and Cu and the oxidation state, crystallographic direction and surface morphology of the Cu grains, being all these parameters determined by the polycrystalline

nature of the Cu sheet. In fact, all these factors that influence on the ZnO growth are presented as local inhomogeneities (about >1 μm size) on the as received graphene/Cu samples, restricting a homogeneous growth of the ZnO. However, the artificial modification of the chemical state of the initial graphene/Cu substrate opens the door to perform well controlled and homogenous growth of ZnO. In this way, the studied issue could become, at the same time, the solution to overcome the problems associated with the deposition of different kind of materials on graphene substrates while preserving its quality and terrific properties.

Bibliography

[1] K. S. Novoselov, A. K. Geim, S. V. Morozov, D. Jiang, Y. Zhang, S. V. Dubonos, I. V. Grigorieva, A. A. Firsov; "Electric Field Effect in Atomically Thin Carbon Films"; *Science*, 306, (2004); pp: 666-669; DOI: 10.1126/science.1102896

[2] C. Mattevi, H. Kima, M. Chhowalla; "A review of chemical vapour deposition of graphene on copper"; *J. Mater. Chem.*, 21, (2011); pp: 3324-3334; DOI: 10.1039/c0jm02126a.

[3] J-H Chen, C Jang, S. Xiao, M. Ishigami, M.S. Fuhrer*;* "Intrinsic and extrinsic performance limits of graphene devices on SiO2"; *Nature Nanotechnology*, 3, (2008); pp: 206-209; DOI:10.1038/nnano.2008.58

[4] X. Du, I. Skachko, A. Barker, E.Y. Andrei; "Approaching ballistic transport in suspended graphene"; *Nat. Nanotechnol.*, 3, (2008); pp: 491-495. DOI:10.1038/nnano.2008.199

[5] R. R. Nair, P. Blake, A. N. Grigorenko, K. Novoselov, T. J. Booth,T. Stauber, N. M. R. Peres, A. K. Geim; "Fine Structure Constant Defines Visual Transparency of Graphene"; *Science*, 320, (2008); pp: 1308; DOI: 10.1126/science.1156965

[6] J. S. Bunch, S. S. Verbridge, J. S. Alden, A. M. van der Zande, J. M. Parpia, H.G. Craighead, P. L. McEuen; "Impermeable Atomic Membranes from Graphene Sheets"; *Nano Lett*. 8, (2008); pp: 2458-2462. DOI: 10.1021/nl801457b

[7] R. S. Weatherup, L. D'Arsié, Andrea Cabrero-Vilatela, S. Caneva, R. Blume, J. Robertson, R. Schloegl, S. Hofmann; "Long-Term Passivation of Strongly Interacting Metals with Single-Layer Graphene"; *J. Am. Chem. Soc.*, 137, (2015); pp: 14358-14366; DOI: 10.1021/jacs.5b08729

[8] Ü. Özgür, Ya. I. Alivov, C. Liu, A. Teke, M. A. Reshchikov, S. Doğan, V. Avrutin, S.-J. Cho, H. Morkoç; "A comprehensive review of ZnO materials and devices"; *J. Appl. Phys*., 98, (2005); pp: 041301; DOI: 10.1063/1.1992666

[9] B. M. Ataev, A. M. Bagamadova, A. M. Djabrailov, V. V. Mamedo, R. A. Rabadanov; "Highly conductive and transparent Ga-doped epitaxial ZnO films on sapphire by CVD"; *Thin Solid Films*, 260, (1995); pp: 19-20; DOI: 10.1016/0040-6090(94)09485-3

[10] H. Kim, C. M. Gilmore, J. S. Horwitz, A. Piqué, H. Murata, G. P. Kushto, R. Schlaf, Z. H. Kafafi, D. B. Chrisey; "Transparent conducting aluminum-doped zinc oxide thin

films for organic light-emitting devices"; *Appl. Phys. Lett.* 76, (2000); 259-261; DOI: 10.1063/1.125740

[11] Li, H.T. Jiang, X. Han, Z.Y. Zhan, H.J. Du, W.Q Lu, Z.J. Li, Z.Y. Tao, Y.X Fan; "Optimizing growth of ZnO nanowire networks for high-performance UV detection" *Ceram. Int.*, 43, (2017); pp: 15978-15985; DOI: 10.1016/j.ceramint.2017.08.183

[12] N.H, Ha, D.D. Thinh, N.T. Huong, N.H. Phuong, P.D. Thach, H.S. Hong; "Fast response of carbon monoxide gas sensors using a highly porous network of ZnO nanoparticles decorated on 3D reduced graphene oxide"; *Appl. Surf. Sci.*, 434, (2018) pp: 1048-1054; DOI: 10.1016/j.apsusc.2017.11.047

[13] T.G.U. Ghobadi, M. Kunduraci, E. Yilmaz; "Improved lithium-ion battery anode performance via multiple element approach"; *J. Alloys Compd.*, 730, (2018); pp: 96-102; DOI: 10.1016/j.jallcom.2017.09.297

[14] G. Zamiri, S. Bagheri; "Fabrication of green dye-sensitized solar cell based on ZnO nanoparticles as a photoanode and graphene quantum dots as a photo-sensitizer." *J. Colloid Interface Sci.*, 511 (2018); pp: 318-324; DOI: 10.1016/j.jcis.2017.10.026

[15] Z. L. Wang; "Zinc oxide nanostructures: growth, properties and applications"; *J. Phys.: Condens. Matter*, 16, (2004); pp: 829-858; DOI: 10.1088/0953-8984/16/25/R01/pdf

[16] A. Dahal; M. Batzill; "Graphene-nickel interfaces: a review"; *Nanoscale*, 6, (2014); pp: 2548-2562; DOI: 10.1039/C3NR05279F

[17] A. Mattausch, O. Pankratov; "Ab Initio Study of Graphene on SiC"; *Phys. Rev. Lett.*, 99, (2007); pp: 076802; DOI: 10.1103/PhysRevLett.99.076802

[18] K. V. Emtsev, F. Speck, T. Seyller, L. Ley, J. D. Riley; "Interaction, growth, and ordering of epitaxial graphene on SiC{0001} surfaces: A comparative photoelectron spectroscopy study"; *Phys. Rev. B,* 77, (2008); pp: 155303; DOI: 10.1103/PhysRevB.77.155303

[19] R. Decker, J. Brede, N. Atodiresei, V. Caciuc, S. Blugel, R. Wiesendanger; "Atomic-scale magnetism of cobalt-intercalated graphene"; *Phys. Rev. B*, 87, (2013); pp: 041403; DOI: 10.1103/PhysRevB.87.041403

[20] I. I. Klimovskikh, M. M. Otrokov, V. Yu. Voroshnin, D. Sostina, L. Petaccia, G. Di Santo, S. Thakur, E. V. Chulkov, A. M. Shikin, "Spin-Orbit Coupling Induced Gap in Graphene on Pt(111) with Intercalated Pb Monolayer"; *ACS Nano*, 11, (2017); pp: 368−374; DOI: 10.1021/acsnano.6b05982

[21] A. Grüneis, D. V. Vyalikh; "*Tunable hybridization between electronic states of graphene and a metal surface*"; *Phys. Rev. B*, 77, (2008); pp: 193401; DOI: 10.1103/PhysRevB.77.193401

[22] M. Petrovic, I. Srut Rakic, S. Runte, C. Busse, J. T. Sadowski, P. Lazic, I. Pletikosic, Z.-H. Pan, M. Milun, P. Pervan, N. Atodiresei, R. Brako, D. Sokcevic, T. Valla, T. Michely, M. Kralj Petrovic; "The mechanism of caesium intercalation of graphene" *Nat. Commun*, 4, (2013); pp: 2772; DOI: 10.1038/ncomms3772

[23] S. Oida, F. R. McFeely, J. B. Hannon, R. M. Tromp, M. Copel, Z. Chen, Y. Sun, D. B. Farmer, J. Yurkas; "Decoupling graphene from SiC (0001) via oxidation" *Phys. Rev. B*, 82, (2010); pp: 041411; DOI: 10.1103/PhysRevB.82.041411

[24] R. Blume, P. R. Kidambi, B. C. Bayer, R. S. Weatherup, Z.-J. Wang, G. Weinberg, M.-G. Willinger, M. Greiner, S. Hofmann, A. Knop-Gerickee, R. Schlögl; "The influence of intercalated oxygen on the properties of graphene on polycrystalline Cu under various environmental conditions"; *Phys. Chem. Chem. Phys.*, 16, (2014); pp: 25989—26003; DOI: 10.1039/c4cp04025b

[25] P. R. Kidambi, B. C. Bayer, R. Blume, Z.-J. Wang, C. Baehtz,, R. S. Weatherup, M.-G. Willinger, R. Schlögl, S. Hofmann; "Observing Graphene Grow: Catalyst−Graphene Interactions during Scalable Graphene Growth on Polycrystalline Copper"; *Nano Lett.*, 13, (2013); pp: 4769−4778; DOI: 10.1021/nl4023572

[26] M. Schriver, W. Regan, W. J. Gannett, A. M. Zaniewski, M. F. Crommie, A. Zettl; "Graphene as a Long-Term Metal Oxidation Barrier: Worse Than Nothing"; *ACS Nano*, 7, (2013); pp: 5763-5768; DOI: 10.1021/nn4014356

[27] R. Wu, L. Gan, X. Ou, Q. Zhang, Z. Luo; "Detaching graphene from copper substrate by oxidation-assisted water intercalation"; *Carbon*, 98, (2016); pp: 138-143; DOI: 10.1016/j.carbon.2015.11.002

[28] S. Gottardi, K. Müller, L. Bignardi, J. C. Moreno-López, T. A. Pham, O. Ivashenko, M. Yablonskikh, A. Barinov, J. Björk, P. Rudolf, M. Stöhr; "Comparing Graphene Growth on Cu(111) versus Oxidized Cu(111)"; *Nano Lett.*, 15, (2015); pp: 917−922; DOI: 10.1021/nl5036463

[29] H.T. Quang, A. Bachmatiuk, A. Dianat, F. Ortmann, J. Zhao, J.H. Warner, J. Eckert, G. Cunniberti, M.H. Rümmeli; "*In Situ* Observations of Free-Standing Graphene-like Mono- and Bilayer ZnO Membranes"; *ACS Nano*, 9, (2015); pp: 11408; DOI: 10.1021/acsnano.5b05481

[30] A. H. Castro Neto, F. Guinea, N.M R. Peres, K.S. Novoselov, A. K. Geim; "The electronic properties of graphene"; *Rev. Mod. Phys*. 81, (2009); pp: 109-162. DOI: https://doi.org/10.1103/RevModPhys.81.109

[31] A.K. Geim, K.S. Novoselov; "The rise of graphene"; *Nat. Mat*, 6, (2007); pp: 183-191. DOI: 10.1038/nmat1849

[32] R. Viswanatha, S. Sapra, B. Satpati, P. V. Satyam, B. N. Dev, D. D. Sarma; "Understanding the quantum size effects in ZnO nanocrystals"; *J. Mater. Chem.,* 14, (2004); pp: 661-668. DOI: 10.1039/B310404D

[33] H-K Hong, J. Jo, D. Hwang, J. Lee, N.Y. Kim, S. Son,J.H. Kim, M.-J. Jin, Y.C. Jun, R. Erni, S.K. Kwak, J.-W. Yoo, Z.Lee; "Atomic Scale Study on Growth and Heteroepitaxy of ZnO Monolayer on Graphene"; *Nano Lett.* 17, (2017); pp: 120-127. DOI: 10.1021/acs.nanolett.6b03621

[34] S. Huh, J. Park, Y.S. Kim, K.S. Kim, B.H. Hong, J.M. Nam; "UV/ozone-oxidized large-scale graphene platform with large chemical enhancement in surface-enhanced Raman scattering"; *ACS Nano*, 5, (2011); pp: 9799-806. DOI: 10.1021/nn204156n

[35] D. Briggs, M. P. Seach, 1990, Practical Surface Analysis. Volume 1. Augr and X-ray Photoelectron Spectroscopy, second edition; Weinheim, Germany; Wiley

[36] G. Deroubaix, P. Marcus; "X-ray photoelectron spectroscopy analysis of copper and zinc oxides and sulphides" *Surf. Interface Anal*. 18, (1992); pp: 39-46; DOI: 10.1002/sia.740180107

[37] Yutong Wu, E. Garfunkel, T. E. Madey; "Initial stages of Cu growth on ordered Al2O3 ultrathin films"; *J. Vac. Sci. Technol. A*, 14, (1996); pp 1662-1667; DOI: 10.1116/1.580315

[38] J. A. Rodriguez, R. A. Campbell, D. W. Goodman; "Interaction of ultrathin films of copper with rhodium(100) and ruthenium(0001): an XPS study"; *J. Phys. Chem.*, 95, (1991); pp 2477-2483; DOI: 10.1021/j100159a068

[39] D. Díaz-Fernández, E. Salas, J. Méndez , R.J.O. Mossanek, M. Abbate, C. Morales, G. Domínguez-Cañizares, G.R. Castro, A. Gutiérrez, L. Soriano; "Ultra-thin CoO films grown on different oxide substrates: Size and support effects and chemical stability"; *J. Alloys Compd*, 758, (2018); pp: 5-13; DOI: 10.1016/j.jallcom.2018.05.112

[40] J.-C. Dupin, D. Gonbeau, P. Vinatier, A. Levasseur; "Systematic XPS studies of metal oxides, hydroxides and peroxides"; *Phys. Chem. Chem*. Phys, 2, (2000); pp: 319-1324; DOI: 10.1039/A908800H

[41] R. Al-Gaashania,, S. Radiman, A.R. Daud, N. Tabet, Y. Al-Douri; "XPS and optical studies of different morphologies of ZnOnanostructures prepared by microwave methods"; *Ceram. Int.*, 39, (2013); pp: 2283-2292; DOI: 10.1016/j.ceramint.2012.08.075

[42] N. Benito, G. Recio-Sánchez, R. Escobar-Galindo, C. Palacio "Formation of antireflection Zn/ZnO core-shell nano-pyramidal arrays by O_2^+ ion bombardment of Zn surfaces"; *Nanoscale*, 9, (2017); pp: 14201-14207 DOI: 10.1039/c7nr03691d

[43] Q. Bao, X. Liu, Y. Xia, F. Gao, L. D. Kauffmann, O. Margeat, J. Ackermann, M. Fahlman; "Effects of ultraviolet soaking on surface electronic structures of solution processed ZnO nanoparticle films in polymer solar cells"; *J. Mater. Chem. A*, 2, (2014); pp: 17676-17682; DOI: 10.1039/C4TA02695K

[44] K. Kotsis, V. Staemmler; "Ab initio calculations of the O1s XPS spectra of ZnO and Zn oxo compounds"; *Phys. Chem. Chem. Phys.*, 8, (2006); pp: 1490-1498; DOI: 10.1039/B515699H

[45] B. Rousseau, H. Estrade-Szwarckopf, A.-L. Thoman, P. Brault; "Stable C-atom displacements on HOPG surface under plasma low-energy argon-ion bombardment"; *Appl. Phys. A*, 77, (2003); pp: 591-597. DOI: 10.1007/s00339-002-1538-x

[46] D. Yang, A. Velamakanni, G. Bozoklu, S. Park, M. Stoller , R.D. Piner, S. Stankovich, I. Jung, D.A. Field, C.A. Ventrice Jr., R.S. Ruoff; "Chemical analysis of graphene oxide films after heat and chemical treatments by X-ray photoelectron and Micro-Raman spectroscopy"; *Carbon*, 47, (2009); pp: 145-152. DOI: 10.1016/j.carbon.2008.09.045

[47] K. Haubner, J. Murawski, P. Olk, L. M. Eng, C. Ziegler, B. Adolphi, E. Jaehne; "The route to functional graphene oxide"; *Chem. Phys. Chem.*, 11, (2010); pp: 2131-2139. DOI: 10.1002/cphc.201000132.

[48] M.J. Webb, P. Palmgren, P. Pal, O. Karis, H. Grennberg; "A simple method to produce almost perfect graphene on highly oriented pyrolytic graphite"; *Carbon*, 49, (2011); pp: 3242-3249. DOI: 10.1016/j.carbon.2011.03.050

[49] M. Scepanovic, M. Grujic-Brojcin, K. Vojisavljevic, S. Bernikcm T. Sreckovic; "Raman study of structural disorder in ZnO nanopowders"; *J. Raman Spectrosc.*, 41, (2010); pp: 914-921; DOI: 10.1002/jrs.2546

[50] S. Reich, C. Thomsen; "Raman spectroscopy of graphite"; *Phil. Trans. R. Soc. Lond.* 362, (2004); pp: 2271-2288; DOI: 10.1098/rsta.2004.1454

[51] Measurement Services Division of the National Institute of Standards and Technology (NIST), Wagner plot, https://srdata.nist.gov/xps/main_search_menu.aspx: 05, 2018.

[52] S. A. Leontiev, S. V. Koshcheev, V. G. Devyatov, A. E. Cherkashin, P. Mikheeva; "Detailed XPS and UPS studies of the band structure of zinc oxide"; *J. Struct. Chem*., 38, (1997); pp: 725-731 DOI: 10.1007/BF02763884

[53] P. Mikheeva, G. M. Zhidomirov, S. F. Ruzankin, S. A. Leontiev, V. G. Devyatov, S. V. Koshcheev, A. E. Cherkashin; "Modeling the photoelectron spectra of the valence $O2_p$-band of zinc oxide by the Xα-scattered wave method"; *J. Struct. Chem*., 38, (1997); pp: 732-741. DOI: 10.1007/BF02763885

[54] S.S. Fu, G.A. Somorjai; "Surface studies of zinc oxide growth on Cu(110)"; *Surf. Sci*. 237, (1990); pp: 87-98; DOI: 10.1016/0039-6028(90)90521-9

[55] J. Wintterlin, M.-L. Bocquet; "Graphene on Metal Surfaces"; *Surf. Sci*., 603, (2009); pp: 1841-1852, DOI: 10.1016/j.susc.2008.08.037

[56] M. Petrović, I. Šrut Rakić, S. Runte, C. Busse, J. T. Sadowski, P. Lazić, I. Pletikosić, Z.-H. Pan, M. Milun, P. Pervan, N. Atodiresei, R. Brako, D. Šokcević, T. Valla, T. Michely, M. Kralj; "The mechanism of caesium intercalation of graphene"; *Nat. Commun*., 4, (2013); pp: 2772; DOI: 10.1038/ncomms3772.

[57] M.J. Webb, P. Palmgren, P. Pal, O. Karis, H. Grennberg; "A simple method to produce almost perfect graphene on highly oriented pyrolytic graphite*"; Carbon*, 49, (2011); pp: 3242-3249. DOI: 10.1016/j.carbon.2011.03.050

[58] K. C. Kwon, J. Ham, S. Kim, J.-L. Lee, S. Y. Kim; "Eco-friendly graphene synthesis on Cu foil electroplated by reusing Cu etchants"; *Sci. Rep.* 4, (2014), pp: 4830; DOI: 10.1038/srep04830

[59] C. Mattevi, G. Eda, S. Agnoli, S. Miller, K. A. Mkhoyan, O. Celik, D. Mastrogiovanni, G. Granozzi, E. Garfunkel, Manish Chhowalla; "Evolution of Electrical, Chemical, and Structural Properties of transparent and Conducting Chemically Derived Graphene Thin Films"; *Adv. Funct. Mater*. 19, (2009); pp: 2577-2583; DOI: 10.1002/adfm.200900166

[60] A. Kumar, A.A. Voevodin, D. Zemlyanov, D.N. Zakharov, T.S. Fisher "Rapid synthesis of few-layer graphene over Cu foil"; *Carbon*, 50, (2012); pp: 1546-1553; DOI: 10.1016/j.carbon.2011.11.033

[61] S. Poulston P. M. Parlett P. Stone M. Bowker; "Surface Oxidation and Reduction of CuO and CuzO Studied Using XPS and XAES"; *Surf. Interface Anal*. 24, (1996); pp: 811-820; DOI: 10.1002/%28SICI%291096-9918%28199611%2924%3A12<811%3A%3AAID-SIA191>3.0.CO%3B2-Z

[62] T. Jiang, X. Zhang, S. Vishwanath, X. Mu, V. Kanzyuba, D. A. Sokolov, S. Ptasinska, D. B. Go, H. G. Xing, T.i Luo; "Covalent bonding modulated graphene-metal interfacial thermal transport"; *Nanoscale*, 8, (2016); pp: 1093-1100; DOI: 10.1039/c6nr00979d

[63] V.I. Bukhtiyarov, A.I. Boronin, I.P. Prosvirin, V.I. Savchenko.; "Stages in the Modification of a Silver Surface for Catalysis of the Partial Oxidation of Ethylene: II. Action of the Reaction Medium"; *J. Catal.* 150, (1994); pp: 268-273; DOI: 10.1006/jcat.1994.1345

[64] V.I. Bukhtiyarov, A.I. Boronin, V.I. Savchenko "Stages in the Modification of a Silver Surface for Catalysis of the Partial Oxidation of Ethylene: I. Action of Oxygen"; *J. Catal*. 150, (1994); pp: 262-267; DOI: 10.1006/jcat.1994.1344

[65] H. Tillborg, A. Nilsson, B. Hernnäs, N. Mårtensson, R.E. Palmer; "X-ray and UV photoemission studies of mono-, bi- and multilayers of physisorbed molecules: O_2 and N_2 on graphite"; *Surf. Sci.* 295, (1993); pp: 1-12 DOI: 10.1016/0039-6028(93)90180-R

[66] M. K. Rajumon, M. S. HegdeC. N. R. Rao; "Adsorption of carbon monoxide on Ni/Ti and Ni/TiO2 surfaces prepared *in situ* in the electron spectrometer: A combined UPS-XPS study"; *Catal. Lett.* 1, (1988); pp: 351-359; DOI: 10.1007/BF00766164

[67] M. Lundholm, H. Siegbahn, S. Holmberg, M. Arbman, "Core electron spectroscopy of water solutions"; *J. Electron Spectrosc. Relat. Phemon.*, 40, (1986); pp: 163-180; DOI: 10.1016/0368-2048(86)80015-9

[68] A. C. Ferrari, J. C. Meyer, V. Scardaci, C. Casiraghi, M. Lazzeri, F. Mauri, S. Piscanec, D. Jiang, K. S. Novoselov, S. Roth A. K. Geim; "Raman Spectrum of Graphene and Graphene Layers"; *Phys. Rev. Lett*., , 97, (2006); pp: 187401; DOI: 10.1103/PhysRevLett.97.187401

[69] M. Favaro, H. Xiao, T. Cheng, W. A. Goddard, J. Yano, E. J. Crumlin "Subsurface oxide plays a critical role in CO_2 activation by Cu(111) surfaces to form chemisorbed CO_2, the first step in reduction of CO_2"; *PNAS*, 114, (2017); pp: 6706-6711; DOI: 10.1073/pnas.1701405114

[70] G. Hee Han, F. Günes, J. J. Bae, E. S. Kim, S. J. Chae, H.-J. Shin, J.-Y. Choi, D. Pribat, Y. Hee Lee "Influence of Copper Morphology in Forming Nucleation Seeds for Graphene Growth"; *Nano Lett.*, 11, (2011); pp: 4144-4148; DOI: 10.1021/nl201980p

[71] Y. Xiao, H. Kim, C. Mattevi, M. Chhowalla, R. C. Maher, L. F. Cohen: "Influence of Cu substrate topography on the growth morphology of chemical vapour deposited graphene"; *Carbon*, 65, (2013); pp: 7-13; DOI: 10.1016/j.carbon.2013.06.090

[72] A. Kaniyoor, S. Ramaprabhu "A Raman spectroscopic investigation of graphite oxide derived graphene"; *AIP Advances*, 2, (2012); pp: 032183; DOI: 10.1063/1.4756995

[73] M. Sánchez-Agudo, F. Yubero, G. G. Fuentes, A. Gutiérrez, M. Sacchi, L. Soriano, J. M. Sanz; "Study of the growth of ultrathin films of NiO on Cu(111)"; *Surf. Interface Anal.* 30, (2000); pp: 396-400; DOI: 10.1002/1096-9918(200008)30:1<396::AID-SIA804>3.0.CO;2-3

[74] S. Berciaud, S. Ryu, L.E. Brus, T.F. Heinz,; "Probing the Intrinsic Properties of Exfoliated Graphene: Raman Spectroscopy of Free-Standing Monolayers"; *Nano Lett.*, 9, (2009); pp: 346-352; DOI: 10.1021/nl8031444

[75] K. Kneipp, Y. Wang, H. Kneipp, L.T. Perelman, I. Itzkan, R. Dasari, M. S. Feld; "Single molecule detection using surface-enhanced Raman scattering (SERS)"; *Phys. Rev. Lett.* 78, (1997); pp: 1667-1670; DOI: 10.1103/PhysRevLett.78.1667

[76] G. Tsoukleri, J. Parthenios, K.s Papagelis, R. Jalil, A. C. Ferrari, A. K. Geim, K. S. Novoselov, C. Galiotis; "Subjecting a Graphene Monolayer to Tension and Compression"; *Small*, 5, (2009); pp: 2397-2402; DOI: 10.1002/smll.200900802

[77] J.E. Lee, G. Ahn, J. Shim, Y.S. Lee, S. Ryu; "Optical separation of mechanical strain from charge doping in graphene"; *Nat. Commun.*, 3, (2012); pp: 1024; DOI: 10.1038/ncomms2022

[78] A. Das, S. Pisana, B. Chakraborty, S. Piscanec, S. K. Saha, U. V. Waghmare, K. S. Novoselov, H. R. Krishnamurthy, A. K. Geim, A. C. Ferrari, A. K. Sood; "Monitoring dopants by Raman scattering in an electrochemically top-gated graphene transistor"; *Nat. Nanotechnol.*, 3, (2008); pp: 210-215; DOI: 10.1038/nnano.2008.67

[79] P. O. Gartland, S. Berge, B. J. Slagsvold; "Photoelectric Work Function of a Copper Single Crystal for the (100), (110), (111), and (112) Faces"; *Phys. Rev. Lett.*, 28, (1972); pp 738-739; DOI: 10.1103/PhysRevLett.28.738

[80] G. Giovannetti, P. A. Khomyakov, G. Brocks, V. M. Karpan, J. van den Brink, P. J. Kelly; "Doping Graphene with Metal Contacts"; *PRL*, 101, (2008); pp: 026803; DOI: 10.1103/PhysRevLett.101.026803

[81] Paul A. Anderson; "The Contact Difference of Potential Between Barium and Zinc The External Work Function of Zinc"; *Phys. Rev.*, 57, (1940); pp: 122-127; DOI: 10.1103/PhysRev.57.

[82] N. D. Lang, W. Kohn; "Theory of Metal Surfaces: Work Function"; *Phys. Rev. B*; 3, (1971); pp: 1215-1223; DOI: 10.1103/PhysRevB.3.1215

[83] M. Seidl, K.H. Meiwes-Broer, M. Brack.; "Finite-size effects in ionization potentials and electron affinities of metal clusters"; *J. Chem. Phys*. 95, (1991); pp: 1295-1303; DOI: 10.1063/1.461111

[84] D Díaz-Fernández, J Méndez, F Yubero, G Domínguez-Cañizares, A Gutiérrez, L Soriano; "Study of the early stages of growth of Co oxides on oxide substrates"; *Surf. Interface Anal*.; 43, (2014); pp: 975-979; DOI: 10.1002/sia.5366

[85] I Preda, RJO Mossanek, M Abbate, L Alvarez, J Méndez, A Gutiérrez, L Soriano; "Surface contributions to the XPS spectra of nanostructured NiO deposited on HOPG"; *Surf. Sci*.; 606, (2012); pp: 1426-1430; DOI: 10.1016/j.susc.2012.05.005

Chapter 5

Free standing ultra-thin Al_2O_3 membranes

"Bringing Science Solutions to the World"

Berkeley Lab

5.1 Introduction

This chapter presents the main part of the work done during the pre-doctoral stay at the Lawrence National Berkeley Laboratory (California, USA) in the group of Professor Miquel Salmeron, and it was performed on both the Material Science Division and Molecular Foundry facilities. The main goal was to develop electron transparent ultra-thin metal oxide membranes for ambient pressure spectroscopies and atomic-scale studies.

Heterogeneous catalysts (solid/liquid and solid/gas) are essential for virtually all chemical reactions used to produce fuels and chemicals, as well as conversion of environmentally harmful components into useful products. The catalysts performance is directly related to its atomic structure and composition, and therefore the ability to image catalysts *in situ* at the atomic scale is essential to develop a deep scientific understanding on how the catalyst composition and structure control the activity and selectivity in each chemical reaction. While tremendous strides toward this aim have come through the use of high-resolution electron microscopy and spectroscopy (individually or in combination), the ability to observe catalytic processes at the atomic level during reaction, and the ability to correlate its dynamics with atomic-scale variations in the catalyst composition and structure, remains a challenge. This is especially true for solid/liquid interfaces, where measurements without substantial interference from the bulk materials are extremely difficult to be achieved [1]. Meeting these challenges requires merging information from TEM, XAS and XPS obtained on the same sample and under reaction conditions.

Focusing in first place on the TEM imaging, the actual challenge consists on the acquisition of images under real operating conditions of the atoms and molecules adsorbed on the surfaces in order to follow their dynamics and changes. The pioneers

works of Hashimoto [2] and Baker [3,4,5] opened the door for environmental TEM (ETEM), which has been developed during the last decades, increasing the resolution near to 30 mbars [6,7,8]. In general, there are two different configurations of ETEM: 1) differential pumping, where commercial sample holders can be used [9] and 2) reaction cells, which have been the focus of the work of many research groups [10,11], including graphene based cells [12]. However, the detection of single atoms results evasive due to the existing methods for sample preparation and imaging configurations, because they are responsible of the uncontrolled beam-sample-cell interactions and falsification of the information content in atomic-resolution images from single-digit nanostructures. In addition, further improvement and co-development of ultra-low dose (<10 $e^-/Å^{-2}s^{-1}$) environmental electron microscopy, integration of pulsed electrons coupled with aberration corrected optics and ultra-low noise detectors are required for really manage the desired atomic resolution goals.

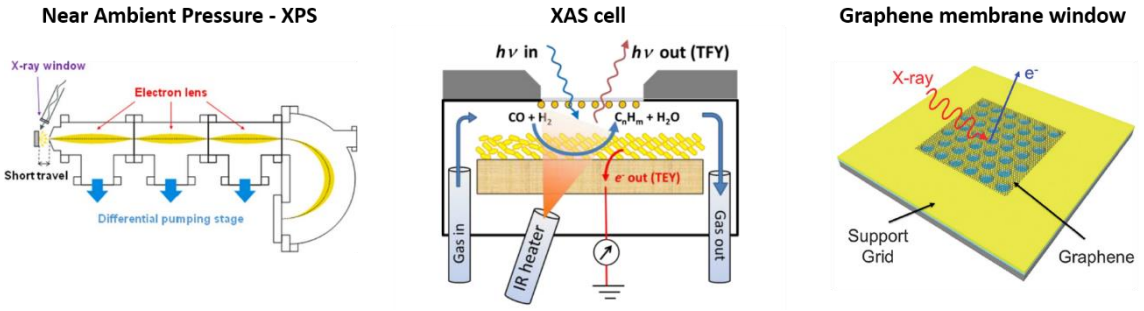

Figure 5.1 Schematic representation of three technical approaches for ambient pressure X-ray spectroscopies measurements. From left to right, NAP-XPS, XAS cell and graphene membrane windows.

On the other hand, for X-ray spectroscopies, different approaches can be found in order to bring the measuring conditions closer to the reality in terms of pressure and temperature. In this way, Figure 5.1 shows three technical solutions for near ambient pressure X-ray spectroscopies measurements. Going into detail, the penetration depth of soft X-rays photons is about a few hundreds of nanometers in solid materials. Accordingly, 100 nm silicon nitride (SiN) membranes are used as photon windows of XAS cells to measure gases, liquids and catalytic nanoparticles at high pressures (~1bar) and temperatures (~300°C) in XAS fluorescence and total-electron-yield detection modes [13,14,15]. More complicated is the case for electron detection spectroscopies. For the

XPS field, near-ambient-pressure XPS (NAP-XPS) is commercially available and can be found in the majority of synchrotron facilities over the world [16,17]. The use of electron lenses to focus the photoelectrons through several apertures as part of a differentially pumped multistage lens system allows to increase the photoelectron collection efficiency and to extend the measurement pressure range up to tens of mbar. Nevertheless, multiple real chemical reactions occur at higher pressures (~1bar), thus limiting the utility of this technique. In recent years, the amazing mechanical and impermeable properties of graphene have allowed the development of graphene windows, which can separate liquid and gas phases at high pressures from high vacuum. In addition, the reduced thickness of graphene allows a limited loss of collected electrons at typical XPS working energies [18,1].

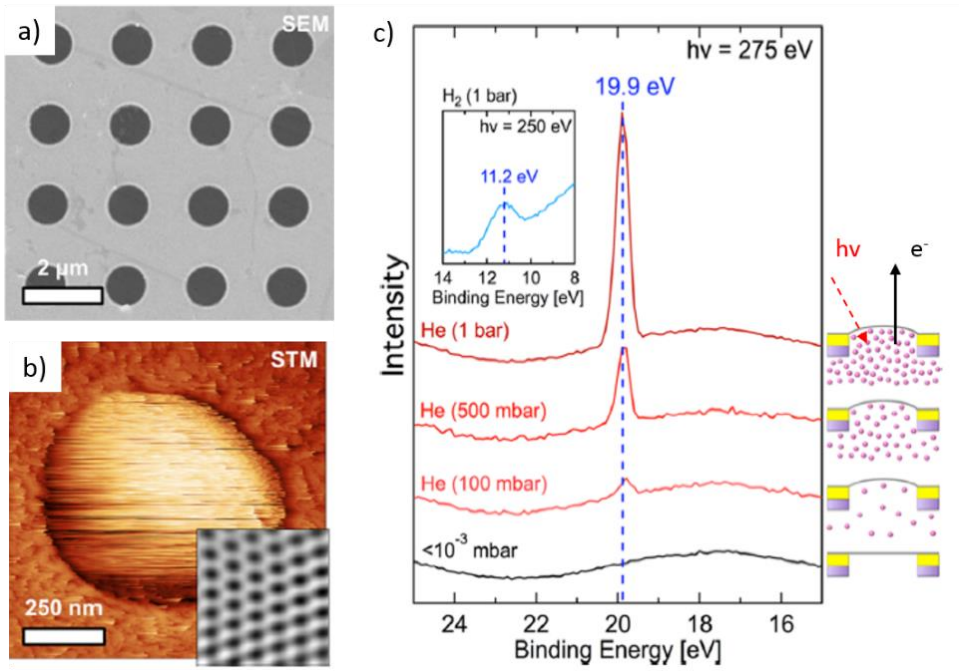

Figure 5.2 Figures taken from [20] a) SEM image of a region of a SLG covered membrane; b) TM image of one the holes in the membrane with SLG suspended across it (VS = 1.5 V, It = 300 pA). Inset: Atomic resolution STM image of free-standing graphene measured in the hole region (VS = 0.18 V, It = 500 pA, 2D-FFT filtered); c) He 1s XP spectra collected using a single layer graphene membrane with the reaction cell under vacuum ($<10^{-3}$ mbar), and filled with He (100 mbar, 500 mbar, and 1 bar) with photon energies, hν = 275 eV. Inset: H 1s spectra measured with the same membrane, with the reaction cell filled with H_2 (1 bar) and photon energy, hν = 250 eV.

A very recent review from Weatherup [19] summarizes the state of art of these novel and interesting devices. In particular, two studies can be highlighted in order to draw a general picture of this field. In first place, the work of Weatherup et. al. [20], which in fact was accomplished at Salmeron's group in 2016, demonstrated that mono and bilayers graphene membranes can separate mediums with a pressure difference up to six orders of magnitude. The test performed under real operando conditions at the ALS showed that these membranes can enclose gases up to 1.5 bars, measuring the XPS spectra of He 1s at different pressures, and even a tight H 1s signal from H_2 gas could be detected (see Figure 5.2). In addition, this same publication shows the behavior of Cu nanoparticles deposited on the graphene window under different oxygen doses, reporting reversible changes on their oxidation state as a function of the pressure. The work from Juan J. Velasco-Velez et. al. [21] constitutes the second example. In this case, cobalt nanoparticles were electrochemically deposited on the graphene membrane, showing a reduction from the initial Co^{3+} state at the nanoparticles bulk to Co^{2+} state at the Co/graphene interface. Under different conditions, including liquids, these nanoparticles were measured in order to study there catalytic behavior, suggesting that the previous reduction of the oxidation state of cobalt at the interface is the origin of their enhanced catalytic power. Therefore, these publications show the impressive possibilities that graphene membranes could offer in the study of catalytic process by means of XPS measurements at more realistic pressures.

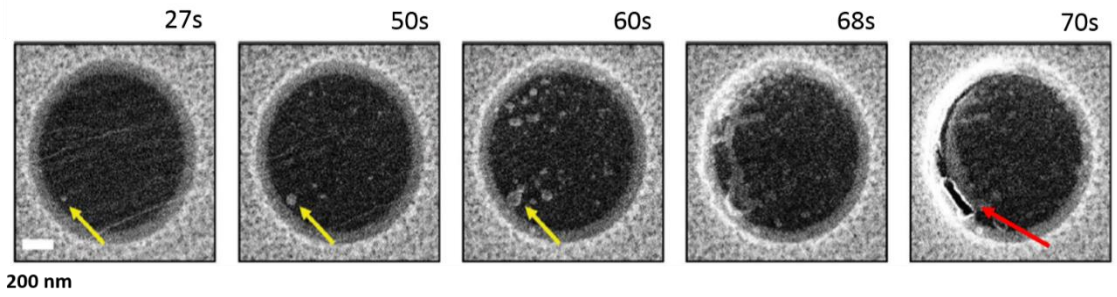

Figure 5.3 Figure taken from [1]**.** Series of SEM images of a graphene window with liquid water sealed underneath the membrane. The images were taken sequentially in the same region with an incident beam of 15 keV electrons. Yellow arrows indicate the nucleation of bubbles beneath the graphene. Red arrow indicates the final rupture of graphene.

In spite of these studies, the use of graphene membranes has not been widely extended. The reason of this is the radiolysis of liquid and gas molecules induced by the X-ray (or electron) beam, which can produce gas bubbles (for liquids) and radicals that chemically attack the membrane, finally causing its rupture. This fact has been elegantly shown in [1] by a series of SEM images as a function of time of a monolayer graphene window which encloses water (see Figure 5.3). Thus, these graphene windows have limitations regarding their structural and chemical stability, leading to a limited shelf time. In this experimental and technical context, the development of a new generation of ultra-thin electron transparent windows (1-3 nm) based on metal oxides could overcome the graphene limitations and could be used in multiple imaging and spectroscopic techniques as part of reaction cells. Besides, the development of these oxide thin films constitute *per se* an important new method and an improvement on existing capabilities for studying liquid/solid and gas/solid interfaces of nanoparticles, as metal oxides are more relevant substrates for supporting catalysts than graphene.

This chapter presents the first stages of the development and viability of these membranes in terms of their simple nanofabrication process and utility under high pressure conditions, being able to maintain pressure differences up to ten orders of magnitude. The chapter is divided into three main sections. Section 5.2 discusses the characterization of the Al_2O_3 ALD deposition by means of AFM and XPS measurements. The other two sections are dedicated to the elaboration of the ultra-thin Al_2O_3 membranes using two different free standing sacrificial layers: graphene in section 5.3 and Formvar polymer in section 5.4. Although the structure of both sections is similar (first a brief explanation of their elaboration process followed by a chemical and structural characterization of the oxide membranes), there is an important difference. In the case of using free standing graphene as initial support, there was no success on creating non-broken membranes, and the reason of this is discussed. On the other hand, by using Formvar polymer, complete Al_2O_3 membranes (1-3 nm) were successfully developed, and therefore a real test in operando conditions could be performed at the ALS facility in a similar way to that performed by Weatherup with graphene membranes. A brief conclusion where the applicability on different characterization techniques of these new generation of transparent electron membranes is discussed will close this chapter.

5.2 Al_2O_3 deposition by ALD

The atomic layer deposition (ALD) process has been previously exposed in Chapter 2, subsection 2.3.3. Al_2O_3 was selected as the first candidate material since it is chemically inert and some groups have demonstrated that ultra-thin films of 1 nm can be growth on graphene without pinholes [22,23]. Therefore, the following text will cover only the results regarding the deposition of Al_2O_3 on four different substrates: silicon nitride wafer (SiN), SiN coated with 30 nm of gold (Au/SiN), graphene transferred into SiN (G/SiN) and finally, graphene transferred into SiN coated with 30 nm of gold (G/Au/SiN). The aim of this preliminary study was to clarify the characteristics of the Al_2O_3 deposition in terms of chemical and morphological homogeneity in samples gradually more similar to the final TEM percolated grids of SiN coated with gold and with graphene transferred into it. Before the gold coating, 3nm of chromium were deposited in order to enhance the homogeneity of the gold growth.

5.2.1 Morphological and chemical characterization

The morphology of the initial substrates have been studied by means of AFM measurements, depicted on Figure 5.4. The root mean squared (RMS) roughness for the clean SiN wafer is very low, less than 0.5 nm. On the other hand, once the gold is deposited the roughness increases up to 9.5 nm. In the case of transferred graphene by free polymer methods, the wrinkles associated to the different coefficient of thermal expansion of copper and graphene during the cooling stage of the CVD process, in addition to the defects developed during the transfer, give rise to agglomerations and strips up to several tens of nanometers which can distort the roughness calculation. For example, in the case of Figure 5.4 b the roughness is about 6.5 nm. Finally, the graphene transferred into gold seems to be like a veil over the gold grains. The sample is not completely covered by graphene, and in fact in some areas the gold grains are shown bare. The roughness in this case is about 7 nm. These RMS roughness have been calculated from 1x1 μm images. Although the graphene transfer process presents some limitations regarding homogeneity (as it will be discussed in section 5.3.2), the AFM measurements were taken at significant areas, inside and outside the zone where graphene was transferred.

In this way, after Al_2O_3 deposition, no relevant differences could be appreciated in the AFM measurements. Figure 5.5 shows AFM images of G/SiN and G/Au/SiN

samples before and after the growth of 3 nm of Al_2O_3. The deposit seems to follow the original roughness of the sample, and no clusters were observed. These measurements have been performed for a series of Al_2O_3 coverages (0.5 nm, 1 nm, 2 nm, 3 nm, 5 nm and 10 nm) with the same results in all cases. Finally, the roughness is almost constant, with a slight increase at the 10 nm stage of about 15%, what could be related to the roughness of the Al_2O_3 layer.

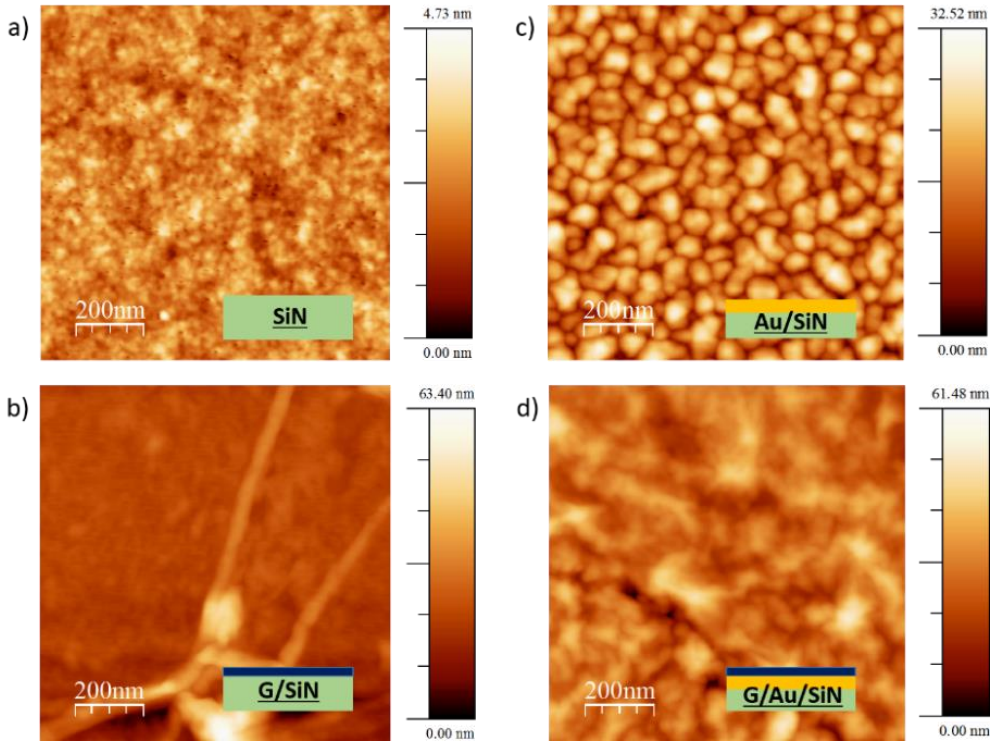

Figure 5.4 AFM topography images of a) SiN wafer, b) graphene transferred into SiN wafer, c) 30 nm of gold on SiN substrate and d) graphene transferred into 30 nm of gold on SiN wafer.

On the other hand, XPS measurements were taken in order to perform a chemical characterization of the oxide thin film. Surface atomic concentrations of the four substrates were calculated from the surveys spectra as a function of the Al_2O_3 coverage. As it can be appreciated in Figure 5.6, the evolution of the atomic concentration is quite similar in all cases. In fact, from 5 nm nominal thickness (red box drawn for each substrate), the surface concentrations measured by XPS are constant. Taking into account that this measurements were taken with an Al anode ($h\nu$ = 1486.6 eV), the IMPF at a kinetic energy of 1000 eV is about 2 nm for the Al_2O_3 matrix. Therefore, as the 90% of

the elastic photoemitted electrons come from a distance up to three times the IMPF, the saturation of the surface concentration is indicating that the deposit is homogenous and performed layer by layer, covering all the substrate without holes. In fact this result matched perfectly with the previous discussion of the AFM measurements. The ALD method effectively guarantees a layer by layer mode of growth, whereas the nucleation stage is not critical on these four substrates (for example, on section 4.2.1 the growth of ZnO clusters on HOPG was determinate by the limited nucleation process). This last point is very important in the ALD deposition process: different rates can lead to an island growth mode or not complete layers rather than a wetting one of constant thickness and same roughness as the initial substrate. For example, there are some publications regarding the Al_2O_3 deposition by this technique on different substrates, especially HOPG, copper and graphene on copper [24,25], reporting this kind of issues related to the chemical state of the substrate surface and to the chemical interaction between the crystallographic direction of the substrate surface and the organic precursor used. In the present case, none of this problems is reported.

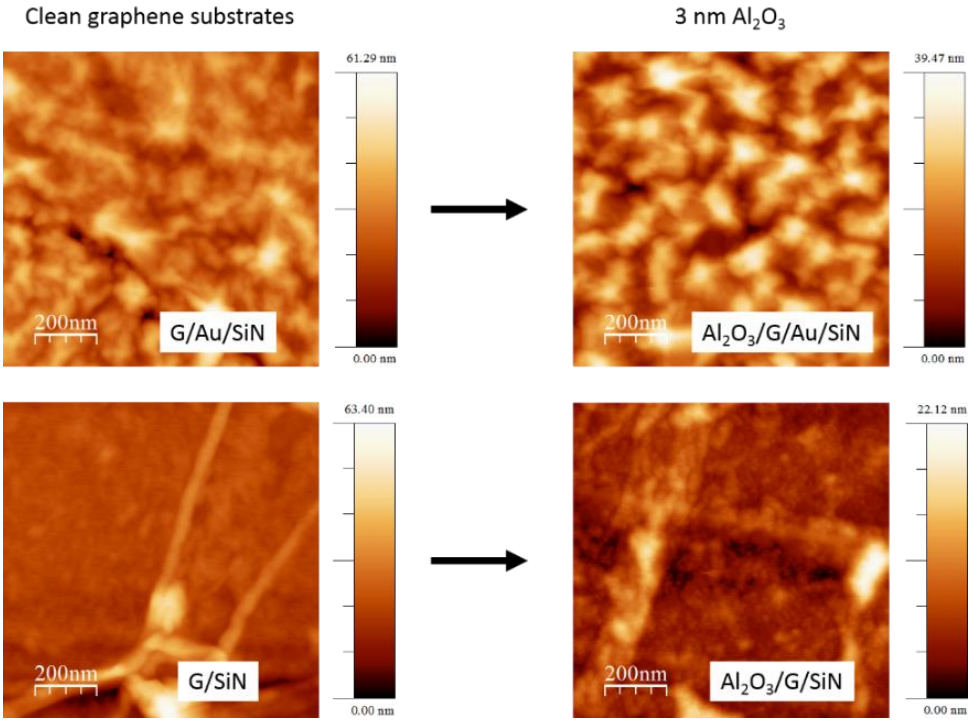

Figure 5.5 AFM topography images of a) SiN wafer substrate, b) graphene transferred into SiN wafer, c) 30 nm of gold on SiN substrate and d) graphene transferred into 30 nm of gold on SiN wafer substrate.

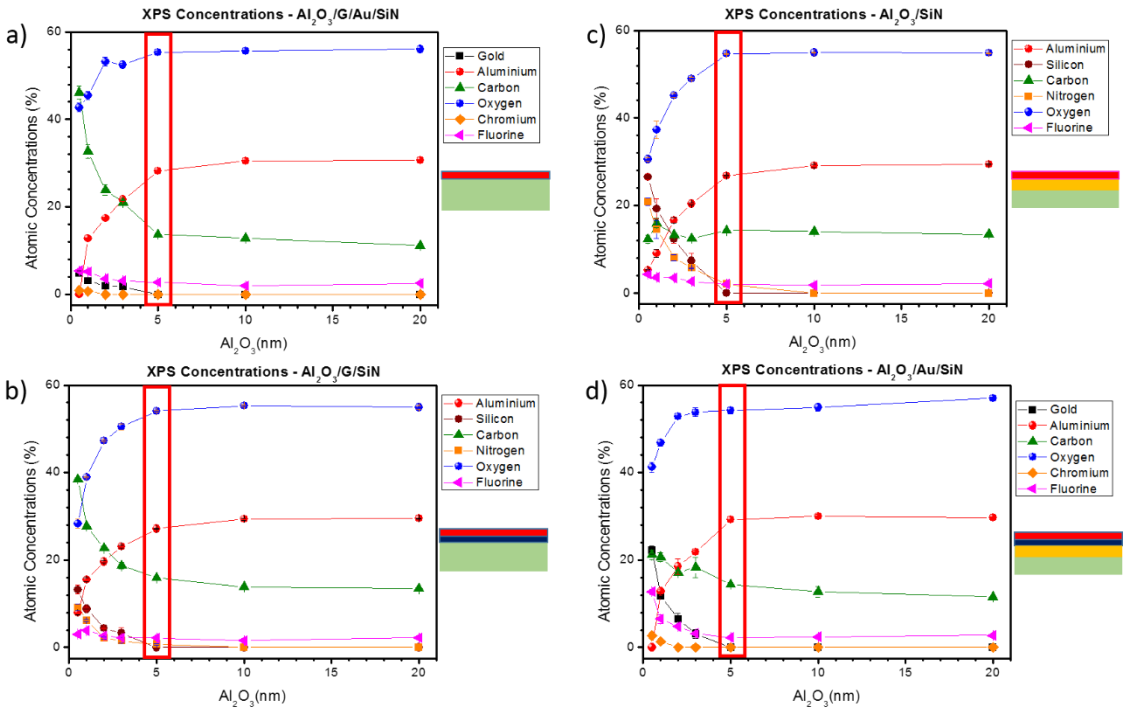

Figure 5.6 Surface concentrations from XPS measurements as a function of Al_2O_3 ALD nominal coverage of a) SiN wafer substrate, b) graphene transferred into SiN wafer substrate, c) 30 nm of gold on SiN substrate and d) graphene transferred into 30 nm of gold on SiN wafer substrate.

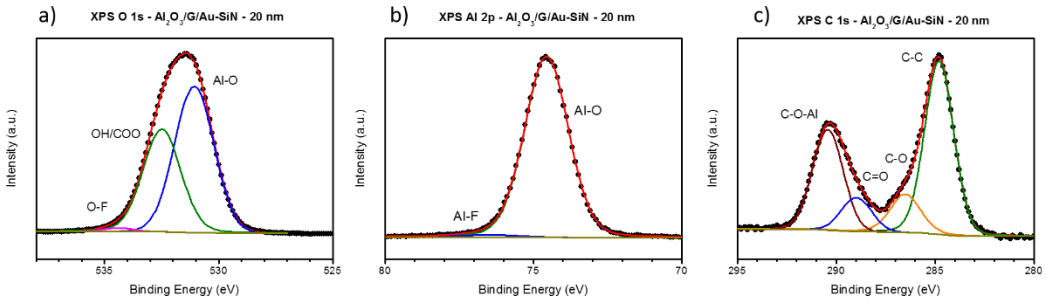

Figure 5.7 a) Fitting of the XPS O 1s spectrum for an Al_2O_3 thin film of 20 nm on a SiN wafer used as substrate; b) the same for the Al 2p region; c) the same for the C 1s region.

After a quantitative morphological analysis, a chemical characterization was done. For these purposes, and in order to avoid substrate distortions, a 20 nm Al_2O_3 thin film was grown on a SiN substrate. Figure 5.7 shows the XPS spectra of the O 1s, Al 2p and C 1s regions. The O 1s region has a very broad peak divided in two contributions; the main one at ~530.5 eV is assigned to aluminum oxide [26], whereas the second one

corresponds to hydroxyl and other carbon-oxygen (COO) groups [27]. A third contribution found at ~534.8 eV is suggested to come from the oxygen-fluorine bond. As it can be appreciated, the Al 2p region is basically composed by only one contribution assigned to the Al-O at ~74.5 eV [26] (the reduced S-O splitting allows to adjust this region to only one peak). However, a small contribution related again to fluorine contamination was appreciated at ~76.5 eV [28]. The origin of this fluorine contamination was due to the ALD growth chamber, and it is constant in all the processes performed on it, independently of the protocol and the selected material to be deposited. On the other hand, the C 1s region is much more complex. As it can be seen, four different contributions were assigned. In first place, at high energies C-Al-O carbonates complexes can be found at ~290.6 eV [27]. These cross bonds between these three elements could come from a not complete oxidation and purge of the TMA organic precursor, so some carbon is kept at the Al_2O_3 matrix. In a similar way, C=O (288.7 eV), C-O (286.2 eV) and C-C (284.5 eV) contributions have exactly the same origin, although these XPS measurements have been *ex situ* performed, and therefore a small surface contamination from adventitious carbon was expected.

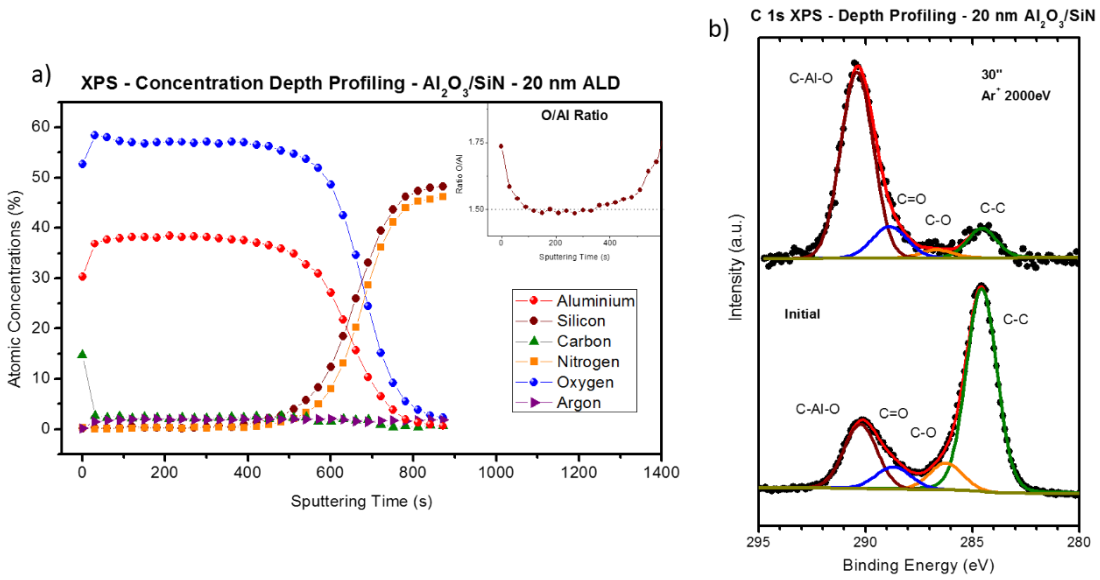

Figure 5.8 a) Depth profiling performed by monoatomic Ar+ at 2000eV, cycles of 30s, on 20nm of Al_2O_3 deposited by ALD on SiN wafer. Top right insert: O/Al ratio as a function of etching time; b) C 1s region before and after one cycle of 30" using Ar^+ at 2000 eV.

The content of carbon on the Al_2O_3 matrix deposited by ALD depends on the temperature of growth. It is well known that at such low temperatures of growth as those used here (40 °C), the ALD gives a high content of carbon (about 15%) [29] and an O/Al ratio deviated from the 1.5 stoichiometric value, i.e. 1.9-1.8 or 1.2 (depending if the complete O 1s region was counted [29,30] or if the OH^- ions contribution is subtracted [29]). These values match perfectly with those inferred from the survey XPS spectrum taken from the 20 nm sample, where the percentage of carbon is ~15% and the O/Al ratio 1.8 or 1.1, depending also on the subtraction of the OH^- component. However, this deviation from stoichiometry is corrected in the bulk. Figure 5.8 shows the XPS depth profiling study performed on this same sample, done by 30 cycles of 30 seconds of sputtering and using monoatomic Ar^+ ions accelerated at 2000 eV. After the first cycle, the content of carbon dropped to less than 2%, while aluminum and oxygen increased and maintained a 1.5 O/Al ratio (see top right insert). A small contribution of Ar appeared after the first cycle due to ion implantation. Besides, further experiments indicated that a mild etching with Ar^{+75} clusters at 800 eV during 30 seconds leads to the removal of the carbon atoms and the recovery of the bulk stoichiometry (not shown here), together with the absence of implanted Ar atoms.

Therefore, the ALD deposition of Al_2O_3 guarantees a layer by layer growth on these four substrates, especially important for the graphene/Au/SiN case. An efficient nucleation process ensures that there were no pinholes for, at least, coverages greater than 5 nm, although the evolution of the XPS spectra and AFM topography images indicated that this could be also true for lower coverages. In addition, the Al_2O_3 has a good stoichiometry in the bulk, whereas the surface has fluorine and carbon contamination. However, these contaminants can be easily removed by a short and gentle sputtering with Ar^{+75} clusters at low energy, remaining unchanged the Al_2O_3 film.

5.3 Al_2O_3 on free standing graphene

The first idea to develop these ultra-thin Al_2O_3 membranes was to use the well-known free standing graphene membranes [20] as the initial support for the metal oxide deposition. The preparation of the free standing graphene on the percolated TEM grid has been already deeply explained in section 2.6.3.1 of Chapter 2, “Experimental details”. Nevertheless, Figure 5.9 shows a schematic representation of the complete preparation process. Four steps describe the complete fabrication: 1) the perforated SiN TEM grid

surface is coated with gold for grounding proposes (100 nm thick SiN window with either a 25 × 25 array of Ø 1 μm and 0.5 μm circular holes at a 2 and 1 μm pitch); 2) the Au/SiN grids are covered with a sacrificial layer (in this case graphene); 3) then this free standing material is used as a support for deposition of the metal oxide. In the case of graphene, the Al_2O_3 deposition can be done at any of the both sides of the grid, top or bottom (for example Figure 5.9, shows at step 3 the bottom case). 4) Finally, if the graphene suffers some damage, it could be removed, and therefore, only the metal oxide covers the grid holes. In this last case, a new graphene monolayer can be transferred in order to correct charge accumulation during measurements.

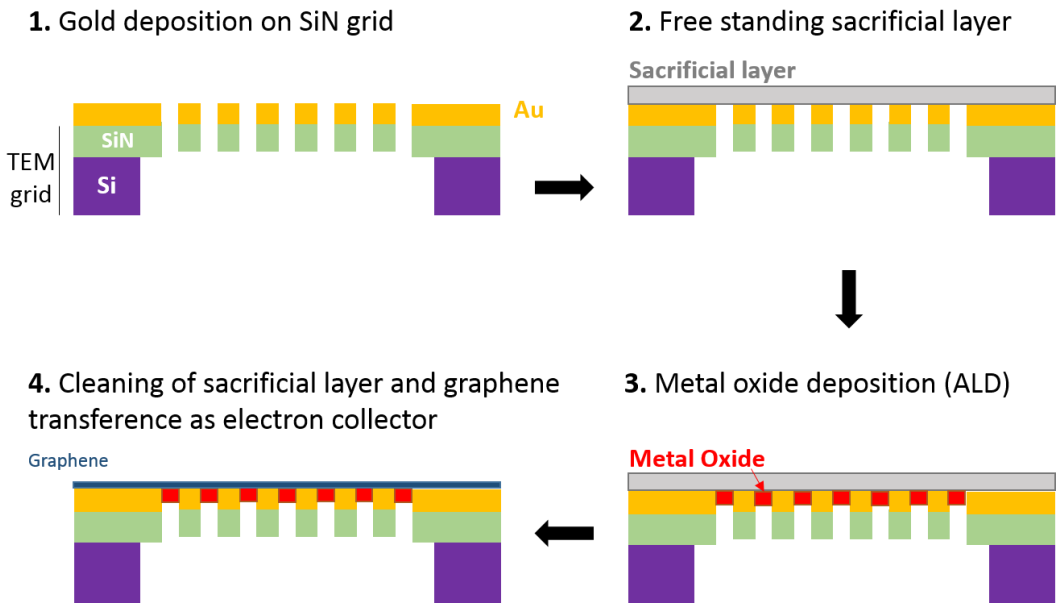

Figure 5.9 Schematic representation of the fabrication steps of an electron transparent metal oxide window for spectroscopic and imaging techniques by using free standing graphene as initial support for the metal oxide.

The use of graphene presents two main advantages over known polymers: first, it is electrical conductive, so there is no need to remove it after the Al_2O_3 deposition, and second, the use of non-polymer transfer method (see section 2.5.3.1) involves less contamination. However, as it will be explained in depth, handling commercial graphene grown by CVD on polycrystalline copper presents some well-known difficulties (as it was exposed previously in Chapter 4). This type of graphene growth is sensitive to the different crystallographic directions in terms of nucleation and growth rate [31,32], what leads to the formation of graphene grain boundaries and defects where it can easily break

during the transfer process. This circumstance reduces the success rate of completely covering all the holes and highly depends on the ability and know-how of the researcher and the size and number of holes.

5.3.1 Morphological and chemical characterization

Ultra-thin Al_2O_3 membranes of 3 nm thickness were grown on the back and top sides of the graphene membranes. The graphene was not removed after the ALD deposition process. In addition to a third graphene membrane used for comparison purposes, these samples were submitted to different characterization techniques (SEM-EDX, XPS, TEM-ELLS and AFM) in order to study the viability of depositing the metal oxide on the free standing graphene and its structural integrity.

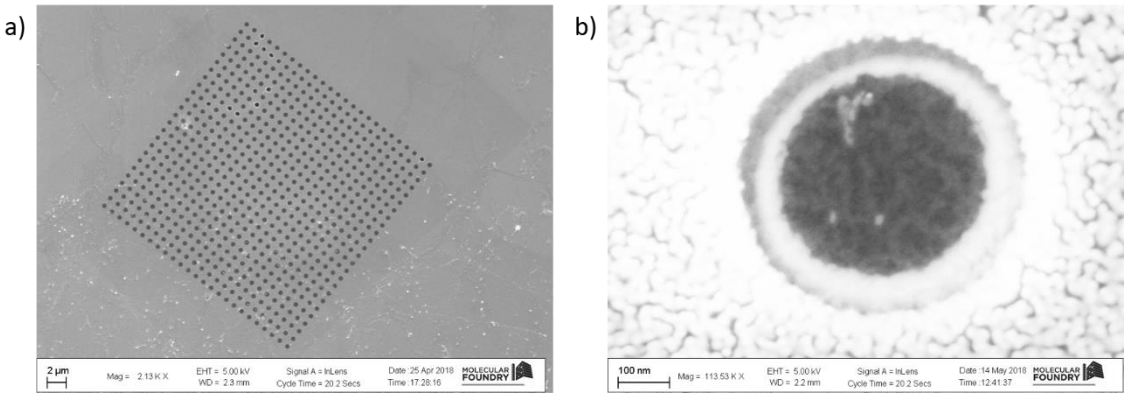

Figure 5.10 a) x213.000 magnification SEM image of a 3nm Al_2O_3/graphene covered membrane; b) x11.353.000 maginification SEM image of an individual perforated hole covered by 3nm Al_2O_3/graphene.

Figure 5.10 a shows a SEM image of a complete grid of 25x25 holes with the Al_2O_3 at the top. Some of these holes are clearly not covered by Al_2O_3/graphene (darker holes). Figure 5.10 b is a detail of one of these holes covered by the free standing metal oxide. As it can be appreciated, the image of the hole presents some kind of roughness, with few small particles on it. There was no difference between Al_2O_3 deposition on top or bottom side (from now, just top (Al_2O_3/graphene) or bottom (graphene/Al_2O_3)).

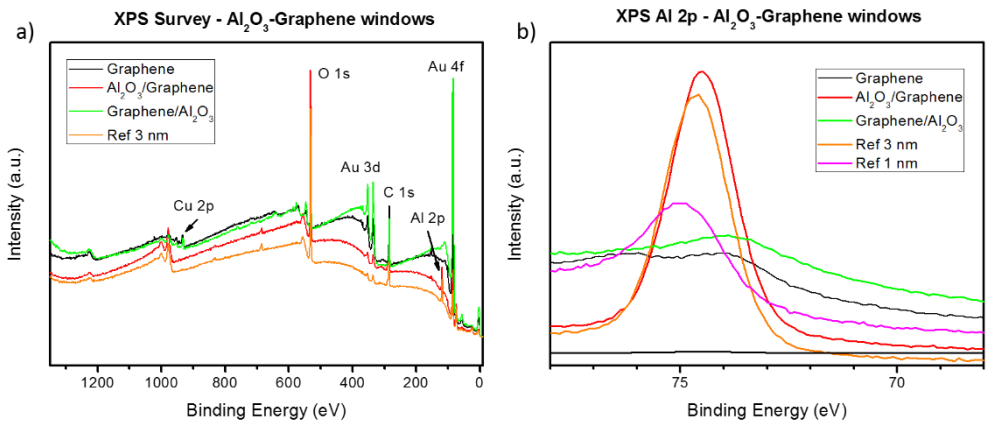

Figure 5.11 a) XPS survey spectra of graphene free standing membrane (black), 3 nm Al_2O_3/graphene free standing membrane (red), 3 nm graphene/Al_2O_3 free standing membrane (green) and, as reference, 3 nm of Al_2O_3 grown on Au/SiN substrate. b) The same for the XPS Al 2p region.

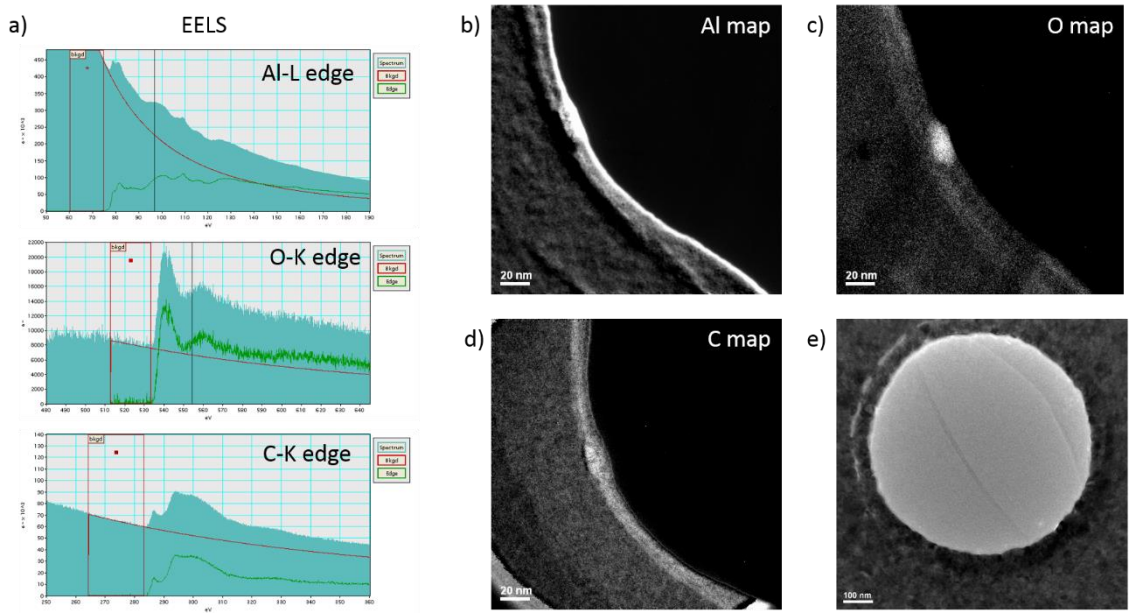

Figure 5.12 a) EELS spectra for Al L edge, O K edge and C K edge, from top to bottom respectively; b) Bottom right TEM image of a broken Al_2O_3/graphene hole with a tear in the central section; top left, top right and bottom left aluminum, oxygen and carbon contrast map performed by EELS, respectively.

On the other hand, XPS measurements showed basically the same features than those discussed previously on section 5.2. Figure 5.11 depicts the XPS survey and Al 2p spectra for the top and bottom metal oxide membranes in comparison with the free

graphene membrane and the Al_2O_3, 3 nm nominal coverage on graphene/Au/SiN substrate from last section. The top membrane shows a very similar spectra as the 3 nm film grown on the previous substrate, but as it can be appreciated, the bottom membrane does not show any signal from the aluminum (although the Al 2p spectrum shows a slight difference in comparison to the graphene membrane that could indicate the presence of the alumina). The reason for this is that the spot size of the XPS is about 400 µm and in the present grid, the holes with Al_2O_3 only represent a 0.4% of the total measured area.

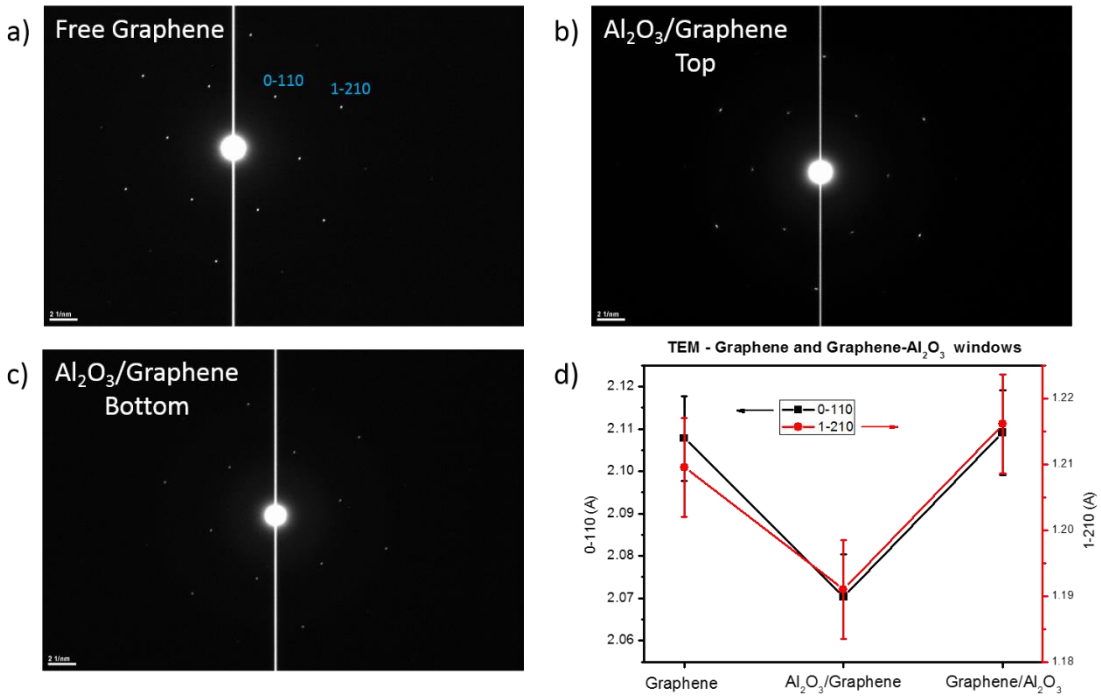

Figure 5.13 a) TEM diffraction pattern of free standing graphene membrane, b) free standing 3 nm Al_2O_3/graphene (top) membrane and c) free standing 3 nm Al_2O_3/graphene (bottom) membrane. d) From the previous TEM diffraction patterns graphene net parameters 0-110 and 1-210 for these three situations.

For a more complete characterization, TEM measurements were performed on the top, bottom and graphene membranes. The used electrons were accelerated up to 200 keV, so the penetration depth was high enough to cross the whole 100 nm SiN window. Due to this, no chemical contrast regarding carbon, aluminum or oxygen could be measured between the inside and outside of the holes in any situation. Nevertheless, Figure 5.12 shows the EELS spectra and chemical contrast images of a hole not completely covered by the Al_2O_3/graphene due to an initial rupture of the last one. This

type of measurements confirmed the Al_2O_3 growth on both, top and bottom sides of graphene. The diffraction pattern of an unbroken hole is shown in Figure 5.13 [33]. No signal from the Al_2O_3 was observed and only the graphene hexagonal diffraction pattern could be seen, indicating the amorphous growth of the oxide and ensured by the low deposition temperature (40°C). Differences on the atomic distances inferred from graphene 0-110 and 1-210 crystallographic directions between the top and bottom growths could indicate some kind of corrugation and/or stress induced by the metal oxide (see Figure 5.13 d). In fact, as the top and bottom sides of the TEM grid have different geometry (in the top case Al_2O_3 would form a continues flat layer, while in the bottom case at the end of graphene it would cover the hole wall forming a ~90° angle respect the free standing graphene), it could be possible that the Al_2O_3 presents small structural differences and therefore stresses the graphene in different ways. No further measurements were performed with more samples and with different thicknesses to demonstrate these kind of correlations.

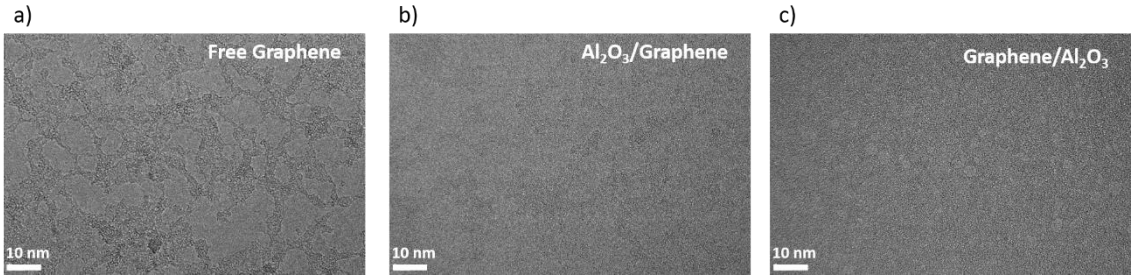

Figure 5.14 a) TEM image of free standing graphene membrane, b) free standing 3 nm Al_2O_3/graphene membrane and c) free standing 3 nm graphene/Al_2O_3 after 2 minutes at 200 keV.

Continuing with the TEM measurements, the integrity of the membranes as a function of the electron dose was checked. Figure 5.14 shows the high resolution image of graphene and Al_2O_3 top and bottom free standing membranes. Although initially the three samples had the same appearance, after being exposed during 2 minutes to electrons accelerated at 200 keV there were clear differences. The free graphene showed spots without a visible structure that grow with time. The reason of this might be that the electrons energy is much greater than the graphene knock-on threshold (~80 keV) [34,35], i.e. the energy transfer from the high-energy electrons is sufficient to break the bonds of the atoms with all their neighbors and hence "knock" the atom out of the lattice. In fact,

graphene can be cut by focused TEM beam at the present energies [35,36]. In this way, it seems clear that doses of high energy electrons can damage the graphene. On the other hand, these kind of spots, although they can also be seen in the case of Al_2O_3 deposition, show a clear structure, suggesting that even if the graphene is destroyed, the Al_2O_3 resists the electron dose, being more stable these kind of metal oxide membranes than the free graphene one.

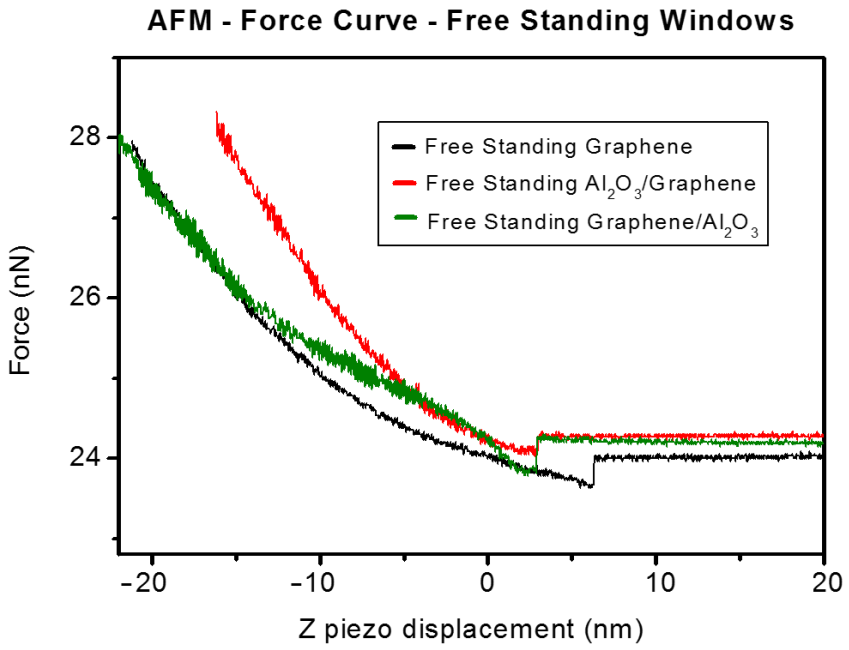

Figure 5.15 Force-curves of free standing Al_2O_3 windows grown on the top and the bottom of free standing graphene. Free standing graphene window is shown for comparison purposes.

Regarding the structural and mechanical properties, Figure 5.15 shows the AFM force-curves for free standing Al_2O_3 grown on graphene. There exists a clear increment on the stiffness and a decrease of the deformation of the membrane once the oxide is deposited. In vacuum systems, the presence of large differences of pressure between both sides of the window would lead to a more rigid behavior compared to graphene, which combined with its high elasticity (as for graphene, the approach and withdraw force-curves are equivalents), would imply more tolerance to mechanical strain. Finally, in comparison to the Al_2O_3 top membrane and the free graphene, the bottom membrane presents a different curvature for low Z piezo displacement. Whereas the top and free

graphene membrane force-curves have same shape as those reported previously for monolayer and multilayer graphene [37,38], the bottom curve does not match with any of them. Therefore, it seems that in this case the Al_2O_3 affects in a different way to the mechanical behavior. Again, this difference between top and bottom could be related to the different geometry of the TEM grid in the deposition process, being also related to the observed difference on the atomic distances calculated from the diffraction pattern.

5.3.2 Issues regarding the initial free standing graphene membranes

As it was mentioned in the introduction of section 5.3, graphene presents some issues that make difficult to work with it and, basically, to cover completely all the holes of the TEM grid with a low degree of contamination. Beginning with this last issue, all the graphene transfer methods available in the laboratory implied the use of different chemical substance which could lead to non-depreciable amount of residues. A common situation using graphene as free standing support, and transferred by a free polymer method, is shown in Figure 5.16, where four EDX spectra corresponding to different localizations of the insert SEM image are shown. As it can be appreciated, not only gold, silicon and nitride from the substrate and carbon, aluminum and oxygen from the thin film were measured. In addition, copper and fluorine are also reported. Whereas the origin of fluorine has been already discussed in terms of contamination from the ALD growth chamber, copper can only come from the initial graphene/Cu sheet and the chemical etching process. In particular, it seems that the squares shown in the SEM image (positions 1 and 2) are formed essentially by this element. XPS survey spectra also show the presence of sulfur, sodium, silicon and silver in the surface of the grids.

As it is described in section 2.6.3.1 of Chapter 2, the copper etching is performed using sodium persulfate, so it seems clear that both contaminants, sulfur and sodium, come from this chemical. In the same way, the Cu 2p spectrum indicated, for all samples, a mixture between Cu^+ and Cu^{2+}, and not the metallic state. Therefore, probably the squares of the insert SEM image of Figure 5.16 are copper salt crystallites attached to the graphene during the transfer process. The silicon could be related to the presence of PDMS polymer. TEM grids are stored in a commercial box with a film of this polymer (silicon based polymer: $(C_2H_6OSi)_n$), so it cannot be excluded the possibility of this contamination. Finally, silver reported by XPS does not have a clear origin. It could come from the aluminum foil and tape utilized for the fabrication of the frame, which was used

in the transfer process to hold the graphene after the copper etching in the absence of any polymer, but at the moment this is not clear.

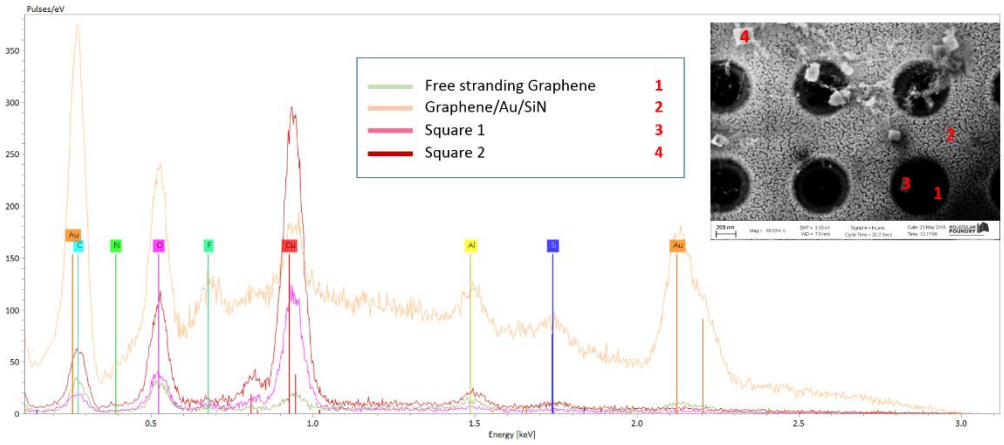

Figure 5.16 EDX spectra for four different positions as indicated on the SEM image inset. The measured sample is a 3 nm Al_2O_3/graphene membrane. The graphene was transferred by free polymer method.

On the other hand, Table 5.1 summarizes the presence of all type of contaminants measured by XPS on different kind of substrates and after different treatments. The columns correspond to different residues (sodium, sulfur, copper, silver and silicon), while the rows indicate the sample studied and its treatment. For example, *Clean Au/SiN PDMS box* indicates the use of Au/SiN substrates without graphene kept in the box where the TEM grids where stored, which had a PDMS film where the grids were attached. The color code makes reference to the where and when the contaminant appears: green if the contaminant is present before the graphene transfer; yellow if it appears after the graphene transfer and the contaminant can be found inside and outside the areas with graphene, and finally red, if the residue is only inside the zones with graphene.

Therefore, only sodium and silicon could be measured before the transfer. It seems clear that the immersion on water (same reservoirs than those used during the graphene transfer process) implies sodium contamination, while silicon comes from the PDMS of the storage box. On the other hand, it is after the graphene transfer when the problem is really presented. Only the silver appears in all kind of substrates and just on the graphene areas, including the case when PMMA was used to transfer graphene into a SiO_2 substrate. This could discard the hypothesis of silver coming from the aluminum tape and foil used in the frame, as for PMMA it was not necessary. As the clean graphene/Cu sheet

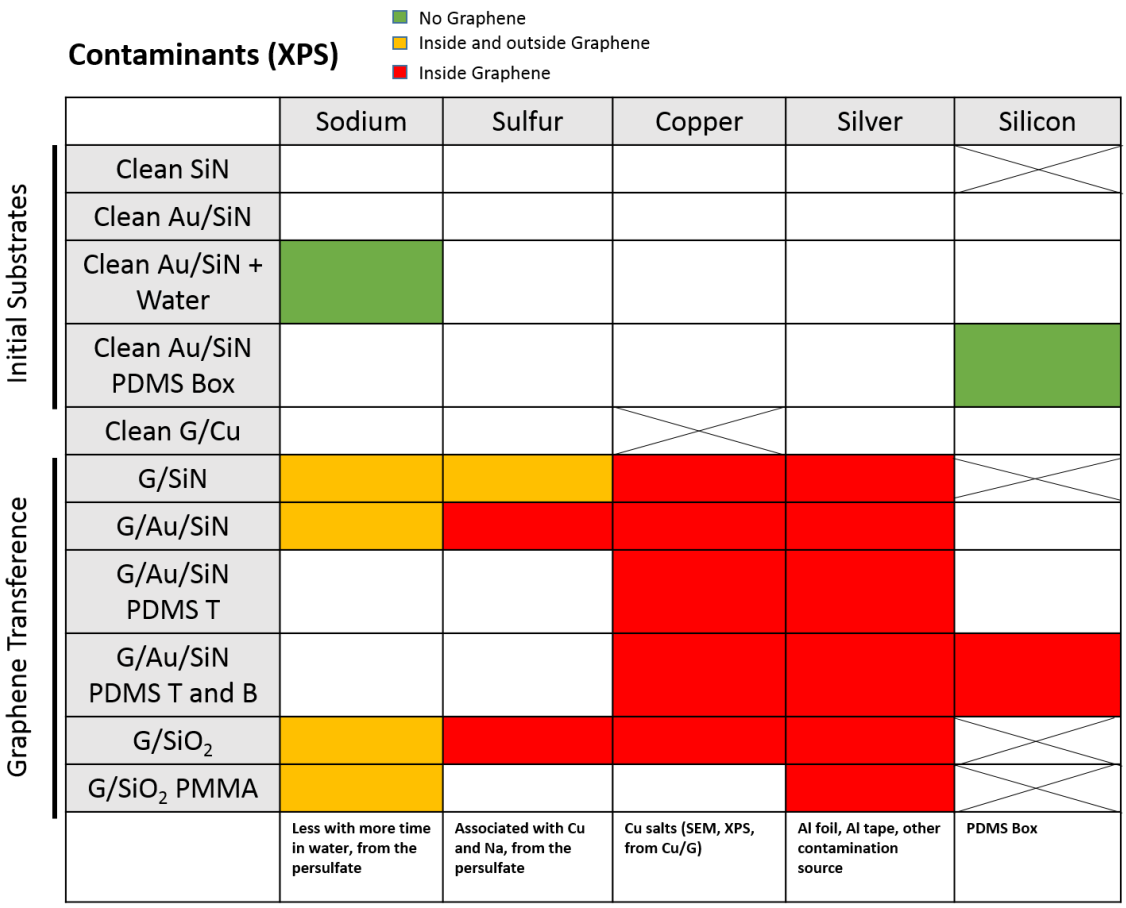

Table 5.1 Superficial contaminants measured by XPS on a set of substrates before and after graphene transfer by different methods.

does not have any trace of silver, its presence is still not clear and could be related to some kind of contamination not controlled of the chemical room where this process was performed, and which was shared with other scientist. The case of copper and sulfur seems clear, and was previously explained in terms of crystallites of salts formed from copper, sulfur and also oxygen. However, the XPS atomic sensibility factor of copper is much greater than for sulfur, and in most of the cases the signal from copper was very small. This could be the reason why not every time there is signal from copper, there is also an appreciable peak from sulfur. In addition, while copper is only found inside the graphene area, sulfur also appears outside, as sodium. Therefore, the cleaning step with water after the sodium persulfate etching seems not to be completed and some residues from this solution can be found in the samples. Finally, silicon could only be found in the case when the sample was stored in the box with PDMS (B), and not when PDMS film was used to attach the substrate and *fish* the graphene on the water reservoir in order to complete the transfer (T). In the case of using PMMA in the transfer method, there was

not a significant increase of the organic contaminants seen by XPS, although by AFM the surface was slightly dirtier. The presence of contaminants is important because they can distort or prevent the experimental measurements. For example, they could interact with the gases or liquids enclosed by the membrane, modifying their spectra. Other possibility, especially referred to the salt crystallites, is that these residues could stress the initial free standing graphene, breaking it, and therefore, keeping open holes that prevent the use of the membrane to enclose gases or liquids.

The second issue of using graphene is the difficulty to completely cover the grid with it. Although of course the expertise of the scientist has a very important role, the problems seem to come from the commercial graphene source. In this way, the successful rate started to change unexpectedly from a new purchase order of new graphene sheets of the same company, maintaining exactly the same transfer process. Graphene from different companies (Graphenea, Graphene Supermarket, ACS and Sigma Aldrich) were used always with negative results. Figure 5.17 shows the study performed on the pristine graphene/Cu sheets and after its transfer into SiO_2, in order to enhance the Raman signal from graphene. Figure 5.17 a shows the XPS C 1s spectra for the same graphene/Cu sample at two different positions (the sample was a 1x1 cm^2 square). As it can be seen, the width of both main peaks is different due to the remarkable amount of defects on the top spectrum. Therefore, the original graphene does not have an excellent quality, and, as we have observed, there are inhomogeneities that can lead to problems during the transfer process (in fact this is a very similar situation to the study performed and discussed in Chapter 4). The next figure 5.17 b shows the same XPS region but after the graphene transfer by using PMMA (top) and a free polymer method (bottom). Firstly, there is no presence of residues from the PMMA, as mentioned before. Secondly, the graphene seems to be of good quality and there is only a minor increase on the intensity of C-O and C=O contributions. Finally, Figure 5.17 c depicts an optical image of the graphene and a series of Raman spectra of graphene on different punctual localizations (spot around 20 μm). First, the optical image shows how the graphene does not cover completely all the surface. Instead, there are free graphene bands which have a clear color. The Raman spectra show in general a good monolayer graphene, with a 2D/G band ~2, although this ratio varies, indicating that there could be bi- or multi-layer areas. The D band referred to defects shows different intensities, indicating structural inhomogeneities. And finally, there are zones of very poor quality, as that shown in the bottom spectra.

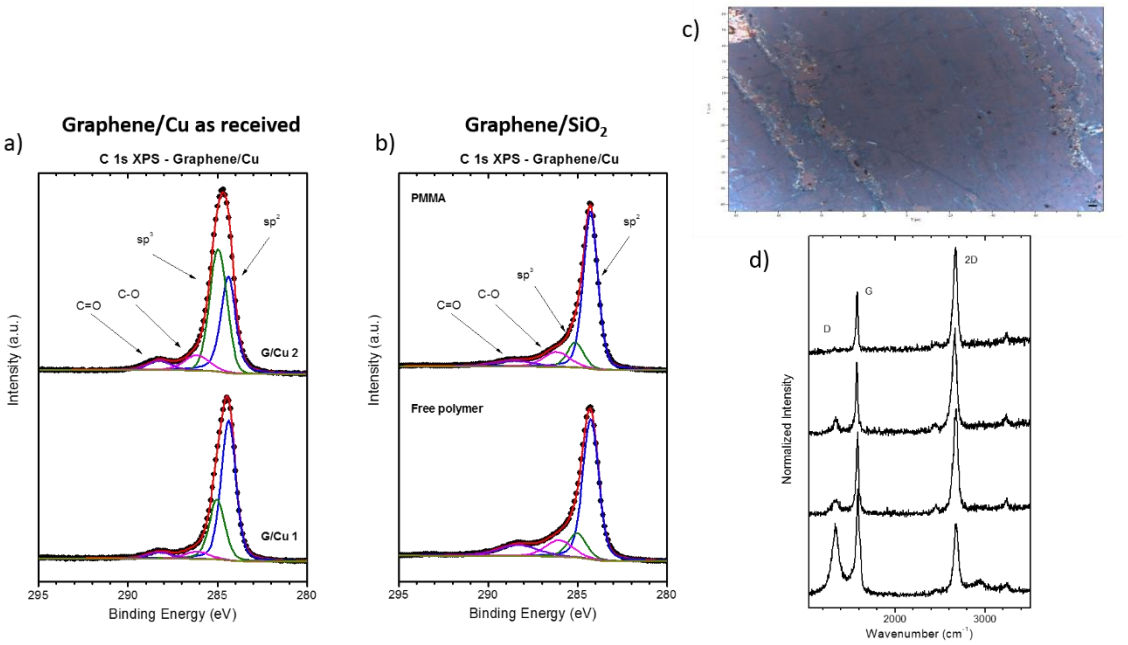

Figure 5.17 a) XPS C 1s spectra of a commercial graphene grown by CVD on polycrystalline copper measured at two different positions; b) XPS C 1s spectra of commercial graphene transferred into SiO_2 by two different methods: by using PMMA (top) and free polymer method (bottom); c) Optical image of transferred graphene (free polymer method) into SiO_2; d) Raman spectra at different positions of transferred graphene into SiO_2 (free polymer method).

Hence, there is an important problem with the initial graphene, which clearly presents big areas (the XPS spot size was about 400 μm) of different quality that can lead to problems during the transfer process. Although none of the transfer methods, with or without using polymers, present an especial degradation of the graphene or an important amount of residues on the surface, the final result is a broken graphene, with no kind of control on where and when in breaks. Taking into account that the percolated SiN window is slightly above the rest of the SiN grid, this could induce more strain on the graphene sheet, facilitating its rupture precisely on the percolated area and deepening on the rupture problem of graphene. As a last note, measurements shown in Figure 5.17 were performed for different commercial graphene sheets. No remarkable difference between them could be reported and the measurements shown here can be considered general results.

Finally, the AFM image of Figure 5.18 a shows an example of the consequences of the rupture of graphene on the SiN window. Although it is true that a second graphene could be transferred in order to cover all the holes, the problem was that nothing could

ensure that precisely the free holes were going to be covered, and second, it is not good to have a very thick graphene layer taking into account that subsequently there is going to be a deposition of few nanometers of Al_2O_3 and that the total thickness is critical to perform XPS measurements without an important decrement of the intensity. Lastly, Figure 5.18 b shows a SEM detail of some holes partially cover with graphene. This image is useful to emphasize that just one of these ruptures prevent the use of this membrane to separate a gas or liquid from high vacuum.

As a final conclusion, it is clear that, although graphene membranes can be used for these purposes, and in fact they have been successfully tested on real experiments with gases and liquids, the high costs of the graphene/sheets, the non-trivial transfer process and finally the low rate of success, prevents the graphene as a realistic free standing support. However, it is true that membranes with only some few holes not covered can be used on other techniques were no high vacuum is needed at the other side, such as KPFM or Raman spectroscopy. Therefore, although for the main purpose the graphene has to be discarded, in other applications it could be useful as the initial stage.

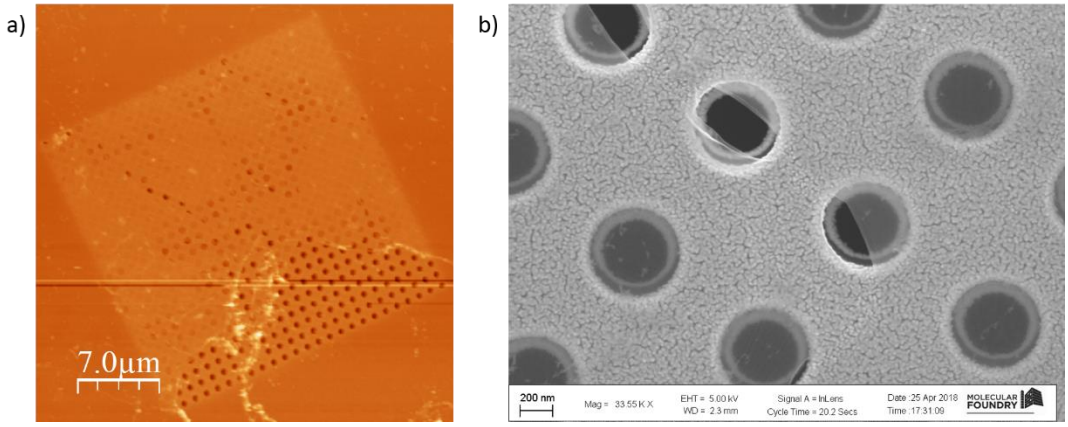

Figure 5.18 a) AFM image of graphene unsuccessfully transferred into an Au/SiN percolated membrane; b) SEM detail of 3nm Al_2O_3/graphene membrane shown in Figure 5.10 with some holes only partially covered by Al_2O_3/graphene due to initial problems with the graphene transfer process.

5.4 Al_2O_3 on free standing Formvar

In the face of the issues derived from the graphene, a second approach consisted on the use of Formvar polymer as the initial free standing sacrificial layer. This polymer has been extensively deployed on copper TEM grids as a free standing support for

nanoparticles due to its low interaction with electrons. Figure 5.19 shows a schematic representation of the four elaboration steps regarding the use of this polymer (the experimental details of the Formvar treatment are summarized on Chapter 2, section 2.5.3.2). The main difference with graphene is that the Formvar film is about various hundreds of nanometers thicker, so that, the Al_2O_3 can only be deposited on the bottom side. On the other hand, the most delicate step consists on removing the Formvar film with chloroform minimizing the contamination of the surface. In addition to this treatment, in some samples it was also necessary to heat them up to 100 °C and perform an oxygen plasma etching.

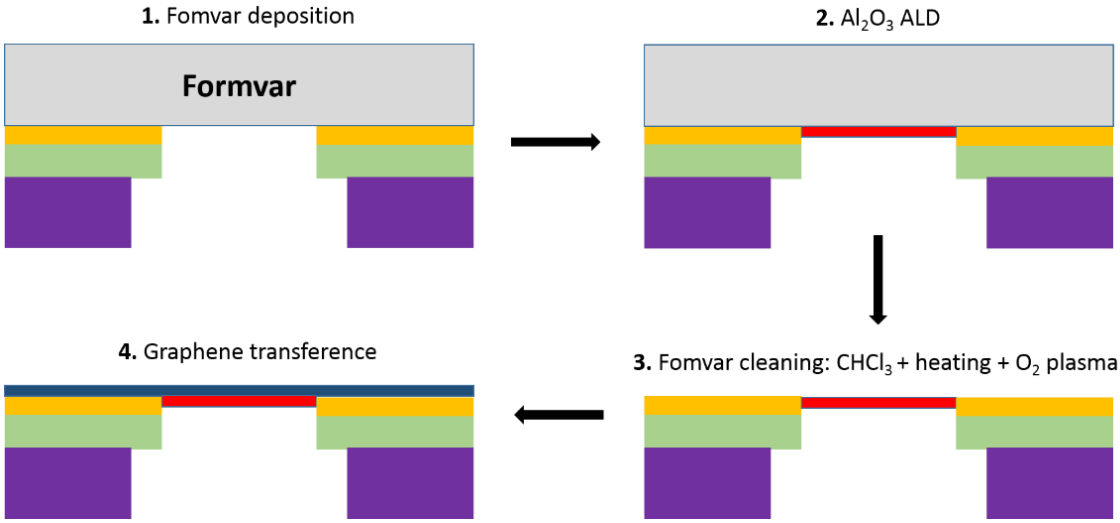

Figure 5.19 Schematic representation of the fabrication steps of an electron transparent metal oxide window for spectroscopic and imaging techniques by using Formvar as the sacrificial layer.

The contamination problems analyzed for the case of transferred graphene disappeared, and the XPS and SEM-EDX did not show any contribution coming from the polymer after its removal. Nevertheless, the top side of the grid showed an important XPS signal from aluminum, indicating that in some way, the Formvar polymer was permeable to TMA and oxygen plasma molecules used in the ALD deposition process. Also deposition on the top side occurred. This issue is important, not because this excess of Al_2O_3 could alter the measurement (as it is in the top side, not in contact with gas or liquid), but because if the whole top side gives aluminum signal instead of gold signal, it would be very difficult to find the window with the X-ray beam at the synchrotron, where

no optical image of the grid surface is available. However, this problem could be easily resolved by attaching the top side to a PDMS film during the ALD deposition process.

5.4.1 Chemical and structural characterization

The main advantage of using Formvar is that all the grid holes are completely covered by it, ensuring that the Al_2O_3 will also seal the complete window. As an example, Figure 5.20 a shows an AFM image of Formvar on a TEM grid. On the other hand, Figure 5.20 b shows the SEM image of free standing Al_2O_3 after the removal of the polymer. Although the holes seem to have a halo, no contaminants could be measured by EDX or XPS in the window zone. Therefore, it can be related to some kind of morphological effect due to the deposition growth and the possible curvature of the Formvar surface at the hole.

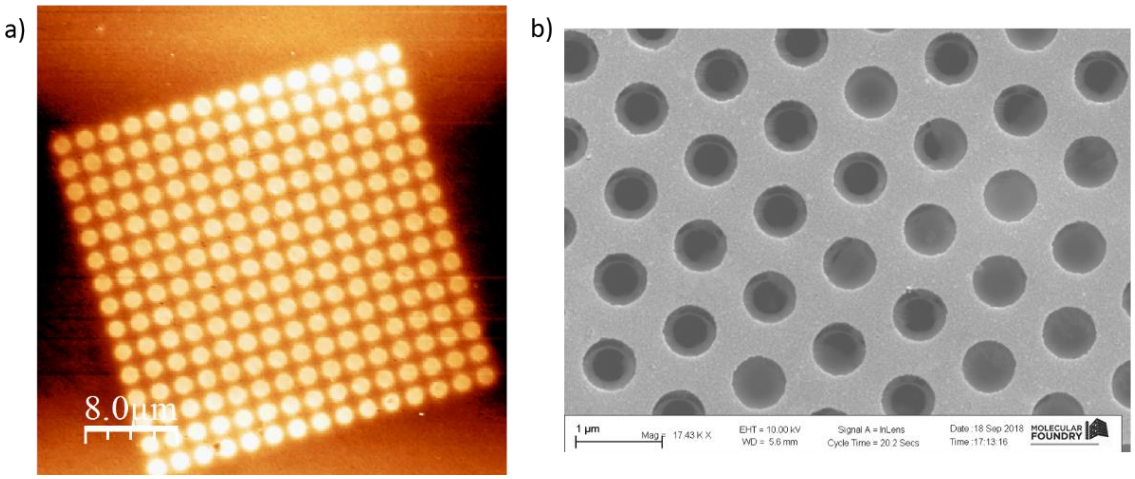

Figure 5.20 a) AFM topography image of a percolated Au/SiN membrane covered completely with Formvar before Al_2O_3 deposition; b) x1.743.000 magnification SEM image of a free standing 2 nm Al_2O_3 membrane.

The ALD deposition process is independent of the substrate as far as its surface has enough OH groups as starting nucleation points, so the growth is really layer by layer. In this way, the chemical and structural characterization of the Al_2O_3, i.e. good stoichiometric Al/O ratio in the bulk and amorphous structure, is the same as for the graphene supporting layer. AFM force-curves regarding the 2nm Al_2O_3 membranes grown on Formvar with and without transferred graphene after the removal of the supporting polymer are shown in Figure 5.21. The free standing Al_2O_3 graphene is

qualitatively stiffer than free graphene, but this quality increases if graphene is transferred to the oxide window.

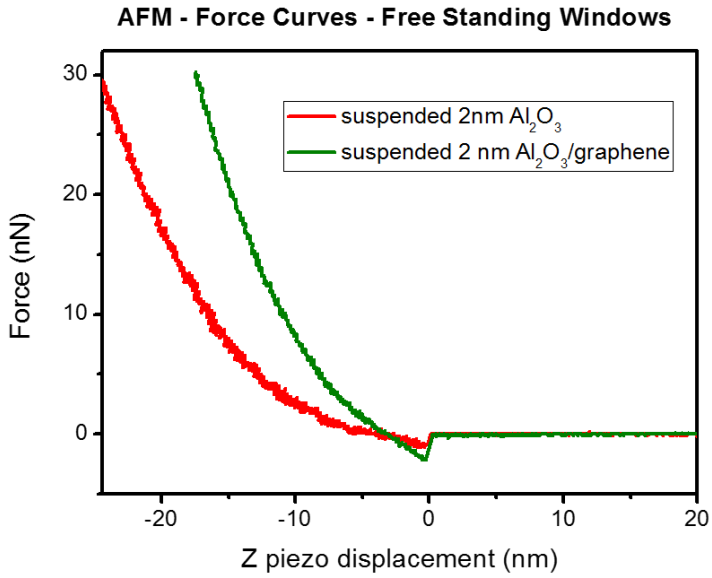

Figure 5.21 Force-curves of free standing Al_2O_3 windows grown on Formvar. A 2 nm Al_2O_3/graphene window is shown for comparison purposes.

5.4.2 Testing under real operando conditions

The success using the Formvar as supporting layer offers the option to test these ultra-thin metal oxide membranes under realistic operando conditions. For this purpose, free standing Al_2O_3 windows of 1 and 2 nm thickness were fabricated using TEM SiN grids with a 150 × 150 array of Ø 1 μm circular holes at a 2 μm pitch. In fact, the ALD deposition process for this material on this substrate guarantees a uniform growth without pinholes from 1 nm thickness. This thickness is below the IMPF through the Al_2O_3 matrix of the photoelectron typically collected in XPS using soft X-rays. In this way, thicknesses of 1 and 2 nm for electrons with a kinetic energy of ~700 eV (IMPF of ~16.8Å [39]) give acceptable intensity reductions of 45% and 70%, respectively. Therefore, the XPS measurement of enclosed gases and liquids is theoretically possible. Besides, this Al_2O_3 windows of 1 and 2 nm thickness, without transferred graphene, were tested in an ultra-high-vacuum chamber, being able to separate atmospheric air and water from $5 \cdot 10^{-8}$ mbar vacuum, being mechanically stable under these conditions for many hours.

These last 2nm Al_2O_3 electron transparent windows were successfully tested by XPS measurements at the environmental beamline 11.0.2 (ALS, Berkeley), being able to separate air (1 bar) from high vacuum conditions. Figure 5.22 shows XPS N 1s and O 1s regions. In the first case, Figure 5.22 a shows a sharp peak at ~405 eV corresponding to N_2 gas phase was measured, while a small contribution from the SiN grid can be seen at ~400 eV. On the other hand, Figure 5.22 b shows the O 1s region, where the O_2 gas phase contribution is situated at ~538 eV, although the main and broad peak at ~531.5 eV corresponds to the sum of Al-O and OH contributions of the oxide film.

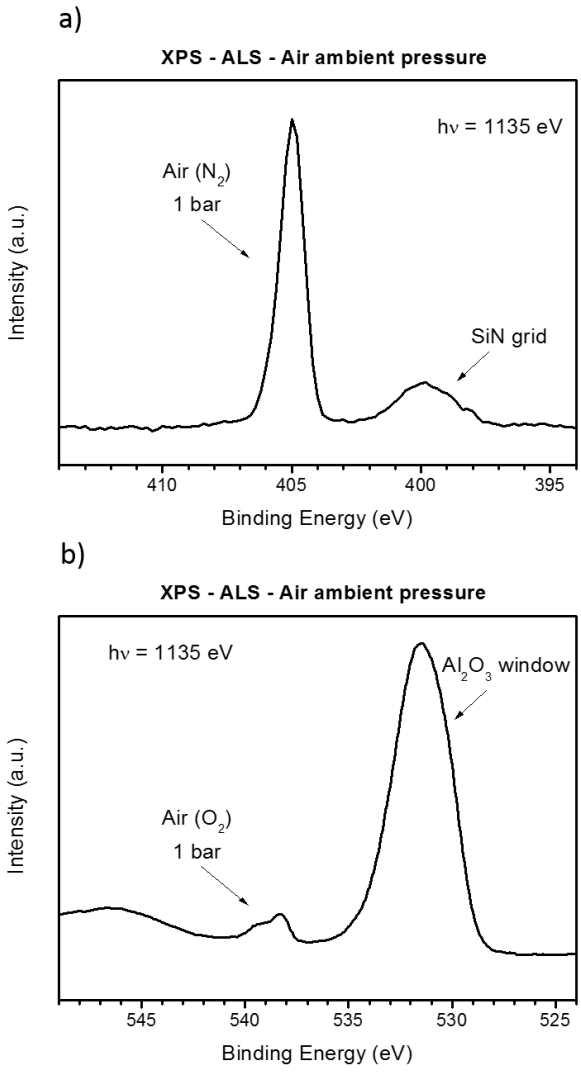

Figure 5.22 a) XPS N 1s and b) O 1s spectra measured at the ALS facility to test the performance of free standing Al_2O_3 membranes. Measurements were done at 1 bar and with a photon energy of 1135 eV.

The contamination of the top side with aluminum complicated the localization of the Al_2O_3 window with the X-ray beam and the XPS analyzer. Instead of Au 4f or Al 2p contributions, it was necessary to look for the weaker contribution of nitrogen from the air, i.e. the N 1s region. After the measurement of the air, water was introduced but the membrane broke up. In spite of the failure, this ending was expected considering that these membranes were the same than those tested for hours in the ultra-high vacuum system with both, air and water. Therefore, although the ultra-thin membranes are structurally robust, several cycles can damage them. Another interesting result is that in the absence of transferred graphene, just with the free standing metal oxide, it was not necessary to perform a charge correction. Therefore, it is not necessary to add the graphene as charge collector. These promising results showed that these membranes can be potentially used in reaction cells for many characterization techniques, from XPS to TEM measurements, and also other characterization techniques which does not need to separate the medium under study from high vacuum.

5.5 Conclusions

The present chapter has described the first stages of the project devoted to the development of free standing ultra-thin metal oxides membranes (< 3nm) to work as electron transparent windows. The chemical and structural characterization of these membranes indicates that the low temperature used on the ALD deposition ensures an amorphous growth of the film while it preserves its chemical composition at the bulk, with some carbon and fluorine contamination at the surface that can be easily removed by a gentle etching with argon clusters at low energy without any film modification.

Two different fabrication routes have been tested. In first place, free standing graphene has been used as initial support for the Al_2O_3 deposition. Nevertheless, graphene is not a good option due to the initial undesirable quality of commercial graphene/Cu sheets, which after any kind of transfer process (with or without using polymers) can easily break up and does not cover all the TEM grid holes, preventing its use as reaction cells windows at XPS and TEM experimental setups. A second problem is related to the surface contamination due to the transfer of graphene. Although it is not critical, it could represent a problem if it chemically interacts with the gas or liquid under study, modifying its spectra. On the other hand, Formvar polymer has been used as the sacrificial layer for the same purpose, allowing us the successful preparation of a complete window with free

standing Al_2O_3 of 1 and 2 nm. This thickness is enough to guarantee no pinholes and a perfect sealed of the window. For instance, both thicknesses were able to separate atmospheric air and water from $5 \cdot 10^{-8}$ mbar vacuum, being stable for many hours and some cycles.

Finally, these membranes were successfully tested under realistic conditions at the NAP-XPS endstation of beamline 11.0.2 at the ALS: N 1s and O 1s contribution from air at 1 bar could be measured. The election of the Al_2O_3 is not arbitrary and depends on two factors. In first place, from the chemical point of view, this oxide is very inert, ensuring a low interaction with the medium. This fact makes Al_2O_3 an excellent support for catalytic materials. Secondly, Al_2O_3 is a very easy material to work with in an ALD deposition system. In fact, previous scientific publications report that 1 nm films without pinholes could be grown on free standing graphene by this technique.

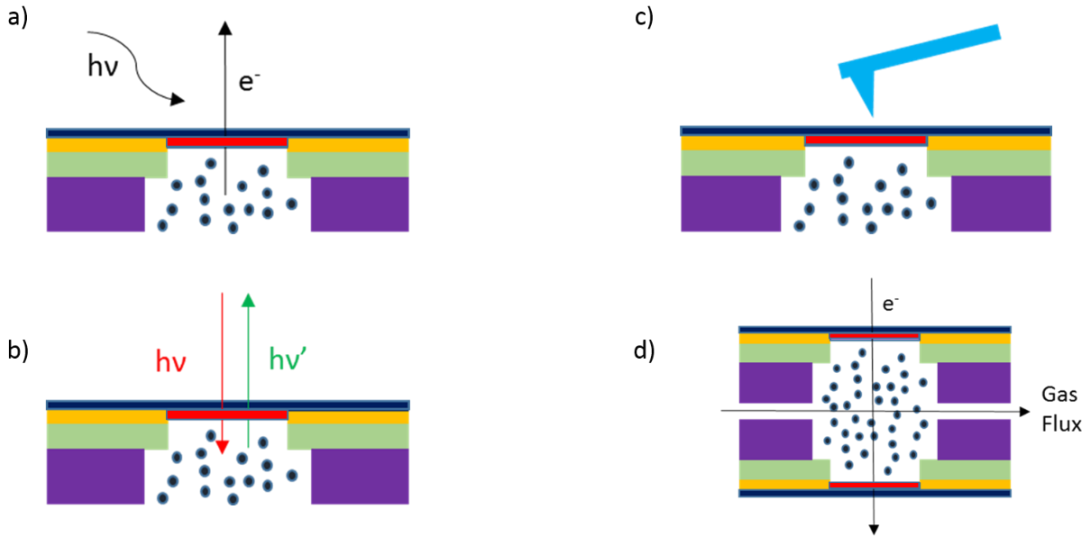

Figure 5.23 Schematic representation off possible applications of metal oxide membranes: a) electron microscopies such as XPS; b) photon spectroscopies such as Raman; c) AFM-KPFM measurements; d) TEM imaging under real operando conditions.

However, once these metal oxide membranes have demonstrated their viability, the possible ramifications of the project increase dramatically. Many others metal oxides can be deposited by ALD ensuring a layer by layer growth. Besides, metal oxide windows are a more realistic support for catalytic materials and can even be interesting by itself, as many oxides, such as CoO_x ot TiO_x, have important catalytic behavior. On the other hand, reactions cells using this kind of membranes can be applied in many

characterization techniques. Figure 5.23 summarizes four possible situations where these membranes could be used, such as photoelectron spectroscopies (a), photon spectroscopies like Raman or XAS on fluorescence yield mode (b), scanning probe microscopies such as KPFM or infrared scattering-scanning near-field microscopy (c) and finally TEM imaging under real operando conditions.

Bibliography

[1] C. Hao Wu, R. S. Weatherup, M. B. Salmeron; "Probing electrode/electrolyte interfaces *in situ* by X-ray spectroscopies: old methods, new tricks"; *Phys. Chem. Chem. Phys*., 17, (2015); pp: 30229-30239; DOI: 10.1039/c5cp04058b

[2] H. Hashimoto, T. Naiki, T. Eto, K. Fujiwarra; "High Temperature Gas Reaction Specimen Chamber for an Electron Microscope"; *Jpn. J. Appl. Phys*. 7, (1968); pp: 946; DOI: 10.1143/JJAP.7.946

[3] R. T. K. Baker, F. S. Feates, P. S. Harris; "Continuous electron microscopic observation of carbonaceous deposits formed on graphite and silica surfaces"; *Carbon*, 10, (1972); pp: 93-94. DOI: 10.1016/0008-6223(72)90014-0

[4] R. T. K. Baker, P. S. Harris; "Controlled atmosphere electron microscopy"; *J. Phys. E*, 5, (1979); pp: 793-797. DOI: 10.1088/0022-3735/5/8/024

[5] R. T. K. Baker; "*In Situ* Electron Microscopy Studies of Catalyst Particle Behavior"; *Catal. Rev*. 19, (1979); pp: 161-209. DOI: 10.1080/03602457908068055

[6] R. J. Sharma; "An Environmental Transmission Electron Microscope for *in situ* Synthesis and Characterization of Nanomaterials"; *Mater. Res.*, 20, (2005); pp: 1695-1707. DOI: 10.1557/JMR.2005.0241

[7] J. B. Wagner, F. Cavalca, C. D. Damsgaard, L. D.L. Duchstein, T. W. Hansen; "Exploring the environmental transmission electron microscope"; *Micron*, 43, (2012); pp: 1169-1175; DOI: 10.1016/j.micron.2012.02.008

[8] S. Takeda, H. Yoshida; "Atomic-resolution environmental TEM for quantitative *in situ* microscopy in materials science"; *Microscopy*, 62, (2013); pp: 193-203; DOI: 10.1093/jmicro/dfs096

[9] E.D. Boyes, P.L. Gai; "Environmental high resolution electron microscopy and applications to chemical science"; *Ultramicroscopy*, 67, (1997); pp: 219-232. DOI: 10.1016/S0304-3991(96)00099-X

[10] T. Kawasaki, K. Ueda, H. Tanaka, T. Tanji, M. Ichihashi; "*In situ* Observation of Gold Nano-particle Catalysts by High-Resolution Closed-type Environmental-Cell Transmission Electron Microscope"; *Microsc. Microanal*. 13, (2007); pp: 644-645. DOI; 10.1017/S1431927607077331

[11] S. Giorgio, S. S. Joao, S. Nitsche, D. Chaudanson, G. Sitja, C. R. Henry; "Environmental electron microscopy (ETEM) for catalysts with a closed E-cell with

carbon windows"; *Ultramicroscopy*, 106, (2006); pp: 503-507. DOI: 10.1016/j.ultramic.2006.01.006

[12] J. M. Yuk, J. Park, P. Ercius, K. Kim, D. J. Hellebusch, M. F. Crommie, J. Y. Lee, A. Zettl, A. P. Aivisatos; "High-Resolution EM of Colloidal Nanocrystal Growth Using Graphene Liquid Cells"; *Science*, 336, (2012); pp: 61-64. DOI: 10.1126/science.1217654

[13] A.Tuxen, S. Carenco, M. Chintapalli, C.-H. Chuang, C. Escudero, E. Pach, P. Jiang, F. Borondics, B. Beberwyck, A. P. Alivisatos, G. Thornton, W.-F. Pong, J. Guo, R. Perez, F. Besenbacher, M. Salmeron; "Size-Dependent Dissociation of Carbon Monoxide on Cobalt Nanoparticles"; *J. Am. Chem. Soc.*, 135, (2013); pp: 2273-2278; DOI: 10.1021/ja3105889

[14] T. Herranz, X. Deng, A. Cabot, J. Guo, M. Salmeron; "Influence of the Cobalt Particle Size in the CO Hydrogenation Reaction Studied by *In Situ* X-Ray Absorption Spectroscopy"; *J. Phys. Chem. B*, 113, (2009); pp: 10721-10727; DOI: 10.1021/jp901602s

[15] H. Zhanga, W.-C. Wangb, P.-A. Glans, Y.-S. Liu, M. Kapilashrami, J.-L. Chenb, C. Chang, M. Salmeron, C. Escudero, E. Pach, A. Tuxen, M. Chintapalli, S. Carenco, X. Sun, J. Guo; "Developing soft X-ray spectroscopy for *in situ* characterization of nanocatalysts in catalytic reactions"; *J. Electron. Spectrosc. Relat. Phenom.*, 197, (2014); pp: 118-123; DOI: 10.1016/j.elspec.2014.11.001

[16] D.F. Ogletree, H. Bluhm, G. Lebedev, C.S. Fadley, Z. Hussain, M. Salmeron; "A differentially pumped electrostatic lens system for photoemission studies in the millibar range"; *Rev. Sci. Instrum.*, 73, (2002); pp: 3872-3877; DOI: 10.1063/1.1512336

[17] M. Salmeron, R. Schlogl; "Ambient pressure photoelectron spectroscopy: A new tool for surface science and nanotechnology"; *Surf. Sci. Rep*, 63, (2008); pp: 169-199; DOI: 10.1016/j.surfrep.2008.01.001

[18] A. Kolmakov, D. A. Dikin, L. J. Cote, J. Huang, M. K. Abyaneh, M. Amati, L. Gregoratti, S. Günther, M. Kiskinova; "Graphene oxide windows for *in situ* environmental cell photoelectron spectroscopy"; *Nat. Nanotechnol.*, 6, (2011); pp: 651-657. DOI: 10.1038/NNANO.2011.130

[19] R. S. Weatherup; "2D Material Membranes for Operando Atmospheric Pressure Photoelectron Spectroscopy"; *Top. Catal.*, 61, (2018); pp: 2085-2102; DOI: 10.1007/s11244-018-1075-2

[20] R. S. Weatherup, B. Eren, Y. Hao, H.Bluhm, M. B. Salmeron; "Graphene membranes for atmospheric pressure photoelectron spectroscopy"; *J. Phys. Chem. Lett*. 7, (2016); pp: 1622-1627; DOI: 10.1021/acs.jpclett.6b00640

[21] J. J. Velasco-Velez, V. Pfeifer, M. Hävecker, R. S. Weatherup, R. Arrigo, C.-H. Chuang, E. Stotz, G. Weinberg, Mi. Salmeron, R. Schlçgl, Axel Knop-Gericke; "Photoelectron Spectroscopy at the Graphene-Liquid Interface Reveals the Electronic Structure of an Electrodeposited Cobalt/Graphene Electrocatalyst"; *Angew. Chem. Int. Ed.*, 54, (2015); 1-6; DOI: 10.1002/anie.201506044

[22] B. Dlubak, M.-B. Martin, C. Deranlot, K. Bouzehouane, S. Fusil, R. Mattana, F. Petroff, A. Anane, P. Seneor, A. Fert; "Homogeneous pinhole free 1 nm Al_2O_3 tunnel barriers on graphene"; *Appl. Phys. Lett.,* 101, (2012); pp: 203104; DOI: 10.1063/1.4765348

[23] L. Wang, J. J. Travis, A. S. Cavanagh, X. Liu, S. P. Koenig, P. Y. Huang, S. M. George, J. S. Bunch; "Ultrathin Oxide Films by Atomic Layer Deposition on Graphene"; *Nano Lett.*, 12, (2012); pp: 3706-3710; DOI: 10.1021/nl3014956

[24] A. Gharachorlou, M. D. Detwiler, X.-K. Gu, L. Mayr, B. Klötzer, J. Greeley, R. G. Reifenberger, W. N. Delgass, F. H. Ribeiro, D. Y. Zemlyanov; "Trimethylaluminum and Oxygen Atomic Layer Deposition on Hydroxyl-Free Cu(111)"; *ACS Appl. Mater. Interfaces.,* 7, (2015); pp: 16428-16439; DOI: 10.1021/acsami.5b03598

[25] F. Speck, M. Ostler, J. Röhrl, K. V. Emtsev, M. Hundhausen, L. Ley, T. Seyller; "Atomic layer deposited aluminum oxide films on graphite and graphene studied by XPS and AFM"; *Phys. Status Solidi C,* 7, (2010); pp: 398-401; DOI: 10.1002/pssc.200982496

[26] E. Paparazzo; "XPS analysis of iron aluminum oxide systems"; *Appl. Surf. Sci.,* 25, (1986); pp: 1-12; DOI: 10.1016/0169-4332(86)90021-8

[27] T. Gougousi, D. Barua, E. D. Young, G. N. Parsons; "Metal Oxide Thin Films Deposited from Metal Organic Precursors in Supercritical CO_2 Solutions", *Chem. Mater.*, 17, (2005); pp: 5093-5100; DOI: 10.1021/cm0510965

[28] B. R. Strohmeier; "Surface characterization of aluminum foil annealed in the presence of ammonium fluoborate"; *Appl. Surf. Sci.* 40, (1989); pp: 249-263; DOI: 10.1016/0169-4332(89)90009-3

[29] J. Haeberle, K. Henkel, H. Gargouri, F. Naumann, B. Gruska, M. Arens, M. Tallarida, Dieter Schmeißer; "Ellipsometry and XPS comparative studies of thermal and

plasma enhanced atomic layer deposited Al_2O_3-films"; *Beilstein J. Nanotechnol*., 4, (2013); pp: 732-742; DOI: 10.3762/bjnano.4.83

[30] J. L. van Hemmen, S. B. S. Heil, J. H. Klootwijk, F. Roozeboom, C. J. Hodson, M. C. M. van de Sanden, W. M. M. Kessels; "Plasma and Thermal ALD of Al2O3 in a Commercial 200 mm ALD Reactor"; *J Electrochem Soc*, 154, (2007); pp: 165-169; DOI: 10.1149/1.2737629

[31] K. C. Kwon, J. Ham, S. Kim, J.-L. Lee, S. Y. Kim; "Eco-friendly graphene synthesis on Cu foil electroplated by reusing Cu etchants"; *Sci. Rep.*, 4, (2014); pp: 4830; DOI: 10.1038/srep04830

[32] Y. Xiao, H. K. Kim, C. Mattevi, M. Chhowalla, R. C. Maher, L. F. Cohen; "Influence of Cu substrate topography on the growth morphology of chemical vapor deposited graphene" *Carbon*, 65, (2013); pp: 7-12; DOI: 10.1016/j.carbon.2013.06.090

[33] J. C. Meyer, A. K. Geim, M. I. Katsnelson, K. S. Novoselov, T. J. Booth, S. Roth; "The structure of suspended graphene sheets"; *Nature*, 446, (2007); pp: 60-63 ; DOI: 10.1038/nature05545

[34] J. C. Meyer, Eder, S. Kurasch, V. Skakalova, J. Kotakoski, H. J. Park, S. Roth, A. Chuvilin, S. Eyhusen, G. Benner, A. V. Krasheninnikov, U. Kaiser; "Accurate Measurement of Electron Beam Induced displacement Cross Sections for Single-Layer Graphene"; *PRL*, 108, (2012); pp: 196102; DOI: 10.1103/PhysRevLett.108.196102

[35] F. Börrnert, L. Fu, S. Gorantla, M. Knupfer,† B. Büchner, M. H. Rümmeli; "Programmable Sub-nanometer Sculpting of Graphene with Electron Beams"; *ACS Nano.*, 6, (2012); pp: 10327-10334; DOI: 10.1021/nn304256a

[36] Z. Liao, L. M. Sandonas, T. Zhang, M. Gall, A. Dianat, R. Gutierrez, U. Mühle, J. Gluch, R. Jordan, G. Cuniberti, E. Zschech; "*In situ* Stretching Patterned Graphene Nanoribbons in the Transmission Electron Microscope"; *Sci. Rep.*, 7, (2017); pp: 211; DOI:10.1038/s41598-017-00227-3

[37] C. Lee, X. Wei, J. W. Kysar, J. Hone; "Measurement of the Elastic Properties and Intrinsic Strength of Monolayer Graphene"; 321, (2008); pp: 385-388; DOI: 10.1126/science.1157996

[38] C. Lee, X.Wei, Q. Li, R. Carpick, J. W. Kysar, J. Hone; "Elastic and frictional properties of graphene"; *Phys. Status Solidi B* 246, (2009); pp: 2562-2567; DOI: 10.1002/pssb.200982329

[39] S. Tanuma, C.J. Powell, D.R. Penn; "Proposed formula for electron inelastic mean free paths based on calculations for 31 materials"; *Surface Science Letters*, 192, (1987); pp: 849-857. DOI: 10.1016/0167-2584(87)90829-2.

Chapter 6

Main conclusions and future lines of work

"I never think of the future. It comes soon enough."

Albert Einstein

6.1 Main conclusions of this work

The previous pages condense four years of initiatory journey on the science paths. Four years in which I have learned, or at least tried to do so, the basic rules of the scientific work. From the original project goals devoted to the study of the interaction between ZnO and graphene for future applications on solar cells, some of them have been successfully achieved. But science constantly mutates, transforms the questions and changes the final aim. Thus, at the end of these four years, three metal oxides, and not only ZnO, have been studied in regard of their interaction with graphitic systems, such as HOPG and graphene. In fact, apart from energy conversion devices, alternative applications on catalysis and development of measurement devices can be derived from the presented results. The main results and conclusions regarding each of these oxides (CoO, ZnO and Al_2O_3) are summarized in the next lines to close this report.

CoO on HOPG

The most astonishing result previously reported by our group, and the main motivation to continue this line, was the nano-patterning of the graphite surface at lower temperatures than for Co metallic nanoparticles. However, there was a lack on the understanding of what chemical mechanisms make this possible. In Chapter 3, novel results regarding the characterization of the electronic structure of the CoO wetting layer and the in situ study of the carbon gasification reaction through NAP-XPS have been presented. It has been demonstrated how the initial CoO wetting layer is able to introduce oxygen in the HOPG structure by breaking the graphitic rings and introducing defects: hence, moving from sp^2 to sp^3 hybridization. Although after the reduction process the C-O and C=O bonds induced by the initial deposition of CoO disappeared, the broken graphitic rings weakened the graphite network and therefore the carbon gasification

reaction could take place with quicker kinetics than for typical metallic nanoparticles. By means of these experiments the initial hypothesis, by which the reason of this low temperature nano-pattering was related to the weakening of the HOPG σ bonds, was proven. On the other hand, the oxidation at room temperature from CoO to Co_3O_4 seems a reversible process, although the re-oxidation at 400 °C of metallic Co leads to a not stable transition at high pressures, where the ratio between Co^{3+} and Co^{2+} cations changes with time until the equilibrium is reached in a Co_3O_4/CoO mixture. This fact is due to 1) the size of the nanoparticles, i.e. surface is predominant over volume, and 2) the strong variations on the oxidation-reduction conditions during the carbon gasification reaction.

Two more final nanostructures have been studied as final products present on the HOPG surface after the re-oxidation process: nanorings and nanostrips. Although the focus of the study was mainly topographical, new KPFM measurements point out that these two structures share a same origin, self-assembled structures of organic and/or inorganic molecules which could be present in the laboratory atmosphere (these nanostructures could only be seen after air exposure). The chemical modification of the graphite surface due to the carbon gasification reaction can induce changes on the hydrophobicity and reactivity of the HOPG surface, facilitating the adsorption of molecules and the curvature of the typical nanostrips near the CoO_x clusters, where defects concentration increases.

ZnO on HOPG and graphene/Cu sheets

In regard of the mode of growth of ZnO, although the first atomic layer of both substrates is identical, the presented results indicated that the growth of ZnO on HOPG and graphene/Cu substrates were completely different. The early stages of growth of ZnO on the HOPG substrate consist on the deposition of micrometric ZnO clusters at the HOPG steps and point defects at the graphite terraces with a large diffusion rate of the Zn atoms. The oxidation of Zinc atoms was complete, forming ZnO clusters. Besides this, the final stages of the growth give a microstructured ZnO thin film. However, the growth on the graphene/Cu sheets consisted in the deposition of Zn atoms on the graphene/Cu surface, remaining metallic, followed by the growth of many ZnO small clusters and leading to the formation of a sub-oxide (ZnO_x) at the ZnO/Zn interface, forming a ZnO/ZnO_x/Zn/graphene/Cu structure. In this picture, the early deposition of the Zn atoms on the graphene layer seemed to act as nucleation centers of ZnO, leading to a

nanostructured ZnO thin film. The role of graphene seemed crucial to create such nucleation centers, and made possible the growing differences. These experiments have evidenced the different electronic structure, and hence the corresponding interaction with other materials, of graphene with respect to HOPG.

Moving to the interaction between ZnO and the graphene/Cu system, it has been shown how the cross relationship between the copper substrate, graphene and the intercalated chemical species due to air exposure determine the whole picture. It has been proposed that the deposited ZnO/Zn initial layer probably induces, by electron transference to graphene from metallic zinc, the electronic decoupling of graphene from the metallic substrate. The presence of zinc accelerated the galvanic corrosion of copper by the formation of hydroxyl moieties from the initial intercalated water and oxygen molecules. This reaction, which is essentially the same observed for graphene/Cu immersed on water led to the formation of a complex interface between ZnO/ZnO_{1-x}/Zn/graphene/Cu_2O/Cu. The electronic decoupling of graphene from copper depended essentially on two factors: the time which the as received graphene/Cu sheet was exposed to air before the ZnO deposition and the presence of zinc evaporated from metallic zinc under O_2 atmosphere.

Precisely, the initial chemical nature and structural state of the as received graphene/Cu sheets was extremely important on the subsequently ZnO growth. Meanwhile the growth characteristics of the oxide (in terms of nucleation, deposition and compositional rates) depend on the initial electronic coupling of graphene with Cu, this last condition already depended on the number of graphene defects, the chemical species intercalated between graphene and Cu, and the oxidation state, crystallographic direction and surface morphology of the Cu grains, being all these parameters determined by the polycrystalline nature of the Cu sheet. In fact, all these factors that influence on the ZnO growth were presented as local inhomogeneities (about >1 μm size) on the as received graphene/Cu samples, avoiding a homogeneous growth of the ZnO. However, the external modification of the chemical state of the initial graphene/Cu substrate opens the door to perform well controlled and homogenous growth of ZnO.

Free standing ultra-thin Al_2O_3 membranes

Chapter 5 described the first stages of the project devoted to the development of free standing ultra-thin metal oxides membranes (< 3nm) to work as electron transparent windows. The chemical and structural characterization of these membranes indicated that the low temperature used in the ALD deposition ensured an amorphous growth of the film while it preserved its chemical composition at the bulk, with some carbon and fluorine contamination at the surface that could be easily removed by a gentle etching with argon clusters at low energy without any film modification.

Two different fabrication routs were tested. In first place, free standing graphene was used as initial support for the Al_2O_3 deposition. Nevertheless, graphene was not a good option due to the initial quality of commercial graphene/Cu sheets. Precisely, this sheets could easily break up after any kind of transfer process (with or without using polymers). Therefore, not all the TEM grid holes would be cover, preventing its use as reaction cells windows at XPS and TEM experimental setups. A second issue was related to the surface contamination due to the transfer of graphene. Although it was not critical, it could represent a problem if it chemically interacts with the gas or liquid under study, modifying its spectra. On the other hand, Formvar polymer has been used as the sacrificial layer for the same purposes, being in this case successful on fabricating a complete window with free standing Al_2O_3 of 1 and 2 nm. This thickness was enough to guarantee no pinholes and a perfect seal of the window. For instance, both thicknesses were able to separate atmospheric air and water from $5 \cdot 10^{-8}$ mbar vacuum, correctly working for many hours and some cycles.

Finally, these membranes were successfully tested under realistic condition at the NAP-XPS endstation of beamline 11.0.2 at the ALS: XPS N 1s and O 1s contribution from air at 1 bar could be measured.

6.2 Future lines of work

A Ph.D. work never ends by itself, you close it once your funds and/or employment contract(s) are finished. Hence, it always remains open questions and, above all, new ideas and work proposals. Some of them are exposed in the following points:

- After the study of the CoO interaction with the HOPG and the observed capability to induce nano-chanelling at low temperature, the next step seems obvious: translate these results into controlled nano-patterning of graphene systems. From the technological point of view this new approach seems more useful than using graphite substrates. However, the graphene/substrate interaction (if it is not free standing graphene) can lead to some challenges, as graphene properties could be modified and therefore the CoO/graphene interaction may change as a function of the material under graphene.

- Concerning the ZnO interaction with the graphene/Cu system, although the cross relationships between different elements have been clarified, there was no time to apply these results on current energy conversion devices, as it was the initial aim of the thesis. The lack of a homogenous growth of ZnO due to the initial local inhomogeneities of the graphene/Cu sheets prevented further steps in this direction. However, the possibility to induce changes on the initial state of the graphene/substrate system to modify the growth behavior of the metal oxide opens the door to overcome this challenge. The easiest way to do so is by changing the substrate below the graphene, for example, transferring it into SiO_2 wafers, as the electronic coupling changes completely depending on the Cu situation. Actually, current work in the laboratory is focused on the study of the early stages of growth of ZnO on graphene/SiO_2 and GO and reduced-GO systems. The deep understanding on which chemical and structural parameters from the graphene affect the posterior growth is key to really control the growth and properties of the metal oxide, and will open the possibility to transfer this knowledge into real devices, where a heteroestructure graphene-ZnO of good quality may conserve and enhance the properties of both materials.

- Once the ultra-thin Al_2O_3 membranes have demonstrated their viability, the possible ramifications of the project increase dramatically. First of all, the election of the Al_2O_3 was not arbitrary and depended on two factors. In first place, from the chemical point of view, this oxide is very inert, ensuring a low interaction with the medium, which makes Al_2O_3 an excellent support for

catalytic materials. Secondly, Al_2O_3 is a very easy material to work with in an ALD deposition system. However, many others metal oxides can be deposited by ALD ensuring a layer by layer growth. Besides, metal oxide windows are a more realistic support for catalytic materials than graphene, and can even be interesting by itself, as many oxides, such as CoO_x or TiO_x, show an important catalytic behavior. On the other hand, reactions cells using this kind of membranes can be applied in many characterization techniques. These membranes could be used for the study of gases, liquids, solutions, solid/gas and solid/liquids interfaces, etc. in may techniques and experimental set ups as: photoelectron spectroscopies, photon spectroscopies like Raman or XAS on fluorescence yield mode, scanning probe microscopies such as KPFM or infrared scattering-scanning near-field microscopy, or finally TEM imaging under real operando conditions, among others.

Epílogo

Una reflexión personal sobre el estado del trabajo científico

"Es demasiado fácil ser original limitándose simplemente a hacer lo contrario de lo que hacen los demás; esto es sólo mecánica. Lo que es de verdad difícil es insistir en la disciplina y la socialidad, y seguir profesando la sinceridad, la espontaneidad, la originalidad y la personalidad."

Antonio Gramsci

En estos cuatro años de trabajo en la ciencia, cinco si contamos el trabajo científico desarrollado en la consecución del máster, apenas he podido encontrar tesis doctorales en el ámbito de las ciencias exactas, de la salud o ingenieriles donde se realice una reflexión sobre el estado actual de la ciencia. Es cierto que en las introducciones se encuentran justificaciones bien estructuradas y profundas sobre los motivos, *los problemas*, que impulsan a llevar a cabo la investigación específica de dichos trabajos. Sin embargo, una evaluación general de *cómo se hace* la ciencia, desde la elección del tema de la investigación hasta la forma de publicación de los resultados, queda completamente olvidada. Considero que esta ausencia no es casualidad, sino que es parte del marco ideológico en el que se lleva a cabo este trabajo. El no hablar del método de forma pública, sino solamente de forma reservada en círculos de confianza, es parte ya de la cosmovisión de los científicos, y en mi humilde opinión, denota un cierto dogmatismo que en etapas tan tempranas de la formación científico-académica, como es la realización de un doctorado, puede conllevar un encorsetamiento mental de no cuestionamiento. Y el aprendizaje de qué no se debe hacer o decir porque puede tener consecuencias negativas en la carrera profesional es tremendamente difícil de romper en el futuro.

Sin embargo, es cierto que existe hoy por hoy una reflexión en torno a ciertos problemas que resultan ya evidentes en el campo de la investigación, y que tienen que ver con la gestión de resultados y la reproducibilidad de éstos. Sin embargo, estos debates se siguen dando dentro de los círculos puramente científicos, sin prácticamente trascendencia hacia el exterior, hacia el conjunto de la sociedad. Y además, las tribunas desde las que existe posibilidad de llevarlos a cabo complican que jóvenes profesionales puedan ocuparlas, ya sea porque aún carecen del suficiente prestigio para poder intervenir

en estos espacios (charlas invitadas a congresos o tribunas en espacios de reflexión de revistas de alto impacto como *Nature* o *Science*) o porque pongan en riesgo el prestigio de su incipiente carrera investigadora.

Por todo ello creo que un epílogo reflexivo en la tesis doctoral de la que uno es autor es un espacio cómodo y tremendamente útil para llevar a cabo este tipo de cuestionamientos que no buscan sino la preservación y mejora del método científico mediante la identificación de los errores que puedan estar cometiéndose en la actualidad. Además, constituye un ejercicio de sinceridad y amor con respecto a la Ciencia, con mayúsculas, y sobretodo, buscando que la acumulación de pequeños, y por separados *superfluos*, errores no desemboquen en un abrupto fallo tanto del método científico como del traslado del nuevo conocimiento a la sociedad.

Espero que las siguientes líneas ofrezcan al menos puntos de debate, que, sin llegar a estar de acuerdo con el lector, permitan una discusión sana que conlleven la mejora de nuestra forma de hacer ciencia o, en el más sencillo de los casos, corregir mis equivocadas apreciaciones.

***

Decía el filósofo de la ciencia Thomas Kuhn que el avance y cambio en la forma de hacer ciencia, y por tanto lo que definía a las diferentes escuelas científicas a través de la historia, "*no fue éste o aquel error de método, y aún menos el desprecio del método científico por parte de algunas de ellas, sino más bien la forma de ver el mundo, lo que incluye un determinado concepto de método y un modo de operar en la práctica*" [1]. Es decir, resulta imposible definir y discutir la actividad científica de forma ajena al contexto sociohistórico. Los investigadores están sujetos a un marco ideológico, a una cosmovisión que determina tanto el método que aplican, como la interpretación de cada una de sus fases. Esto es: la identificación del problema a resolver, cómo afrontarlo, cómo diseñar el experimento y la discusión final de los resultados, queda todo ello sustancialmente determinado por una compleja red de relaciones causa-efecto sociales y que se proyectan sobre el individuo y determinan su forma de ver el mundo.

Intentemos ahora aterrizar este monto abstracto. El conjunto de ideas que determinan la manera de pensar y actuar de las personas que forman parte de una determinada sociedad, y en nuestro caso concreto del investigador, está determinado por

la época histórica en la que se encuadra. O dicho de otra manera más precisa, está sujeto por cómo se relaciona el ser humano con la naturaleza, cómo, de qué forma y con qué medios, transforma a ésta para dar satisfacción a sus necesidades y qué relaciones se establecen entre los individuos y entre éstos y esos medios de transformación. Pongamos dos casos particulares que permitan aclarar esto. Es un ejemplo clásico en los manuales básicos de Filosofía de la etapa pre universitaria que la filosofía en la Antigua Grecia nace a partir de la creación social de un conjunto de individuos en las polis que tienen sus necesidades ya cubiertas por el trabajo de otros. Es decir, con los excedentes de la producción de alimentos, servicios y riqueza (en términos generales), existe la posibilidad de que se pueda vivir sin llevar a cabo un trabajo productivo, solamente intelectual. Este cambio social lo permite el paso de una sociedad de cazadores y recolectores a otra de agricultores y ganaderos, donde las poblaciones quedan fijadas a un territorio y dada la mayor productividad se comienzan a generar excedentes, que se acaparan por una élite, con el consiguiente aumento y concentración de la población en torno a posiciones defensivas ante otros grupos humanos que buscan dichos sobrantes. Si avanzamos rápidamente por la Historia hasta nuestro segundo ejemplo a mediados del siglo XX, vemos cómo básicamente los medios de producción (esto es, los medios por los cuales transformamos la naturaleza), son iguales en las dos potencias predominantes: los Estados Unidos de América (EEUU) y la Unión de Repúblicas Socialistas Soviéticas (URSS). Sin embargo, en cada una de estas naciones las personas establecen diferentes relaciones de propiedad con los medios de producción y por ende entre ellas. El entramado ideológico que justifica y da cuerpo teórico al sentido común imperante en cada potencia es diferente, y tiene evidentemente repercusión en la forma de entender la vida de los individuos.

Este segundo ejemplo es pertinente, ya que los avances científicos en los EEUU y la URSS fueron básicamente paralelos hasta el colapso de la segunda. ¿Se había alcanzado por tanto un método científico universal que, de alguna forma, superaba el contexto social en el que se desarrollaba la ciencia? Es cierto que tanto el liberalismo como el socialismo beben de un mismo cuerpo filosófico europeo y por ende de un mismo esquema básico del método científico. Sin embargo, existen dos factores que hacen dudar de la respuesta afirmativa a la pregunta.

En primer lugar, la ideología de los individuos, y por tanto su cosmovisión, era diferente. Esto determina que las motivaciones a la hora de iniciar o dar prioridad a una línea de investigación puedan divergir. En el contexto de un enfrentamiento latente que

definía la Guerra Fría, las motivaciones eran equivalentes entre ambos: superar tecnológica y científicamente (tanto desde el punto de vista puramente bélico como propagandístico) al rival. Sin embargo, en cuestiones que afectaban a estrategias geopolíticas la aproximación al problema era diferente. El ejemplo más claro podemos encontrarlo quizás en los límites del crecimiento que fueron anunciados por el Club de Roma en la década de 1970. En este encuentro se denunció que el ser humano había superado la capacidad de carga del planeta dado al excesivo consumo de recursos no renovables (y renovables por encima de las tasas de regeneración) y la alteración de los ecosistemas por el vertido de residuos tanto a la atmosfera como a la biosfera. Sin embargo, los países del bloque socialista lo interpretaron (incluida su comunidad académica) como un ataque al desarrollo productivo del socialismo y a las esencias marxistas que definían al socialismo como el modelo económico en el que se desarrollaría completamente toda la capacidad de las fuerzas productivas. Es cierto que intelectuales marxistas como Wolfgang Harich, considerado el padre del ecosocialismo a partir de su obra [2], incorporan este debate que gana posiciones en los centros de toma de decisión de la URSS en la década de los 80 antes de la disolución, pero la pérdida de tiempo desde que se conoce el problema hasta que se comienza a discutir seriamente es destacable. Como apunte, el bloque capitalista tampoco tuvo capacidad de actuar una vez localizado el problema, principalmente por la contradicción que suponía la solución (no crecer) frente a la esencia del capitalismo: crecer indefinidamente como condición necesaria para la reproducción de capital. Es decir, con este ejemplo, con consecuencias dramáticas 50 años después y que estamos sufriendo actualmente, vemos como el método científico no se aplica para la resolución de un determinado problema porque intervienen otros factores, dogmas ideológicos de una determinada corriente de pensamiento que encorsetan la forma de actuar de la comunidad científica (tanto desde fuera a ella como por la propia cosmovisión que tienen los científicos).

En segundo lugar, las interpretaciones que se realizan de las pruebas y evidencias en la construcción de nuevas teorías era también diferente, dependiendo evidentemente del campo y de la cantidad de evidencias irrefutables que hubiese sobre la mesa (lo cual no deja de ser interesante, ya que las teorías previamente formuladas determinan también los caminos que llevará la ciencia a partir de ahí). Por ejemplo, la teoría evolutiva del equilibrio puntuado (1972, ya hoy refutada por los avances en el campo) propuesta por Niles Eldredge y Stephen Jay Gould determinaba que aun existiendo una evolución gradual, los cambios se acumulan dando lugar a grandes saltos evolutivos [3]. Con esta

teoría se trataba de explicar los importantes cambios evolutivos que tenían lugar en espacios de tiempo geológico muy breves, de forma que se explicase los vacíos en el registro fósil de formas evolutivas intermedias. Es decir, había un cambio en el concepto de lapso de tiempo en comparación con teorías gradualistas. No es casualidad que Stephen Jay Gould tuviera reconocidas raíces marxistas, y que ésta teoría no fuese sino una adaptación de una de las tres leyes de la dialéctica al campo de la biología evolutiva: "*la acumulación de cambios cuantitativos da lugar a cambios cualitativos*". Cabe decir también que la epigenética costó ser aceptada en el bloque occidental precisamente por la fuerte influencia del medio sobre la expresión del genoma e incluso sobre el mismo, siendo esta una de las bases ideológicas del marxismo y a la que se contraponía el sentido común liberal en el que los individuos tienen ciertas capacidades de carácter inmutable desde el nacimiento.

Con estos ejemplos sencillos y particulares se ha querido mostrar como el método, aun siendo formalmente el mismo, se desarrollaba de forma diferente y, sobretodo, permite llegar a conclusiones diferentes dependiendo de cómo se aplique en cada una de sus fases, desde la localización y elección del problema a resolver, como las conclusiones del estudio y, desde el punto de vista más práctico, sus posibles aplicaciones.

***

Habiendo discutido esta base, considero suficientemente establecidos los cimientos de la reflexión como para aseverar que no desarrollamos ciencia en un marco aséptico y apolítico, sino que lo hacemos en un marco ideológico determinado tanto por el desarrollo de las fuerzas productivas (esto es, insisto, como nos relacionamos con la naturaleza y de qué forma satisfacemos nuestras necesidades) como por las relaciones entre las personas que se establecen en función de las relaciones de propiedad con los primeros. Es decir, actualmente desarrollamos ciencia en sistemas políticos y económicos neoliberales, con un alto grado tecnológico, sobre todo en lo que se refiere a rapidez de movimientos de personas, mercancías e información, y esto conlleva una forma particular de ver el mundo. Precisamente, considerar la ciencia como un estadio superior, desvinculado, apolítico y meramente técnico es una de las marcas distintivas del sentido común imperante. Por ejemplo, el discurso de que las ideologías se han superado y la gobernanza se debe hacer desde criterios puramente técnicos, eso sí, solo aplicando

ciertos dogmas económicos que no pueden ser cuestionados (véase las recomendaciones de la Troika o la intervención de ciertos gobiernos europeos como el griego o el italiano en los años de mayor profundidad de la crisis económica en la Unión Europea) es parte del sentido común imperante, de no cuestionamiento del régimen político-económico actual. La ciencia, como elemento que se trata de regir neutral, es parte de este entramado de justificación ideológico, y ello explicaría la falta de cuestionamiento de los problemas que hoy por hoy presenta el método científico.

Centrándome en la última afirmación volcada, la idea fuerza que trato de transmitir es que la ideología dominante actual impide que la propia comunidad científica desarrolle de forma espontánea un ejercicio de autocrítica, necesario, para adaptar la ciencia a los tiempos modernos y a los avances tecnológicos de creación, almacenamiento y transmisión de la información. Dotarla de un áurea de neutralidad y superioridad solamente la impide purgarse de los elementos negativos (muchos de ellos de carácter técnico y de fácil solución en mi opinión). Por otra parte, los errores que está acumulando en las últimas décadas *la forma de hacer ciencia* considero que, aunque se han visto influenciados y seguramente exagerados por el marco ideológico en el que se hace ciencia, no son necesariamente derivados del mismo. Es decir, el marco ideológico impide dar solución porque impide el cuestionamiento de uno de los cimientos en los que descansa: la confianza ciega y supuestamente neutral en la ciencia y la técnica.

En las siguientes líneas trataré de analizar los aspectos más preocupantes que, en mi opinión, he podido localizar en estos años, tratando de ofrecer, cuando pueda, una propuesta de posible solución a los mismos.

***

Quizás uno de los mayores problemas que nos encontramos actualmente en ciencia es la llamada crisis de reproducibilidad, que ya ha sido puesta encima de la mesa en repetidas ocasiones [4,5]. Precisamente, Monya Baker firmaba en el 2016 una encuesta publicada en la revista Nature en torno a esta crisis y cómo era vista desde dentro de la propia comunidad científica [6]. Habiendo preguntado a 1576 científicos de diferentes disciplinas, los resultados arrojaban que un 52% reconocía que existía una fuerte crisis de reproducibilidad, seguido de un 38% que aun reconociendo su existencia rebajaba la profundidad de ésta. Solo un 3% de los encuestados negaba que existiera tal problema.

Los resultados son dispares dependiendo de la disciplina. Así, los físicos y químicos es cierto que son los más confiados en el trabajo de sus compañeros de profesión, con porcentajes de confianza superiores al 75% para el conjunto de artículos publicados. La reproducibilidad no solo afecta a la capacidad de reproducción de los resultados publicados por otro grupo, sino a la capacidad de reproducir de forma sistemática resultados en el propio grupo. Siguiendo con la encuesta, en el caso de la física y la ingeniería, más del 60% reconocía problemas para reproducir los resultados de otros grupos de investigación, pero la falta de reproducibilidad dentro del mismo laboratorio alcanzaba el 50%. Esta cifra es solo ligeramente inferior y podría explicarse por la diversidad de equipos de laboratorio que pueden alterar ligeramente los tratamientos y medidas aplicadas a las muestras.

Bien es cierto que hacer ciencia puntera significa moverse en el borde del abismo de la reproducibilidad, en el sentido de que desarrollar nuevas líneas de investigación significa hacer todo nuevo, sin referencias claras en las que basarse y sin capacidad de control sobre todos los factores que influyen en los resultados. Por lo tanto, a pesar de describir correctamente y (no en todos los casos) en detalle el método experimental seguido, es posible que no se obtengan los mismos resultados debido a que no se ha puesto el foco en factores determinantes de los que se desconoce su rol.

Por supuesto, un resultado no reproducible no quiere decir falso. El resultado en sí, el estudio, la medida y la discusión científica pueden ser correctos (y personalmente estoy seguro de que el porcentaje de engaños es llanamente residual) y sin embargo los procesos llevados a cabo durante el experimento pueden no estar controlados correctamente. El por qué se está dando esta circunstancia, y sobre todo por qué no se pone remedio a pesar de que es algo de lo que la comunidad científica es consciente, habría que buscarlo en cómo funciona la publicación y financiación de la ciencia, que evidentemente está sujeta al marco económico y social explicado con anterioridad.

En mi opinión, la pregunta clave que nos deberíamos hacer es, *¿está bien valorado, tanto científica como curricularmente, la reproducción de resultados ya publicados?* La respuesta sincera es no. Existen grandes problemas tanto para publicar resultados ya puestos en conocimiento de la comunidad científica como para justificar proyectos de investigación, esto es, financiación, que se ocupen de validar resultados como paso imprescindible del método científico y como base para el desarrollo de nuevas líneas de investigación. La segunda pregunta que se deriva inmediatamente de la primera

es, *¿está bien valorado, tanto científica como curricularmente, la publicación de resultados negativos (entendiendo estos, en sentido amplio, como no satisfactorios con las pretensiones iniciales)?* De nuevo, la respuesta correcta es negativa. De hecho, existe una tendencia a publicar solamente la parte positiva y simplificar el método experimental de forma que todos aquellos problemas quedan fuera para construir así una imagen de la ciencia monolítica y perfecta. Y sin embargo, es una pérdida de información fundamental. *¿Cuánto tiempo total acumulado entre toda la comunidad internacional podríamos ahorrarnos si supiésemos qué no funciona, no solo qué funciona?*

Esta última pregunta nos permite movernos hacia el siguiente error que se está cometiendo, y que tiene que ver con la *competitividad*, palabra que ha sido sustituida en los documentos oficiales del Estado español por *excelencia*. Podríamos decir que existen dos modelos de funcionamiento de grupos de trabajo que se dedican a una misma actividad, en este caso la científica: la competición o la cooperación. Es cierto que existen colaboraciones entre diferentes grupos, sobre todo con el objetivo de crear líneas de investigación interdisciplinares. Sin lugar a dudas, mi experiencia personal en el LBL, y en concreto con las sinergias que disfruté en el Molecular Foundry, marca que apueste claramente por la colaboración y la cooperación interdisciplinar, la discusión científica entre varios actores, la búsqueda del experto en cada materia para consejo y colaboración profunda en ciertos casos, etc. Sin embargo, en términos generales se da la competición. Existe una carrera, tanto a nivel de instituciones como a nivel personal, por llegar primero a un resultado bueno, verdadero pero no necesariamente reproducible, que pueda publicarse en una revista de alto índice de impacto. Esta carrera se lleva a cabo por dos motivos. En primer lugar, a nivel institucional y de grupo, la obtención de este tipo de publicaciones permite continuar con la financiación de futuros proyectos. Esto es, si se ha demostrado que se obtienen excelentes resultados, entonces tiene sentido que se siga financiado esta u otra línea de investigación de este mismo grupo de profesionales. Además, la competición por recursos cada vez más escasos conlleva que haya una retroalimentación de aquellos grupos con publicaciones en revistas de alto índice de impacto, de modo que ante la posibilidad de obtener más recursos podrán seguir en esa posición aventajada, frente aquellos que no lo consigan y resulte prácticamente imposible reengancharse al grupo de la excelencia. En segundo lugar, a nivel individual estas publicaciones de prestigio son imprescindibles para la elaboración de un buen currículum personal que permita la estabilización laboral del trabajador y unas condiciones de trabajo dignas (las que por cierto son cada vez más complicadas de adquirir). Además, como son

múltiples los grupos que están trabajando en una misma línea, la competición por ver quién llega primero hace que, a pesar de ser ciencia de calidad, la reproducibilidad pueda quedar en entre dicho. De esta manera, lo importante es el primer resultado. Llegar segundo carece de mérito. Y sin lugar a dudas, la crisis de reproducibilidad y la ausencia de publicación de resultados negativos tienen que ver con esto, con la nula valoración que tiene replicar o *fallar*. Además, otro problema en el que no ahondaré pero si me permito la licencia de nombrar es la necesidad de publicar por publicar, ya que en muchas ocasiones, principalmente en España, hay una valoración más cuantitativa que cualitativa del conocimiento científico creado y publicado.

La otra cara de la moneda son las empresas editoriales encargadas de la publicación de los resultados científicos [7]. Cinco empresas editoriales publican la mitad de toda la ciencia que se hace en el mundo: Reed Elsevier, Springer, Taylor & Francis, Wiley-Blackwell y la American Chemical Society. Todas son de pago, y como es conocido, o bien las instituciones pagan cuotas por el libre acceso a sus revistas o bien los particulares deben desembolsar entre 20 y 50 dólares por cada artículo. Sin embargo, resulta perverso que la ciencia desarrollada con dinero público no sea de libre acceso para el conjunto de los ciudadanos de un país, que puedan beneficiarse justamente del nuevo conocimiento desarrollado. De hecho, el de las editoriales parece el negocio perfecto, dado que bajo la excusa de que ordenan y ponen a disposición del público científico todo el conocimiento creado, obtienen unos beneficios inmensos sin haber desarrollado trabajo alguno. Es decir, existe un doble pago del conocimiento científico, primero en la producción del mismo y en segundo lugar en su acceso. No deja de ser paradójico, de hecho, que el conocimiento creado hasta el momento de su publicación es de titularidad pública, dado que se ha llevado a cabo en una institución estatal, pero que posteriormente pertenece a una empresa privada que se dedica a su distribución. La solución más evidente, y que de hecho está ya encima de la mesa, es la creación de agencias estatales o supranacionales (en el caso europeo) que lleven a cabo este trabajo de revisión por pares, almacenaje y distribución del conocimiento.

Aunque nunca se mencione, quizás la científica Alexandra Elbakyan sea una de esas heroínas que ella sola ha podido poner en jaque el poderío de este monopolio, aunque ello la haya costado una vida escondida de la justicia occidental que defiende los intereses de las grandes empresas editoriales. En ese sentido, su portal de pirateo de artículos científicos Sci-Hub sin duda ha posibilitado que instituciones y grupos de investigación

de países con recursos limitados hayan podido llevar a cabo ciencia a la orden del día, conociendo los últimos avances en sus campos. Sin embargo, en una situación muy parecida Aaron Swartz acabó quitándose la vida tras intentar compartir públicamente más de 5 millones de artículos científicos [8]. La posibilidad de pasar décadas de su vida en una prisión federal estadounidense por intentar devolver el conocimiento científico al conjunto de la sociedad le llevó a tomar esta decisión.

Un problema más secundario, pero que creo pertinente tratar en este bloque sobre las editoriales, es la forma perversa en la que se realiza la revisión por pares, la cual es completamente necesaria porque garantiza una revisión de los resultados y una validación de los mismos previo a su publicación al conjunto de la comunidad científica (que evidentemente luego podrá refutarlos). Digo perversa porque no es completamente ciega. Los revisores conocen los nombres, países e instituciones de pertenencia de los autores de dicho artículo. Una rápida búsqueda en internet puede ofrecer una panorámica de cada uno de estos autores, si son conocidos o no, si el artículo se encuadra dentro de una tesis doctoral o si procede de investigadores seniors y postdocs, etc. Esto puede crear la paradoja de que, ante un mismo contenido, se valore de forma diferente en función de los autores. No existe la completa objetividad, de forma que no puede confiarse todo en el buen comportamiento de los revisores (ahí están los ejemplos de investigaciones de género en ciencia que analizan currículos profesionales mostrando o no el nombre del solicitante, existiendo una clara preferencia para, a igual méritos, la elección del hombre [9]). Y sin embargo la solución es sencilla, evaluación ciega del contenido científico sin conocer el autor hasta el momento de su publicación.

En las últimas líneas he dejado mencionado un problema clave, que es la igualdad de acceso para hombres y mujeres a los mismos puestos de trabajo y mismas responsabilidades en el mundo académico y científico (siendo este un problema social que evidentemente permea en las instituciones académicas y científicas). Si bien no voy a desarrollar extensamente este apartado, sí que quiero situar este problema como uno de los más graves a los que se enfrentan las instituciones científicas en España. Aunque desde ciertos institutos y universidades se están poniendo medidas para paliarlo, el propio modelo de producción científica y de estabilización laboral impide que pueda ser realmente compatible una conciliación entre vida familiar y trabajo, más cuando la mujer, por cuestiones de género y fundamentado en la opresión del patriarcado, es usualmente la que se hace cargo de los cuidados. Es simplemente vergonzante la cantidad de talento

que estamos perdiendo como sociedad por expulsar del sistema científico a una parte considerable de sus integrantes y forzando a la que se queda a hacer auténticos malabarismos para poder ocuparse de la crianza.

***

Me gustaría reflexionar también brevemente en torno al enfoque estratégico de la ciencia en mi país, y por extensión, de la Unión Europea. ¿Cuál es exactamente? Creo que simplemente no hay un objetivo claro, porque no existe un análisis de cuáles son los problemas acuciantes a resolver. Sin embargo, éstos son realmente dignos de consideración, como el agotamiento de los combustibles fósiles y la necesidad imperiosa de una transición ecológica, o la adaptación a las terribles consecuencias del cambio climático. Me resulta chocante que no haya un debate amplio en la sociedad que de forma decisiva permee en la comunidad científica y en la gestión de la misma, enfocando los recursos, tanto materiales como humanos, en estos temas. Considero que falta una auténtica política científica, con un ordenamiento claro de los recursos y unos objetivos a cumplir que tengan en cuenta una transferencia real de conocimiento y técnica al conjunto de la sociedad, incluyendo evidentemente los sectores productivos.

Ahora bien, con esto no quiero decir que se deba abandonar la ciencia base o la capacidad de decisión de los propios grupos a la hora de elegir qué hacen en lo concreto. La ciencia base es completamente necesaria porque constituye la base de nueva tecnología. La posibilidad de resolver problemas científicos a niveles elementales implica el diseño y desarrollo de nueva tecnología que posteriormente puede ser transferida, más allá de que el propio conocimiento científico generado pueda ser posteriormente aplicado. En cuanto a la capacidad de acción de los propios científicos, la creatividad no debe ser coartada en ningún momento. Pero sí creo que puede estar dirigida hacia ciertos fines.

***

Quiero cerrar esta reflexión con un último apartado dedicado a la salud mental de los doctorandos. Se trata de un tema peliagudo que afecta en lo personal, y la forma de tratarlo es imposible que pueda desprenderse de las experiencias vividas. Quiero decir en primer lugar que, tal y como escribo en los agradecimientos, creo que no he podido tener

más suerte a la hora de haber tenido como director de tesis a Leonardo. He podido trabajar sin presión, y cuando he tenido que ausentarme en el trabajo por motivos personales, algunos felices y otros tristes, no me he encontrado con ningún problema, sino todo lo contrario, con cariño y comprensión. Así mismo, cuando la ciencia se mostraba desagradecida y no había ningún resultado positivo, mi frustración ha encontrado ánimos desde la experiencia, y efectivamente, era cuestión de tiempo y aprendizaje. Si bien he tenido momentos de mayor tensión y presión, muchas veces impuesta por mí mismo como reflejo de la presión social que se da en el mundo científico y que he tratado de analizar ya previamente, no ha sido excesivo y por suerte puedo decir que yo soy parte de ese porcentaje de la población doctoranda que no ha sufrido (al menos que yo sea consciente) problemas de salud mental graves. Aun así, considero imprescindible hablar sobre este silenciado problema que está afectando a tanta gente.

Los problemas de salud mental entre los doctorandos han sido recientemente objeto te atención, como así demuestran numerosas publicaciones al respecto [10,11]. El estudio de Teresa M. Evans [10] indica que este sector es seis veces más propenso a sufrir enfermedades de este tipo que el resto de la población general, esto es, un porcentaje del 39% frente al 6%. El estudio realizado sobre la población belga [11] (que puede ser asimilable a un caso general europeo, y en particular al español dada la semejanza de cultura y sobretodo programas de formación y doctorado regidos por una normativa común europea), añade que los doctorandos se ven afectados en un mayor número en comparación con otras profesiones de alta cualificación académicas y altamente especializadas. Por lo tanto, existe una causa particular entre los doctorandos que hace que aproximadamente el 40% de aquellos que realizamos una tesis doctoral suframos de problemas de salud mental durante el desarrollo de la misma. En este último estudio se pregunta a un total de 3600 doctorandos si han sufrido en las últimas semanas alguno de los doce síntomas asociados con trastornos de ansiedad y/o depresivos. Entre estos síntomas considero importante destacar estar bajo presión constante (41%), sentirse infeliz o deprimido (30%), con falta de confianza o sencillamente inútil (16%). Más de la mitad de los encuestados reconocía haber sufrido al menos dos de estos síntomas en las últimas semanas. Continuando con las estadísticas, un 32% de los doctorandos reconocía cuatro de estos síntomas, frente al 15% de los grupos de control. El doble.

Evidentemente hay situaciones vitales que nada tienen que ver con el desarrollo de una tesis doctoral que pueden inducir este tipo de problemas de salud. Sin embargo, el

repunte indica claramente que la realización de una tesis doctoral bajo las condiciones actuales implica estar expuesto a un entorno hostil que puede facilitar la aparición de estos problemas por factores que en una situación laboral diferente no indujesen problemas mentales de la gravedad que estamos tratando, como la depresión. El factor de género aquí es de tremenda importancia. En comparación con sus compañeros hombres, las mujeres que realizan un doctorado tienen un 27% más de probabilidades de desarrollar este tipo de problemas mentales.

Considero que esta situación se debe a la precariedad, tanto material durante la realización de la tesis, como la precariedad vital asociada a la carrera académica. ¿Qué tipo de planificación vital puede llevarse a cabo cuando por un trabajo altamente especializado se cobran a penas 1.300 €, estando en Madrid la renta media para una vivienda de 80-90 m^2 en 1.220 €? ¿Qué tipo de planificación vital puede pensarse si la estabilización en el sector de la investigación es prácticamente imposible hasta una edad avanzada? ¿Puede realmente una persona apostar su vida al encadenamiento de trabajos de uno, dos o tres años en diferentes centros de investigación internacionales de prestigio y compatibilizarlo con la creación de un núcleo familiar a una edad equivalente a la generación de nuestros padres? ¿Qué tipo de efectos puede tener en la confianza en uno mismo, en su futuro y en el sistema entender que, aun habiéndose esforzado durante toda la etapa académica, al final las condiciones laborales y vitales no son las prometidas?

En una sociedad donde el individuo está cada vez más aislado por comportamientos narcisistas y puramente hedonistas, en la que las redes de apoyo se debilitan y la colectividad es cada vez dejada en mayor medida en un segundo plano, el toque final lo da la brutal competitividad que se establece entre compañeros en el mundo de la ciencia. Dicho de forma llana, somos demasiados doctorandos para las pocas plazas estables que hay, y el modelo económico español no tiene capacidad de integración para tanto doctorando de tantas disciplinas (no solo científicas, de la salud o técnicas, sino también humanísticas). Se produce así una competición exacerbada entre nosotros mismos, entre compañeros, por ser los mejores, evidentemente soterradas por la educación y las buenas formas del día a día. Se trata en definitiva de tener mejor currículum que la persona que tienes al lado, que deja de ser compañero para convertirse en rival. Bajo este marco es simplemente imposible no estar en riesgo de desarrollar una patología mental si eres una buena persona que a nivel inconsciente y natural simplemente vives y dejas vivir.

Tras esta etapa formativa en la que uno se educa como científico, aparece la gran pregunta. *¿Qué hacer ahora?* En unas circunstancias normales, donde el Estado, la sociedad en su conjunto, ha apostado una gran partida de recursos en ti para formarte como cuadro altamente especializado, tendría sentido una estabilización tras un periodo de unos años en un país extranjero, de forma que se establezcan y existan lazos culturales y profesionales entre diferentes países que aporten, ya no al individuo en sí, sino al conjunto de la sociedad a través de éste, de nuevas formas y experiencias para afrontar los problemas. Sin embargo, esto no ocurre. Puede ser que marches al extranjero, con el desgaste familiar, de pareja si la hubiese, de amistad, que esto supone y no encontrar ningún tipo de recompensa en tu regreso. Estamos hablando por tanto de empezar de cero con 30-35 años. ¿Tiene esto lógica? Yo creo que no, y las consecuencias las estamos viendo en estos estudios de salud mental. Quiero recalcar que no se trata de dar una solución individual, de pensar que la persona que cae en una depresión es simplemente débil. No. La clave es social, en crear una sociedad justa donde la vocación no sea una excusa para encadenarnos a la precariedad material y existencial más absoluta. Porque se trata de vivir, no sobrevivir.

La música y la poesía siempre han sido el instrumento perfecto para expresar lo que no cabe en el folio. Quizás la mejor forma de resumir esta extensa reflexión sea a través de los versos de *Mao a mà,* canción del grupo gallego Ezetaerre, que traducidos de su lengua original vienen a decir:

¿Por qué somos tan jóvenes para ser tan infelices?
No es derrotismo ni dejamos de soñar,
pero la realidad aprieta y no deja respirar.
Viendo la foto de los colegas, confirmo la teoría.
Dime tú, ¿cómo construyo yo mi vida?

¡Venga, sí! Seamos jóvenes por un rato.
Vivamos el mandato de ejercer el desacato.
Y en las jóvenes del mundo, que quede el recuerdo
de que en medio de la barbarie, somos la esperanza.

Bibliografía

[1] F. Fernández Buey; 1991; *La ilusión del método*; Barcelona, España; Crítica

[2] W. Harich; 1975; *¿Comunismo sin crecimiento?*; Barcelona, España, Editorial Materiales

[3] N. Eldredge, S. J. Gould; 1972; *"Punctuated equilibria: an alternative to phyletic gradualism". Models in paleobiology* pp: 82-115, San Francisco, Estados Unidos, Freeman Cooper and Co.

[4] J. P. A. Ioannidis; "Why Most Published Research Findings Are False"; *PLOS Medicine*, 2, (2005); pp: 696-701; DOI: 10.1371/journal.pmed.0020124

[5] R. Peng; "The reproducibility crisis in science: A statistical counterattack"; *Significance*, 12, (2015); pp: 30-32; DOI: 10.1111/j.1740-9713.2015.00827.x

[6] M. Baker; "1,500 scientists lift the lid on reproducibility: survey sheds light on the 'crisis' rocking research"; *Nature*, 533, (2016); pp: 452–454; DOI: 10.1038/533452a

[7] Página web: https://www.eldiario.es/theguardian/estafa-revistas-cientificas-acerca-fin_0_814368712.html

[8] Página web: https://www.theguardian.com/commentisfree/2015/feb/07/aaron-swartz-suicide-internets-own-boy

[9] C.A. Moss-Racusina, J. F. Dovidio, V. L. Brescoll, M. J. Grahama, J. Handelsman; "Science faculty's subtle gender biases favor male students"; *PNAS*, 9, (2012); pp: 16474–16479; DOI: 10.1073/pnas.1211286109

[10] T. M. Evans, L. Bira, J. B. Gastelum, L T. Weiss, N. L Vanderford; "Evidence for a mental health crisis in graduate education"; *Nature Biotechnology*, 36, (2018); pp: 282–284; DOI: 10.1038/nbt.4089

[11] K. Levecque, F. Anseel, A. De Beuckelaer, J. Van der Heyden, Lydia Gisle; "Work organization and mental health problems in PhD students"; *Research Policy*, 46, (2017); pp: 868-879; DOI: 10.1016/j.respol.2017.02.008

List of publications and communications to conferences

Papers published in journals included in SCI:

- Directly related with the present work:

Study of the Interface of the Early Stages of Growth under Quasi-Equilibrium Conditions of ZnO on Graphene/Cu and Graphite; C. Morales, An. Black, F. J. Urbanos, D. Granados, J. Méndez, A.del Campo, F. Yubero, and L. Soriano; Adv. Mater. Interfaces; 6; (2018); 1801689; DOI: 10.1002/admi.201801689

Influence of the CoO wetting layer on the growth of CoO/HOPG and the subsequent oxidation of the HOPG substrate; *Submitted to Advanced Materials Interfaces*

In-situ study of the carbon gasification reaction on Graphite using cobalt oxides for nanopatterning at low temperature; *In preparation*

Electronic uncoupling of Graphene from polycrystalline copper induced by reactive thermal evaporation of ZnO; *In preparation*

Development of Ultra-thin Oxides Membranes as Electron Transparent Windows for Atmospheric Pressure Photoelectron Spectroscopy and Atomic-scale Imaging; *In preparation*

- Other publications:

On the van der Pauw's method applied to the measurement of low thermal conductivity materials; C. Morales, E. Flores, J. Bodega, F. Leardini, I. J. Ferrer, J. R. Ares, C. Sánchez; *Rev. Sci. Instrum.; 87; (2016); pp 084902; DOI: 10.1063/1.4960331*

Improving the Efficiency of Thin Film Thermoelectric Generators under Constant Heat Flux by Using Substrates of Low Thermal Conductivity; C. Morales, E. Flores, Jose R. Ares, C. Sánchez, and I. J. Ferrer; *PSS-RRL; 12; (2018); pp 1800277; DOI: 10.1002/pssr.201800277*

Ultra-thin CoO films grown on different oxide substrates: size and support effects and chemical stability; D. Díaz-Fernández, E. Salas, J. Méndez, R.J.O. Mossanek, M. Abbate, C. Morales, G. Domínguez-Cañizares, G.R. Castro, A. Gutiérrez, L. Soriano; *J. Alloys Compd.; 758 (2018); pp 5-13; DOI: 10.1016/j.jallcom.2018.05.112*

Pyrite thin films on amorphous substrates: Interaction with the substrate and doping effects; E. Flores, S. Yoda, C. Morales, O. Caballero-Calero, P. Díaz-Chao, M. Martín-González, J.R. Ares, I.J. Ferrer, C. Sánchez; *Thin Solid Films; 672; (2019); pp 138–145; DOI: 10.1016/j.tsf.2019.01.020*

An XPS investigation on the influence of the substrate and growth conditions on pyrite thin films surface composition; C. Morales, E. Flores, S. Yoda, M.A. Niño, D. Martín y Marero, L. Soriano, J. Rojo, J. R. Ares, I. J. Ferrer, C. Sánchez; *Submitted to Applied Surface Science*

Glancing angle magnetron sputtering deposition of silver nanopillar coatings for reducing multipactor effect in space; *In preparation*

Communications to conferences:

- Directly related with the present work:
    - Oral presentations:

Early stages of growth of ZnO of graphene/Cu: graphene decoupled from Cu Workshop on "Understanding Materials Structure and Performance by Raman Confocal Microscopy" organized by Instituto de Cerámica y Vidrio (ICV), CSIC, 2017, Madrid, Spain.

Early stages of growth of ZnO on HOPG and graphene/Cu: a comparative study; 17th European Conference on Applications on Surface and Interface Analysis, ECASIA, 2017, Montpellier, France.

Early stages of growth of ZnO on graphene/Cu: graphene decoupled from Cu; Iberian Vacuum Conference RIVA-X organized by ASEVA, 2017, Bilbao, Spain.

- Posters:

Low temperature nanopatterning on Graphite via carbon gasification reaction using cobalt oxides; SIMS USA, 39th symposium of Applied Surface Analysis and 29th symposium of the AVS Pacific Northwest Chapter organized by the American Vacuum Society, 2018, Richland, USA

Development of Ultra-thin Oxides Membranes as Electron Transparent Windows for Atomic-scale Imaging; Molecular Foundry User Meeting, LBNL, 2018, Berkeley, California, EEUU.

Influence of the CoO/HOPG wetting layer on the growth of CoO and the oxidation of HOPG; SpLine Meeting 2019, ICMM, 2019, Madrid, Spain.

- Other communications:

Transport properties of sulphurated Pd/Ti bilayers; 12th European Conference on Thermoelectrics ECT, 2014, organized by European Thermoelectric Society in Madrid, Spain. *Poster contribution.*

Variable electrical and optical properties of Co_3O_4 ultra-thin-films grown by RF Magnetron Sputtering; 16th European Conference on Applications on Surface and Interface Analysis, 2015, ECASIA, Granada, Spain. *Poster contribution.*

Towards an enhancement on the efficiency of thin film thermoelectric generators (TFTG) by using poor thermal conductor substrates; E-MRS Spring Meeting 2017, organized by European Material Research Society, Strasbourg, France. *Oral contribution.*

Apéndice I

Capítulo 1
Introducción

"La física es como el sexo: seguro que debe ofrecer algún resultado práctico, pero ese no es el motive por el que lo hacemos"

Richard P. Fayman

1.1 El mundo gigante de los óxidos metálicos

De seguro, es tremendamente difícil imaginar un mundo sin compuestos tan familiares como los óxidos metálicos. No es solo que el oxígeno y los elementos metálicos sean ladrillos esenciales en la composición y en la estructura del Universo, y por tanto, ocupen roles esenciales en una gran variedad de procesos físicos, químicos y biológicos. Tanto la tecnología actual como el profundo entendimiento de nuevos fundamentos físicos descansan en el trabajo acumulado en este campo por miles de científicos a lo largo de los últimos siglos hasta nuestros días.

En todo caso, si todos los óxidos metálicos se consideran desde la misma perspectiva, estaremos simplificando enormemente el cuadro. Estos materiales exhiben un amplio rango de propiedades que son características de los conductores, semiconductores y aislantes, de modo que por sí mismos o bien en combinación con otros materiales, pueden ser aplicados en un amplio abanico de dispositivos. Este amplio rango de opciones descansa básicamente en dos factores: las diferentes estructuras cristalinas, polimorfos y disposiciones geométricas que pueden ser encontradas, y segundo en la estructura electrónica de cada metal y su interacción electrónica con el oxígeno [1]. De esta forma, los elementos metálicos cubren la práctica totalidad de la Tabla Periódica, excluyendo aquellos elementos con elevada electronegatividad en el margen derecho de la tabla. Esto se traduce en que configuraciones electrónicas como las *ns* (metales alcalinos y alcalinotérreos), *nd* (metales de transición) y *np* (post-metales de transición) van a interaccionar en diferentes maneras con la configuración electrónica del oxígeno $[He]2s^2 2p^4$, dando lugar a diferentes tipos de enlace (iónico, covalente o mezcla) y

configuraciones electrónicas del óxido. Por lo tanto, diferentes propiedades químicas y físicas podrán ser descritas en función de la estructura de bandas del sólido.

El objetivo principal de este primer capítulo introductorio no trata la discusión en detalle de la física que se encuentra detrás de la interacción metal/oxígeno y sus consecuencias, sino que intenta ofrecer una visión general del excitante mundo de los óxidos metálicos y el hecho de por qué este trabajo ha consistido en la combinación de tres óxidos (CoO_x, ZnO y Al_2O_3) con sustratos de grafito y grafeno. Por lo tanto, pido al lector ser paciente y esperar a los próximos capítulos para una discusión profunda de estos puntos.

Continuando con la última cuestión enunciada, tanto el cobalto como el zinc son metales de transición, mientras que el aluminio es un post-metal de transición, considerado en algunos casos como un metaloide. Respecto al primer tipo, las múltiples configuraciones *nd* dan lugar a propiedades diferentes dependiendo del número de electrones ocupando los orbitales *d*, la correlación e hibridación *d-d*, la hibridación metal anión (*p-d*), la configuración de spin y el campo cristalino del óxido, entre otros aspectos. Precisamente, prácticamente todos los nuevos fenómenos descubiertos y estudiados en el campo de la materia condensada durante el siglo XX (paramagnetismo de Pauli, transición Mott, elevada T_c, superconductividad, ferromagnetismo, antiferromagnetismo, antiferroelectricidad, ferroelectricidad, transiciónes alto/bajo spin, magnetorresistencia gigante, ordenamiento de carga, formación de bipolaron…) están relacionados con los metales de transión [2,3,4]. Ahora, en el caso del cobalto su configuración electrónica es [Ar] $4s^2$ $3d^7$, donde los electrones 3d están fuertemente hibridados y participan en la banda de valencia. Encontramos dos formas de óxido de cobalto estables: CoO (Co^{2+}, estructura de halita) y Co_3O_4 (Co^{2+} and Co^{3+} en estructura de espinela). Ambos óxidos han sido ampliamente estudiados en las pasadas décadas debido a su elevada reactividad [5,6], siendo muy interesantes en aplicaciones como sensores de gas [7,8], dispositivos magnéticos [9], almacenamiento de energía [10,11] y aplicaciones catalíticas [12,13]. Precisamente, el comportamiento catalítico del óxido de cobalto destaca en la literatura científica, sin lugar a dudas por su buen conocido papel (al menos en el nivel macroscópico) del proceso Fischer–Tropsch [14]. Sin embargo, los detalles a nivel atómico de la interacción entre el cobalto con los diferentes sustratos y reactivos continúa bajo discusión.

Por otra parte, el caso del óxido de zinc (ZnO, Zn^{2+}, mayormente con estructura hexagonal de wurtzita bajo condiciones normales) es diferente debido a la estructura electrónica del mismo: [Ar] $4s^2$ $3d^{10}$ [15]. En este elemento los orbitales 3d están completos, participando pobremente en la banda de valencia del óxido [16,17]. Esta circunstancia reduce su reactividad en comparación con los óxidos de cobalto, aunque se usa en ciertas aplicaciones químicas como en fotocatálisis de la vulcanización de la goma [18] o en superficies antibacterianas [19]. Más allá de esto, su elevado gap (3.3 eV), su elevada energía de ligadura del excitón (60 meV) y la facilidad de dopaje tipo-n con elevada conductividad eléctrica aun preservando una elevada transparencia [20] permite que el ZnO se convierta en un material excelente para muchas aplicaciones optoelectrónicas, como paneles solares [21], supercapacitadores [22], sensores [23], etc.

Finalmente, el óxido de aluminio (Al_2O_3, Al^{3+}, fase-α estable con estructura hexagonal compacta, corindón) es completamente diferente a los dos anteriores óxidos [24]. Se trata de un aislante eléctrico, enmarcado en el grupo de las materiales cerámicos y caracterizado por su dureza y fuerza [25]. Ha sido ampliamente utilizado como sustrato para múltiples aplicaciones debido a su baja reactividad con el entorno [26,27,28]. De hecho, como será discutido en los siguientes capítulos, estas propiedades pueden ser también utilizadas en la escala nanométrica.

1.2 Sistemas grafiticos como sustratos: de la monocapa al volumen

En 2010 Andre Gein y Konstantin Novoselov recibieron el Premio Nobel de Física por sus experimentos con grafeno bidimensional, abriendo una nueva era para la ciencia de materiales [29]. El paso de materiales 3D a 2D ha supuesto una auténtica revolución en las propiedades y aplicaciones esperadas para muchos compuestos. Es más, su combinación en heteroestructuras compuestas por varios de estos materiales 2D y otros 3D ofrece multitud de posibilidades en nuevos diseños y aplicaciones [30].

Tal vez el grafeno sigue siendo el material 2D más excitante, entre otras razones debido al tiempo que se ha dedicado a su estudio y la cantidad de fondos y recursos humanos dedicados a su investigación desde su descubrimiento. Este alótropo de carbono consiste en una lámina 2D de átomos dispuestos en una estructura hexagonal con hibridación sp^2. Cuenta con excelentes propiedades eléctricas [31] (se trata de un semimetal cero-gap con elevada conductividad eléctrica), mecánicas [32] (se dice que es

el material más fuerte testado jamás, con un Módulo de Young de 1TPa) y ópticas [33] (absorción de aproximadamente un 2.3% de la luz blanca). Así mismo, el entendimiento de sus propiedades electrónicas desde los principios fundamentales de la mecánica cuántica ha extendido el conocimiento y dominio de las quasipartículas, ya que los electrones del grafeno se propagan a través de la red perdiendo su masa efectiva, resultando en quasipartículas que son descritas por la ecuación de Dirac y no por la usual ecuación de Schrödinger [34].

El número de monocapas apiladas de grafeno determina las propiedades del conjunto del sistema. Como así refleja la literatura, se reportan cambios en los espectros Raman desde una hasta siete monocapas, número a partir del cual se obtiene el espectro del grafito [35]. Esto indica una transición en las propiedades 2D del grafeno hasta las 3D del grafito [36]. En particular, el grafito pirolítico altamente ordenado (HOPG) es la mejor aproximación a un *volumen* de grafeno. Consiste en un apilamiento de láminas de grafeno enlazadas débilmente por fuerzas de Van der Waals. Como en el anterior caso, debido al electrón deslocalizado de cada átomo de carbono, elevadas conductividades eléctricas son reportadas (especialmente en *el plano*), mientras que es fácilmente exfoliado debido a las susodichas interacciones débiles entre planos [37]. De hecho, la primera lámina de grafeno que fue aislada fue obtenida mediante exfoliación mecánica del HOPG.

Los cambios en las propiedades del carbono con hibridación sp^2 en función del espesor sugieren a su vez posibles variaciones dependiendo en los materiales crecidos o depositados encima del grafeno. De hecho, el dopaje y funcionalización de éste por los sustratos, láminas ultra-delgadas o moléculas ha sido el propósito de múltiples investigaciones [38,39,40,41]. Sin embargo, este es un problema de dos caras: los sustratos, las láminas ultra-delgadas o moléculas en contacto con el grafeno también pueden ser influenciados por éste [42,43,44].

1.3 Una interacción compleja: intercaras grafíticas-óxidos metálicos.

El último párrafo de la sección anterior constituye la clave del presente trabajo. Las interrelaciones cruzadas entre sustratos y láminas ultra-delgadas o nano-racimos pueden modificar las propiedades de ambos. De hecho, intercaras (sólido/sólido, sólido/líquido y sólido/gas) y superficies (sólido/vacío) están acaparando cada vez más

atención, ya que muchas propiedades pueden ser modificadas de forma controlada en estas zonas y de hecho muchas reacciones ocurren precisamente en ellas.

De este modo, dos aproximaciones pueden seguirse en los campos de la física aplicada y la ciencia de intercaras y superficies. En primer lugar, la investigación se puede centrar en la interacción fundamental entre sustrato y material depositado (intercaras). El profundo entendimiento de como diferentes materiales interactúan y comparten carga y elementos a través de la misma frontera determinará el control preciso del modo de crecimiento y también de la modificación de las propiedades químicas y físicas [45]. Se requiere remarcar que este preciso control es indispensable para futuras aplicaciones reales en dispositivos. Además, si el depósito es muy delgado, entonces la intercara estará lo suficientemente cercana a la superficie como para hacer posible que el entorno químico (gaseoso o líquido) interaccione con ambos materiales en la intercara. La complejidad del problema se presenta ahora en un poliedro de tres caras (sustrato-depósito-entorno) [46].

La segunda aproximación consiste en el estudio de las intercaras sólido/gas y sólido/líquido, mucho menos investigadas que las previas intercaras sólido/sólido, debido a la interferencia proveniente del volumen de los materiales y las limitaciones técnicas asociadas con los ambientes líquidos y gaseosos. En este caso, el reto actual consiste en el desarrollo de nuevos dispositivos y técnicas que permitan la media de estas intercaras [47]. Este tipo de investigaciones son especialmente importantes para los procesos catalíticos. El comportamiento de los catalizadores se encuentra directamente relacionado con su estructura y composición atómica, y por lo tanto la capacidad de estudiar y mapear a los catalizadores en la escala atómica durante el desarrollo de los procesos reactivos es completamente esencial a la hora de establecer un entendimiento profundo en cómo la composición y estructura del catalizador determina la actividad y selectividad en cada reacción química. En este sentido, en los últimos años se han desarrollado membranas de grafeno para la realización de medidas de XPS a elevadas presiones en intercaras sólido/líquido y sólido/gas [48,49], aunque la limitada estabilidad química y mecánica del grafeno frena su uso generalizado.

Resumiendo estas primeras tres secciones, el potencial de combinar óxidos metálicos con sustratos grafíticos parece claro. La gran variedad de tipos y propiedades de óxidos metálicos combinados con las increíbles propiedades del grafeno permiten estimular nuestra imaginación hacia nuevas heteroestructuras con novedosas propiedades y usos. Por ejemplo, nanopartículas CoO_x pueden facilitar la nano-litografía en

superficies de grafito y grafeno a menores temperaturas que otras nanopartículas metálicas [50]. La combinación de las propiedades del grafeno con ZnO puede conllevar la fabricación de dispositivos que podrán ser utilizados en múltiples aplicaciones tecnológicas como producción y almacenamiento energético [51,52]. Finalmente, las excelentes propiedades mecánicas y la inactividad química de la superficie del Al_2O_3 pueden ayudar en el desarrollo de nuevos dispositivos para la investigación, superando los problemas que presenta el grafeno a la hora de separar alto vacío de gases y líquidos.

1.4 Objetivo y estructura de la presente tesis doctoral

El objetivo general de la presente memoria es explicar la interacción entre diferentes óxidos metálicos y sustratos grafíticos, tales como monocapas de grafeno y HOPG, y buscar posibles aplicaciones. Por interacción entenderemos las características del crecimiento y las interacciones químicas y físicas que se establezcan entre sustrato y los óxidos. En particular, tres óxidos metálicos serán estudiados. Primero se describirá y explicará la interacción de CoO_x con el HOPG, especialmente en la intercara entre ambos y en la cinética de la reacción de gasificación del carbono que tiene lugar cuando el sistema CoO_x/HOPG es re-oxidado a baja temperatura (~400 °C). El siguiente punto será la interacción de ZnO con HOPG y grafeno crecido mediante deposición química de vapor (CVD por sus siglas en inglés) sobre cobre policristalino. Nos centraremos en la influencia del estado inicial del grafeno en el crecimiento del ZnO y en los cambios en el acople electrónico entre grafeno y el sustrato de cobre debido al ZnO. Finalmente, se expondrá el desarrollo de láminas ultra-delgadas de Al_2O_3 como ventanas transparentes de electrones para medidas de fotoemisión de electrones llevadas a cabo en condiciones de alta presión y en toma de imágenes en escala atómica. Para este propósito las membranas de grafeno anteriormente mencionadas serán utilizadas como soporte para el depósito de estas láminas ultra-delgadas de óxidos metálicos.

De esta forma, el cuerpo de la tesis será dividido en cuatro capítulos. El próximo será dedicado a los detalles experimentales: caracterización de materiales (óxidos y sustratos) y presentación de los principios fundamentales de las técnicas experimentales utilizadas durante el presente trabajo. Cada uno de los siguientes capítulos será dedicado a cada uno de los óxidos. El Capítulo 3 corresponde al CoO_x. Se trata de una continuación del trabajo previo realizado en el grupo GRIN, y completa con nuevos resultados la Tesis Doctoral presentada por el Dr. Daniel Díaz Fernández y supervisada por el Profesor

Leonardo Soriano de Arpe [53]. Como fue mencionado anteriormente, en primer lugar se llevará a cabo una breve discusión sobre la intercara CoO-HOPG, con nuevos datos provenientes de técnicas consistentes en espectroscopia de electrones fotoemitidos por rayos-X (XPS), espectroscopia de electrones fotoemitidos por rayos-X duros (HAXPES) y XPS en presiones cercanas al ambiente (NAP-XPS). Tras esto se presentará el estudio *in situ* mediante NAP-XPS y espectroscopia de absorción de rayos-X (XAS) de la reacción de desgasificación de carbón que tiene lugar bajo atmósfera de oxígeno a 400°C. Se han realizado medidas *ex situ* de microscopia de fuerzas atómicas (AFM) y microscopia de sonda de barrido (KPFM) para la caracterización de las nanoestructuras (nano-tiras y nano-anillos) que aparecen tras el proceso de re-oxidación.

El siguiente Capítulo 4 representa la parte principal del presente trabajo. Mostrará los resultados del crecimiento de ZnO sobre HOPG y grafeno/Cu. De esta manera, primero se describirá el modo de crecimiento de ZnO sobre HOPG y la interacción entre ambos. El estudio *in situ* fue realizado mediante XPS, mientras que medidas *ex situ* de AFM, microscopia de electrones secundarios (SEM) y espectroscopia Raman complementarán la discusión. Además y por propósitos comparativos, el sistema ZnO/HOPG fue sometido a los mismos procesos de re-oxidación que el sistema CoO/HOPG. El siguiente punto consiste en la caracterización del crecimiento de ZnO sobre grafeno/Cu, con especial énfasis en los primeros estadios de crecimiento del ZnO y la influencia en ellos del estado inicial y local del sustrato grafeno/Cu. Para este estudio, medidas *in situ* de XPS se han llevado a cabo, completadas con medidas *ex situ* de AFM, SEM, espectroscopia Raman y microscopia de electrones fotoemitidos (PEEM). Tras esto se discutirán los cambios observados en el acoplamiento electrónico entre grafeno y cobre tras el crecimiento de ZnO, relacionándolos con el desacoplamiento inducido por el agua en el sistema grafeno/Cu. Para este propósito las principales técnicas utilizadas han sido XPS, AFM, microscopía de transmisión de electrones (TEM) y espectroscopia Raman.

El último Capítulo 5 está dedicado al desarrollo de membranas de Al_2O_3 de entre 1 y 3 nm de espesor para separar alto vacío de líquidos y gases con el fin de realizar medias de XPS de intercaras de sólido/gas y sólido/líquido. Esta parte se corresponde con el trabajo desarrollado en el Lawrence Berkeley National Laboratory, bajo la supervisión del Profesor Miquel Salmerón. El óxido metálico es crecido primeramente en un soporte suspendido (grafeno o polímero Formvar dispuestos en membranas perforadas de SiN y recubiertas de Ay/Cr) mediante depósito atómico de capas (ALD). Estas membranas son

posteriormente caracterizadas *ex situ* mediante XPS, AFM, SEM, TEM y espectroscopia Raman, y fueron testadas bajo condiciones reales de funcionamiento, llevándose a cabo medidas *in situ* de NAP-XPS.

Cada uno de los capítulos anteriores contiene una discusión de los resultados y una sección final con las principales conclusiones. Como último capítulo se presentará una evaluación crítica de los resultados aportados en el presente trabajo en cada uno de los campos científicos y tecnológicos aquí descritos, de modo que se enfatice el contexto científico en el cual se presenta esta memoria.

La última sección, escrita solamente en castellano, no tiene ningún contenido específicamente científico. Por el contrario, se trata de una discusión personal a cerca de la política científica de España, repasando tanto los puntos fuertes como débiles. En particular, las nociones de *competitividad* y *excelencia*, que en las últimas décadas definen la *producción* de ciencia y la promoción de normas basadas en (solo) el criterio de publicación. Realmente considero que es necesario una revisión de cómo hacemos ciencia para poder mejorar y solucionar los aspectos negativos y reforzar los positivos. Esta última sección no es necesaria para una comprensión global del presente trabajo.

Bibliografía

[1] V. E. Henrich, P. A. Cox; 1996; *The Surface Science of Metal Oxides*; New York, USA; Cambridge University Press

[2] J. Manhart, D. G. Schlom; "Oxide Interfaces-An Opportunity for Electronics"; *Science* 327, (2010); pp: 1607-1611; DOI: 10.1126/science.1181862.

[3] H. Y. Hwang, Y. Iwasa, M. Kawasaki, B. Keimer, N. Nagaosa, Y. Tokura; "Emergent phenomena at oxide interfaces"; *Nature materials* 11, (2012); pp: 103-113; DOI: 10.1038/nmat3223

[4] P. Yu, Y. H. Chu, R. Ramesh; "Oxide interfaces: pathways to novel phenomena"; *Materials Today* 15, (2012); pp: 320-327; DOI: 10.1016/S1369-7021(12)70137-2

[5] T. Takami; 2011, *Functional Cobalt Oxides: Fundamentals, Properties and Applications*; Singapore, Pan Stanford Publishing

[6] B. Raveau, M. Seikh; 2012, *Cobalt Oxides: From Crystal Chemistry to Physics*; Weinheim, Germany; Wiley

[7] J. Park, X. Shen, G. Wang; "Solvothermal synthesis and gas-sensing performance of Co3O4 hollow nanospheres"; *Sensor. Actuator. B Chem*. 136, (2009); pp: 494-498; DOI: 10.1016/j.snb.2008.11.041

[8] J. Yang, W.-D. Zhang, S. Gunasekaran; "A low-potential, H_2O_2-assisted electrodeposition of cobalt oxide/hydroxide nanostructures onto vertically-aligned multi-walled carbon nanotube arrays for glucose sensing"; *Electrochim. Acta* 56, (2011); pp: 5538-5544; DOI: doi.org/10.1016/j.electacta.2011.03.087

[9] H. Xing, W. Kong, C. Kim, S. Peng, S. Sun, Z. Xu, H. Zeng; "Giant positive magnetoresistance in Co@CoO nanoparticle arrays"; *J. Appl. Phys*. 105, (2009); pp: 063920; DOI: 10.1063/1.3099594

[10] X.-C. Dong, H. Xu, X.-W. Wang, Y.-X. Huang, M.B. Chan-Park, H. Zhang, L.-H. Wang, P. Cheng; "3D Graphene-Cobalt Oxide Electrode for High-Performance Supercapacitor and Enzymeless Glucose Detection"; *ACS Nano* 6, (2012); pp: 3206-3213.; DOI: 10.1021/nn300097q

[11] T.-Y. Wei, C.-H. Chen, K.-H. Chang, S.-Y. Lu, C.-C. Hu; "Cobalt Oxide Aerogels of Ideal Supercapacitive Properties Prepared with an Epoxide Synthetic Route"; *Chem. Mater.* 21, (2009); pp: 3228-3233; DOI: 10.1021/cm9007365

[12] F. Jiao, H. Frei,; "Nanostructured Cobalt Oxide Clusters in Mesoporous Silica as Efficient Oxygen-Evolving Catalysts"; *Angew Chem. Int. Ed.* 48, (2009); pp: 1841-1844; DOI: 10.1002/anie.200805534

[13] Y. Liang, Y. Li, H. Wang, J. Zhou, J. Wang, T. Regier, H. Dai; "Co_3O_4 nanocrystals on graphene as a synergistic catalyst for oxygen reduction reaction"; *Nat. Mater*. 10, (2011); pp: 780-786; DOI: 10.1038/NMAT3087

[14] G. Melaet, W. T. Ralston, C-S. Li, S. Alayoglu, K. An, N. Musselwhite, B. Kalkan, and G. A. Somorjai; "Evidence of Highly Active Cobalt Oxide Catalyst for the Fischer-Tropsch Synthesis and CO2 Hydrogenation*"; J. Am. Chem. Soc*.,136, (2014); pp: 2260-2263; DOI: 10.1021/ja412447q

[15] C. F. Klingshirn, B. K. Meyer ,A. Waag, A. Hoffmann, J. Geurts; 2010; *Zinc Oxide: From Fundamental Properties Towards Novel Applications*; Berlin, Germany; Springer

[16] P. Mikheeva, G. M. Zhidomirov, S. F. Ruzankin, S. A. Leontiev, V. G. Devyatov, S. V. Koshcheev, A. E. Cherkashin; "Modeling the photoelectron spectra of the valence O-2p band of Zinc Oxide by the Xα-scattered wave method"; *J. Struct. Chem*, 38, (1997); pp: 732-741; DOI: 10.1007/BF02763885

[17] S. A. Leontiev, S. V. Koshcheev, V. G. Devyatov, A. E. Cherkashin, and P. Mikheeva; "Detailed XPS and UPS studies of the band structure of Zinc Oxide"; *J. Struct. Chem*, 38, (1997); pp: 725-731; DOI: 10.1007/BF02763884

[18] M. C. Yeber, J. Rodríguez, J. Freer, N. Durán, H. D. Mansilla; "Photocatalytic degradation of cellulose bleaching effluent by supported TiO_2 and ZnO"; *Chemosphere* 41, (2000); pp: 1193-1197; DOI: 10.1016/S0045-6535(99)00551-2

[19] A. Sirelkhatim, S. Mahmud, A. Seeni, N. H. M. Kaus, L. C. Ann, S. Khadijah M. Bakhori, H. Hasan, D. Mohamad; "Review on Zinc Oxide Nanoparticles: Antibacterial Activity and Toxicity Mechanism"; *Nano-Micro Lett.*7, (2015); pp: 219-242; DOI: 10.1007/s40820-015-0040-x

[20] Ü. Özgür, Ya. I. Alivov, C. Liu, A. Teke, M. A. Reshchikov, S. Doğan, V. Avrutin, S.-J. Cho, H. Morkoç; "A comprehensive review of ZnO materials and devices"; *J. Appl. Phys.* 98, (2005); pp: 041301; DOI: 10.1063/1.1992666

[21] I. Gonzalez-Valls, M. Lira-Cantu; "Vertically-aligned nanostructures of ZnO for excitonic solar cells: a review"; *Energy Environ. Sci.,* 2, (2009); pp: 19-34; DOI: 10.1063/1.1992666

[22] Y. Zhang, H. Li, L. Pan, T. Lu, Z. Sun; "Capacitive behavior of graphene-ZnO composite film for supercapacitors"; *J. Electroanal. Chem*. 634, (2009); pp: 68-71; DOI: 10.1016/j.jelechem.2009.07.010

[23] L. Zhu, W. Zeng; "Room-temperature gas sensing of ZnO-based gas sensor: A review"; *Sens. Actuators, A,* 267. (2017); pp: 242-261; DOI: 10.1016/j.sna.2017.10.021

[24] S. Ciraci , Inder P. Batra "Electronic structure of a-alumina and its defect states"; Phys. Rev. B 28, (1984); pp: 982-992; DOI: 10.1103/PhysRevB.28.982

[25] E. Dörre, H. Hübner, 1984, *Alumina: Processing, Properties, and Applications*, Berlin, Germany; Springer

[26] P. C. Bormant, K. R. Westerterp;" An Experimental Study of the Kinetics of the Selective Oxidation of Ethene over a Silver on a-Alumina Catalyst"; *Ind. Eng. Chem. Res.* 34, (1995); pp: 49-58; DOI: 10.1021/ie00040a002

[27] M. Trueba, S. P. Trasatti ; "γ-Alumina as a Support for Catalysts: A Review of Fundamental Aspects"; *Eur. J. Inorg. Chem.* 2005, (2005); pp: 3393-3403; DOI: 10.1002/ejic.200500348

[28] J. Y. Parka, J. M. Leeb, J. H. Jeb, S. S. Kim; "Early stage growth behavior of ZnO nanoneedle arrays on Al2O3 (0001) by metalorganic chemical vapor deposition"; *J. Cryst. Growth*, 281, (2005); pp: 446-451; DOI: 10.1016/j.jcrysgro.2005.04.035

[29] K. S. Novoselov, A. K. Geim, S. V. Morozov, D. Jiang, Y. Zhang, S. V. Dubonos, I. V. Grigorieva, A. A. Firsov; "Electric Field Effect in Atomically Thin Carbon Films"; Science 306, (2004); pp: 666-669; DOI: 10.1126/science.1102896

[30] A.Gupta, T. Sakthivel, S. Seal; "Recent development in 2D materials beyond graphene"; *Prog. Mater Sci.* 73, (2015); pp: 44-126 DOI: 10.1016/j.pmatsci.2015.02.002

[31] D. R. Cooper, B. D'Anjou, N. Ghattamaneni, B. Harack, M. Hilke, A. Horth, N. Majlis, M. Massicotte, L. Vandsburger, E. Whiteway, V. Yu; "Experimental Review of Graphene"; *ISRN Condensed Matter Physics*, 2012, (2011); pp: 1-56; DOI: 10.5402/2012/501686

[32] C. Lee, X. Wei, J.W. Kysar, J. Hone; "Measurement of the Elastic Properties and Intrinsic Strength of Monolayer Graphene". *Science* 321, (2008); pp: 385-388; DOI: 10.1126/science.1157996

[33] R. R. Nair, P. Blake, A. N. Grigorenko, K. S. Novoselov, T. J. Booth, T. Stauber, N. M. R. Peres, A. K. Geim; "Fine Structure Constant Defines Visual

Transparency of Graphene"; *Science* 320, (2008); pp: 1308-1308; DOI: 10.1126/science.1156965

[34] A. Bostwick, T. Ohta, T. Seyller, K. Horn, E. Rotenberg; "Quasiparticle dynamics in graphene"; *Nature Physics*, 3, (2007); pp: 36-40; DOI: 10.1038/nphys477

[35] A. C. Ferrari, J. C. Meyer, V. Scardaci, C. Casiraghi, M. Lazzeri, F. Mauri, S. Piscanec, D. Jiang, K. S. Novoselov, S. Roth, A. K. Geim; "Raman Spectrum of Graphene and Graphene Layers"; *PRL* 97, (2006); pp: 187401 DOI: 10.1103/PhysRevLett.97.187401

[36] B. Partoens, F. M. Peeters; "From graphene to graphite: Electronic structure around the K point"; *Phys. Rev. B* 74, (2006); pp: 075404; DOI: 10.1103/PhysRevB.74.075404

[37] See: http://nanoprobes.aist-nt.com/apps/HOPG%20info.htm

[38] G. Giovannetti, P. A. Khomyakov, G. Brocks, V. M. Karpan, J. van den Brink, P. J. Kelly "Doping Graphene with Metal Contacts"; *Phys. Rev. Lett*. 101; (2008); pp: 026803; DOI: 10.1103/PhysRevLett.101.026803

[39] Y. Shao, J. Wang, H. Wu, J. Liu, I. A. Aksay, Y. Lin; "Graphene Based Electrochemical Sensors and Biosensors: A Review"; *Electroanal*, 22, (2010); pp: 1027-1036; DOI: 10.1002/elan.200900571

[40] H. Liu, Y. Liu, D. Zhu; "Chemical doping of graphene"; J. Mater. Chem., 21, (2011); pp: 3335-3345; DOI: 10.1039/C0JM02922J

[41] M. Pykal , P.Jurečka , F. Karlický, M. Otyepka; "Modelling of graphene functionalization"; *Phys. Chem. Chem. Phys*., 18, (2016); pp: 6351-6372; DOI: 10.1039/C5CP03599F

[42] A. Mishchenko, J. S. Tu, Y. Cao, R. V. Gorbachev, J. R. Wallbank, M. T. Greenaway, V. E. Morozov, S. V. Morozov, M. J. Zhu, S. L. Wong, F. Withers, C. R. Woods, Y-J. Kim, K. Watanabe, T. Taniguchi, E. E. Vdovin, O. Makarovsky, T. M. Fromhold, V. I. Fal'ko, A. K. Geim, L. Eaves, K. S. Novoselov; "Twist-controlled resonant tunnelling in graphene/boron nitride/graphene heterostructures" *Nature Nanotechnology* 9, (2014); pp: 808-813; DOI: 10.1038/NNANO.2014.187

[43] R. S. Weatherup, L. D'Arsié, A. Cabrero-Vilatela, S. Caneva, R. Blume, J. Robertson, R. Schloegl, S. Hofmann; "Long-Term passivation of strongly interacting metals with single-layer graphene"; *J. Am. Chem. Soc.* 137, (2015); pp: 14358-14366; DOI: 10.1021/jacs.5b08729

[44] M. Schriver, W. Regan, W. J. Gannett, A. M. Zaniewski, M. F. Crommie, A. Zettl; "Graphene as a long-term metal oxidation barrier: worse than nothing" *ACS Nano*; 7, (2013); pp: 5763-5768; DOI: 10.1021/nn4014356

[45] X. Liu, C. Z. Wang , M. Hupalo , W. C. Lu , M. C. Tringides , Y. X. Yao, K. M. Ho; "Metals on graphene: correlation between adatom adsorption behavior and growth morphology"; *Phys. Chem. Chem. Phys.*, 14, (2012); pp: 9157-9166; DOI: 10.1039/C2CP40527J

[46] R. Wu, L. Gan, X. Ou, Q. Zhang, Z. Luo; "Detaching graphene from copper substrate by oxidation-assisted water intercalation"; *Carbon*, 98, (2016); pp: 138-143; DOI: 10.1016/j.carbon.2015.11.002

[47] C. Hao Wu, R. S. Weatherup, M. B. Salmeron; "Probing electrode/electrolyte interfaces *in situ* by X-ray spectroscopies: old methods, new tricks"; *Phys.Chem.Chem.Phys*.17, (2015); pp: 30229-30239; DOI: 10.1039/c5cp04058b

[48] R. S. Weatherup, B. Eren, Y. Hao, H. Bluhm, M. B. Salmeron; "Graphene Membranes for Atmospheric Pressure Photoelectron Spectroscopy"; J. Phys. Chem. Lett., 7, (2016); pp: 1622−1627; DOI: 10.1021/acs.jpclett.6b00640

[49] J. J. Velasco-Velez, V. Pfeifer, M. Hävecker, R. S. Weatherup, R. Arrigo, C.-H. Chuang, E. Stotz, G. Weinberg, M. Salmeron, R. Schlçgl, A. Knop-Gericke "Photoelectron Spectroscopy at the Graphene-Liquid Interface Reveals the Electronic Structure of an Electrodeposited Cobalt/Graphene Electrocatalyst"; *Angew. Chem. Int. Ed.*, 54, (2015); pp: 1-6; DOI: 10.1002/anie.201506044

[50] D. Díaz-Fernández, J. Méndez , A. del Campo, R.J.O. Mossanek, M. Abbate, M.A. Rodríguez, G. Domínguez-Cañizares, O. Bomatí-Miguel, A. Gutiérrez, L. Soriano; "Nanopatterning on highly oriented pyrolytic graphite surfaces promoted by cobalt oxides"; *Carbon*, 85, (2015); pp: 85-89; DOI: 10.1016/j.carbon.2014.12.049

[51] T.G.U. Ghobadi, M. Kunduraci, E. Yilmaz; "Improved lithium-ion battery anode performance via multiple element approach"; *J. Alloys Compd*, 730, (2018); pp: 96-102; DOI: 10.1016/j.jallcom.2017.09.297

[52] G. Zamiri, S. Bagheri; "Fabrication of green dye-sensitized solar cell based on ZnO nanoparticles as a photoanode and graphene quantum dots as a photo-sensitizer"; *J. Colloid Interface Sci*. 511, (2018); pp: 318-324; DOI: 10.1016/j.jcis.2017.10.026

[53] D. Diaz-Fernández; 2015; Ph.D Thesis "*Study of the growth and interaction of cobalt oxides on graphite and oxides surfaces*"

Apéndice II

Capítulo 6
Conclusiones principales y futuras líneas de trabajo

"Nunca pienso en el futuro. Ya viene suficientemente deprisa."

Albert Einstein

6.1 Principales conclusiones de la memoria

Las páginas anteriores condensan cuatro años de viaje iniciático en los caminos de la ciencia. Cuatro años en los que he aprendido, o al menos lo he tratado, las reglas básicas del trabajo científico. Del proyecto original consistente en el estudio de la interacción entre el ZnO y el grafeno para futuras aplicaciones en células solares, podemos afirmar que algunos de aquellos objetivos han sido alcanzados exitosamente. Pero la ciencia constantemente muta, transforma cuestiones y cambia el propósito final. Por lo tanto, en la finalización de estos cuatro años, tres óxidos metálicos, y no solo ZnO, han sido estudiados en relación a su interacción con sistemas grafíticos, tales como HOPG y grafeno. De hecho, de dispositivos de conversión energética, a partir de los resultados obtenidos se ha pasado a aplicaciones alternativas en catálisis y desarrollo de nuevos dispositivos de medida. Los resultados y conclusiones principales para cada uno de estos óxidos (CoO, ZnO y Al_2O_3) serán presentados en las siguientes líneas con el fin de cerrar la presente memoria.

CoO en HOPG

El resultado más impresionante previamente reportado por nuestro grupo, y que ha sido la causa de la continuación de esta línea de trabajo, fue la nano-litografía inducida en la superficie de grafito a menores temperaturas que para nanopartículas metálicas de Co. Sin embargo, existía una falta de entendimiento sobre qué rutas químicas hacían esto posible. En el Capítulo 3 se han presentaron nuevos resultados referidos tanto a la caracterización electrónica de la monocapa de CoO como a la caracterización *in situ* de la reacción de gasificación de carbono mediante XPS-NAP. Ha podido demostrarse como el depósito inicial de CoO es capaz de introducir oxígeno en la estructura del HOPG,

rompiendo los anillos del grafito e introduciendo defectos: por tanto, tornandose de hibridación sp^2 a sp^3. Aunque tras el proceso de reducción desaparecen los enlaces C-O y C=O inducidos por el depósito inicial de CoO, los anillos ya rotos del grafito debilitan la red de éste, y por lo tanto la reacción de gasificación de carbono puede tener lugar con una cinética mayor que para típicas nanopartículas metálicas. Mediante estos experimentos, se pudieron probar las asunciones iniciales por las que la razón de esta nano-litografía a bajas temperaturas era posible debido al debilitamiento de los enlaces σ de la red del HOPG. Por otra parte, la oxidación a temperatura ambiente de CoO a Co_3O_4 parece un proceso reversible, aunque la re-oxidación a 400 °C del Co metálico implica una transición no estable a altas presiones, en el que el ratio entre los cationes Co^{3+} y Co^{2+} cambia con el tiempo hasta que el equilibrio es alcanzado en la mezcla Co_3O_4/CoO. Este hecho se debe a 1) el tamaño de las nanopatículas, donde la superficie predomina sobre el volumen, y 2) las fuertes variaciones en las condiciones de oxidación-reducción durante la reacción de gasificación de carbono.

Finalmente, otras dos nanoestructuras han sido estudiadas como productos finales en la superficie del HOPG tras los procesos de re-oxidación: nanoanillos y nanotiras. Aunque el aspecto principal del estudio ha sido topográfico, medidas de KPFM indican que estas dos estructuras comparten un mismo origen: estructuras auto-ensambladas de moléculas orgánicas y/o inorgánicas que pudieran estar presentes en la atmósfera del laboratorio (estas estructuras solo pudieron ser observadas tras la exposición de las muestras al aire). La modificación química de la superficie de grafito debido a la reacción de gasificación de carbono puede inducir cambios en la hifrofobicidad y reactividad de la superficie del HOPG, facilitando la absorción de moléculas y la curvatura de las típicas nanotiras cerca de las nanopartículas de CoO_x, donde la concentración de defectos aumenta.

ZnO en HOPG y láminas de grafeno/Cu

Respecto al modo de crecimiento de ZnO, aunque la primera capa atómica de ambos sustratos es idéntica, los resultados presentados indican un crecimiento completamente diferente entre los sustratos de HOPG y grapfeno/Cu. Los estadios iniciales de crecimiento en HOPG consisten en la deposición de partículas micrométricas de ZnO en los escalones y puntos de defectos de las terrazas del HOPG, con un elevado ratio de difusión de los átomos de Zn. La oxidación del ZnO en este caso es completa

Además, los estados finales del crecimiento dan lugar a una lámina delgada microestructurada de ZnO. Sin embargo, el crecimiento sobre las láminas de grafeno/Cu consiste en la deposición de átomos de Zn en la superficie, manteniéndose en estado metálico, seguido del crecimiento de una gran cantidad de pequeñas nanopartículas de ZnO, dando lugar a la formación de un subóxido (ZnO_x) en la intercara ZnO/Zn, formando una estructura ZnO/ZnO_{1-x}/Zn/grafeno/Cu. Bajo este marco, la primera deposición de átomos de Zn en la monocapa de grafeno parece que actúa como centro de nucleación para el óxido, dando lugar finalmente a una lámina delgada nanoestructurada de ZnO. Comparando ambos sustratos, el rol del grafeno parece crucial para crear estos centros de nucleación. Los experimentos llevados a cabo han evidenciado nuevamente la diferente estructura electrónica de ambos sustratos, y por tanto la diferenciada interacción del grafeno con otros materiales respecto al HOPG.

Tratando ahora la interacción entre el ZnO y el sistema grafeno/Cu, se ha mostrado como las relaciones cruzadas entre el sustrato de cobre, grafeno y las especies químicas intercaladas entre amos debido a la exposición al aire determinan el cuadro completo. Se ha propuesto que la capa inicialmente depositada de ZnO/Zn probablemente induzca, mediante transferencia de electrones del Zn metálico al grafeno, el desacople electrónico del grafeno respecto al sustrato metálico. La presencia de Zn acelera la corrosión galvánica del cobre mediante la formación de hidroxilos a partir de las moléculas de oxígeno y agua intercaladas. Esta reacción, que es esencialmente la misma que la reportada cuando el grafeno/Cu se sumerge en agua (también discutida en el texto, añadiendo a las medidas Raman anteriormente reportadas nuevas medidas de XPS), conlleva la formación de una estructura compleja formada por ZnO/ZnO_{1-x}/Zn/graphene/Cu_2O/Cu. El desacople electrónico del grafeno del cobre depende esencialmente de dos factores: el tiempo de exposición al aire de la lámina grafeno/Cu antes del depósito de ZnO, y la presencia de zinc evaporado de una fuente de Zn metal bajo una atmósfera de oxígeno.

Precisamente, el estado químico y estructural inicial de grafeno/Cu recibido es de extrema importancia en el posterior crecimiento de ZnO. Mientras que las características del crecimiento del óxido (en términos de ratios de nucleación, depósito y composición) dependen del acople electrónico inicial del grafeno con el Cu, esta última condición depende a su vez del número de defectos del grafeno, las especies químicas intercaladas entre el grafeno y el Cu, y del estado de oxidación, dirección cristalográfica y morfología

de la superficie de los granos de Cu, estando todos estos parámetros determinados por el carácter policristalino del sustrato metálico. De hecho, todos estos factores que influyen en el crecimiento de ZnO se presentan como inhomogeneidades (tamaño >1 μm) en las muestras de grafeno/Cu recibidas, restringiendo un crecimiento homogéneo de ZnO. De todas formas, la modificación externa del estado químico inicial de los sustratos de grafeno/Cu abre la puerta para crecimientos homogéneos y bien controlados de ZnO.

Membranas ultra-delgadas y suspendidas de Al_2O_3

El Capítulo 5 describe los primeros pasos del proyecto dedicado al desarrollo de membranas ultra-delgadas de óxidos metálicos (< 3nm) que sirvan como ventanas transparentes para electrones. La caracterización química y estructural de estas membranas indica que la baja temperatura utilizada durante el proceso de deposición mediante ALD asegura un crecimiento amorfo de la lámina mientras a su vez preserva su composición química en el volumen, existiendo una ligera contaminación tanto de carbono como de flúor en la superficie que puede ser, sin embargo, fácilmente eliminada sin modificación de la lámina mediante un ataque con clusters de átomos de Ar a baja energía.

Dos rutas de fabricación fueron testadas. En primer lugar, grafeno suspendido fue utilizado como soporte inicial para la deposición de Al_2O_3. Sin embargo, el grafeno no es una buena opción debido a la calidad inicial de las láminas comerciales de grafeno/Cu, las cuales tras el proceso de transferencia (con o sin uso de polímeros) pueden romperse fácilmente, sin llegar a cubrir todos los agujeros perforados en la rejilla de TEM, y por tanto impidiendo su uso como ventanas en celdas de reacción de sistemas experimentales de XPS y TEM. El segundo problema está relacionado con la contaminación de la superficie debido a la transferencia del grafeno. Aunque ésta no es crítica, puede presentar problemas si interactúa químicamente con el líquido o gas bajo estudio, modificando su espectro. Por otra parte, el polímero Formvar ha sido utilizado como capa de sacrificio para estos mismos propósitos, siendo en este caso exitosos en la fabricación de una ventana completa de Al_2O_3 suspendido de un grosor de entre 1 y 2 nm. Este espesor es suficiente para garantizar que no existen pequeñas fisuras y que la ventana se encuentra completamente sellada. De esta forma, ambos espesores fueron capaces de separar aire y agua a presión atmosférica de un vacío de $5 \cdot 10^{-8}$ mbar, funcionando correctamente por muchas horas y varios ciclos.

Finalmente, estas membranas fueron exitosamente testadas bajo condiciones reales de funcionamiento en la estación NAP-XPS de la línea 11.0.2 del sincrotrón ALS. Así, espectros XPS N 1s y O 1s de aire a presión atmosférica pudieron ser medidos.

6.2 Futuras líneas de trabajo

El trabajo de una tesis doctoral nunca se acaba por sí mismo, se cierra una vez que se acaba la financiación y los contratos laborales que han permitido la dedicación a este proyecto. De esta forma, siempre permanecen preguntas abiertas y, por encima de todo, nuevas ideas y líneas de trabajo. Algunas de ellas se exponen en los siguientes puntos:

- Tras el estudio de la interacción de CoO con HOPG y la capacidad de aquel de producir nano-litografía a baja temperatura, el siguiente paso parece obvio: trasladar estos resultados a nano-litografía sobre sistemas basados en grafeno. Desde el punto de vista tecnológico, esta nueva aproximación parece más aventajada que utilizar sustratos de grafito. Sin embargo, la interacción grafeno/sustrato (si no se encuentra libremente suspendido el grafeno) puede conllevar algunos retos, ya que las propiedades de éste podrían ser modificadas, y por lo tanto la interacción CoO/grafeno podría cambiar en función del material que sirva de soporte al grafeno.

- En cuanto a la interacción del ZnO con el sistema grafeno/Cu, aunque las relaciones cruzadas entre los diferentes elementos han sido clarificadas, no ha habido tiempo de aplicar estos resultados en dispositivos de conversión energética, objetivo inicial de la presente tesis doctoral. La falta de un crecimiento homogéneo del ZnO debido a las inhomogeneidades químicas y estructurales presentes en las láminas grafeno/Cu han impedido dar pasos en esta dirección. Sin embargo, la posibilidad de inducir cambios en el estado inicial de los sustratos de grafeno/Cu, y con ello modificar el comportamiento del crecimiento del óxido metálico, abre la puerta para superar este reto. La forma más sencilla de hacer esto consiste en el cambio de sustrato que soporta al grafeno, por ejemplo, transfiriendo éste a obleas de SiO_2, ya que el acople electrónico cambia completamente respecto al Cu metálico. En este sentido, el trabajo actual en nuestro laboratorio se focaliza en el estudio de los primeros

estadios de crecimiento de ZnO en los sistemas grafeno/SiO_2, GO y GO-reducido. El entendimiento profundo de qué parámetros químicos y estructurales del grafeno afectan al posterior crecimiento es la llave que realmente hace posible controlar el crecimiento y propiedades del óxido metálico, siendo entonces capaces de transferir este conocimiento a dispositivos reales, en los que heteroestructuras grafeno-ZnO de buena calidad puedan conservar y mejorar las propiedades de ambos materiales.

- Una vez que las membranas ultra-delgadas de Al_2O_3 han demostrado su viabilidad, el número de posibles ramificaciones del proyecto crece dramáticamente. En primer lugar, la elección de Al_2O_3 no fue arbitraria, sino que dependió de dos factores. Primero, desde el punto de vista químico, este óxido es muy inerte, asegurando una baja interacción con el medio, lo que convierte al Al_2O_3 en un excelente sustrato para materiales catalíticos. Segundo, el Al_2O_3 es un material muy sencillo de operar con la técnica ALD, asegurando un crecimiento capa a capa. Además, los óxidos metálicos son materiales más relistas que el grafeno en su uso como soportes de materiales catalíticos, y pueden ser de hecho interesantes por sí mismos, ya que muchos óxidos, como los CoO_x o TiO_x, muestran un importante comportamiento catalítico. Por otra parte, celdas de reacción que utilicen este tipo de membranas pueden ser utilizas en diferentes técnicas. Algunas aplicaciones y tecnologías en las que estas membranas podrían encontrar su uso en el estudio de gases, líquidos, soluciones, intercaras sólido/gas, sólido/líquido, etc. formando parte de celdas de reacción de distinto tipo serían: espectroscopias de electrones fotoemitidos, espectroscopias fotónicas como el Raman o XAS en modo de fluorescencia, microscopías de sonda de barrido como el KPFM o IR-sSNOM, o finalmente toma de imágenes TEM bajo condiciones reales de reacción.